

MINISTRY OF EDUCATION AND SCIENCE OF UKRAINE

Odessa I. I. Mechnikov National University

ФОТО ЭЛЕКТРОНИКА

PHOTOELECTRONICS

INTER-UNIVERSITIES SCIENTIFIC ARTICLES

Found in 1986

Number 10

Odessa
«Astroprint»
2001

The results of theoretical and experimental studies in problems of optoelectronics, solar power and semiconductor material science for photoconductive materials are adduced in this collection. The prospective directions for photoelectronics are observed.
For lecturers, scientists, post-graduates and students.

У збірнику наведені результати теоретичних і експериментальних досліджень з питань оптоелектроніки, сонячної енергетики і напівпровідникового матеріалознавства фотопровідних матеріалів. Розглянуто перспективні напрямки розвитку фотоелектроніки.

Для викладачів, наукових працівників, аспірантів, студентів.

Editorial board:

SMYNTYNA V. A. (editor-in-chief) — academician, Higher School Academy of Ukraine; **KUTALOVA M. I.** (executive secretary); **MAK V. T.** — Dr. Sci. (Physics and Mathematics); **LITOVCHENKO V. G.** — Associate Member of Ukrainian Academy of Sciences; **VIKULIN I. M.** — Dr. Sci. (Physics and Mathematics), Professor; **CHEMERESYUK G. G.** — Professor; **SHEINKMAN M. K.** — Associate Member of Ukrainian Academy of Sciences.

Address of editorial board:

Odessa I. I. Mechnikov National University 42, Pasteur str, Odessa, 65026, Ukraine

Здано у виробництво 13.03.2001. Підп. до друку 02.07.2001.
Формат 60×84/8. Папір офсетний. Гарнітура Літературна.
Друк офсетний. Ум. друк. арк. 13,25.
Тираж 100 прим. Зам. № 286.

Видавництво і друкарня «Астропринт»
(Свідоцтво ДК № 132 від 28.07.2000 р.)
65026, м. Одеса, вул. Преображенська, 24.
Тел.: (0482) 26-98-82, 26-96-82, 68-77-33.
www.astroprint.odessa.ua

J. KAPPLER, N. BARSAN, U. WEIMAR

Institute of Physical and Theoretical Chemistry, Center of Interface Analysis and Sensors,
University of Tübingen, Tübingen**STATE OF THE ART OF GAS SENSORS — MOX SENSORS
AS A WORKING EXAMPLE**

This paper summarises the state of the art of metal oxide sensors. The characteristics of the two principal types of MOX sensors, thick film and thin film MOX sensors, are described in detail. Recent results and the future potential of an innovative sensor type, which is based on a combination of thin and thick film technology, are discussed.

Introduction

In principle the measurement of gas composition is simple with very expensive and versatile instruments e. g. spectrometers. In contrary the increasing market volume and the expansion to new application fields calls for gas and odour monitor systems which are not only sensitive and selective but also small, inexpensive and with low power consumption. Metal oxide (MOX) semiconductor sensors are due to their prospects for cheap and easy detection and their known high sensitivity and stability a promising candidate. They consist of MOX sensing layers deposited on substrates provided with electrodes and heater and work at temperatures in the range 200...450 °C. The sensing principle is based on the observation that the conductivity of metal oxides depends on the ambient gas composition. Reducing gases release electrons into the semiconductor layer and thus reduce the electrical resistance; oxidising gases capture electrons from the sensitive layer and hence cause a resistance increase. The most established material is SnO_2 in combination with noble metal additives. Many reviews on semiconductor gas sensors are available [1, 2, 3].

State of the Art of MOX sensors

At present, two major technologies for sensor fabrication have been established. Thick film technology is used to produce sensitive MOX layers with a thickness of few to several hundred micrometers on ceramic substrates. Typical examples of thick film MOX sensors are shown in figure 1.

On the other hand, the physical vapour deposition of sensitive MOX on substrates, which have been fabricated in silicon technology, i. e. the production of MOX sensors in thin film technology results in MOX layers with a thickness in the range of some nanometers.

The major advantages of thick film sensors are their good sensitivity and stability as it can be seen by typical results shown in figure 2 and figure 3. The high stability is due to the fact that the properties needed for gas sensing (microstructure, doping,

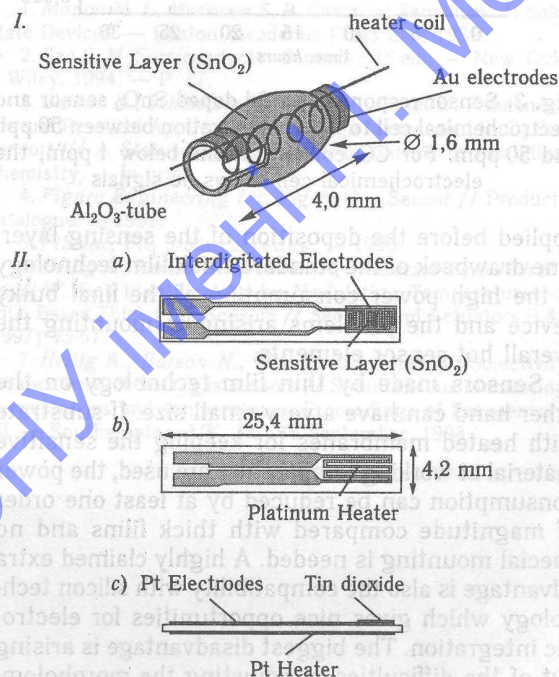
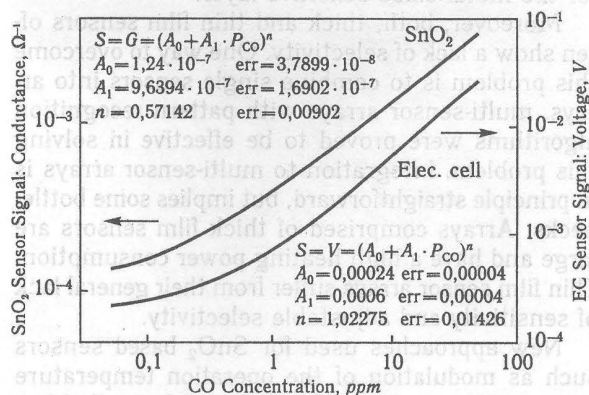


Fig. 1. Typical MOX thick film sensors:

I — Tubular Taguchi sensor; II — Flat ceramic sensor

Fig. 2. Stability of SnO_2 sensors and electrochemical cells:

The error bars represent the standard deviation for a period of 3 months. For low concentrations, the MOX sensor shows much higher stability

and small crystallite size) are already fixed by the chemical powder preparation and thermal treatments

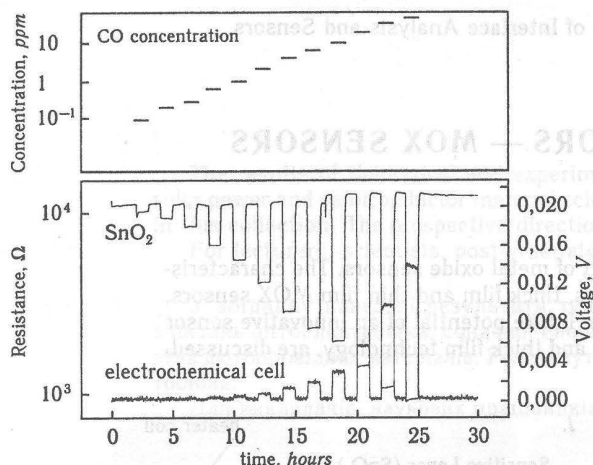


Fig. 3. Sensor response of a Pd doped SnO_2 sensor and electrochemical cell to CO concentration between 50 ppb and 50 ppm. For CO concentrations below 1 ppm, the electrochemical cell shows no signals

applied before the deposition of the sensing layer. One drawback of the standard thick film technology is the high power consumption of the final bulky device and the problems arising in mounting the overall hot sensor elements.

Sensors made by thin film technology on the other hand can have a very small size. If substrate with heated membranes for keeping the sensitive material at working temperature are used, the power consumption can be reduced by at least one order of magnitude compared with thick films and no special mounting is needed. A highly claimed extra advantage is also the compatibility with silicon technology which gives nice opportunities for electronic integration. The biggest disadvantage is arising out of the difficulties in adjusting the morphology of the sputtered or evaporated films for high sensitivity and stability. This seems to be a conceptual problem of the physical vapour deposition method for the metal oxide sensitive layer.

Moreover, both, thick and thin film sensors often show a lack of selectivity. One way to overcome this problem is to combine single sensors into arrays. multi-sensor arrays with pattern recognition algorithms were proved to be effective in solving this problem. Integration to multi-sensor arrays is in principle straightforward, but implies some bottlenecks. Arrays comprised of thick film sensors are large and have a high heating power consumption. Thin film sensor arrays suffer from their general lack of sensitivity and adjustable selectivity.

New approaches used for SnO_2 based sensors such as modulation of the operation temperature increase the number of sensor variables, called features [4, 5]. The key point in using this new approach is the low thermal inertia (as for micro-machined substrates) and a good sensitivity and stability of the sensing layer (as for thick film sensors).

Innovative sensor type

Recent developments led to innovative sensors fabricated by the combination of the two different technologies. The substrate is produced in silicon micro-machining technology onto which thick film sensing layers are deposited by drop deposition. A typical example for such a sensor is given in figure 4.

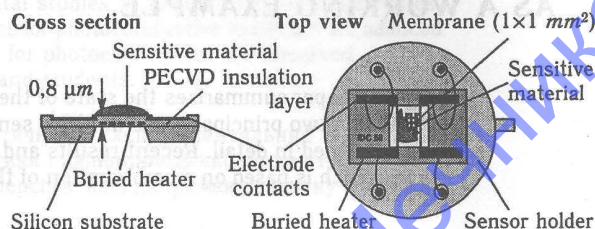


Fig. 4. Sensor produced by symbiosis of thick and thin film technology: Thick film layer on a micro-machined substrate

The resulting devices are powerful tools, which bear the advantages of both technologies. They are sensitive, long term stable, small, inexpensive due to a possible mass production, they show a low thermal inertia and a low power consumption (some ten milliwatts for temperatures between 200 °C and 400 °C). Due to this they do not only prevail the established sensor types in many application fields, in addition, their better functionality and the resulting selectivity increase open new application fields. Two ways to take advantage of this better functionality will be illustrated in the following by two typical examples.

If the sensor temperature of a micro-machined sensor is modulated sinusoidally, the resulting resistance pattern is characteristic for the ambient atmosphere. A subsequent fast fourier transform (FFT) can be applied to determine the first harmonics of the resistance pattern. If a radar chart of the normalised amplitudes of the first harmonics is drawn (as an example see figure 5), the shape of

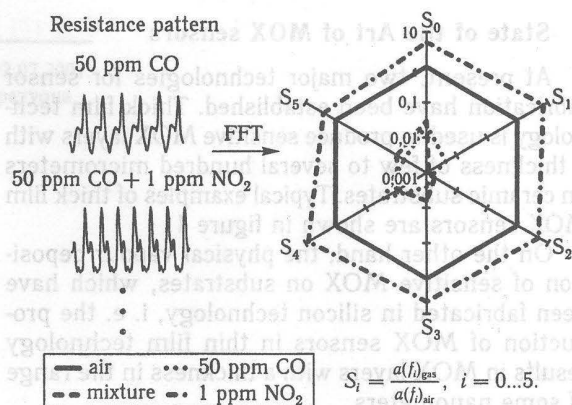


Fig. 5. Sinusoidal modulation of the sensor temperature:

The obtained sensor resistance shows characteristic patterns dependent on the ambient atmosphere. The polarplot of the normalised first harmonics — obtained by FFT — shows the discrimination of the gas mixtures

the polygon is characteristic for the ambient gas atmosphere. By comparing the amplitudes of the

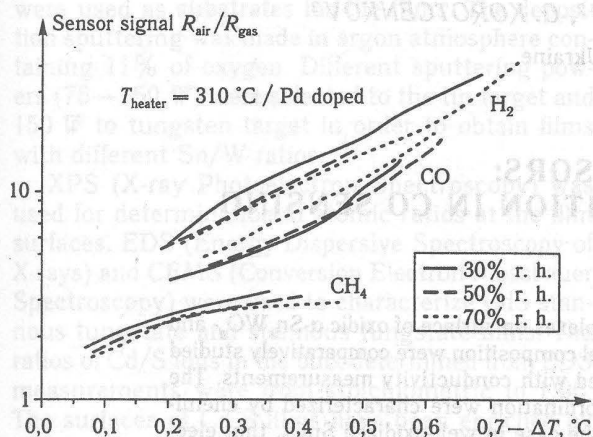


Fig. 6. Simultaneous resistance and sensor temperature measurements with a Pd doped SnO_2 sensor operated at 310 °C:

A discrimination between H_2 , CO and CH_4 for ambient humidities between 30% r. h. and 70% r. h. has been achieved

normalised harmonics a discrimination of different ambient gas atmospheres can be obtained. In figure 5, an example for such a discrimination between different ambient atmospheres (air, 50 ppm CO, 1 ppm NO_2 and 50 ppm CO + 1 ppm NO_2) is shown [6].

An alternative method for increasing the number of independent parameters, which can be obtained simultaneously by means of one micro-machined sensor is the simultaneous monitoring of sensor tem-

perature and sensor resistance, which are both depending on the gas interaction. A typical result [7], the discrimination of H_2 , CO and CH_4 , is shown in figure 6.

Summary and Conclusions

It has been shown that by combination of two established technologies — thick and thin film technology — innovative sensors can be fabricated, which do not only combine the advantages of thick and thin film technology, i. e. sensitivity, long term stability, small size, low price, low thermal inertia and low power consumption, but also lead to a selectivity improvement due to their better functionality.

References

1. Madou M. J., Morrison S. R. Chemical Sensing with Solid State Devices. — Boston: Academic Press Inc., 1989.
2. Sze S. M. Semiconductor Sensors / 1st edn. — New York: J. Wiley, 1994. — P. 17.
3. Barsan N., Schweizer-Berberich M., Gopel W. Fundamentals and Practical Applications to Design Nanoscaled SnO_2 Gas Sensors // A Status Report, Fresenius Journal of Analytical Chemistry. — In print.
4. Figaro Engineering Inc. Figaro Gas Sensor // Products Catalogue. — 1995.
5. FiS Inc. FiS products review. — 1995.
6. Heilig A., Barsan N., Weimar U., Schweizer-Berberich M., Gopel W. Gas Identification by Modulating Temperatures of SnO_2 Based Thick Film Sensors // Sensors and Actuators B 43 (1997) 45-51.
7. Heilig A., Barsan N., Weimar U., Gopel W. Selectivity enhancement of SnO_2 gas sensors // Simultaneous monitoring of resistances and temperatures, Proceedings of Eurosensors XII. — Southampton, UK, 13—16 September, 1998.

Cd_xS- AND Sn_xWO_y-BASED GAS SENSORS: THE ROLE OF CHEMICAL COMPOSITION IN CO SENSING

Electronic structure of chemisorption complexes on surface of oxidic α -Sn_xWO_y- and Cd_xS-based gas sensors with different elemental composition were comparatively studied by XPS, CEMS and IR-spectroscopy combined with conductivity measurements. The surface sites of Cd and Sn with different coordination were characterized by chemisorption of CO. It was found, differing from the case in well-oxidized SnO₂, that electrical conductance of Sn_xWO_y and Cd_xS films appeared to either increase or decrease when exposed to CO depended on concentration of surface Sn and Cd ions, partial pressure of analyzed gas and operating temperature.

It is argued that surface metallic species on the investigated films are responsible for oxidizing and reducing types of chemisorption reactions. The relative location of energy levels, formed in band gap by external orbitals of chemisorbed complex to Fermi energy was considered as determining factor for the observed different chemisorption mechanisms.

1. Introduction

The molecular understanding of sensing mechanisms on prototype materials has proved to be prerequisite for the development of new sensor systems. On the other hand, the role of adsorption/desorption mechanism and that of surface sites in creation of transducing conductance signal in semiconductor gas sensors is, to some extent, in a controversial state. For instance, two different models are commonly discussed to explain the role of metallic surface species at chemisorption and catalysis in influencing electronic charge-transfer reactions: metallic surface defect may act as specific sites for chemisorption and/or dissociation of molecules to be detected or they may pin Fermi energy.

The approach applying model of external orbitals within the band scheme of semiconductor was reported by author in Ref. [1]. In this case, the interaction between separate orbitals of adsorbate and semiconductor surface should be considered taking into account the energy position of orbitals in band gap of semiconductor. Therefore, studies of observed low-temperature dual response induced by CO in conductance of α -SnWO₄- and CdS-based sensors depending on partial pressure of analyzed gas and operating temperature together with similar effects caused by SO₂ [2] can be extended by considering the interaction between the sorption subsystem

characterized by local parameters of chemisorbed complex (e. g., configuration and location of external orbitals) and the electronic subsystem, described by collective characteristics of crystal (e. g., values of band bending and bulk position of conduction-band edge relative to Fermi level).

The values of collective parameters of crystal can be calculated on the basis of modified Volkenstein model [1, 3]. Local characteristics of the sorption subsystem can be estimated using methods of quantum chemistry, dealing with limited molecular systems, and considering the interaction between corresponding molecular fragments [4]. Cluster model is particularly convenient for the understanding of interactions between chemisorbed molecules and surface sites with different degree of coordination. For instance, metal atoms on extended faces, edges, steps and corners can be easily simulated with cluster model.

Cluster approach was used to study electronic structure of SnO₂ and to simulate adsorption of oxygen and carbon monoxide on surfaces of SnO₂ and CdS. Energy levels related to metallic surface species with different coordination and different kind of oxygen vacancies were described for the basic SnO₂ and CdS clusters together with levels originating from O₂ and CO adsorbates [5].

2. Experimental

The electro-hydro-dynamical technique was used for deposition of CdS thin films from CdCl₂ and (NH₄)₂CS solution on heated (480 °C) glass substrate [3]. A variation of stoichiometric composition of CdS films was obtained by mixing the initial solutions in different proportions of Cd/S ions.

Stannous tungstate films were grown by means of refractive co-sputtering with Balzers BAS 450 magnetron sputtering system, where tin target was

in d. c. mode and tungsten target in r. f. mode, respectively. Both thermally oxidized Si(111) and glass were used as substrates for the films. The deposition sputtering was made in argon atmosphere containing 11% of oxygen. Different sputtering powers (75—150 W) were selected to the tin target and 150 W to tungsten target in order to obtain films with different Sn/W ratios.

XPS (X-ray Photoelectron Spectroscopy) was used for determination of atomic ratios at the film surfaces. EDS (Energy Dispersive Spectroscopy of X-rays) and CEMS (Conversion Electron Mossbauer Spectroscopy) were used to characterize CdS stannous tungstate and stannous tungstate films. The ratios of Cd/S ions in the bulk determined from EDS measurements were from stoichiometric to 1,96. The surfaces of Cd_xS films have been enriched by metal species. Three different film types with Cd/S surface ratios of 1,6 (I-type), 2,4 (II-type) and 3,2 (III-type) were used in the study. The values of x from 0 to 1,5 were determined by EDS measurements for Sn_xWO_y thin films. The samples Cd_xS and Sn_xWO_y used in the study are identified in table 1.

IR spectra were recorded with Perkin-Elmer-577 spectrometer interfaced with a 3600 Data Station. The pellet was mounted in an IR cell, which allowed both heating and cooling *in situ* under vacuum or controlled atmosphere.

Two-point method was used in electrical conductivity measurements and wire contacts to stannous tungstate films were made with low-temperature gold paste. The computer-controlled measuring system employing the flow-through principle was used for varying gas concentration, heater voltages of the films and for data acquisition, handling and storage. The d. c. voltage of 1 V was used in conductance measurements of the films.

3. Results

The unusual dual response in case of exposure of n-type semiconductor CdS as thin films to CO and SO₂ in low-temperature interval (300—500 K) was reported by author in Refs. [2, 6]. Here we describe the dual response caused by carbon monoxide in conductance of Cd_xS and α-Sn_xWO_y thin films with different elemental composition on the surface.

Figure 1 shows the conductance response G_g/G_0 above the border temperature T^* and G_0/G_g below T^* to 100 ppm of CO in dry nitrogen (oxygen and humidity concentrations are few ppm) for three different CdS film types I, II and III. G_0 is the measured conductance in nitrogen and G_g — the conductance after exposure to CO. CO behaves as a reducing gas at all temperatures with I-type film, but has the border temperatures T^* at 300 K and 320 K with the II- and III-type films, respectively. With these two film types, the behavior of CO changes from reducing to oxidizing when temperature of films decreases through T^* . The enrichment of surface by Cd (III-type films) has decreasing effect

on T^* . The increase of the sensitivity to CO with increasing surface content of Cd is also shown in fig. 1, both above and below T^* .

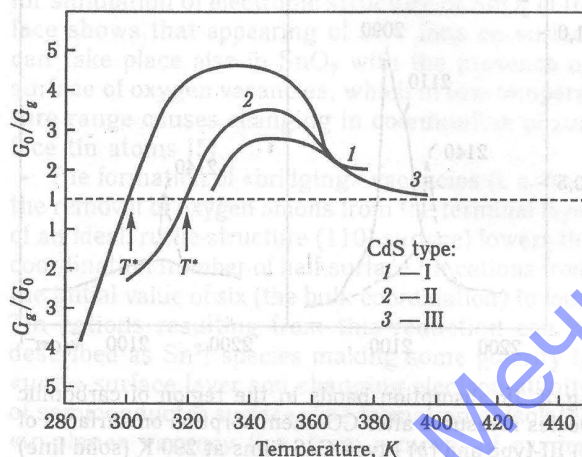


Fig. 1. Conductance response G_g/G_0 (and G_0/G_g) of I-, II- and III-type CdS films to 100 ppm CO in nitrogen at different temperatures:

T^* is the border temperature between oxidizing and reducing behaviour of CO

Figure 2 shows typical response (τ_{res}) and recovery (τ_{rec}) times (corresponding to a change of 90% of the total change) of III-type films in case of exposure to 100 ppm of CO in nitrogen at different temperatures. The temperature T^* plays important role in temperature behavior of both τ_{res} and τ_{rec} .

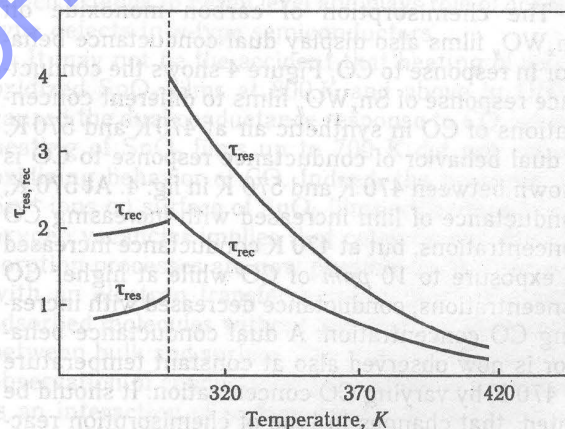


Fig. 2. Response (τ_{res}) and recovery (τ_{rec}) times of an III-type CdS film at different temperatures for 90% conductance changes after introducing and removing 100 ppm of CO in nitrogen, respectively

IR spectroscopy has been used in order to study possible changes in chemisorption of CO on CdS surfaces above and below temperature T^* . Typical results in absorption region of carbonic species, 2000...2300 cm^{-1} are shown in fig. 3 for I-type and III-type films. An exposure of III-type films to 100 ppm of CO in nitrogen at 290 K led to the immediate appearance of broad and intense absorption peak in region 2085...2115 cm^{-1} . The peak consisted

of two components at 2090 cm^{-1} and 2110 cm^{-1} . At the same time, the decrease was observed in con-

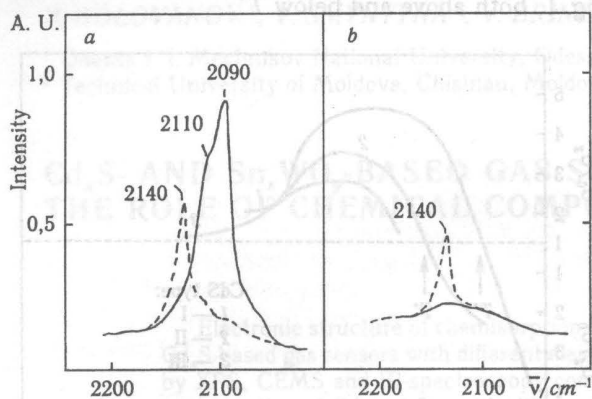


Fig. 3. IR absorption bands in the region of carbonilic species measured after CO chemisorption on surfaces of (a) III-type and (b) I-type CdS films at 290 K (solid line) and 340 K (dashed line)

ductivity of films. After removing of CO from the atmosphere, the band at 2110 cm^{-1} disappeared first, while the band at 2090 cm^{-1} decreased gradually and vanished after 15 min. A shift of adsorption peak up to 2140 cm^{-1} was found after increasing film temperature above T^* to 340 K. At the same time, inversion of CO behavior from oxidizing to reducing has been observed. IR spectra measured from I-type films, did show only a less intense peak at 2140 cm^{-1} (fig. 3, b) and was accompanied by reducing behavior of CO.

The chemisorption of carbon monoxide on Sn_xWO_y films also display dual conductance behavior in response to CO. Figure 4 shows the conductance response of Sn_xWO_y films to different concentrations of CO in synthetic air at 470 K and 570 K. A dual behavior of conductance response to CO is shown between 470 K and 570 K in fig. 4. At 570 K, conductance of film increased with increasing CO concentrations, but at 470 K conductance increased at exposure to 10 ppm of CO while at higher CO concentrations, conductance decreased with increasing CO concentration. A dual conductance behavior is now observed also at constant temperature of 470 K by varying CO concentration. It should be noted, that changes in type of chemisorption reaction from oxidizing to reducing was observed also on III-type of CdS thin films, when CO concentration has been increased from 5 to 100 ppm. As it is shown in fig. 4, both response and recovery times have large differences between 470 K and 570 K.

It was found that dual conductance response to CO did not depend only on temperature and CO concentration, but also on tin content in $\alpha\text{-Sn}_x\text{-WO}_y$ films. This is shown in fig. 5 where conductance ratios between synthetic air (G_0) and 250 ppm of CO in synthetic air (G_g) are plotted for different films in table 1, having different tin concentration in temperature range between 420 K and 670 K. Only III-type films show dual conductance behavior with

respect to temperature. The border temperature T^* is around 500 K. $\alpha\text{-SnWO}_4$ was found from SEM and

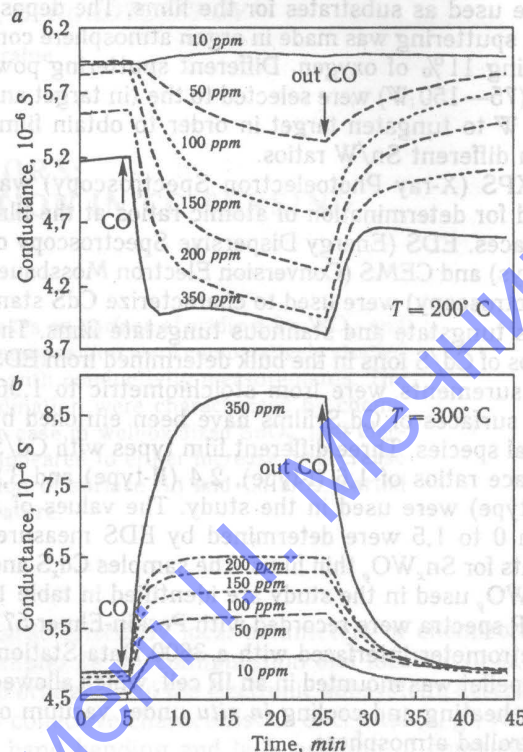


Fig. 4. Conductance response of III-type $\alpha\text{-Sn}_x\text{WO}_y$ film to different concentrations of CO in dry synthetic air (a) at 470 K and (b) — 570 K

AFM images to be the matrix phase in these films. The strong increase of the conductance ratio G_g/G_0 of pure WO_3 film (I-type film) at 320 K is shown in fig. 5.

The unusual conductance response of some SnO_2 thick films to CO after fast cooling process is de-

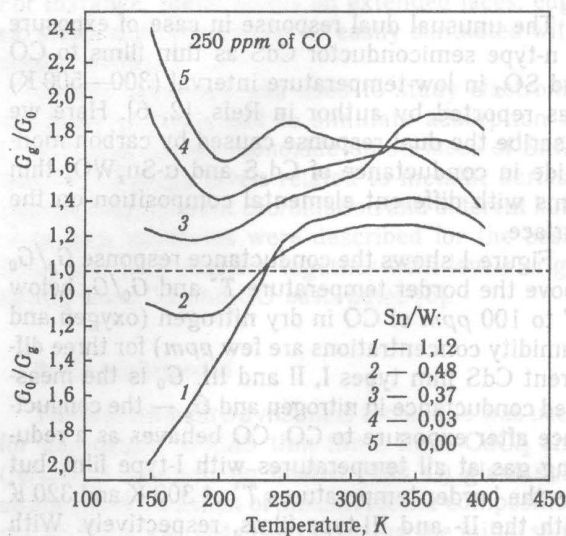


Fig. 5. Conductance response G_g/G_0 (and G_0/G_g) of different Sn_xWO_y films in table 1 ($x = \text{Sn}/\text{W}$ ratio) to 250 ppm of CO in synthetic air at different temperatures

scribed in Ref. [7]. The situation with those SnO_2 films resembles the present situation where the unusual dual conductance behavior appears only by films with high cation concentrations and high conductivity at temperatures below T^* . It should be noted, that study of SnO_2 films prepared by usual thick-film technology, shows that CO behaves as reducing gas increasing the conductance of n -type semiconductor on the well-oxidized (1 Torr of O_2 at 700 K for 10 min) SnO_2 films, but only heating at 800 K and above in UHV causes the dual conductance response to CO in low-temperature range (300—500 K).

4. Discussion

The oxidizing behavior of CO, in connection with dual response, is very difficult to explain. Its appearance in both oxidic $\alpha\text{-Sn}_x\text{WO}_y$ and CdS films may rule out changes in the amount of donors as the origin for the behavior. Different electrode materials used for CdS (indium) and $\alpha\text{-Sn}_x\text{WO}_y$ (gold) films may also rule out electrodes as the origin for the behavior. Then, the origin should be at the film surfaces. The abrupt changes in response and recovery times (fig. 2) and in CO chemisorption (fig. 3) at border temperature T^* also support this reasoning.

It is well known, that carbon monoxide in carbonylic form coordinates onto metal sites via carbon atom [8]. This fact along with appearance of oxidizing behavior of CO only on CdS and Sn_xWO_y films with high cation concentrations permits to conclude that metallic atoms at surface of investigated films play an important role in CO chemisorption.

The possibility for oxidizing behavior is that CO behaves as surface acceptor trapping electrons on surface of semiconductor. The red shift in carbonyl stretching band in fig. 3, *a*, when the CO behavior changes from reducing to oxidizing below T^* , is in agreement with that interpretation. The transfer of an electron from surface site to antibonding $2\pi^*$ orbital of CO leads to significant weakening of C—O bond and is attributed to the typical band in 2085...2115 cm^{-1} region.

The important consequence of the approach considering interaction between collective and local subsystems is the dependence of local energy levels, originating from adsorbates, on configuration and location of external orbitals of surface defects. Indeed, charge transfer reactions between adsorbates and semiconductor surface may cause the changes in collective electronic subsystem of semiconductor. On the other hand, changes in local subsystem i. e. in polar surface layers of ionic semiconductors and corresponding changes in electron affinity of semiconductor may reflect in injection rates of electrons from adsorbed species. For that reason, characterization of the surface sites, their coordination and charge state are of great importance for atomistic understanding of sensing mechanisms.

It is possible to conclude from CEMS results that, differing from the case in SnO_2 , tin is the divalent form Sn^{+2} in $\alpha\text{-Sn}_x\text{WO}_y$ films. Cluster approach used for simulation of electronic structure of SnO_2 (110) face shows that appearing of Sn^{2+} ions on surface can take place also in SnO_2 with the presence on surface of oxygen vacancies, which in low-temperature range causes changing in coordination of surface tin atoms [5].

The formation of «bridging» vacancies (i. e. from the removal of oxygen anions from the terminal layer of an ideal, rutile-structure (110) surface) lowers the coordination number of half surface tin cations from the initial value of six (the bulk coordination) to four. Tin cations resulting from this reduction can be described as Sn^{2+} species making some polarity to «unit» surface layer and changing electron affinity of semiconductor surface. The formation of isolated «in-plane» vacancy (i. e. from removal of oxygen anion from what is normally the second, tin-containing, atomic plane of ideal (110) surface) lowers coordination number of one adjacent surface tin cation from four to three, while the other two nearest neighbours go from fivefold to fourfold coordination.

It was shown in ref. [9] that defect electronic states which appeared low in band gap for annealing temperatures less than 800 K in UHV arised from «bridging» oxygen vacancies. Heating at 800 K or above causes the formation of «in-plane» oxygen vacancy. The «in-plane» oxygen vacancy is characterized by occupied states higher in band gap which extends to Fermi level and plays role of donor-type defects in n -type semiconductors.

It may not be the accident that heating of well-oxidized SnO_2 films at 800 K and above in UHV caused the dual conductance response to CO, while heating of SnO_2 films up to 700 K did not cause oxidizing behavior of CO. Indeed, the presence of Sn^{2+} ions on surface of SnO_2 films with «bridging» oxygen vacancies implies that catalytic and chemisorption processes are now possible on the surface with an electron transfer between Sn^{+2} ions and adsorbed molecules without any electron exchange between bulk and surface. The important factor for observation of conductance decreasing in this case is an interaction of surface defects with collective subsystem of crystal, e. g., location of external orbitals of such surface defects near Fermi level, as it takes place with formation of «in-plane» oxygen vacancies.

The temperature-stimulated conductance measurements on freshly deposited CdS III-type films in pure nitrogen exhibit Arrhenius slope of 0,05 eV, related to cadmium interstitial species [3]. $\alpha\text{-Sn}_x\text{WO}_y$ III-type films also feature by Arrhenius slope of 0,05...0,07 eV, corresponding to donor-type defects related to Sn^{2+} ions [6]. Therefore, on investigated films CdS and $\alpha\text{-Sn}_x\text{WO}_y$, Cd^+ and Sn^{2+} surface species play dual role of centers determining dark conductivity behavior and basic sites for chemisorption. This fact provides a good opportunity for studies

of interaction between local and collective subsystems in semiconductor surface-active structures.

The increase of operating temperature above 320 K for CdS films and above 450 K for $\alpha\text{-Sn}_x\text{WO}_y$ films caused the considerable reduction of electron presence in external orbitals of metallic species and, hence, the shift of Fermi level towards the middle of band gap promoting the changes in type of chemisorption reaction from oxidizing to reducing.

The atoms with the lowest coordination on surface are the most reactive towards the interaction with gas phase. On such «active centers», reactions take place with appreciably reduced activation energies. These atoms or groups of atoms normally represent a modest fraction of total number of exposed ones and are thought to be located on edges, steps, corners or other defects of microcrystals or microparticles. The III-type CdS and Sn_xWO_y films, enriched by Cd and Sn species, may have the high number of those presented on such edges, steps, corners and other surface defects, where coordination number can be exceptionally low. Conversely, at surface of I-type film Cd and Sn atoms are basically with higher coordination at crystal faces. For that reason, different features in IR spectra, measured from CdS films with different surface composition, may be considered in terms of interaction of adsorbates with surface Cd atoms having different coordination.

The peaks fitting results for the IR spectrum show presence of two types of chemisorbed complexes on the surface of I-type CdS films. One absorbing at 2090 cm^{-1} , is assigned to Cd(0)CO complex stabilized on interstitials reduced cadmium species with low coordination number (Cd_i). The other, absorbing at 2110 cm^{-1} , is attributed to Cd(I)CO acceptor-type complex chemisorbed above surface cadmium ions with higher coordination in crystal. The last ones featured by reduced density of valence electrons on external orbitals resulting of donation into semiconductor conduction system and chemisorption take place with trapping of conduction electron from the collective subsystem of the crystal. The spectra peak at 2140 cm^{-1} has been attributed to the donor-type Cd(I)CO chemisorbed complexes, which are characteristic of less reduced areas, where electron availability is poor, while the acceptor-type Cd(I)CO complexes related to spectra peak at 2110 cm^{-1} characteristic of more reduced areas, where electron availability was large. This assumptions corresponded to the results of IR, VIS, UV study of CO chemisorption reported in ref. [8].

The charge-transfer reactions involving surface sites with high coordination may proceed with capture of conductance electrons from collective electronic subsystem, as it takes place, for instance, for chemisorption of acceptor-type Cd(I)CO complexes. On the other hand, interaction between chemisorbed molecules and surface sites with low degree of coordination has the high probability for charge — transfer reactions to occur only in local subsystem at semiconductor surface (i. e. chemisorption of Cd(0)CO complexes). Indeed, the differences between

between t_{rec} ($\sim 3\text{ min.}$) for conductivity changes (fig. 2) and time requested for disappearance of the peak at 2090 cm^{-1} , corresponding to Cd(0)CO complexes ($\sim 15\text{ min.}$) after evacuation of CO show that decreasing of conductance caused mainly by Cd(I)CO complexes, related to the peak at 2110 cm^{-1} , involving capture of conductance electron, while Cd(0)CO complexes does not influence essentially on the changes in conductance.

The change of stoichiometric composition towards the decrease of metal component (I-type films) leads to the essential decrease of concentration of reduced Cd, defects with low coordination number and promotes chemisorption of CO on bare surface cations. For this reason, the band at $2085\text{--}2115\text{ cm}^{-1}$ has vanished together with acceptor-type of chemisorption reaction. The decrease of total concentration of surface metallic species may lead to decrease of sensitivity also in donor-type region and the intensity of the peak at 2140 cm^{-1} , which has been observed experimentally (figs. 1, 3).

It is well known, that CO preferentially attacks low-coordinated surface ions. Therefore, the inversion of charge state of chemisorbed complex together with shift in an IR spectra caused by increasing of CO partial pressure may be connected with the sequential interaction of CO molecules with the highly coordinated cation adsorption sites, when Cd_i defects became completely occupied. Oxidizing behavior of CO is in fact predominant at the lowest coverage.

Donor-type M(I)CO complexes are generally characterized by low stability, owing to the nature of the ion — carbon interaction, essentially in the highly charged ions, and to the electron donor properties of CO molecule. Conversely, acceptor-type M(I)CO and M(0)CO complexes are characterized by the higher stability, owing to the ability of low valence ions and metal atoms to form p -bond with CO molecule. For that reason, the change of type of chemisorption reaction should cause inversion of the ratio between t_{res} and t_{rec} , that corresponded to observed experimental results (fig. 2).

In the same way as the ions and/or the atoms with different coordination numbers show different reactivity towards simple molecules, they can show also different response to excitation. As discussed in Ref. [10], radiative decay pathways are more efficient for low-coordinated ions than for those with high-coordination. The ions with high coordination have the larger number of bonds to crystal and they couple more strongly with phonon and electron transitions of lattice, providing high probability for non radiative decay and charge — transfer reaction.

Indeed, the behavior of IR spectra peaks at 2090 cm^{-1} and 2110 cm^{-1} after evacuation of gas atmosphere shows that at the earlier stages of treatment only sites with larger coordination number became free from surface contaminants (carbonyl groups). Absorption at 2090 cm^{-1} assigned to the Cd(0)CO complexes was still observed. At the final step of treatment (after 15 min) the ab-

sorption due to CO molecules adsorbed above low coordinated surface sites was also decreased to zero level. The situation with CO chemisorption resembles the situation where CdS films with different elemental composition were characterized by oxygen chemisorption [11]. In that case, the increase of stability of molecular oxygen, chemisorbed at low coordinated cadmium atoms led to «frozen-in» states of adsorbates at surface.

5. Conclusions

From combined measurements of XPS, CEMS, IR spectroscopy and conductance changes, we deduce that surface metallic species are the basic centers for carbon monoxide chemisorption on CdS films. Interaction with low coordinated Cd atoms features by increased stability of chemisorbed complexes. Reduction of coordination number in the case of CO chemisorption, leads to inversion in type of chemisorption reaction from reducing to oxidizing. Sn^{2+} ions in Sn_xWO_y films are responsible for dual response in the case of exposure of Sn_xWO_y films to CO.

References

1. Golovanov V., Smyntyna V. Interaction between collective and local subsystems in semiconductor surface-active structures // *Sensors and Actuators B*. — 1994. — 25, № 1—3. — P. 647—652.

2. Golovanov V., Gudis A., Smyntyna V. Semiconductor sensor based upon CdS // *Russian J. Analit. Chem.* — 1991. — 46. — P. 2374—2379.

3. Golovanov V., Serdiuk V. et al. Mechanism of oxygen chemisorption on the surface of CdS polycrystalline films // *Ukr. Phys. J.* — 1988. — 33, № 3ю — P. 157—162.

4. Rantala T. T., Rosen A., Hellsing B. A finite cluster approach to the electron-hole pair damping of the adsorbate vibration: CO adsorbed on Cu(100) // *J. Electron Spectroscopy and Related Phenomena*. — 1986. — 39. — P. 173—181.

5. Rantala T., Golovanov V., Lantto V. A cluster approach for the adsorption of oxygen and carbon monoxide on SnO_2 and CdS surfaces // *Tech. Digest, 5th Int. Chemical Sensors Meet.* — Rome, Italy, 11—14 July, 1994. — P. 666—669.

6. Solis J. L., Golovanov V., Lantto V., Leppavuori S. A Study of dual conductance response to carbon monoxide of CdS and $\alpha\text{-SnWO}_4$ thin films // *Physica Scripta*. — 1994. — T. 54. — P. 248—251.

7. Lantto V., Rantala T. S. Equilibrium and non-equilibrium conductance response of sintered SnO_2 samples to CO // *Sensors and Actuators B*. — 1991. — 5. — P. 103—107.

8. Ghiotti G., Boccuzzi F., Chiorino A. Surface characterization of Cu/ZnO catalysts: IR, VIS, UV study of CO chemisorption / Che M., Bond G. C. *Adsorption and Catalysis on Oxide Surfaces*. — Amsterdam: Elsevier Science Publishers B. V., 1985.

9. Cox D. F., Fryberger T. B., Semancik S. Oxygen vacancies and defect electronic states on the SnO_2 (110)- 1×1 surface // *Phys. Rev. B*. — 1988. — 38. — P. 2072—2083.

10. Zecchina A. and Scarano D. Electronic and vibrational states at the surface of ionic and covalent solids / Che M., Bond G. C. *Adsorption and Catalysis on Oxide Surfaces*. — Amsterdam: Elsevier Science Publishers B. V., 1985.

11. Golovanov V., Smyntyna V., Mattogno G., Kasiulis S., Lantto V. Oxygen interaction of CdS-based gas sensors with different stoichiometric composition // *Sensors and Actuators B*. — 1995. — 26—27. — P. 108—112.

REAL NANODIMENSIONAL SILICON PARTICLES: CLUSTER APPROXIMATION

It is proposed that silicon sphere-like atomic cluster (AC) system of intermediate size ($10 < n \leq 100$) correspond to structures, which are «bricks» of core of the real nanometers range particles. A simplified parameterisation density functional theory (PDFT) scheme for calculations of electronic structure of these clusters is presented. The small computational effort of PDFT treatment allows to perform molecular dynamics (MD) simulations of clusters up to a hundred atoms. The accuracy of the method is illustrated by the results of calculations for Si-AC with different sizes.

Silicon nanodimensional structures

In recent years, optical properties of silicon nano structures (Si-NS) have been the subject of intense investigations, because the quantum confinement of electrons and holes leads to linear and non-linear optical properties, much different from those of bulk crystals. Since Canham's discovery of visible light emission from porous Si (see ref. [1]), great deal of efforts have been devoted to investigate the optical properties of Si-NS. There are direct experiments on the geometry of the Si-NS [1, 2].

Besides, optical data [3] indicated the existence of atomic clusters (AC) in films and was mediated by the localized electronic states associated with the clusters. In particular, there were observed peculiar Raman spectra in Si-SiO₂ systems, being different from those of bulk c-Si, a-Si, and micro-crystalline Si, but very similar to the density of state spectra of Si₃₃ and Si₄₅ [4]. The experimental data strongly suggest that these films are the systems of AC much smaller than about 2 nm embedded in SiO_x matrices. Although the size and size distribution of the clusters are not known, introduction of various size of clusters randomly into SiO₂ thin films may generate localized electronic states. If these previous results are taken into account, it is rather straightforward to attribute presently observed $\ln \sigma$ (σ — conductivity) versus $T^{-1/4}$ (T — temperature) behaviour to the VRH (variable range hopping) conduction through the localized electronic states associated with the C, Si, and Ge clusters [3]. As Si concentration increases, the slopes (B) of $\ln \sigma$ versus $T^{-1/4}$ straight lines decrease. Since the increases in Si concentration lead to the increases in the size and/or number of Si clusters, the decreases in B may be attributed to the increase in size and/or number of Si clusters. Thus optical data indicated the existence of clusters in the films, the present VRH conduction was thought to be mediated by the localized electronic states associated with the clusters.

In the other hand, small silicon clusters of atoms

(Si-AC) have recently become the subjects of intense study [4—13] in the hope that their properties can provide new insight to physical and chemical behaviour of the nanodimensional materials [1—3]. Probably, the Si-NS consists from Si-AC structures. The large surface-to-volume ratio and the large step and defect density are expected small Si-AC to be highly reactive. Moreover, the flexibility afforded by the small number of atoms could give rise to novel structures, which can possibly lead to the synthesis of artificial materials with uncommon properties.

In this paper a new approach to the study of small, intermediate-size Si-AC and Si-NS is proposed. Some calculations [6—8] predict that Si-AC in these size range have tetrahedral bonded network structures whereas others predict more compact structures. Taking the above said into consideration we based on the following premises. First, for small Si-AC ($n \leq 10$) it is possible to construct a tree with core of fourfold-co-ordinate atoms, similar to bulk Si (for example, see [11]). Second, for larger Si-AC ($10 < n \leq 100$) it is possible to construct a network containing a core of fourfold-co-ordinate atoms, similar to bulk Si, which are surrounded by a surface of atoms with optimal (threefold or fourfold) co-ordination, similar to Si surfaces (as [9]). Structures of exceptional stability can be obtained when exactly all surface atoms participate in the surface reconstruction and any change in the size (addition or removal of atoms) introduces «defects» similar to those on c-Si surfaces. To construct a real Si-NS, our model used: 1) a core of fourfold — co-ordinated atoms, similar to bulk Si (complete Si-NS), or 2) 5-, 6- and 7-membered Si-rings and their combinations for the construction of surface blocks (empty Si-NS).

Reactivity and size effects of the atomic silicon clusters

The nature of Si-NS and reconstruction of Si-AC in the range size $1 < n \leq 100$ (n is a number of atoms in AC) remains open to intense debate too. Si-AC is small piece of nature in the range of nano-

meters and is not molecule, and it can not to represent itself as the bulk material also. For example, J.R. Chelikowsky and Phillips J. C. [8, 12] has suggested that the small Si-AC was metallic rather than covalent in nature. This is due to their physical size. Clusters of covalently bound non-metals usually have more open geometries that satisfy the specific highly-directional bonding requirements of silicon and germanium. Si-AC form prolate structures up to $n \approx 25 \dots 35$ [4, 10], but then rearrange to more spherical morphologies [7, 8]. In fact Si-AC appears to be more closely related to the high-pressure metallic phases of bulk silicon than to the diamond structure [6, 7, 12]. These works appears to define metallic clusters as those, which have bond angles of 60° .

The absorption spectra from 0,94—5,58 eV are obtained for gas-phase neutral Si-AC containing 18...41 atoms [10]. The spectra of all clusters are essentially identical. The optical signature of these clusters has much in common with that of c-Si. These spectra are unexpected: theoretical calculations predict [6] wide variation in structure over the size range, but experimentally Si-AC has numerous strong sharp absorption which does not shift in energy over Si-AC size range. Furthermore, the partial spectra of Si-AC are smaller than Si_{18} and larger than Si_{41} . The spectral signature common to Si_{18} — Si_{41} persists for sizes up to at least 70 atoms. This spectral similarity is completely unexpected. Because of a molecular point of view, these clusters span sufficiently large size range to have structural differences, which should show up in their optical spectra.

From these data follows that Si-AC in this size range are expected to undergo rapid structural change because of the large surface/volume atom ratio. Nonetheless, major changes occur in the geometric structures of Si-AC as a function of size below 50 atoms. Such changes are mirrored in the photoelectron spectra measured for Si-AC anions containing 3...12 atoms [8, 12]. Structural differences of Si-AC (similar size range) for positively charged AC have also been inferred from mobility and chemical reactivity data [10]. Thus, the electronic spectra of neutral Si-AC larger than Si_{18} do not any show evidence for any structural changes. This leads us to conclude that all of these small silicon clusters share one or more common structural entities. One possibility is that small Si-AC shares a common bonding network, which persists and extends as the cluster grows in size.

Yet, the absorption spectrum of crystalline silicon has much in common with the silicon cluster spectra. Strong absorption features at energies above 3 eV dominate both Si-AC and c-Si spectra. The 800 K bulk spectrum, which is red shifted by the thermal expansion of the lattice, more closely corresponds to cluster spectrum. Nonetheless, a number of discrepancies between the bulk and cluster spectrum should still be explained. For instance, the cluster spectrum has six peaks between 3,0 and 5,6 eV

whereas the bulk spectrum contains only three features. Furthermore, a comparison with 800 K bulk spectrum neglects effects of lattice contraction and quantum confinement which are known for Si-NS and these characteristics do not change as a function of AC size range.

Given that Si-AC containing only few tens of atoms are too small to have either band structures or bulk excitations, the similarity of their optical signature to crystalline silicon is unexpected. Moreover, these spectra are far more similar to spectrum of the most stable crystalline form of Si than to the spectra of other Si forms.

Furthermore, optical spectra of small InP-AC [10] exhibit like absorption's analogous to a-InP [13]. Other forms of more compact Si such as the β -tin and primitive hexagonal metallic phases [14] are also candidates for comparison in light of theoretical calculations, which predict high co-ordination numbers in small Si-AC. But none of these structures have optical properties, which are as closely related to Si-AC spectra as c-Si. And Si-AC spectra cannot be easily compared to Si surface spectra [10].

Besides, it is reasonable to be concentrate on models for experimentally observed sizes of exceptional stability (so-called «magic numbers» (MN) [15]). MN is observed and reflects differences in Si-AC [6, 7, 9, 11]. MN can be understood basing on structures predicted theoretically and observed experimentally. Si-AC of somewhat larger size (for example, $10 < n \leq 100$) shows the dramatic changes in their chemical reactivity, depending on the number of atoms in the cluster.

Using thermodynamic force field the equilibrium structures of Si-AC ($n = 11 \dots 25$) were calculated in [12]. The interesting outcomes about structure of these clusters were obtained. Since Si-AC containing 7 atoms (and $n = 13$ or $n = 19$) clusters has pentagonal pattern (or icosahedral plus associated face capping). These results are fully consistent with MN found in the reaction rates for addition of first C_2H_4 molecules to Si_n^+ clusters.

These experimental and theoretical data showing the spectral regularity of Si-AC challenge all known theoretical models, which used for the construction of space structures in the size range $10 < n \leq 100$. This leads to the intriguing conclusion that silicon clusters containing tens of atoms are derived from a common structural entity. We do not know the nature of this entity but its spectral similarities to the bulk crystalline spectrum provide the proving ground for further theoretical investigation. However, this is not optimal practical procedure for cluster with larger sizes: for a system with many degrees of freedom, the problem of identifying the lowest-energy configuration becomes computationally difficult and depends on the sizes of clusters. Si-AC with size range $10 < n \leq 100$ requires to search the possible new calculation schemes. In addition to this, in order to elucidate the properties of their AC, the development of different specific models has the great importance.

These facts became the motivation of our computer researches. To attack this problem we investigated electronic and geometry structures of Si-AC theoretically using parameterised density-functional theory (DFT).

PDFT simulation method

To study the dynamics of the clusters we offer the approximate calculation scheme. This is the density-functional theory (DFT) in the realisation of Kohn and Sham (KS) [16], using few empirical parameters [17]. This method, which named parameterised DFT — PDFT, is based on Hartree — Fock scheme plus a proper treatment of electron correlation. The use of only a few parameters minimises the effort for the determination of the parameters, it yields the close relation to full *ab initio* DFT schemes (for example, GAMESS [16]). This is guarantee of the good «transferability» of the parameters, going from one system to another. On the other hand, the use of some approximations in connection with few empirical parameters makes the scheme computation extremely fast. PDFT allows also the study of dynamical processes through the coupling with molecular dynamics (MD) [19, 20].

The method is based on an LCAO ansatz for the KS wave functions:

$$\Psi(\vec{r}) = \sum_{\mu} C_{\mu} \zeta_{\mu}(\vec{r} - \vec{R}_{\mu}), \quad (1)$$

here ζ_{μ} — atomic orbital, which we shall utilise as basic wave functions (BWF) in the form [9, 11]:

$$\zeta_{\mu} = N_{\mu} r^{\alpha_{\mu}-1} e^{-\alpha_{\mu} r} Y_{lm}, \quad (2)$$

where N_{μ} is constant; α_{μ} is Slater's parameter which defined on algorithm [11]; Y_{lm} are spherical harmonic functions, n^* is effective quantum number. The LCAO ansatz leads to the secular problem. The matrix elements of Hamiltonian $H_{\mu\nu}$ and the overlap matrix elements $S_{\mu\nu}$ are defined as

$$H_{\mu\nu} = \langle \zeta_{\mu} | \hat{H} | \zeta_{\nu} \rangle, \quad S_{\mu\nu} = \langle \zeta_{\mu} | \zeta_{\nu} \rangle, \quad (3)$$

In the offered method PDFT, Hamiltonian of the system is:

$$\hat{H} = \hat{T} + V_{\text{eff}}(\vec{r}), \quad (4)$$

where \hat{T} is operator of kinetic energy, $V_{\text{eff}}(\vec{r})$ is effective KS potential. It is approximated as a simple superposition for potentials of neutral atoms V_j^0 :

$$V_{\text{eff}}(\vec{r}) = \sum_i V_i^0(\vec{r}_i), \quad (5)$$

where $r_j = |\vec{r} - \vec{R}_j|$. Such approximation for potential is consistent with the following approximations in the matrix elements of Hamiltonian,

$$H_{\mu\nu} = \begin{cases} \langle \zeta_{\mu} | \hat{T} + V_i + V_k | \zeta_{\nu} \rangle, & \mu \cap \nu \in \{i, k\} \\ 0 & \text{otherwise} \end{cases} \quad (6)$$

Thus, only two-centre terms in Hamiltonian matrix are considered, but all two-centre terms $H_{\mu\nu}$, $S_{\mu\nu}$ are calculated exactly.

The approximations formulated above lead to the same structure of the secular equations as in (non-orthogonal) tight-binding (TB) [19] or Iterative Extended Huckel (IEHT) [11] schemes, but it has the important advantage that all matrix elements are calculated, and non of them is handled as an empirical parameter. P. Blaudeck and co-workers [18] shows that the quality of results, especially concerning binding energies, can be improved distinctly by using basis functions and potentials from slightly «compressed atoms» rather than from free atoms. This «compression» is achieved by the introduction of an artificial additional repulsive potential of the form $(r/r_0)^*$ in atomic calculations. Eschrig originally developed such potential for optimisation of LCAO-LDA [18] band structure calculations. The main effect of this term is a damping of long-range part of basis functions. Practically, it optimises the basis functions concerning the approximations, mainly neglecting the 3-centre terms.

The total energy $E[\rho(\vec{r})]$ may be written in a form using KS eigenvalues ϵ_i :

$$E[\rho(\vec{r})] = \sum_i^{\text{occ}} \epsilon_i - \frac{1}{2} \left[\int d^3r V_{\text{eff}} \rho - \int d^3r V_{\text{ext}} \rho \right] + E_{\text{xc}} - \frac{1}{2} \int d^3r V_{\text{xc}} \rho + E_n, \quad (7)$$

The external potential V_{ext} is electron-nucleus potential, E_{xc} is exchange-correlation energy, V_{xc} is corresponding potential, and E_n stands for nuclear repulsion energy.

The representation of the density and the potential as superposition of atomic-like contributions, i. e.: $\rho = \sum_i \rho_i$, $V = \sum_i V_i$ allows to write the total energy in the following form:

$$E[\rho(\vec{r})] = \sum_i^{\text{occ}} \epsilon_i - \frac{1}{2} \sum_i \sum_j \int d^3r V_i \rho_j - \frac{1}{2} \sum_i \sum_j \int d^3r \frac{Z_i \rho_j}{r_{ij}} + \frac{1}{2} \sum_i \sum_j \int d^3r \tilde{V}_{\text{xc}ij} \rho_j + \frac{1}{2} \sum_i \sum_{j \neq i} \int d^3r \frac{Z_i Z_j}{R_{ij}}, \quad (8)$$

R_{ij} is inter nuclear distance: $R_{ij} = |\vec{R}_i - \vec{R}_j|$, Z_i is charge which has i -atom, ρ_j is electronic density, localised on j -atom, ϵ_i is one-electron energy.

For large inter nuclear distances, the electron-nucleus energy compensates strongly the nuclear repulsion energy, and two-centre terms with potential vanish also: $\int d^3r V_i \rho_j = 0$, $j \neq i$, due to the screening of the potential. Assuming additionally that $\int d^3r \tilde{V}_{\text{xc}ij} \rho_j = 0$ and writing the total energy $E[\rho(\vec{r})]$ of single atom in the corresponding form as (8), one can evaluate the binding energy approximately by

KS eigenvalues ϵ_B and KS energies ϵ_{n_i} of atomic orbital n_i :

$$\epsilon_B = E - \sum_i E_i \approx \sum_i \epsilon_i - \sum_i \sum_{n_i} \epsilon_{n_i}. \quad (9)$$

The binding energy calculated in this way and the binding energy from full SCF-LDA calculation, using algorithm GAMESS [16] ($\Delta E = \epsilon_B - E_B^{\text{GAMESS}}$) for Si-AC are in good agreement, as it was illustrated in [17]. The differences between these energies increase with decreasing internuclear distance (r). However, this increase is rather smooth and the difference has practically vanishes already at about $3/2$ times the equilibrium distance (r_0).

With PDFT approximations the forces on atoms (F_m) can be calculated easily using the LCAO coefficients ($C_{i\mu}$) and the derivatives of Hamiltonian and overlap matrices ($\partial H_{\mu\nu}/\partial x_i$, $\partial S_{\mu\nu}/\partial x_i$), respectively:

$$F_m = \sum_i \sum_{\mu} \sum_{\nu} C_{i\mu} C_{i\nu} \left[-\frac{\partial H_{\mu\nu}}{\partial x_i} + E \frac{\partial S_{\mu\nu}}{\partial x_i} \right] + \sum_{j \neq i} \frac{\Delta E_{ij}}{\partial x_i}. \quad (10)$$

Having the forces, MD simulations may be performed easily (see e. g. [19]). In order to obtain relaxed atomic geometries for the models described below, we have performed extensive energy-minimization calculations. The PDFT Si-AC database includes total energies of clusters, energy fragmentation, overlap integral matrix, charge on the atoms etc.

We have tested a new PDFT approach to the total energy of complicated atomic geometry, which have included the electron-electron interaction in self-consistent manner.

Results of the Si-NS simulation

We start with bulk-like Si-AC size of 4 atoms and examine the cluster-size dependence of electronic states for Si up to 60 atoms. AC-size dependence of calculated energy levels, local densities of states, and charge distributions are examined for Si-AC, it is found that 10-atom cluster, which had three possible space configuration [7, 8] was good enough AC-core to identify and to study optical spectra [10]. To study regularity of behaviour of big AC (among of them the AC with $n=18...41$) it is very important to define properties of Si-AC with 10 atoms. The PDFT method (with different basis sets: *STO-3G*, *HF/3-21G*) was utilised for the analysis of geometry and electronic structures of Si-AC with range size $1 < n \leq 60$.

Also, the surface elementary Si-AC models are investigated. The PDFT method is applied to isolated 5-, 6- and 7- atomic rings reconstructed as a fragment of Si(111) 2×1 surfaces of materials crystallising in the diamond structure. In fig. 1 the example of simulation of 5-atomic silicon ring is reduced. We researched possibility of derivation for planar Si-cyclic 5-AC structure. The energy transition is present in fig. 1. The displacement of the 1, 4, 5-th atoms is equal $\Delta R_{kj} = 0,11 \text{ \AA}$; for 2-nd and 3-rd atoms — $\Delta R_{kj} = 0,18 \text{ \AA}$. Let's note that as sur-

face Si-atom is moved inward, the hybridisation of local orbital on surface atom is changed to keep

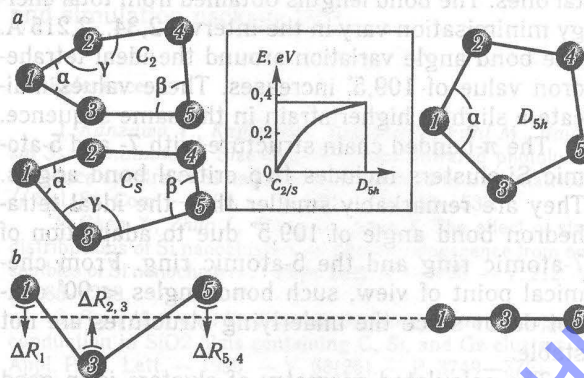


Fig. 1. The illustration of possible space orientation of 5-membered cyclic Si-AC and transition energy E (a), and direction of the displacement of Si-atom for obtaining of planar (b)

them orthogonal. Therefore, we forced the study for dehybridization of Si-atomic sp^3 -orbitals from the equivalent form in terms of the relative position of Si-atoms. The detail algorithm to carry out the estimations of hybridization degree is described in [11]. Clearly, this is consistent with the intuitive consideration that upon relaxation (to the planar position) dangling-orbital becomes more p_z -like and back-bonds become more s -like tending toward the trigonal sp^2 form. Dangling-orbitals on raised atoms become s -like, while those on lowered atoms become more p_z -like. The calculated lengths of Si-Si bonds (r_{kj}) and angles between chemical bonds (α, β, γ) for the most probable space configurations are written in table 1.

Table 1

Bond lengths r_{kj} (in \AA) and bond angles α, β, γ (in deg) for 5-membered Si-AC with different symmetry (C_2, C_s, D_{5h}). Basis set is *STO-3G* (or *HF/3-21G*)

Si-AC	$r_{kj}, \text{\AA}$			α	β	γ
	k	j	r_{kj}			
C_2	1	3	2,234	110,0°	103,5°	103,6°
	3	5	2,271	(110,2°)	(103,3°)	(103,6°)
	5	4	2,269			
C_s	1	3	2,234	108,5°	108,1°	101,0°
	2	4	2,271	(109,0°)	(108,0°)	(101,0°)
	5	4	2,269			
D_{5h}	1	3	2,215	108,0°	108,0°	108,0°
	3	5	2,215	108,0°	108,0°	108,0°
	5	4	2,215			

The ideal, relaxed, and reconstructed cyclic i -atomic ($i=5, 6, 7$) Si-clusters bound between itself are dealt with too. The minimum-energy surface geometry's resulting in the framework of π -bonded chain model have been compared with atomic positions extracted from other calculations [5, 6] and especially from experimental data [4].

Altogether the theoretical Si-AC structure seems to be somewhat less strained than the experimental ones. The bond lengths obtained from total energy minimisation vary in the interval 2,34...2,215 Å. The bond angle variation around the ideal tetrahedron value of 109,5° increases. These values indicate a slightly higher strain in the same sequence.

The π -bonded chain structure with 7- and 5-atomic Si-clusters includes two critical bond angles. They are remarkably smaller than the ideal tetrahedron bond angle of 109,5° due to adaptation of 7-atomic ring and the 5-atomic ring. From chemical point of view, such bond angles < 90° cannot occur since the underlying structures are not stable.

The calculated geometry of clusters is in good agreement with results from corresponding DFT *ab initio* calculations, provided using GAMESS algorithm [17]. The nearest neighbour distances in Si lattice are obtained correctly [9]. Energetic positions and equilibrium distances of high-pressure modifications of silicon are described rather well [12].

In the next step, Si-NS was constructed. For inter Si-polyhedral clusters (Si-PC) interaction the pairwise additive approximation (PAA) [5, 15] was used. The calculation analyses of Si-PC, which has spherical symmetry, were performed. Formally, the total energy of an ensemble of N Si-AC can be written as:

$$E_N = \sum_{i<j} E_{ij}(r_{ij}, \Omega_{ij}) + \sum_{i<j<k} E_{ijk}(r_{ij}, r_{ik}, r_{jk}, \Omega_{ijk}) + \dots + \sum_{i<j<k<l} E_{ijkl}(r_{ij}, r_{ik}, r_{il}, r_{jk}, r_{jl}, r_{lk}, \Omega_{ijkl}) + \dots \quad (11)$$

where the first term is the sum of all two-body (pair, E_{ij}) interactions (each as function of the separation r_{ij} and relative orientation Ω_{ij} of the two «ball»). The three-body term E_{ijk} provides the difference between the actual energy for a trio of Si-PC in a given orientation and the sum of the three pair potential terms; similarly, E_{ijkl} is the corresponding correction to give the correct energy for a quartet of «ball»; and so on. For the system which consist of Si-PC, the pairwise additive approximation by only using the first term in this expansion was used. NS consists of Si-PC with an average diameter d (as shown in fig. 2). For choice of potential (E_{ij} , E_{ijk}) in stick and ball model may be recommend [21].

In the conclusion we will report the results of PDFT-calculations for nanometers particles of silicon. The geometrical characteristics of Si_{60} , having symmetry I_h , are listed in table 2. «Si-ball» is constructed from twelve 5-atomic Si-rings (5-Si-AC) and twenty 6-Si-AC. Using PDFT we have estimated diameter (d) such Si-PC.

Let's note that in table 2 Si-Si inter atomic distances in 6- and 5-AC rings are reduced. These distances are designated as \bar{r}_{66} and \bar{r}_{65} , respectively. The calculated bond lengths and diameter of Si-AC are given together with the errors in table 2. These data are in quite good agreement with the other




Structure	Geometry	Calculation scheme
NDSP particle		
NS surface structure		PAA
Polyhedral Si-AC		MD PDFT MIEHT— α

Fig. 2. Atomic cluster as a block of nanodimensional structure

Table 2
Geometry characteristics of I_h — Si_{60} Si-AC

\bar{r}_{66} , Å	\bar{r}_{65} , Å	Δr , Å	d , Å	Method and basis Set
2,189	2,226	0,037	$12,3 \pm \pm 0,4$	MIEHT— α [11]
$2,062 \pm \pm 0,04$	$2,152 \pm \pm 0,04$	$0,085 \pm \pm 0,01$	$11,4 \pm \pm 0,4$	STO—3G PDFT
$2,213 \pm \pm 0,04$	$2,301 \pm \pm 0,04$	$0,088 \pm \pm 0,01$	$11,6 \pm \pm 0,4$	HF/3—21G PDFT

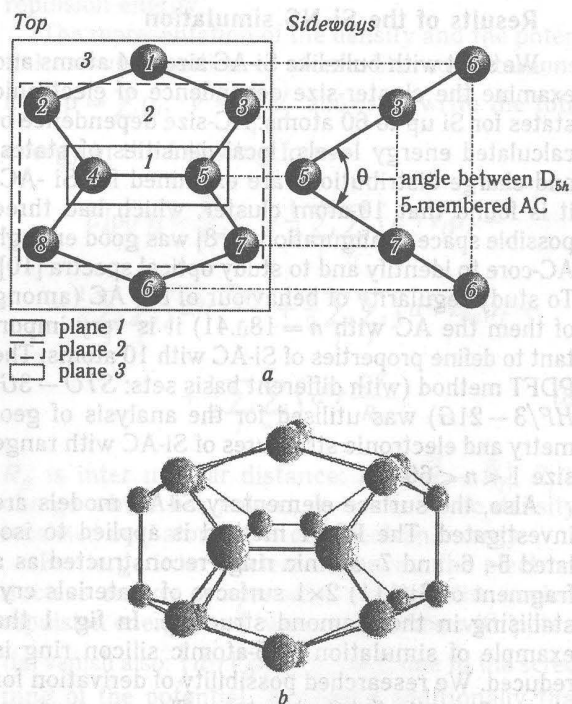


Fig. 3. Cluster surface «blocks», which consist 5-Si atoms (a), and one of polyhedral Si-AC which consist 5-membered rings (b)

results (see ref. [5–7]). Si-Si bond length was generally overestimated by about 2%, and diameter of Si-PC was calculated in the range of the errors 3,5%.

We have analysed others polyhedral AC of silicon too. Among them are follows: 1) $\text{Si}_{50}(\text{D}_{5h}) - \Delta E = 0,0868 \text{ eV}$; 2) $\text{Si}_{30}(\text{C}_{2v}) - \Delta E = 0,252 \text{ eV}$; 3) $\text{Si}_{24}(\text{D}_3) - \Delta E = 0,404 \text{ eV}$. Here ΔE denotes the difference between total energy of PC Si_{60} and Si_{50} (Si_{30} , Si_{24}). 60-atomic Si-structure has appeared more stable than 50, 30, 24 Si-AC. The given fact testifies that the probability of synthesis for such stable structures as AC $I_h - \text{Si}_{60}$ is extremely high.

Therefore, polyhedral silicon structures took part in creation of Si-NS and was identified experimentally [2, 3]. The fig. 3 is demonstrated the space orientation of Si-AC, created Si-PC structure. Let's note, that the angle (θ) between cluster fragments (in given case Si-5-AC) depends on the type of atoms, which passivate the dangling bonds of silicon atoms. This problem demands the separate reviewing.

Summary

We have tested the modified DFT scheme to the total energy of complicated atomic geometry, which included some useful simplicity. Due to the neglect of all three-centre integrals and the use of short-range repulsive interaction potential in energy calculations, the method is computationally extremely fast. It gives reliable results for geometry's, binding energies and vibration frequencies for different AC. The method is applied to building of Si-PC from the Si-surface «blocks» reconstructed as planar. The bond lengths and angles are obtained with an error less than 5%.

Three important reconstruction steps have been considered: 1) isolated Si-cyclic AC (with 5-, 6- and 7-atoms), 2) Si-PC which consists from Si-cyclic AC, and 3) the cluster model of Si-NS. We found reasonable agreement of the different structures for i -fold Si-AC rings per surface elementary cell. However, there are also characteristic discrepancies with respect to the order of magnitude for several effects and quantities: buckling amplitude and bond length in the chain, relaxation in the first and the second atomic layer, bond angles. But these problems will be argued in the following publications.

PDFT scheme may be viewed as «hybrid» between pure *ab initio* method — based on DFT — and the use of purely empirical potentials. It has the advantage over the latter in overcoming the «transferability» problem, and it requires much less computational effort than full *ab initio* methods. And even in comparison to traditional TB schemes [20], which are computationally as fast as our method, the transferability is much better, since only very few parameters are used and their determination is straightforward.

Acknowledgements. It is a pleasure to thank Dr. V. Yanchuk for useful discussions. I would like

also like to thank Dr. Tsukuru Ohwaki from University of Tokyo for sending me GAMESS algorithm and simulation package DFT.

References

1. Kanzawa Y., Kageyama, Takeoka S., Fujii M., Hayashi S., Yamamoto K. Size-dependent near-infrared photoluminescence spectra of Si nanocrystal embedded in SiO_2 matrices // Sol. St. Com. — 1997. — V. 102. — P. 533–537.
2. Chen X., Zhao J., Wang G., Shen X. The effect of size distributions of Si nanoclusters on photoluminescence from ensembles of Si nanoclusters // Phys. Lett. A. — 1996. — V. 212. — P. 285–289.
3. Fujii M., Inoue Y., Hayashi S., Yamamoto K. Hopping conduction in SiO_2 films containing C, Si, and Ge clusters // Appl. Phys. Lett. — 1996. — V. 68(26). — P. 3749–3751.
4. Jarrold M. F., Constant V. A. Silicon cluster ions: evidence for a structural transition // Phys. Rev. Lett. — 1991 — V. 67. — P. 2994–2997.
5. Theoretical aspects and computer modelling of the molecular solid state / Ed. A. Gavezzotti. — N. Y.: Wiley. — 1997. — P. 33–61.
6. Tomanek D., Sun C., Sharma N., Wang L. Thermal effects in the Equilibrium Structure and Size Distribution of Small Si Clusters // Phys. Rev. B. — 1989. — V. 39. — P. 5361–5365.
7. Jarrold M. F. Nanosurface Chemistry on Size-Selected Silicon Clusters // Science. — 1991. — V. 252. — P. 1085–1092.
8. Chelikowsky J. R. Transition from metallic to covalent structures in silicon clusters // Phys. Rev. Lett. — 1988. — V. 60. — P. 2669–2673.
9. Kovalchuk V. V., Chislov V. V., Yanchuk V. A. Cluster Model of the Real Silicon Surface // Phys. Stat. Sol. (b). — 1995. — V. 187. — P. K47–K50.
10. Rinnen K.-D., Mandich M. L. Spectroscopy of neutral silicon clusters, $\text{Si}_8 - \text{Si}_{41}$: Spectra are remarkably size independent // Phys. Rev. Lett. — 1992. — V. 69. — P. 1823–1826.
11. Kovalchuk V. V. IEHT- α investigation of the silicon surface // J. Ukr. Phys. — 1995. — V. 40, № 7. — P. 716–719.
12. Chelikowsky J. R., Phillips J. C. Chemical reactivity and covalent-metallic bonding of Si_n^+ ($n = 11 - 25$) Clusters // Phys. Rev. Lett. — 1989. — V. 63. — P. 1655–1656.
13. Garcia-Ruiz J. M., Louis E., Meakin P., Sander L. M. Growth Patterns in Physical Sciences and Biology // NATO ASI Series B: Physics. — N. Y.: Plenum Publ. — 1993. — v. 304. — 456 p.
14. Vansant E. F., van der Voort P., Vrancken K. C. Characterisation and chemical modification of silica surfaces. — Amsterdam: Elsevier, 1995. — 334 p.
15. Encyclopedia of Computational Chemistry / Eds. P. Schleyer, H. Schaefer, N. Handy. — N. Y.: Wiley. — 1998. — P. 10–455.
16. Schmidt M. W., Baldrige K. K., Boatz J. A., Gordon M. S., Jensen J. H., Koseki S., Matsunaga N., Su S., Windus T. L., Dupuis M., Montgomery J. General Atomic and Molecular Electronic Structure System // J. Comp. Chem. — 1993. — V. 14. — P. 1347–1363.
17. Kovalchuk V. V., Burjak D. V., Krapiva N. V. Molecular dynamics investigation of the polyhedral structures // Scientific Transactions of the Odessa Polytechnic University. — 2000. — № 2(11). — P. 182–187.
18. Blaudeck P., Freuenheim Th., Porezag D., Seifert G., Fromm E. Calculation of Molecules, Clusters and Solids with DFT—LDA Scheme // J. Phys. Condensed Matter. — 1992. — V. 4. — P. 6368–6371.
19. Laasonen K., Nieminen R. M. Molecular dynamics the tight-binding approximation // J. Phys.: Condens. Matter. — 1990. — V. 2. — P. 1509–1520.
20. Feng Y. P., Ong C. K., Poon H. C., Tomanek D. Tight-Binding Molecular Dynamics Simulations of Semiconductor Alloys: Clusters, Surfaces and Defects // J. Phys. Cond. Matt. — 1997. — V. 9. — P. 4345–4351.
21. Khaldeev G. V., Petrov S. N. Computer simulation of the electrochemical processes on the interphases // Uspekhi Chimii. — 1998. — V. 67. — P. 107–124.

TWO MODELS OF QUANTUM BRIDGES CONNECTED WITH SEMICONDUCTORS OR METALS

Two models describing transport and absorption processes that occur in nanoscale fragments of electrical circuits, pulled adsorbed molecules, atomic or molecular chains connecting electrodes are proposed. Discrete chain model of molecular bridge between metallic electrodes considers quantum jumps between atoms containing the chain. The potential approach is represented by three-dimensional Kronig—Penney model. The conductivity theory is developed in supposition that the main contribution into electron transfer belongs to non-equilibrium affinity populated states of the bridge. Current—voltage and thermodynamical characteristics are calculated for different cases. Explanations for experimentally obtained step-like dependencies in I — V characteristics and its asymmetry are made. Charging effect and Coulomb blockade effect are discussed. It is shown the essential role of transitions between different bridge's charge states.

1. Introduction

Semiconductor wires, pulled linear molecules, point contact atomic chains connected with prepared metal or semiconductor surface are examples of quantum fragments embedded into electric circuits [1—8]. These elements may play a role of main functional unites of the circuit sufficiently determining its properties. The subject of our investigation is the most important property of such «bottle neck»-like fragments that electronic structure depends strongly on small number of captured electrons. Statistically quantum bridges are systems with alternating particles number determined by interaction with contacting reservoir. In recent paper [3] the conductivity of adsorbed bistertiothene molecule junction (fig. 1) fabricated by suspended micro-bridges technique combined with mechanically controlled break method was studied experimentally. The results obtained have shown several interesting features including stepwise dependence of current-voltage characteristics and sometimes its asymmetry relatively the sign of applied voltage.

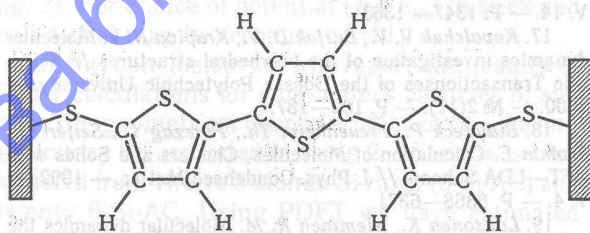


Fig. 1. Bistertiothene molecule as a quantum fragment of electric circuit investigated experimentally in [3]

An example of pure quantum circuit is represented in fig. 2, *a*. A polar molecule embedded into the closed chain can play the role of short pulse voltage source. Quantum voltage source polariza-

tion may be controlled by resonant external electromagnetic field switching the molecule into long lived triplet state. The current pulse arising is caused

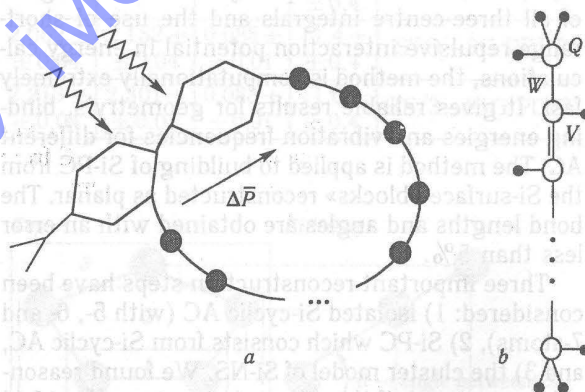


Fig. 2. A dipole molecule as emf source in an electric circuit:

a — complete electric circuit with inverse asymmetric molecule as voltage source activated by light. ΔP is dipole momentum difference in ground and excited states. Zigzag show light causing dipole changing; *b* — a model of hydrocarbon linear molecule. W is transfer amplitude between carbon atoms, V is the same inside the elementary cell, Q is the same for end cells

by the difference of dipole moments in ground and excited states. The stabilization of excited state may be implemented by means of voltage bias between ends of the molecule (fig. 1). Transition process in excited state modifies affinity spectrum of molecule that in turn influences on the electron transport through the molecular bridge.

Our results show that the voltage applied modifies significantly the electronic structure of all kinds of bridges and leads to nonequilibrium redistribution of states population. The theory developed here for contact and transport phenomena in quantum bridges is based on the conception of mesoscopic

system's charge states. Two approaches are discussed in the work for pulled quantum bridges: potential model and discrete chain model (DCM). Potential model proposed describes semiconductor quantum wire connecting semiconductor or metal electrodes shown in fig. 3. The model is based on

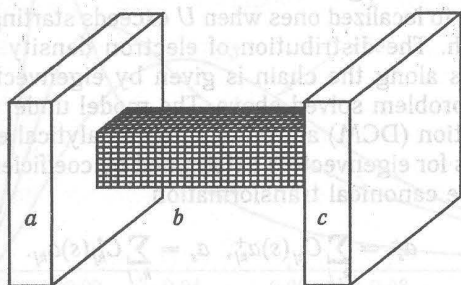


Fig. 3. Semiconductor quantum wire:

a, c — electrodes, b — quantum wire, elementary cells are shown by lines

exactly solved problem for terminated Kronig—Penney crystal.

The DCM approach describing molecular or atomic bridges starts from initial (atomic) generalized affinity energy E_i for external reservoir electron, chain geometry and intersite transfer matrix elements V_i (fig. 4). Index i represents the number of electrons left the chain, E_i is exited states band

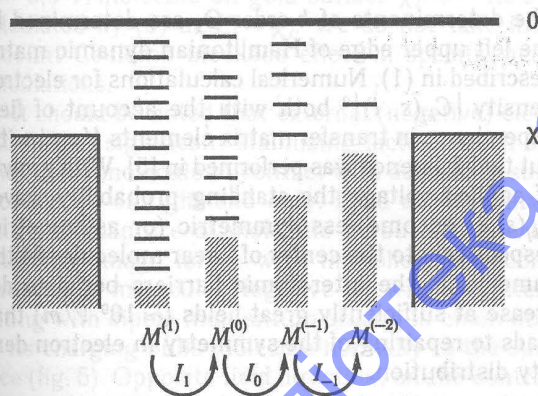


Fig. 4. A scheme of quantum bridge charge states:

$M^{(i)}$ marks quantum bridge charge state with i electrons left the bridge, I_i corresponds to ionization energy of respective state

center for one-fold ionized molecule. Quantum bridge capturing or losing electrons in absorbing process or due to applied voltage changes weakly its charge states $M^{(i)}$ [5, 8]. General picture of charge state transitions for ionized quantum bridge contacting with metal surface is represented in the fig. 3, where χ is electrode chemical potential, I_1 is the first ionization potential, I_0 is affinity energy.

Pulled linear molecular chains adsorbed on prepared metal or semiconductor surface may be very interesting due to its physical properties and possible applications. Extremely large effective surface of these objects (fig. 5) in case its density is sufficiently high makes them attractive as adsorbing

elements for gaseous sensors. We have proposed in [6, 7] to use the forest of molecular chains directed

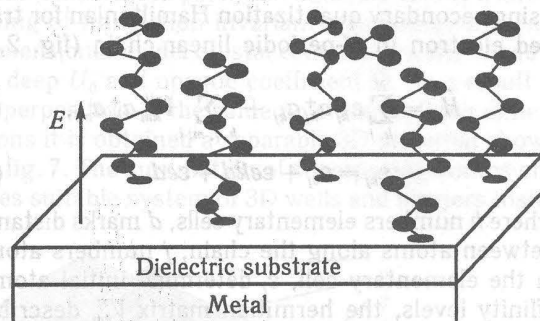


Fig. 5. The forest of linear molecules adsorbed on conducting surface:

Molecular chain forest on substrate. Dark colour marks an adsorbed gas molecule.

by external electric field for adsorbing, storage and testing small concentration of gas molecules in surrounding medium. Adsorbed long molecular constructions are most compact and small contenders for conducting elements of quantum circuits, STM tips and neutral networks. Meanwhile many properties of 1D systems adsorbed in electric field on a semiconductor or dielectric surface demand further theoretical investigations: the conductivity problem at low frequencies, chain-surface local states and states arising due to the capture of air molecules by the chain, electron energy spectrum in external field, mobility of electrons, affinity spectrum, chain topology, interaction with vibrational modes etc.

In the paper we propose theoretical consideration for some of these problems. Our DCM analysis is based on the electron Hamiltonian for a chain with N-sites. The conductivity of quantum bridges is investigated theoretically using the obtained exact solutions for electron states of a linear chain in steady state electric field. It is taken into account quantum interaction between electronic subsystem and either metallic or semiconductor electrodes playing the role of electrons reservoirs. The supposition about main contribution of affinity states into the conductivity of point contacts both semiconductor wires and molecular or atomic junctions lies in the ground of the theory proposed. Transfer matrix method was used out the framework of approximation of translation invariance and periodic boundary conditions. In nearest-neighbour approximation for chain atoms interaction and hopping probability, the current-voltage characteristics are calculated at different temperatures and electronic structures of the chain. The Coulomb blockade effect is taken into account phenomenologically in a self-consistent procedure. It is represented the explanation of current-voltage asymmetry observed experimentally in [3]. It is shown the leading role of field modification of affinity spectrum for conductivity of molecular bridges. Irreversible states population and current Coulomb charging is calculated.

II. Adsorbed linear molecule in electric field

We will describe the problem of field influence using secondary quantization Hamiltonian for trapped electron in N -periodic linear chain (fig. 2, b)

$$\hat{H}_0 = \sum_{k,j} \varepsilon_{kj} a_{kj}^+ a_{kj} + \sum_{k,j,m,i} V_{km}^{ij} a_{kj}^+ a_{mi}, \quad (1)$$

$$\varepsilon_{kj} = \varepsilon_0 + \varepsilon e k d + \varepsilon e d_i, \quad (2)$$

where k numbers elementary cells, d marks distance between atoms along the chain, j numbers atoms in the elementary cell, ε_i determine initial atomic affinity levels, the hermitian matrix V_{km}^{ij} describes interatomic electron transfer, d_i is length of absorption bonds on the left-hand side of linear molecule, ε represents applied electric field.

The matrix of Hamiltonian (1) will be wrote in nearest neighbour approximation for an adsorbed molecular chain like polyacetylene $R-(CH)_n-R$. In the model under consideration the transfer between elementary cells is possible through carbon atoms only; the amplitude of the process equals W , hopping amplitudes inside elementary cells equal to V (Q is its value for end atoms). Considering $U = \varepsilon(Nd - d + d_i)$ as the whole voltage between chain ends we can obtain the energy dispersion equation

$$(\lambda_l, -v_l) \prod_{k=2}^{N-1} \hat{\Lambda}_k \begin{pmatrix} v_r' \\ \lambda_r' \end{pmatrix} = 0, \quad \hat{\Lambda}_k = \begin{pmatrix} \mu_k & v_k \\ \lambda_k & 0 \end{pmatrix}. \quad (3)$$

containing transfer matrix product instead of transfer matrix power. Here

$$\begin{aligned} \mu_k &= (\varepsilon_0 - E + \varepsilon e k d + \varepsilon e d_i) \times \\ &\times (\varepsilon_1 - E + \varepsilon e k d + \varepsilon e d_i) - V^2; \\ v_k &= -\lambda_k = W \cdot (\varepsilon_0 - E + \varepsilon e k d + \varepsilon e d_i); \\ v_r' &= \varepsilon_0 - E + U - \varepsilon e d_i) \times \\ &\times ((\varepsilon_0 - E + U - \varepsilon e d_i)(\varepsilon_1 - E + U - \varepsilon e d_i) - 2Q^2), \\ \lambda_r' &= -W \cdot (\varepsilon_0 - E + U - \varepsilon e d_i)^2, \end{aligned} \quad (4)$$

Using canonical transformation and the procedure described in [5] the equation (3) is transformed to convenient view obtained in absence of external field

$$e^{f_1} (v_r y_{22} - \lambda_r y_{21}) (\lambda_0 y_{11} - v_0 y_{12}) - e^{f_2} (v_r y_{12} - \lambda_r y_{11}) (\lambda_0 y_{21} - v_0 y_{22}) = 0, \quad (5)$$

where f_1 and $f_2 = -f_1$ are eigenvalues of matrix \hat{F} in the power of exponent

$$\begin{aligned} \hat{F} &= L n \prod_k \hat{\Lambda}_k, \\ \prod_{k=2}^{N-1} \hat{\Lambda}_k &= \exp \left(\sum_k \begin{pmatrix} \frac{\lambda_1^k \ln \lambda_1^k - \lambda_2^k \ln \lambda_2^k}{\lambda_1^k - \lambda_2^k} & \frac{1}{\lambda_2^k - \lambda_1^k} \ln \frac{\lambda_2^k}{\lambda_1^k} \\ \frac{1}{\lambda_2^k - \lambda_1^k} \ln \frac{\lambda_2^k}{\lambda_1^k} & \frac{\lambda_1^k \ln \lambda_1^k - \lambda_2^k \ln \lambda_2^k}{\lambda_2^k - \lambda_1^k} \end{pmatrix} \right). \end{aligned} \quad (6)$$

Here $\lambda_i^k = \frac{\mu_k + (\mu_k^2 + 4\lambda_k \cdot v_k)^{1/2}}{2}$ are eigenvalues of transfer matrix taking part in the product. The condition $\mu_k^2 + 4\lambda_k \cdot v_k = 0$ determines imaginary boundary between extended band states and that localised due to the influence of extended field. As another

matter for the states localization may serve structure defects including both ends of the chain. The calculations show that with growth of electric field ε the extended states energy range is narrowed in directions from band edges to the middle. At the same time the band width increases to the value of applied voltage U . The last extended states transform to localized ones when U exceeds starting band width. The distribution of electron density amplitudes along the chain is given by eigenvectors of the problem solved above. The model under consideration (DCM) allows to obtain analytical expressions for eigenvectors determined by coefficients C_{kj} of the canonical transformation

$$a_s^+ = \sum_{k,j} C_{kj}(s) a_{kj}^+, \quad a_s = \sum_{k,j} C_{kj}^*(s) a_{kj}.$$

The summation is performed on chain cells k and on atoms j inside the elementary cell. Index $s = 1, 2, \dots, N$ numbers in the work that electron affinity states. One can obtain the coefficients C_{kj} analytically using the well known Kramer's rule and revealing determinants corresponded to each variable.

$$C_{k1} = d_{k-1} \cdot Q V \prod_{i=k+1}^N (-\varepsilon_{0i} W), \quad C_{k2} = C_{k1} \frac{V}{E_s - \varepsilon_0}, \quad (7)$$

$$d_{k-1} = \frac{1}{\Theta_{k-3}} (e^{f_{k-3}} (v_r y_{22} - \lambda_r y_{21}) (\lambda_0 y_{11} - v_0 y_{12}) - e^{-f_{k-3}} (v_r y_{12} - \lambda_r y_{11}) (\lambda_0 y_{21} - v_0 y_{22})). \quad (8)$$

The determinants of k -order Θ_k are determined by the left upper edge of Hamiltonian dynamic matrix described in (1). Numerical calculations for electron density $|C_{kj}(s, i)|^2$ both with the account of field dependence in transfer matrix elements V and without that influence was performed in [5]. With growth of applied voltage the standing probability waves $C_{kj}(s, i)$ become less symmetric (or asymmetric) respectively to the center of linear molecule. At the same time, the interatomic barriers begin to decrease at sufficiently great fields ($\approx 10^9$ V/m) that leads to repairing of the symmetry in electron density distribution.

III. Electronic specific heat of adsorbed molecules

The contribution of affinity electrons captured by free molecule into the specific heat C_{aff} is determined by expression

$$C_{\text{aff}} = T^{-2} \sum_s (E_s - E_1)^2 n_s (1 - n_s), \quad (9)$$

where $n_s = \left(\exp \left(\frac{E_s - E_1}{T} \right) + 1 \right)^{-1}$, E_1 — the lowest level that plays the role of system chemical potential.

The temperature dependence of C_{aff} calculated by (9) in absence of electric field for long 20-atomic chain is represented in fig. 6, curve 1. Energy parameters of chain were taken $\varepsilon_0 = -4.3$ eV, $V = 0.02$ eV. In case of adsorbed molecule its specific heat

C_{aff} depends on affinity band position relatively to surface chemical potential. We suppose here

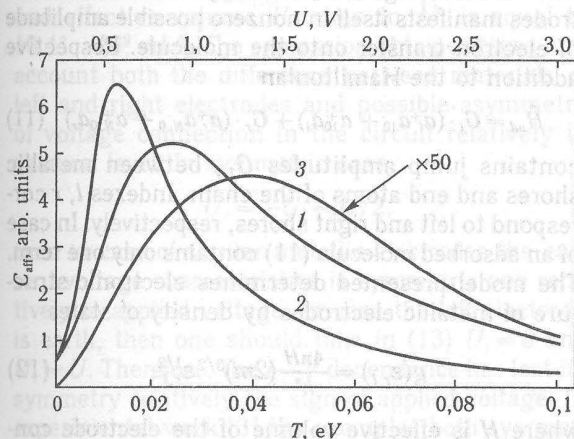


Fig. 6. Specific heat temperature dependence of linear chain:

1, 2 show specific heat for free molecule and for adsorbed molecule, respectively (lower axis); 3 (upper axis) is calculated C_{aff} for molecular bridge under current

that the latter coincides with band center $\chi_l = \varepsilon_0$. In case all levels lying below χ_l the states are filling completely by left reservoir electrons. The curve 2 in fig. 6 shows C_{aff} temperature dependence for molecules adsorbed in external electric field $U = 0.5$ V/molecule on gold surface $\chi_l = -4.3$ eV calculated by (6) at $E_l = \chi_l$. We do not take into account Coulomb blockade effect in specific heat calculations.

It should be noted that external (negative) electric field is significant stabilizing factor, which allows linear molecule to contact with adsorbing surface by left or right end only. Field absence may cause the capture of molecule by surface due to attracting image forces with the following reconstruction of molecule. Negative electric field interacting with dipole momentum arising in chain due to its charging pulls molecule normally to the surface (fig. 5). Opposite field direction, on the contrary, overturns the molecule on adsorbing surface. Change of electric field may influence strongly on molecular strain and orientation that is on the effective volume of molecular forest.

For comparison we observed the same chain connecting two gold electrodes having different potentials. At room temperature $T = 0.025$ eV calculations give falling C_{aff} dependence on applied voltage U (fig 6, curve 3). The maxims observed are the well known thermodynamic Shottky anomalies.

IV. Semiconductor quantum wire in electric field

To describe contact and transport phenomena in semiconductor quantum wires we used exactly solvable 3D Kronig—Penney model with open boundary conditions. The proposed potential model describing quantum bridge with sizes $20 \times 20 \times 100$ elemen-

tary cells is based on exact solution for terminated 1D Kronig—Penney crystal with δ -functional barriers (Dirac'comb potential) obtained in [14] without using of translation invariant approximation. One-dimensional model crystal contains N wells of width a , deep U_0 and opaque coefficient Ω . As a result of superposition of the same potential in three dimensions it is obtained a separable 3D potential shown in fig. 7. The summation of superposing combs creates suitable system of 3D wells and barriers inside

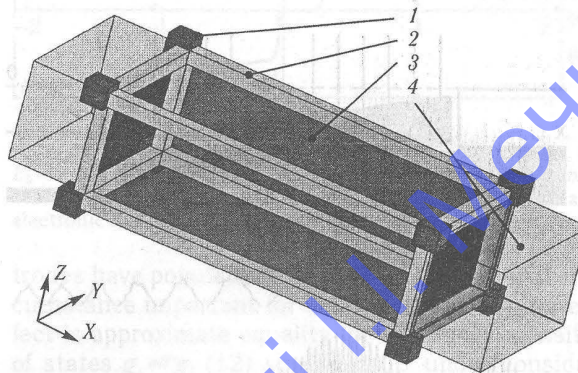


Fig. 7. Potential model of a quantum wire connecting metallic contacts:

The range 1 is additional potential at parallelepiped tops, range 2 is additional potential at ribs, intrinsic range 3 is semiconductor wire and range 4 represents metallic electrodes

crystal volume but there arises simultaneously a potential $\Delta U(x, y, z)$ additional to crystal one. In different ranges $\Delta U(x, y, z)$ takes values U_0 , $2U_0$ and combinations of U_0 and alternating barriers Ω (fig. 7). The Hamiltonian of the problem may be represented as

$$\hat{H} = H_0(x, y, z) - \Delta U(x, y, z),$$

$$\hat{H}_0(x, y, z) = \hat{H}_{0x} + \hat{H}_{0y} + \hat{H}_{0z}, \quad (10)$$

where \hat{H}_0 is separable part of entire Hamiltonian. The main idea of the method proposed is based on the fact that corrections to zero-order results are small because of wave function's tails in additional ranges of $\Delta U(x, y, z)$ are asymptotically small for band states and to some extent for deep local states. Zero wave function is represented in a view of product

$$\tilde{\Psi}_0(x, y, z) = \tilde{\Psi}_{0x}(x) \tilde{\Psi}_{0y}(y) \tilde{\Psi}_{0z}(z),$$

where $\tilde{\Psi}_{0x}(x)$, $\tilde{\Psi}_{0y}(y)$, $\tilde{\Psi}_{0z}(z)$ are 1D solutions obtained exactly in [14]. Non-additive addition leads to asymptotically small corrections for band states. We have studied GaAs and AlGaAs quantum bridges between metallic electrodes using active computer designer of hierarchical structures (ACDHS) which allows to built and to calculate different potential well systems, both periodical and hierarchical.

Electric field modifies states of semiconductor quantum bridge similar to molecular chains considered above. Let we consider GaAs quantum bridge of length 199.15 \AA connecting metallic electrodes in steady state electric field with intensity e . Kronig—Penney crystal parameters in case of GaAs

satisfying to its affinity energy are $U_0 = 1,2278 \text{ eV}$, $\Omega_a = -0,215$, $a = 5,69 \text{ \AA}$. Taking into account GaAs band gap value $E_g = 1,52 \text{ eV}$ we will consider voltage bias small enough to avoid interband transfers $e\mathcal{E}L \ll E_g$, where L is crystal length. Calculations by means of ACDHC give band structure, band position and distribution of electron density in different exited states. Fig. 8, *a* shows system geometry and relative positions of energy bands in semiconductor wire and in metal. Fig. 8, *b* and *c* represent electron density distribution near band bottom and

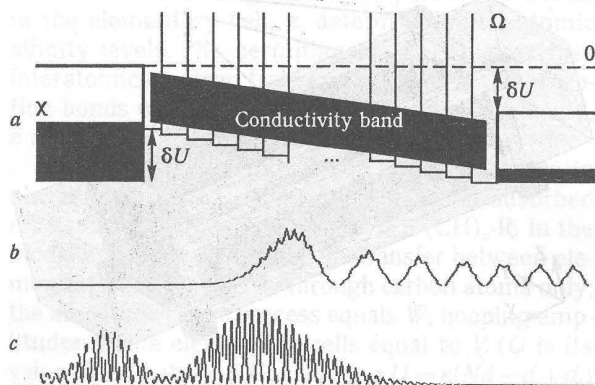


Fig. 8. Quantum wire in electric field:

a — chain of 35 GaAs potential wells at applied voltage $\delta U = 0$, 152 eV , χ is chemical potential of electrodes, $a = 5,69 \text{ \AA}$, $\Omega_a = -2,1337$, $U_0 = 1,2278 \text{ eV}$, dotted line marks the level of vacuum; *b*, *c* — electron wave functions of the lower and the upper exited states $s=3$, $s=35$ respectively

top, respectively. The field applied manifests itself in states modification leading to electron density drive away from left-hand or right-hand shores.

V. Conductivity of quantum bridges

Theoretical analysis of bridge conductivity is based mainly on two approaches. Landauer wave model [10, 11] interprets molecular junction as scattering center reflecting electronic waves moving from cathode. Electrical current is proportional either to transmission coefficient of electronic wave near Fermi energy of electrode or to some integral of transmission in a proper energy range [3, 9]. Calculations of linear conductance in wave model give more intensive current in comparison with experimental data [3, 10, 11]. As it was shown in [5] this effect is the consequence of both neglecting by spectrum field modification and by important role of molecular affinity charge states. Kinetic (sequential) conductivity model [3, 12, 13] operates by phenomenological transfer rate describing threefold tunneling processes of electron's jumps between a cathode and a couple of molecular states. Though calculations of conductance in kinetic model for gold-bistertiothene-gold contact [3] gave good agreement with the experiment as to values order and reflected main features of current voltage dependencies, we supposed that theoretical grounds of the model left much to be desired due to the independent physical

meaning of threefold processes. Let us observed below the conductivity of molecular bridge in DCM. The relation bridge electron subsystem with the electrodes manifests itself in nonzero possible amplitude of electron transfer onto the molecule. Respective addition to the Hamiltonian

$$\hat{H}_{ad} = G_l \cdot (a_l^\dagger a_{10} + a_{10}^\dagger a_l) + G_r \cdot (a_r^\dagger a_{N,0} + a_{N,0}^\dagger a_r) \quad (11)$$

contains jump amplitudes $G_{l,r}$ between metallic shores and end atoms of the chain. Indexes l, r correspond to left and right shores, respectively. In case of an adsorbed molecule (11) contains only one term. The model presented determines electronic structure of metallic electrodes by density of states

$$g(\epsilon_{r,l}) = \frac{4\pi H}{h^3} (2m)^{3/2} \epsilon_{r,l}^{1/2} \quad (12)$$

where H is effective volume of the electrode contacting the molecule, m is electron effective mass, $\epsilon_{r,l} = E_{Frl} - \chi_{r,l} + E_{sj} + U_{l,r}$ expresses the state energy E_{sj} , measured from the beginning of electrode's Fermi-stage with account of the bias value $U_{l,r}$, E_{Frl} marks right or left Fermi-energy. Both chemical potential $\chi_{r,l}$ and energy E_{sj} are measured in respect to vacuum level considered to be zero (fig. 4). Due to field widening of discrete energy band, the affinity levels pass sequentially the active ranges near Fermi surfaces of both shores. Each pass corresponds to sharp current increase in I — V dependence. There is a current dependence on density of states both left-hand and right-hand electrodes. This effect is significant one in case of semiconductor shores. Intrinsic phonons (or vibrons) influence weakly on the electron transfer and non-equilibrium states population putting in molecule with current [5]. The shores play the role of infinite thermodynamically balanced reservoirs of electrons. Equilibrium populations of baths' electronic states are described by Fermi distribution. In model under consideration, injected electron occupies either one of affinity states E_{sj} or one of vibrational sublevels. The possible rate of the process can be expressed in second order of perturbation theory using the well known Fermi golden rule. We suppose that weak absorption contact plays the role of small parameter. We will observe phononless contribution into the conductivity. Then one can obtain from the coinciding for left end and right end electronic currents through bridge's sj -state, the entire current I through the junction

$$I = \frac{2\pi e}{\hbar} \sum_{s,j} |G_{l,sj}|^2 |G_{r,sj}|^2 g_l(E_{sj} - \chi_l + E_{Fl} + U_l) \times \\ \times g_r(E_{sj} - \chi_r + E_{Fr} + U_r) \times \\ \times \frac{N_l - N_r}{|G_{l,sj}|^2 g_l(E_{sj} - \chi_l + E_{Fl} + U_l) + |G_{r,sj}|^2 g_r(E_{sj} - \chi_r + E_{Fr} + U_r)}, \quad (13)$$

where the summation is performed over all affinity states. The dimensional part of entire current

$$I_0 = \frac{e \cdot (2m)^{3/2} H G^2}{\pi \hbar^4} \cdot (1 \text{ eV})^{5/2}, \quad (14)$$

where G is amplitude of shore-bridge transfer, plays the role of current unity. Numerical value I_0 , in case when all energies in (13) are measured in eV and effective volume H taken in \AA^3 , is equal to $10,41 \cdot HG^2 \text{ mkA}$. The expression obtained takes into account both the difference between materials of left and right electrodes and possible asymmetry of voltage connection in the circuit relatively to vacuum level. In symmetric case

$$U_r = -U_l = U/2,$$

then in case of similar metallic electrodes the current-voltage characteristics is symmetric one relatively to applied voltage. In case the left electrode is earth, then one should take in (13) $U_l = 0$ and $U_r = U$. Therefore, the I — V dependence has lost its symmetry relatively the sign of applied voltage. In experimental work [3] the examples both symmetric and asymmetric I — V characteristics of quantum junctions were presented. Our calculations show that current value vs voltage depends sufficiently on distribution of electron densities near ends of the chain $|C_{sj}(1, 0)|^2$ and $|C_{sj}(N, 0)|^2$ in the standing wave as well as from the difference in metallic shores populations on the absolute energy level E_{sj} . The influence of square root energy dependence of state densities g_l and g_r manifests itself not so strongly. An essential fact for understanding the phenomenon of current going through mesoscopic linear system is that characteristic temperatures being of order $T \approx 0,02 \dots 0,03 \text{ eV}$ are as a rule much less than the distances between levels of bridge affinity band. Therefore with growth of applied voltage U the affinity levels one by one pass through the range near Fermi surfaces E_{Fl} and E_{Fr} , where the transfer become very effective. The entry of each new level into the active range accompanies by sharply increasing of current. The energy pauses between levels cause plateau I — V dependence. The charging — entire charge trapped by chain has similar behaviour. Below we will analyze the nature of electron transfer through molecular bridge connecting metal electrodes taking, for example, a simple chain and without taking into account Coulomb blockade effect. The contact conditions may be such that external electric field is negligibly small at comparatively large voltages. It is the case when pulled molecule connects the tips of fine electrodes and the drop of voltage occurs in vicinity of molecular ends. External electrical field doesn't influences the molecular affinity states. The solid line in fig. 9 shows calculated I — V characteristics for a chain with four starting affinity states at $E_0 = -4,0 \text{ eV}$, $V = 0,2 \text{ eV}$, $U_0 = 0,5 \text{ eV}$, $T = 0,01 \text{ eV}$ in case of gold electrodes. Dotted line shows the charging effect. One can see the characteristic tendency of fraction and semi-integer charging the molecule under voltage as the matter of thermodynamically non-equilibrium states population. The almost exactly semi-integer chain's charge arises at sufficiently low temperatures $T \ll V$, if energy range $(\chi, \chi + U)$ contains an odd number of affinity states [5]. States laying

above the range are unoccupied ones, $n_s = 0$, down states are filled completely, $n_s = 1$. Immediate states marked in case of symmetric contacts molecule-electrodes

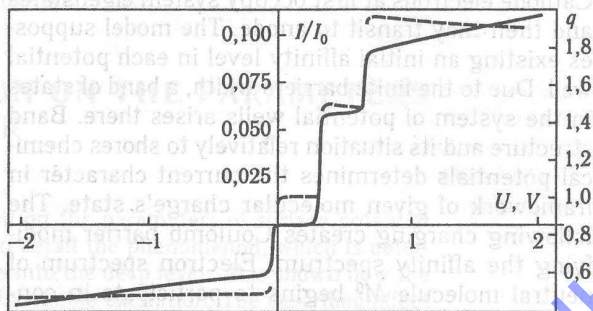


Fig. 9. A quantum bridge I — V characteristics:

$E_0 = -4,0 \text{ eV}$, $V_0 = 0,2 \text{ eV}$, $U_0 = 0,08 \text{ eV}$. Solid line represents current-voltage dependence without charging for intermediate electronic band at $T = 116 \text{ K}$; dotted line shows trapped charge

trodes have populations $n_s \approx 1/2$. An additional circumstance important for semi-integer charging effect is approximate equality for electrodes' density of states $g_r \approx g_l$ (12) small bias U under consideration.

Many body character of the problem may be taken into account phenomenologically in a self-consistent procedure including general spectrum shift due to charging and band widening. We have used for ground state energy ε_i in $M^{(i)}$ -state.

$$\varepsilon_i = \varepsilon_{i+1} + \varphi_i - 2V_{i+1}e^{\frac{\varphi_i}{U}}. \quad (15)$$

Coulomb barrier potentials φ_i are determined in minimization procedure for many electron system of the proper state $M^{(i)}$. Starting from initial charge state $M^{(i)}$ we have for the bridge's many-body energy terms

$$X_1 = \varepsilon_1 - 2V_1 = E_v, \quad X_0 = 2(\varepsilon_0 - 2V_0), \\ X_{-1} = 3(\varepsilon_{-1} - 2V_{-1}), \quad X_{-2} = 4(\varepsilon_{-2} - 2V_{-2}), \quad (16)$$

where E_v is absolute valence band top position of neutral molecule. From (16) and using (15) we obtain ionization potentials of the chain under consideration

$$I_i = X_i - X_{i-1}.$$

Calculations performed in DCM framework show good agreement with experimental data for ionization potentials of carbon nanosystems and molecular wires I — V characteristics.

VI. Conclusion

Quantum bridges under the current are parametric many-body systems having steady state non-equilibrium distribution. The number of electrons captured by molecule's affinity states from outside is controlled by external conditions that determine molecule charge's state described by own electronic structure. Discrete chain model considered as well as Kronig—Penney model belongs to the number

of simplest ones. Nevertheless, it allows to take into account in united formalism the main features of current carrying through the mesoscopic junctions. Cathode electrons at first occupy system eigenstates and then they transit to anode. The model supposes existing an initial affinity level in each potential well. Due to the finite barriers width, a band of states in the system of potential wells arises there. Band structure and its situation relatively to shores chemical potentials determines the current character in framework of given molecular charge's state. The following charging creates Coulomb barrier modifying the affinity spectrum. Electron spectrum of neutral molecule M^0 begins to participate in conductivity in case of a single-ionized molecule. These states are filled partially by an electron transited from electrode. With growth of applied voltage, total population may exceed unity. In the case it is switched on the next affinity spectrum M^1 and so on. In present work Coulomb charging was taken into account phenomenologically. A more correct approach demands the resolution of quantum many-body problem for discrete chain with alternative number of particles depending on voltage applied.

Both models are able to describe low-temperature electron transfer in metallic point contacts. The structures were investigated experimentally in [1, 15] for monoatomic wires between Au, Pt, Al, Nb, Pb, K и Na electrodes. The transfer mechanism through affinity for such systems states leads also to stepwise conductance with both positive and negative step slopes. Our models give the other alternative to explain the vanishing of conductivity at sufficiently long distances between electrode's tips. The matter may be laying in electronic structure transformation lifting due to Coulomb blockade effect the bottom of conductivity band upper than Fermi level.

Quantum fragments of electric circuit play important role in single electron transistors and ratch-

ets [16]. Though the linear models considered can't be directly applied to such systems, one should mark the general equivalence between bridges and quantum dots possessing discrete spectrum and contacting with several electrodes.

References

1. Van Ruitenbeek J. N. Metal Clusters on Surfaces: Structure, Quantum Properties, Physical Chemistry / Ed. by K.-H. Meiwes-Broer, Springer Verlag. — Berlin, 1999.
2. Willig F. Proceedings of Symposium on Electronic Processes in Organic Condensed Matter. — August 1998, University of Rochester, Rochester, New York.
3. Datta S. Electronic Transport in Mesoscopic Systems. — Cambridge: Cambridge Univ. Press, 1995. — Chapt. 3.
4. Kergueris C., Bourgoignie J.-P., Palacin S., Esteve D., Urbina C., Magoga M., Joachim C. // Phys. Rev. — 1999. — B59(19). — 12505.
5. Glushko E. Ya. Low Temp // Phys. 26. — 2000 (to be published).
6. Euteev V. N., Linchuk I. L., Moiseenko M. V., Zhuravel E. V., Glushko E. Ya. Proceedings of the 2nd Workshop «Sensors Springtime in Odessa». — May 29—30, 1999, Odessa, Ukraine // Photoelectronics. — Odessa, 1999. — 9.
7. Euteev V. N., Linchuk I. L., Moiseenko M. V., Zhuravel E. V., Glushko E. Ya. Proceedings of the 59th Annual APS Conference on Physical Electronics, June 18—21, 1999, Berkeley, California, USA.
8. Euteev V. N., Moiseenko M. V., Zhuravel E. V., Glushko E. Ya. Proceedings of 60th Annual APS Conference on Physical Electronics, June 21—24, 2000, Baton Rouge, Louisiana, USA.
9. Buttiker M., Imry Y., Landauer R., Pinhas S. // Phys. Rev. B 31, 6207. (1985).
10. Reed M. A., Zhou C., Muller C. J., Burgin T. P., Tour J. M. // Science, 278, 252 (1997).
11. Aviram A., Joachim C., Pomerantz M. // Chem. Phys. Lett., 146, 490 (1988).
12. Emberly E. G., Kurczonov G. // Phys. Rev. B 58, 10911 (1998).
13. Porath D., Levi J., Tarabiah M., Millo O. // Phys. Rev. B 56, 1 (1997).
14. Glushko E. Ya. // Sov. Phys. FTT, 38, 2051 (1996).
15. Yanson A. I., Yanson I. K., Ruitenbeek J. N. // Nature. — 1999. — V. 400. — 144.
16. Wang X., Junno T., Carlsson S.-B., Thelander C., Samuelson L. // Phys. Rev. Lett. — 2000 (to be published).

INFLUENCE OF PHOTOEXCITATION ON THE PARAMETERS OF SURFACE POTENTIAL BARRIER

In this work the effect of photoexcitation on the parameters of surface potential barrier is investigated. We have examined in detail the phenomenon, which is determined by trapping of nonequilibrium carriers into the deep levels. It is shown how the parameters of surface barrier are governed by visible excitation. The described effect together with the usage of an asymmetric heterojunction permits the fabrication of an image sensor of a quite new type.

1. Introduction

The development of innovations in the operating physical principles, design and technology of electronic devices based on non-crystalline materials to be a significant part of investigations completing the traditional work with monocrystalline ideal semiconductors. The main strategy of semiconductor electronics is to design and fabricate devices made from pure and perfect materials. Such an approach gives rise to the appearance of various arrangement that are successfully used in common. One of the most impressive results is an optical image sensor based on the CCD imaging chip. Orientation toward the most perfect crystals does not allow all the requirements of modern techniques to be satisfied. Very often either a device with a large working surface or a large array of devices is needed. For such a purpose polycrystalline or amorphous materials, fabricated by different technologies, are employed. As a rule, devices based on these materials do not have the same physical principle of operation as the crystalline ones. For instance, electron tubes with a variety of semiconductor layers of high luminescence and photocathode characteristics are used to develop large-area image sensors for X-ray applications. Of course, it is impossible to create a polycrystalline CCD image sensor with a similar large sensitive surface, although no limitations, relative to the matrix array size, exist for the operation principle of a CCD.

2. Theory

A contact between two semiconducting materials, one or both of which are thin-film semiconductors is one of the interesting structures of non-crystalline electronics. We have investigated in detail CdS—Cu₂S heterojunction. In particular, this heterojunction was employed as the basis for a thin-film solar cell, but as is evident from our investigation such a device has wider applications that follow directly from disorder effects of such a structure. Fig. 1 show an energy-band diagram of the CdS—Cu₂S

heterojunction. This heterojunction is a contact between two semiconductors with a lattice mismatch of about 4%. This mismatch

leads to a strong disorder of the regular lattice structure in the regions near the interface. This distinctive feature is that the CdS region, where the space charge is localized, possesses a material with long-range disorder, and consequently with non-zero density $N(E)$ of the localized gap states. Such a property is absolutely distinct from the properties of ideal GaAs—AlGaAs structures and has a strong effect on the photoelectrical characteristics of the heterojunction.

During exposure of the sample to light quanta of sufficient energy, non-equilibrium minority carriers are captured by the localized states in CdS. We can see that even low-level excitation (for which the density of non-equilibrium carriers Δn is much smaller than that of equilibrium carriers n_0) changes the parameters of the heterojunction drastically [1].

Let us consider the special distribution of the trapped holes as

$$\Delta p(x) = \Delta p_0 e^{\frac{\varphi_0}{kT} (1 - \frac{x}{W})}, \quad (1)$$

where Δp_0 is concentration of non-equilibrium holes, captured by the local centres within the quasineutral region of CdS, and W and φ_0 are CdS barrier width and height, respectively. Then the space-charge distribution function $\rho(x)$ is

$$\rho(x) = e \left[N_d + \Delta p_0 e^{\frac{\varphi_0}{kT} (1 - \frac{x}{W})} \right], \quad (2)$$

where N_d represents ionized donor concentration in CdS.

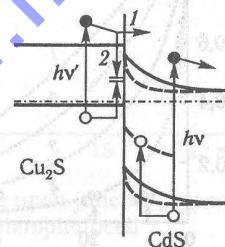


Fig. 1. Band diagram of CdS—Cu₂S heterojunction:

1 — transition of electrons, excited with $h\nu$ photons in Cu₂S, across the junction plane; 2 — surface recombination. Dashed line represent the band profiles under CdS band-gap illumination $h\nu$

From the analytic solution of Poisson's equation for such a dependence, it can be shown that for $x \ll W$, i. e. near the interface

$$\phi(x) = A(N_d, \Delta p_0, \xi) \left[e^{\xi(1 - \frac{x}{W})} - 1 \right], \quad (3)$$

where A is some constant dependent on the density of uncompensated donors in n -type material and values Δp_0 and $\xi = \phi_0/kT$ as parameters.

The main result here is that even a low illumination level changes the electron energy spatial distribution from a parabolic to an exponential one, thus increasing the electric field near the interface. Fig. 2 illustrates the computational dependencies of the potential variation $\phi(x)$ near heterojunction interface under various irradiation conditions.

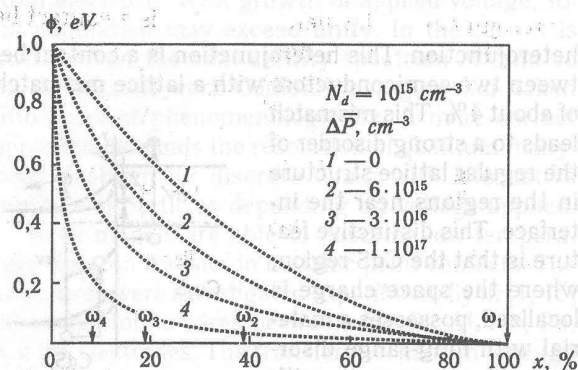


Fig. 2. Spatial distribution of the potential variation $\phi(x)$ in space charge region of heterojunction, calculated for different densities of trapped photogenerated holes. The arrows indicate barrier widths, corresponding to curves 1—4

It should be mentioned that non-equilibrium state of the heterojunction possesses a long time stability [1]. When excitation is turned off, slow emission of non-equilibrium holes from region of space-charge layer begins. The rate of the emission process is governed by the type of the trapping centers. When minority-carrier trapping centers dominates, the time constant τ_t of the process is determined by thermal escape probability γ_t of the centers

$$\frac{1}{\tau_t} = \gamma_t = P_0 v_p \sigma_p e^{-\frac{E_t}{kT}}, \quad (4)$$

where P_0 is density of hole states in valence band of CdS, σ_p is trap depth and v_p is thermal velocity for holes.

If the non-equilibrium holes in the space-charge layer are captured by the recombination centers, the time constant for heterojunction transient from the excited to the equilibrium state will be defined by electron-hole recombination velocity S_r . The occurrence of potential barrier in cadmium sulfide leads to spatial separation of electrons and holes, generated in CdS under illumination of heterojunction. During illumination the photoexcited holes moves toward the interface, where they are promptly trapped by deep levels, whereas electrons are swept

out of barrier region into CdS bulk. So the situation is closed to that of the phenomenon of «stored photoconductivity». In order to re-establish the equilibrium, the photoexcited carriers have to go over potential recombination barrier which height is ϕ_0 . In this case, life time of photoexcited holes with recombination centers becomes extremely large and is given by

$$\tau_p = \tau_p^0 e^{\frac{\phi_0}{kT}}, \quad (5)$$

where $\tau_p^0 = \frac{1}{v_n \sigma_n n}$, is lifetime of holes with recombination centers in bulk of CdS.

It must be emphasized that trapped non-equilibrium charge is stable not only over time, but possesses a spatial stability, also. To clear this point we must remember that lifetime of free non-equilibrium holes τ_p is about 10^{-9} s. From Einstein relation

$$\frac{D_p}{kT} = \frac{\mu}{e} \quad (6)$$

noting that hole mobility in CdS is of $1 \text{ cm}^2/\text{V} \cdot \text{s}$, we can obtain the diffusion length for holes L_p

$$L_p = (D_p \tau_p)^{1/2} = 0.05 \mu\text{m}. \quad (7)$$

Therefore, the holes are being captured by local centers in space-charge region within a distance less then $0.05 \mu\text{m}$ from the place they were generated. As we have mentioned earlier, thermal emission from traps is weak and followed by immediate re-trapping.

When heterojunction is nonuniformly illuminated, an inhomogeneous distribution of space-charge is established over working surface of heterojunction. This space-charge distribution is essentially given by local illumination of surface areas.

Our interest to space-charge distribution $\rho(x)$ and potential distribution $\phi(x)$ arises because of charge collection efficiency from p -type material (in our case Cu_2S) related to the dependencies

$$I_{sc} = I_{sc}^0 + \frac{\mu_n \left. \frac{d\phi(x)}{dx} \right|_{x=0}}{e} + S_r \quad (8)$$

Here I_{sc} is short-circuit photocurrent in heterojunction, the I_{sc}^0 is current in the absence of interface recombination losses, S_r is surface recombination velocity.

The electrons, photoexcited in Cu_2S , can either recombine with interface states or be separated from holes under the action of barrier field, localized in CdS. The relationship between interface recombination velocity S_r and electron drift velocity $v_d = \frac{\mu_n}{e} \left. \frac{d\phi(x)}{dx} \right|_{x=0}$ for the noticed processes determines the magnitude of current I_{sc} and real cell efficiency. The variation in the spatial dependence $\phi(x)$ with CdS band gap illumination strongly influences the drift velocity of electrons in barrier region, consequently increasing charge collection efficiency.

Here, one must bear in mind that we are dealing with collection efficiency of non-equilibrium electrons, excited in *p*-type semiconductor Cu₂S and moving across the junction plane. Thus, as is evident from eq. (8), the current generated in *p*-type material is dependent on illumination conditions in type material.

This means that photocurrent, produced by excitation of heterojunction simultaneously with two light beams, one of which is from IR range and absorbs in Cu₂S, and the other from the visible range and absorbs in CdS, does not equal to the sum of photocurrents resulting from the illumination of heterojunction with each of the beams separately. The above-mentioned effects is of great importance for us. We have called this phenomenon the non-additive formation of current effect, i. e., the NAFC effect.

For solar cells based on CdS—Cu₂S, the NAFC effect has the negative character, so it was of no interest to researchers. Our investigations, however, reveal that the effect, which is a problem for a solar cell, may be turned to advantage and successfully used for manufacturing an innovative image sensor [2–5].

3. Experimental results

Let us examine the experimental data that allow the proposed model to be confirmed. The most direct way to determine the characteristics of space-charge layer of the heterojunction is to measure the corresponding changes in junction capacitance C_j as a function of various factors. Junction capacitance as a function of the exciting light wavelength is illustrated in fig. 3. As is evident from curve 1 in fig. 3, if heterojunction base layer (CdS) of thickness 10 μm

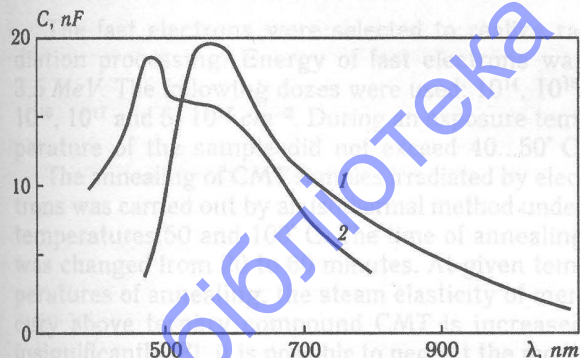


Fig. 3. Spectral dependencies of the barrier capacitance in thin film CdS—Cu₂S heterojunction:

1 — illumination from the side 10 μm thick CdS layer; 2 — illumination from the side 0,2 μm thick Cu₂S layer

is directed toward the illumination, the well-known photoresponse for Cu-doped CdS, resulting from impurity carrier generation, in our case also peaks at about 600 nm. In this case intrinsic light does not reach the interface yet. From curve 2 in fig. 3, corresponding to the illumination of heterojunction from the side of 0,2 μm thick Cu₂S layer, intrinsic-carrier-generation peak at 500 nm can be seen as

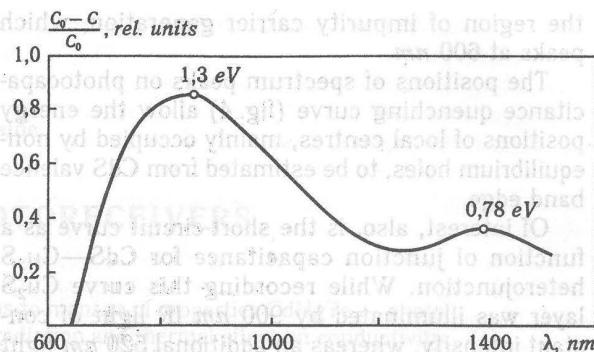


Fig. 4. Photocapacitance quenching spectrum:

C_0 is junction capacitance resulting from illumination of heterojunction with $\lambda = 560 \text{ nm}$

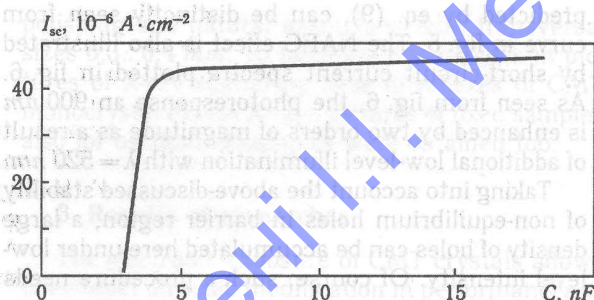


Fig. 5. Short current dependence upon junction capacitance in CdS—Cu₂S heterophotocell

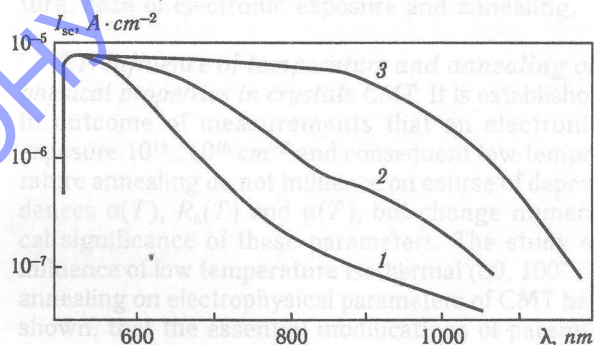


Fig. 6. Increase of photosensitivity in CdS—Cu₂S heterojunction during low-level additional excitation with $\lambda = 520 \text{ nm}$

Curve 1 is without additional excitation. Illumination level of additional excitation increases with the curve number

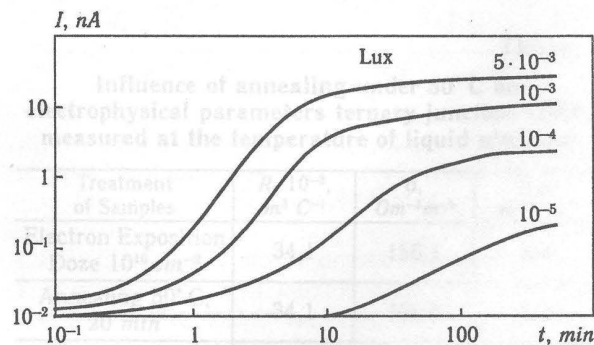


Fig. 7. Increase of sensor photocurrent with time during the adsorption of photons (1,9 eV) for various levels of illumination at 300 K

the region of impurity carrier generation, which peaks at 600 nm.

The positions of spectrum peaks on photocapacitance quenching curve (fig. 4) allow the energy positions of local centres, mainly occupied by non-equilibrium holes, to be estimated from CdS valence band edge.

Of interest, also, is the short-circuit curve as a function of junction capacitance for CdS—Cu₂S heterojunction. While recording this curve Cu₂S layer was illuminated by 900 nm IR light of constant intensity, whereas an additional 520 nm light provides an increase of barrier capacitance. Here the photocurrent obtained in the presence of exciting light only with $\lambda = 520$ nm was subtracted from the measured current value. The saturation of current, predicted by eq. (9), can be distinctly seen from curve in fig. 5. The NAFC effect is also illustrated by short-circuit current spectra plotted in fig. 6. As seen from fig. 6, the photoresponse at 900 nm is enhanced by two orders of magnitude as a result of additional low-level illumination with $\lambda = 520$ nm.

Taking into account the above-discussed stability of non-equilibrium holes in barrier region, a large density of holes can be accumulated here under low-level intensity. Of course, such a procedure needs

a lot of time. Note that photosensitivity of CdS—Cu₂S heterojunction resembles that of a photoemulsion where a latent image is being formed. As shown in fig. 7 for CdS—Cu₂S heterojunction, photoreponse at $\lambda = 900$ nm is modulated by short-wavelength illumination. Thus, we can state that the results obtained satisfy well the above-discussed model of non-ideal heterojunction.

References

1. Vassilevski D. L., Borschak V. A., Vinogradov M. S. Influence of tunnel effects on the kinetics of the photocapacitance in nonideal heterojunctions // Solid-State Electronics. — 1994. — Vol. 37, № 9. — P. 1680—1682.
2. Vassilevski D. L., Borschak V. A., The utilisation of a sensor based on a heterojunction for astronomy // Proc. ICO-16 Satellite Conf. on Active and Adaptive Optics, Garching—Munich, Germany, 2—5 Aug. — 1993. — P. 377.
3. Vassilevski D. L., Borschak V. A., Victor P. A., Vinogradov M. S., Zatonovskaya N. P. A novel heterojunction-based low-illumination image sensor, with applications to astronomy // Sensors and Actuators A. — 1994. — 45. — P. 191.
4. Borschak V., Golovanov V., Stankova E., Zatonovskaya N. Novel Image Sensor for visible and X-ray Spectra // Euroensors XI, conf. Warsaw, Poland, September 21—24, 1997.
5. Vassilevski D. L., Vinogradov M. S., Borschak V. A. Photon induced modulation of surface barrier: investigation and application for a new image sensor // Applied Surface Science. — Dec. 1996. — 103(4). — P. 383—389.

Fig. 5. Short circuit dependence upon junction capacitance for CdS—Cu₂S heterojunction.

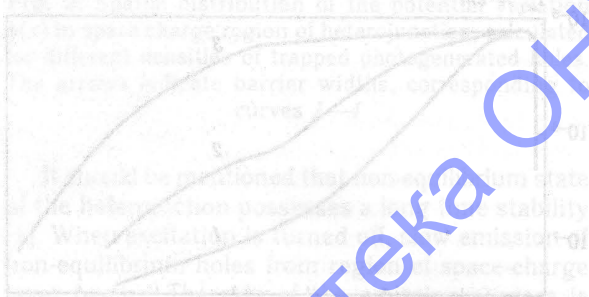


Fig. 6. Increase of photocurrent with $\lambda = 520$ nm non during low-level additional excitation level of CdS.

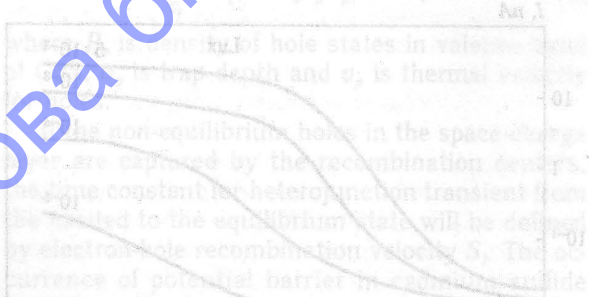


Fig. 7. Increase of sensor photocurrent with time during the absorption of photons (1.5 eV) for various levels of the illumination at 900 nm by light trapped by barrier.

Fig. 8. Short circuit current (I_sc) versus wavelength (lambda) for CdS—Cu₂S heterojunction.

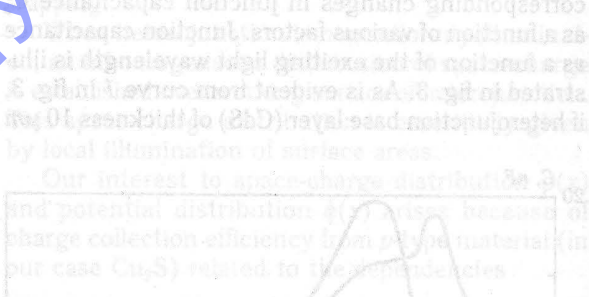


Fig. 9. Increase of photocurrent with time during the absorption of photons (1.5 eV) for various levels of the illumination at 900 nm by light trapped by barrier.

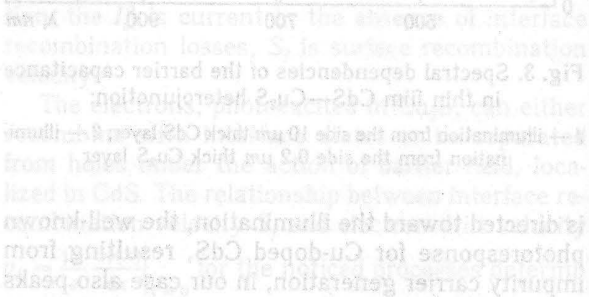


Fig. 10. Increase of photocurrent with time during the absorption of photons (1.5 eV) for various levels of the illumination at 900 nm by light trapped by barrier.

CdHgTe GROWN BY LPE FOR PHOTORECEIVERS

In this work the principles and the means to manage of properties CdHgTe — photoreceivers were investigated: influence of irradiation and thermal effect on conductivity, mobility of charge carriers and photosensitivity. Also were investigated chemical and phase structure of crystals CdHgTe subjected to heat treatment, the analysis in the nature of structure imperfection by RCA methods.

1. Introduction

The purpose of this work is to research the possibilities to manage properties of IR-semiconducting materials, and also to study on this basis the ways to increase reliability of existing receivers on CMT. In the real operating conditions, this material can be subjected to various kind of effects: temperature, radiation etc. The reliability of a material depends on stability of physical properties at different levels of these effects. Therefore, in this work the attempt to install regularities of influence for electronic and neutron exposure, and also temperature on electrical conductivity and mobility of charge carriers is undertaken. Besides, to clear up the nature of instability connected to physical-chemical properties CMT with the help of local RCA were investigated.

2. Technique of researches

The fast electrons were selected to realize radiation processing. Energy of fast electrons was 3,5 MeV. The following doses were used: 10^{14} , 10^{15} , 10^{16} , 10^{17} and $5 \cdot 10^{17} \text{ cm}^{-2}$. During an exposure temperature of the sample did not exceed 40...50° C.

The annealing of CMT samples irradiated by electrons was carried out by an isothermal method under temperatures 50 and 100° C. The time of annealing was changed from 20 to 60 minutes. At given temperatures of annealing, the steam elasticity of mercury above ternary compound CMT is increased insignificantly [3], it is possible to neglect the modification of components ratio in samples owing to evaporation of mercury. Therefore during annealing the samples were in glassboxes with a cover and the mercury was not added.

As parameters describing physical properties of junction CMT, specific electrical conductivity (σ) and Hall constant (R_h) are used in this work. Both magnitudes were measured in galvanic-magnetic researches by standard technique [4] with application of direct current and constant magnetic field. The magnitude of current through samples was 2...5 mA, magnitude of magnetic induction — 0,2T.

RCA research was conducted using single crystal samples of two types: flat, obtained by cutting,

polishing and natural exemplars, with transversal sizes 0,3...0,4 mm. To facilitate the analysis in pictures of X-ray scattering near to reflexes of CMT monocrystal except X-rays pictures of fixed samples also for oscillating samples were obtained too.

3. Results of researches

The electronic exposure of CMT crystals allows to conduct directed modification in performances of a material. We are investigated the dependence of modification in electrical conductivity of samples σ and Hall mobility in n — $\text{Cd}_{0,2}\text{Hg}_{0,8}\text{Te}$ on temperature, dose of electronic exposure and annealing.

3.1. Influence of temperature and annealing on physical properties in crystals CMT. It is established in outcome of measurements that an electronic exposure 10^{14} ... 10^{16} cm^{-2} and consequent low temperature annealing do not influence on course of dependences $\sigma(T)$, $R_h(T)$ and $\mu(T)$, but change numerical significance of these parameters. The study of influence of low temperature isothermal (50, 100° C) annealing on electrophysical parameters of CMT has shown, that the essential modifications of parameters happened during the first 40 minutes of annealing already at the temperature of 50° C. The magnification in duration of annealing up to 60 min changes parameters a little. At the same time the electrical conductivity measured in the interval of tempera-

Table 1

Influence of annealing under 50° C on electrophysical parameters ternary junction CMT, measured at the temperature of liquid nitrogen

Treatment of Samples	$R_h \cdot 10^{-3}, m^3 C^{-1}$	$\sigma, \Omega m^{-1}$	$R_h \sigma, m^2 V^{-1} s^{-1}$
Electron Exposition Doze 10^{16} cm^{-2}	34,1	156,1	5,4
Annealing 50° C, 20 min	34,1	150,8	5,1
Annealing 50° C, 40 min	30,0	223,0	6,7
Annealing 50° C, 60 min	32,1	191,1	6,1

tures 100...250 K, decreases, and in the interval of temperatures 80...100 K — is increased. Hall mobility changed similarly, at the temperature of liquid nitrogen it reached the values being essentially larger, than it was before annealing (see tab. 1).

3.2. Influence of an exposure by fast electrons.

Exposure dependence of electrical conductivity $\sigma(F)$ has an ambiguous character. Its main tendency is the decrease of σ in a range from 10^{14} up to 10^{17} cm^{-2} at the temperature of from 140 up to 250 K.

Curves $\sigma(F)$ for 70...100 K in a range of significances of a dose of an exposure (10^{15} ... 10^{17}) cm^{-2} are of special interest: the temperature dependence $\sigma(T)$ for $F > 10^{15}$ cm^{-2} changes the character. At the temperature lower than 140 K crystals irradiated with doses of electrons more 10^{15} cm^{-2} , reduce their electroconductivity.

The dependence $\mu(F)$ has brightly expressed maximum and minimum for $F = 10^{15}$ cm^{-2} . For the higher temperature, the influence of exposure here is less noticeable. It is necessary to note, that the dose 10^{15} cm^{-2} is a threshold for modification of character both for dependence $\sigma(F)$, and $\mu(F)$.

3.3. Results of RCA. The method of local RCA has allowed to determine chemical structure in spe-

Table 2

Distribution of cadmium, mercury and Te along a sample of monocrystal Cd—Hg—Te (% , at.)

Element	Coordinate meagement point, mm						
	0,1	0,2	0,3	0,4	0,5	0,6	0,7
Cd	11,21	10,99	10,95	11,09	11,04	11,17	11,36
Hg	38,17	38,03	37,93	37,76	38,43	37,51	37,59
Te	50,61	50,98	51,12	51,15	50,53	51,32	51,05
x	0,221	0,216	0,214	0,217	0,218	0,218	0,223

cific points of crystal. The size of a probe was $(1...2) \cdot 10^{-4}$ cm. The analysis was carried out in

points located on one direct line, on a distance 0,1 cm from each other.

Exactitude in realisation of the analysis is $\pm 0,02\%$. The results are represented in table 2.

Conclusions

The research of crystals Cd—Hg—Te has shown, that they are inhomogeneous in chemical and phase structure are inhomogeneous; the availability of the following imperfections is inherent in their structure:

— small crystal inclusions of hardly textured phase;

— areas of the plate-like form with structure being distinct from CMT.

The review of the obtained data about heterogeneity of crystals Cd—Hg—Te together with data on instability and degradation of physical properties shows, that the processes of origin in structure heterogeneity and decrease of properties flow past in identical or close temperature intervals. It allows to assume, that namely the instability of rigid solution predetermines instability of properties in semiconducting material Cd—Hg—Te.

Therefore, the reach of stability in physical properties of crystals Cd—Hg—Te should be based on stability and homogeneity it of a crystalline structure.

Also the possibilities of obtaining CMT crystals with desired properties are discussing in this report.

References

1. Cheung D. T. An overview on defect studies in MCT // J. Vac. Sci. Technol. — 1985. — V. A3, № 1. — P. 128—130.
2. Ivanov-Omsku V. I., Mironov K. E., Mynbaev K. D. // Semicond. Sci. and Technol. — 1993. — 8, № 5. — P. 634—637.
3. Fizika soedineniy A^2B^6 / Pod red. A. N. Georgobian. — M.: Nauka, 1986. — 320 p.
4. Pavlov, L. P. Metody izmereniya parametrov poluprovodnikov materialov. — M.: Vysshaya shkola, 1987. — 239 p.

Table 1
Influence of annealing under 50°C on electrical parameters of junctions of Cd—Hg—Te monocrystals measured at the temperature of liquid nitrogen

Treatment of samples	R_{H} , $\Omega \cdot \text{cm}^{-1}$	σ , $\Omega^{-1} \cdot \text{cm}^{-1}$	R_{H} , $\Omega \cdot \text{cm}^{-1}$
Electron Exposure Dose 10^{16} cm^{-2}	34,1	156,1	5,4
Annealing 50°C, 20 min	34,1	150,8	5,1
Annealing 50°C, 40 min	30,0	223,0	5,7
Annealing 50°C, 60 min	32,1	191,1	5,1

ions was carried out by an isothermal method under temperatures 50 and 100°C. The time of annealing was changed from 20 to 60 minutes. At given temperatures of annealing, the steam elasticity of mercury above ternary compound CMT is increased insignificantly, it is possible to neglect the modification of components ratio in samples owing to evaporation of mercury. Therefore during annealing the samples were in glassboxes with a cover and the mercury was not added.

As parameters describing physical properties of junctions CMT, specific electrical conductivity (σ) and Hall constant (R_{H}) are used in this work. Both magnitudes were measured in galvanic-magnetic resistances by standard technique [4] with application of direct current and constant magnetic field. The magnitude of current through samples was 2...5 mA, magnitude of magnetic induction — 0,2 T.

RCA research was conducted using single crystal samples of two types: flat, obtained by cutting

LUMINESCENCE OF $\text{Ca}_3\text{Ga}_2\text{Ge}_4\text{O}_{14}$ SINGLE CRYSTALS AND THIN FILMS DOPED WITH Tb^{3+} AND Eu^{3+} IONS

The results of optical spectroscopy of the impurity Tb^{3+} and Eu^{3+} ions in trigonal $\text{Ca}_3\text{Ga}_2\text{Ge}_4\text{O}_{14}$ single crystals and thin films are presented. It is shown that Tb^{3+} and Eu^{3+} ions occupy Ca^{2+} sites in the $\text{Ca}_3\text{Ga}_2\text{Ge}_4\text{O}_{14}$ crystal structure according to heterovalent isomorphism $\text{Ca}^{2+} + \text{Ge}^{4+} \rightarrow \text{Ga}^{3+} + \text{Tb}^{3+}$ (Eu^{3+}) under simultaneous Ga^{3+} and Ge^{4+} redistribution over octahedral and 3f-tetrahedral crystallographic positions. The influence of structural disordering caused by randomly occupied cation positions on spectroscopic characteristics of impurity ions is discussed.

Introduction

Rare-earth (RE) activated crystals with Ca-gallogermanate structure have been intensively studied because of their application as luminescent and solid state laser materials [1–3]. The compound with Ca-gallogermanate structure has four kinds of cation sites. They are the distorted Thomson cubes occupied by large ions Ca^{2+} (3e positions with the symmetry 2) octahedra (1a site with the symmetry 32) and tetrahedra of two types: the first ones are placed at 2d positions with the symmetry 3 and the others are 3f sites with the symmetry 2. The X-ray data analysis [1] and spectral characteristics [1–3] of $\text{Ca}_3\text{Ga}_2\text{Ge}_4\text{O}_{14}$ crystals show that the crystals belong to disordered materials. The disorder is due to a statistical occupation of 1a and 3f positions by Ga^{3+} and Ge^{4+} ions. This paper reports the experimental studies of spectral luminescence properties of Tb^{3+} and Eu^{3+} ions in $\text{Ca}_3\text{Ga}_2\text{Ge}_4\text{O}_{14}$ single crystals and the corresponding thin films. Tb^{3+} and Eu^{3+} ions are used as a structural microprobe to study the nearest surroundings of the ions.

Experiment

$\text{Ca}_3\text{Ga}_2\text{Ge}_4\text{O}_{14}:\text{Tb}$ and $\text{Ca}_3\text{Ga}_2\text{Ge}_4\text{O}_{14}:\text{Eu}$ single crystals were grown by Czochralski method using a high-frequency induction heater platinum crucible. The thin films were deposited onto melted quartz substrates using the RF ion-plasma sputtering. For crystallization $\text{Ca}_3\text{Ga}_2\text{Ge}_4\text{O}_{14}$ films were annealed in air or vacuum at the temperatures up to 1100 °C. The oxides of Ga_2O_3 , GeO_2 , Eu_2O_3 , Tb_4O_7 and calcium carbonate CaCO_3 , all of special purity quality, were used as initial components to synthesize the raw material. The doping concentrations in the melt were 0,1–5% Tb (Eu). The optical absorption spectra were measured by «Specord M40» spectrophotometer. The luminescence spectra were investigated using MDR-4 and MDR-23 diffraction monochromator and were corrected for the response of spectrometer-detector system. Photoluminescence

(PL) was excited by 150 W xenon lamp. Cathodoluminescence (CL) was investigated using electron excitation in the energy range from 3,5 to 10 keV.

Results

The transparency region of pure $\text{Ca}_3\text{Ga}_2\text{Ge}_4\text{O}_{14}$ crystals extends from $\sim 0,250$ to 6 μ , that allows us to investigate the electron transitions of RE impurity ions. When interpreting the radiative transitions, we have used theoretical calculation results for energy levels of free Tb^{3+} and Eu^{3+} ions and for the same ions in complex oxide compounds crystals [4, 5]. Fig. 1 and fig. 2 show absorption, PL and excitation spectra of $\text{Ca}_3\text{Ga}_2\text{Ge}_4\text{O}_{14}:\text{Tb}$ and

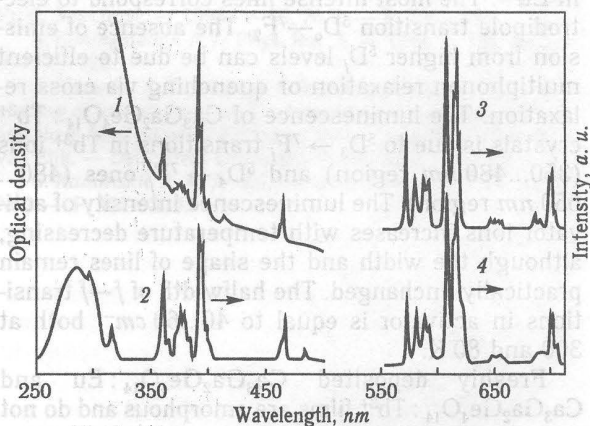


Fig. 1. Optical absorption (1), PL (2, 3) and excitation (4) spectra of $\text{Ca}_3\text{Ga}_2\text{Ge}_4\text{O}_{14}:\text{Eu}$ single crystals at 300 K (1, 2, 3) and 80 K (4)

$\text{Ca}_3\text{Ga}_2\text{Ge}_4\text{O}_{14}:\text{Eu}$ single crystals. The absorption spectrum consists of narrow lines of $f-f$ transitions in Tb^{3+} and Eu^{3+} ions and strong absorption bands near UV region. In $\text{Ca}_3\text{Ga}_2\text{Ge}_4\text{O}_{14}:\text{Eu}$ crystals the broad absorption band is due to broad charge-transfer band $0^{2-}-\text{Eu}^{3+}$ overlapped with intense absorption of fundamental absorption edge.

In contrast to Eu^{3+} ions, small energy difference between the levels of the ground ($4f^8$) and the ex-

intensity, in contrast to that of single crystals. An efficient nonradiative energy transfer from $^5\text{D}_3$ to $^5\text{D}_4$

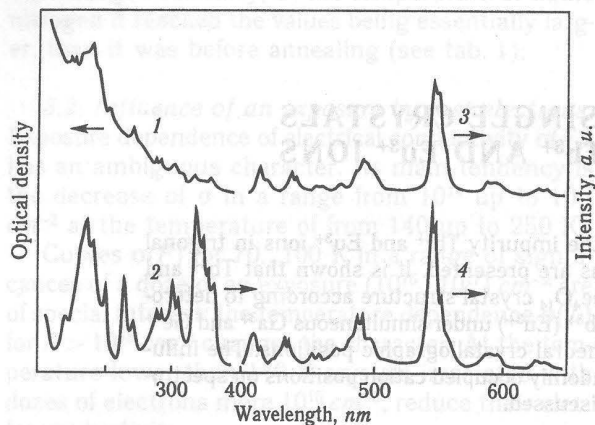


Fig. 2. Optical absorption (1), PL (3, 4) and excitation (2) spectra of $\text{Ca}_3\text{Ga}_2\text{Ge}_4\text{O}_{14} : \text{Tb}$ single crystals at 300 K (1, 3) and 80 K (2, 4)

cited ($4f^75d$) configurations are inherent for Tb^{3+} ions. That is why the broad absorption bands in near UV-region may be referred to the transitions from ground state $^7\text{F}_0$ of $4f^8$ configuration in Tb^{3+} ions to levels of the lowest excited $4f^75d$ configuration. The excitation spectrum of Eu^{3+} and Tb^{3+} luminescence correlates well with absorption spectrum. This spectrum consists of broad charge-transfer band 0^2-Eu^{3+} ($4f-5d$ transitions in Tb^{3+} ions) and narrow lines of $f-f$ transitions in Eu^{3+} (Tb^{3+}) ions. The luminescence spectra of $\text{Ca}_3\text{Ga}_2\text{Ge}_4\text{O}_{14} : \text{Eu}$ crystals are observed in the region between 570...710 nm and mainly due to the transition $^5\text{D}_0-^7\text{F}_0-5$ in Eu^{3+} . The most intense lines correspond to electro-dipole transition $^5\text{D}_0-^7\text{F}_2$. The absence of emission from higher $^5\text{D}_j$ levels can be due to efficient multiphonon relaxation or quenching via cross relaxation. The luminescence of $\text{Ca}_3\text{Ga}_2\text{Ge}_4\text{O}_{14} : \text{Tb}^{3+}$ crystals is due to $^5\text{D}_3 \rightarrow ^7\text{F}_j$ transitions in Tb^{3+} ions (350...480 nm region) and $^5\text{D}_4 \rightarrow ^7\text{F}_j$ ones (480...650 nm region). The luminescence intensity of activator ions increases with temperature decreasing, although the width and the shape of lines remain practically unchanged. The halfwidth of $f-f$ transitions in activator is equal to 40...60 cm^{-1} both at 300 and 80 K.

Freshly deposited $\text{Ca}_3\text{Ga}_2\text{Ge}_4\text{O}_{14} : \text{Eu}$ and $\text{Ca}_3\text{Ga}_2\text{Ge}_4\text{O}_{14} : \text{Tb}^{3+}$ films are amorphous and do not show luminescence. In the course of high-temperature treatment ($T > 800^\circ\text{C}$), these films undergo crystallization resulting in emission which appears under cathode excitation and is caused by transitions in Tb^{3+} and Eu^{3+} ions. $\text{Ca}_3\text{Ga}_2\text{Ge}_4\text{O}_{14}$ films have no luminescence under photoexcitation. CL spectra for compounds under study are presented in fig. 3 and fig. 4. CL spectra of Eu^{3+} ions in thin films of $\text{Ca}_3\text{Ga}_2\text{Ge}_4\text{O}_{14} : \text{Eu}$ correlate well with the PL spectra characteristic of the single crystals. However, $\text{Ca}_3\text{Ga}_2\text{Ge}_4\text{O}_{14} : \text{Tb}^{3+}$ thin film emission in short-wavelength range ($^5\text{D}_3 \rightarrow ^7\text{F}_j$ transitions) is of low

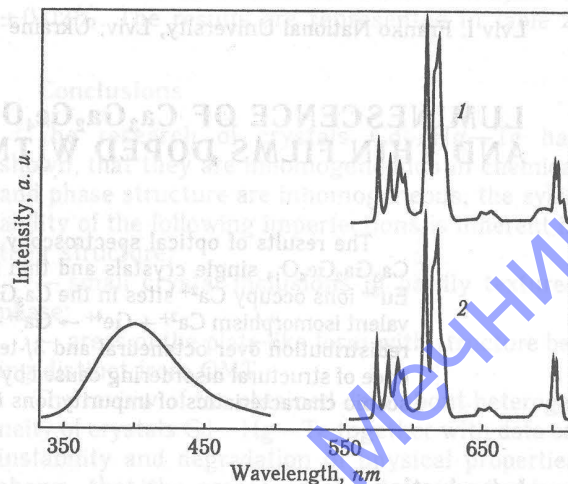


Fig. 3. CL spectra of Eu^{3+} ions in $\text{Ca}_3\text{Ga}_2\text{Ge}_4\text{O}_{14}$ thin films after annealing in air (1), and vacuum (2) at 300 K

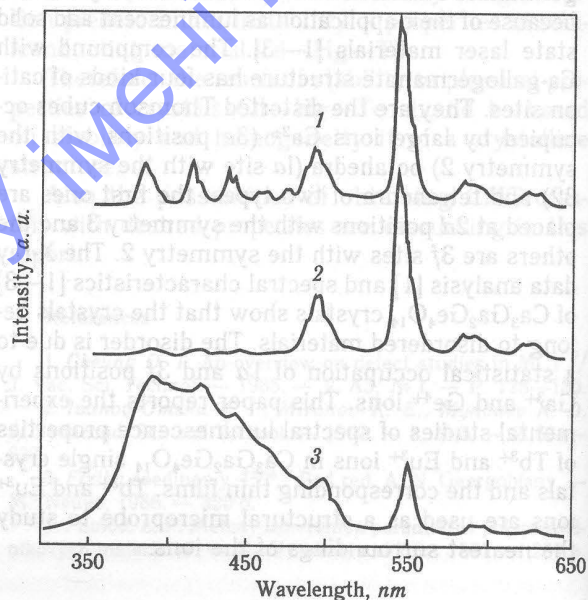


Fig. 4. CL spectra of Tb^{3+} ions in $\text{Ca}_3\text{Ga}_2\text{Ge}_4\text{O}_{14}$ single crystals (1), thin films (2) and mixture (3) at 300 K

levels through matrix defect levels most probably takes place in the $\text{Ca}_3\text{Ga}_2\text{Ge}_4\text{O}_{14}$ films. The highest intensity is characteristic for $^5\text{D}_4 \rightarrow ^7\text{F}_5$ lines both in single crystals and films of $\text{Ca}_3\text{Ga}_2\text{Ge}_4\text{O}_{14} : \text{Tb}^{3+}$.

It is known that number, the relative intensities and the splittings of lines associated with $^5\text{D}_0-^7\text{F}_j$ of Eu^{3+} and $^5\text{D}_4-^7\text{F}_j$ of Tb^{3+} transitions give the valuable information about site symmetry and number of Eu^{3+} and Tb^{3+} sites, respectively. The complete degeneration lifting and relative low ratio between line intensities of magnetic dipole transition $^5\text{D}_0-^7\text{F}_1$ and electric dipole transition $^5\text{D}_0-^7\text{F}_2$ in Eu^{3+} ions ($^5\text{D}_4-^7\text{F}_4$ and $^5\text{D}_4-^7\text{F}_5$ transitions in Tb^{3+} ions) indicate low symmetry sites with any inversion center. In view of crystal structure, it is expected

ted that Eu^{3+} and Tb^{3+} activator ions are incorporated into host lattice replacing Ca^{2+} ions at the site of symmetry 2 in Thomson cube according to the heterovalent isomorphism ($\text{Ca}^{2+} + \text{Ge}^{4+} \rightarrow \text{Ca}^{3+} + \text{Tb}^{3+}$ (Eu^{3+})) under simultaneous Ca^{3+} and Ge^{4+} redistribution over 1a and 3f crystallographic positions. Such isomorphism also agrees well with the data on effective ionic radii of Ca^{2+} , Eu^{3+} and Tb^{3+} ions.

A specific feature of luminescence spectra of $\text{Ca}_3\text{Ga}_2\text{Ge}_4\text{O}_{14} : \text{Tb}^{3+}$ and $\text{Ca}_3\text{Ga}_2\text{Ge}_4\text{O}_{14} : \text{Eu}^{3+}$ compounds, in contrast to luminescence spectra of Tb^{3+} and Eu^{3+} ions in other matrices, consists in weak structurization of bands corresponding to individual intermultiplet radiative transitions in the activator ions. That fact is easy to explain in terms of activator quasi-center model proposed in [6] and turns out to be valid in studies of absorption and luminescence spectra of Nd^{3+} , Sm^{3+} , Ce^{3+} ions in the $\text{Ca}_3\text{Ga}_2\text{Ge}_4\text{O}_{14}$ single crystals [1—3]. The presence of mixed cationic positions 1a and 3f, where Ca^{3+} ions and Ge^{4+} ions are statistically distributed, is crystallochemical feature of structure of compounds studied. While stoichiometry and periodicity of crystal is maintained, the local environment varies throughout the structure. Optically active impurity ions experience different crystal fields as a result of this local variation. A statistical disordering of the cation sublattice results in a disordering of the crystal microstructure, causing, in its turn, some fluctuation of the crystal field acting on Tb^{3+} (Eu^{3+}) ions. Unlike simple multicenter type crystals where clearly resolved lines in emission spectra correspond to each center, there is no such resolution in disordered $\text{Ca}_3\text{Ga}_2\text{Ge}_4\text{O}_{14}$ crystal structure. Thus the luminescence spectrum of Tb^{3+} and Eu^{3+} ions are characterized by broadened lines which are the superpositions of radiative transitions in activator centres of different structure having closely related characteristics of Stark energy levels splitting. The number of lines for all $f-f$ transitions in activator ions does not exceed the theoretical value derived for monoclinic field, thus proving the formation

in $\text{Ca}_3\text{Ga}_2\text{Ge}_4\text{O}_{14}$ of quasicentres of the same type caused by Tb^{3+} (Eu^{3+}) ions.

Distinctions in CL spectra of $\text{Ca}_3\text{Ga}_2\text{Ge}_4\text{O}_{14} : \text{Tb}^{3+}$ films and single crystals can be explained by different conditions of their preparation. Single crystalline $\text{Ca}_3\text{Ga}_2\text{Ge}_4\text{O}_{14}$ samples can be obtained only at elevated oxygen pressure, the main growth defects therein are germanium vacancies. When $\text{Ca}_3\text{Ga}_2\text{Ge}_4\text{O}_{14}$ films are deposited using RF ion-plasma sputtering under reduced pressure, oxygen vacancies may arise along with those of cation sublattice as well as the complexes formed due to interaction of those defects with each other and with activator ions.

For the mixture and $\text{Ca}_3\text{Ga}_2\text{Ge}_4\text{O}_{14}$ films crystallized in vacuum, a broad band is observed while the maximum at 400 nm. Taking into account that anion vacancies are activated in $\text{Ca}_3\text{Ga}_2\text{Ge}_4\text{O}_{14}$ compounds during the reduction annealing, the above band is related to defects occurring in anion sublattice.

Conclusions

The activator ions Eu^{3+} and Tb^{3+} in the $\text{Ca}_3\text{Ga}_2\text{Ge}_4\text{O}_{14}$ structure form the only type of activator quasicentre which nature is associated with disordering in cation sublattice of the matrix.

References

1. Kaminskii A. A., Beloconeva E. L., Mill B. V., Pisarevskii Yu. V., Sarkisov S. E., Silvestrova I. M., Butashin A. V. and Khodzhabayyan G. G. // Phys. Status Solidi A. — 1984. — 86, Vol. 1. — P. 345—365.
2. Nosenko A. E., Leshchuk R. Ye., Kravchishin V. V. // Ukrainian Journal of Physics. — 1998. — 43, № 3. — P. 296—298.
3. Leshchuk R. Ye., Nosenko A. E., Kravchishin V. V. // Zn. Prikl. Spectrosr. — 1998. — 65, № 2. — P. 296—298.
4. Koningstein J. A. // Phys. Rev. A. — 1964. — 136, № 2. — P. 717—725.
5. Nosenko A. E., Kostyk L. V., Kravchishin V. V. // Proceeding of the International Conference on Inorganic Scintillator and their Applications / Edited by Pieter Dorenbos, Carel W. E. van Eijk. — Delft: Delft University Press, 1996. — P. 368—371.
6. Kaminskii A. A. // Zn. Eksper. Teor. Fiz. 1970. — 58, № 2. — P. 407—419.

P. O. FEDCHUK¹, I. O. CHEMYR¹, O. P. FEDCHUK², M. A. HORNEY³¹ Odesa State Academy of Refrigeration, Odesa, Ukraine² Odesa I. I. Mechnikov National University, Odesa, Ukraine³ Oregon State University, Oregon, USA

SEMICONDUCTOR AND LIQUID CRYSTALLINE SENSORS IN THE PROBLEM OF ARTIFICIAL INTELLECT

The interrelation between the peculiarities of artificial intellect model system components' structural self-organization and the possibilities of adaptive dialog human—computer provision is studied. The fractal structure and self-organization of biologically ordered matter are considered to be the basis of signal scaling processes that occur in liquid crystalline—semiconductor contact sensors. It was shown that liquid crystalline structure is the most proper for replication of fractal structure details being always present at the surface of semiconductor wafer and their transfer into bulk of liquid crystal itself. The results obtained by the authors allow to predict the possibility of biomagnetic field registration by means of thin layer fractal structures with internal multiplication of the signal under registration.

1. Organism and Living Cell

The organisms of the higher animals, including human being, are constructed of cells. The cellular associates [1] form various tissues: muscular, connecting, nervous, etc.

The morphologic structures, being formed in organism from various types of tissue are called the organs. Groups of organs, which act in a coordinated manner and are connected anatomically, create the systems of organism, such as nervous one, e. g.

The human organism as the whole could be characterized [2] as the scaling structure with many levels and having fractal properties. One could see the presence of self-similarity on the pictures of aspirating, vascular or nervous systems of human organism.

The fractal type of structure usually makes it real the functioning of all mentioned systems in such a way that that common output has imprinted fractal features as well [3].

Biophysics [4] studies the specific details of organic molecules' behavior and properties. They include mainly proteins, aminoacids, sugars and lipids. These types of molecules are predominantly mesomorphic and could self-organize demonstrating liquid crystalline features [5, 6].

All vital processes in human organism are being strictly coordinated and are subordinate to the main goal of the nature — conservation and continuation of the life. General phenomena appropriate to the control processes occurring at all levels of living systems' organization have also the hierarchical character [7] and are studied by bio-cybernetics.

2. Control in Organism. Direct and Reverse Connections

The general sense of control includes [8] such influence of some elements of the system on the

other which leads the system to the certain state achieving the certain goals or results.

The term «control» concerning the living organism is very wide and includes the process of organism development, maintenance of the grown organism in the working conditions and repair of some worn out elements.

The most complicated control processes are realized in the central nervous system and in the psychic sphere of human individual.

In the complex biological systems the control process has the specialized part including:

- receptors (sensors) which reflect the state of the system (human being + computer), as we propose, and the incoming information at the level needed for the realization of the following stages of the control process;

- solving part (natural intellect of the human being under investigation + artificial intellect of the computer provided by specialized dialogue software), which is also the part of our original proposal and which could evaluate and/or establish the appropriate level of information exchange;

- effectors (executive elements), realized in our case by means of the specialized software, which generates the control signals and influence directly on the balance of intellectual dialogue.

The operational part of the system information exchange is shown in fig. 1.

The control is based on the exchange of information signals within the components of the system. Each chain of the system elements which serves for signals exchange could be treated as the information channel. These channels create direct and reverse connections.

The type of connections is determined according to the general direction input-output. The direct connection is been realized when the signals are transferred from the input to output end of the system.

The sciences dealing with the processes in living organisms (biochemistry, biophysics and biocybernetics) traditionally present control mechanisms as

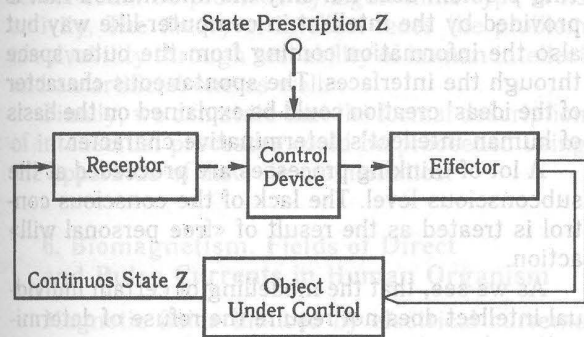


Fig. 1. Scheme of feedback in living organism during perception process

the reverse connection circuits which include the object of the control.

The main scope of exploration of control processes in biological systems becomes the interchange of the control functions between the various levels of nervous system.

The embedded mechanisms of the organism's reaction on the external effects, including problems concerning the intellect's testing and leading to the cardio-vascular system functioning, diffusion velocity correction, metabolic autoregulation, etc. could be measured by the sensorial system and be treated as the objective parameters of the human highest nervous activity.

The control process could be presented by the following steps [1]:

- reception of the information concerning some problem due to be solved through certain interface of the control center (human brain or computer);
- probing of the possible approaches to the problem solution using the existing solutions (personal experience in the field for human or data base for computer);
- choosing of the most appropriate kind of solution;
- realization of the solution chosen.

We propose to use the steps' 2, 3 and 4 realization velocity as a possible quantitative parameters of the intellectual level of information processing.

There is no doubt that almost the same processes take place in the human brain while solving any kind of intellectual problem.

3. Interfaces of Human Organism. Adaptation

Besides, it is well known [9] that the sensing organs of the human organism produces electrical pulses that are, according to Maxwell laws of electromagnetism [10] are always surrounded by electromagnetic waves [11] detectable by the various types of sensors. At this stage, physiological mechanisms of in-coming information in a quite evident

manner compress the information. Then the information is being processed at the different levels of nervous system.

The general picture of the world or the problem due to is solved separated and transferred through various nervous fibers gradually being restored to the initial state — the objective image of the problem.

The highest control levels could be represented by the enormous system of information storage, where all the data about the environment (possibly, also intellectual), the current state of the human organism, its needs, etc. The stored information may be of the highest generalized type as well. The most advanced level of the processing system should be treated as the problem image generation at the inner display of human organism.

One of the problems to be solved on the way to the balanced information exchange in the system human-computer is the adaptation problem. At the level of physiological approach, the adaptation means all types of organism's parameters changes which could be reliably attributed to in-coming information deviation.

The adaptation process could be treated in the framework of compartment model with the sources and the sinks of substance and energy as the stage of relaxation to the new state of balance [12].

The characteristic feature of adaptation process is the temporal (for the duration of the relaxation period) change of the metabolic rate.

The active control mechanisms are the first, which react, and, as the result, the transport process is directed to balance achievement between in-coming and out-coming flows of substance and energy.

The time constant of relaxation process induced by the proposed problem solving seems to be the additional parameter of intellectual level evaluation.

The theory of stress induced intellectual reaction of human [13] could be applied to the discussion conducted hereby as well. The situation of intellectual status of human organism under stress resembles the accelerated testing problem in engineering.

The periodical application and removal of the stress could be used in training process of individuals who are going to operate complicated mechanisms under emergent conditions.

4. Psychophysics Problems of the Artificial Intellect

Psychophysics opens the operational field for application and probing of various models of artificial intellect [14]. Multiple functions of human receptors are not described at the appropriate mathematical level now to say nothing of the fact that the senses of human organism are not the intellect itself but only the part of organism's interface.

The mathematical theory of human sensing is urgently needed at the stage of human-computer dialogue's optimization. The elaboration of sensor processes' theory could create a serious foundation of identification theory which, in turn, is the follow-

ing more advanced level of information processing by means of human or artificial intellect.

According to the existing level of artificial intellect understanding [15], the theory of intellect is the scientific discipline which is going to elaborate the mathematical description of human intellect with the scope of its realization using the means of computer science. One can state that such a determination seriously borders the field of exploration of the theory of intellect by the contemporary level of computer science. The determined, discrete and finite processes are the only processes that could be included into the «magic» circle of intellect theory.

In general we can add that the theory of intellect could be determined as the branch of science which studies both human and artificial intellects with the scope of elaboration of specific mathematical approach to the functions of intellect which will make it possible to realize it at the existing level of microprocessor technique development and to make the computer «clever» enough to be able to feel the level of corresponding participant of the dialogue human-computer.

5. The Factors Limiting Modeling of Human Intellect

The character of intellectual activity depends greatly on the conditions in which individual lives and those, in turn, are determined by eventual coincidence of circumstances. The state of organism is also quite eventual.

At last, the intellectual performance as the whole is the process that occurs by chance. The thoughts that are the combination of temporarily correlated signals emerge spontaneously.

We will try to demonstrate that all the mentioned probabilistic details of thinking process do not contradict the deterministic system of human intellect. Let us assume that human intellect could be represented by determined, discrete and finite system. Then one can easily see that the principal possibility of intellect's description by means of algebra of finite predicates.

It follows that the most common material system that could realize the formulae of finite predicates algebra is the finite automate. This imaginative device which could be modelled by means of the certain and, possibly, very complicated digital computer. In such a way it could be demonstrated that the assumption about determinative, discrete and finite nature of human intellect is quite equivalent to the thesis of principal possibility of artificial representation of the intellect using information processing technique.

Thus the eventuality of the outer space issues signifies only that the signals arrive at the input of the computer that realizes the human intellect's functions quite by chance.

The contradiction between the eventual signals' supply and deterministic way of their processing is overcome in such a way.

The fact that the chance plays significant role in the creative process (the highest level of intellectual activity) demonstrates that human while solving problem uses not only the information that is provided by the intellect in computer-like way but also the information coming from the outer space through the interfaces. The spontaneous character of the ideas' creation could be explained on the basis of human intellect's determinative character.

A lot of thinking processes are proceeded at the subconscious level. The lack of the conscious control is treated as the result of «free personal will» action.

As we see, that the modelling of certain individual intellect does not require the refuse of determinative character of the intellect.

The probabilistic methods could still be applied when we face the case of approximate description of intellectual activity of individual.

But, when we transfer ourselves to the situation of intellects' interaction as in the case of our interest the deterministic approach becomes really insufficient. Particularly, it is impossible to consider the information exchange process between the individuals.

Seems very realistic to assume that the uniqueness of individual intellect is caused by the deterministic character of the interconnections between its components. The difference between individual intellects exhibits through the probabilistic connections between them.

Let us discuss the significance of continuity factor in human intellectual activity. It is stated frequently that continuous processes form the main part of the activity of intellect. This thesis is based on the concept of continuity of physical and chemical processes that occur in human organism, nervous system and brain itself.

It should be noted that this continuity is only imagination because the processes at atomic and molecular levels are of quantum nature. This fact allows us to assume that the intellect could be described mathematically as discretely acting device. It was proved by means of a lot of psychological tests [16] that the appropriate choice of temporal or space quantification step could lead to the image of continuous object creation. The size of this step could serve as well as the quantitative measure of the intellect's interface. The effect of cinema is the best prove of this statement.

The factor of infinity also needs to be tested for the coincidence with the possibility of discrete representation of intellectual processes. Human intellect does not operate with infinite objects but only with special symbols, formulas, sentences and texts. The outstanding mathematician David Hilbert has said [17] that the intellectual activity could be named the «game with symbols». Moreover, this game is conducted according to the certain rules, which present the technique of human thinking. These rules organize the closed system, which could be determined. Hilbert theory's of proof main idea is a

protocol of rules of putting down, comparing and evaluation of the statements.

Another proof of the possibility of infinity of intellect could be provided by algorithmic type of its activity. The theory of intellect faces the problem of solvability through real ability of human intellect and an artificial one as well.

Finally, we can state that the formal description of intellectual processes could be proceeded using the apparatus of discrete mathematics.

6. Biomagnetism. Fields of Direct and Pulse Currents in Human Organism

Magnetic fields induced by electrical currents flowing inside the organism during its vital activities are called biomagnetic ones [18]. Biocurrents emerge as the result of cell electrical activity including muscles and nervous. The electrically active parts of cells are cell membrane.

The processes occurring at membrane interfaces are connected in a bilaterally determined (functional) way with biomagnetic signals.

Thus, knowledge of biomagnetic fields provides the knowledge of state and intensity of the corresponding physiological processes.

The cell membrane has the thickness of about five nanometers and is composed mainly of lipids, which are mesogenic (liquid crystalline) substances [19].

Nernst difference of potentials ΔE_{ion} emerges when the concentration of ions C_0 and C_1 at both sides of half-transparent membrane and could be represented by:

$$\Delta E_{ion} = \frac{k_B T}{e} \ln \frac{C_0}{C_1}. \quad (1)$$

Taking into account that in the stable state sodium and potassium currents equalize one another, one can obtain:

$$j_K = g_K (V_m - E_K), \quad (2)$$

$$j_{Na} = g_{Na} (V_m - E_{Na}), \quad (3)$$

and

$$V_m = \frac{(g_{Na}/g_K)E_{Na} + E_K}{(g_{Na}/g_K) + 1}. \quad (4)$$

The potential shift could take place when ionic concentration of outer-cell liquid changes. Such is, for example, the reaction of glial cell of human brain on local change of sodium concentration in intercellular space due to neuron activity. It is a slow process taking up to minutes.

Much faster temporal changes of potential with time constant up to milliseconds are caused by membranes penetrability change.

It should be mentioned specially that the presence of transmembrane potential and even its pulse or gradual change are not accompanied by currents in intercellular space. Electrical currents that flow through the membrane charging and discharging it could be registered only using the electrode placed directly inside the cell.

As the result of transmembrane currents addition, the macroscopic (volume) currents could emerge that flow in intercellular space. This could occur only when membrane surface is charged non-homogeneously. Such a currents could be detected through extracellular type of registration. Such a monitoring is the scope of the present work and main attention will be paid to this case. Specific macroscopic signals in the cases of correlated membrane polarization non-homogeneity.

The significant difference in the properties of extracellular currents in comparison to intracellular ones is that the first type of currents being detected at macroscopic distances from the cell source exhibit the integral activity of cell groups or that of the organ as a whole.

The effect of these currents could demonstrate itself in two different ways (fig. 2).

The first is the result of the fact that all the organism's tissues are conductors and the potential differences in the range 1...1000 mV arise (fig. 2, a).

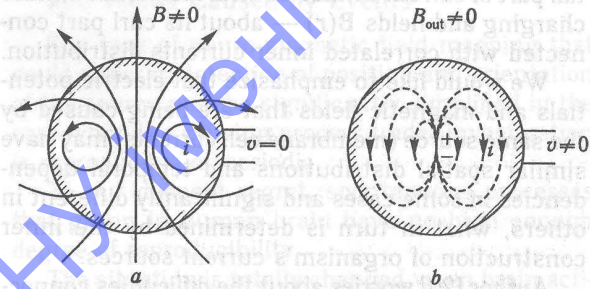


Fig. 2:

a — scheme of inner biomagnetic field structure in conduction media; b — scheme of penetrating biomagnetic fields distribution

The second one is more close to the scope of the present paper and is concerned with magnetic fields that come out of physical borders of living organism (fig. 2, b).

The distribution and the oscillation of potentials and magnetic fields are definitely caused by currents' distribution and oscillation inside the physical body of organism.

In the case of the infinite homogeneous medium, one could write the following expressions for the potential $V(r)$ and magnetic field $B(r)$ caused by the impressed currents j^i :

$$V(r) = -\frac{1}{4\pi\sigma} \int_v \frac{\nabla \cdot j^i(r')}{|r - r'|} d^3r', \quad (5)$$

$$B(r) = \frac{\mu_0}{4\pi} \int_v \frac{\nabla \times j^i(r')}{|r - r'|} d^3r', \quad (6)$$

where σ signifies conductivity of medium.

The real case of human organism could be described by the currents distributed in the ranged space (whole body) divided into the regions with different conductivities (organs). The ranging borders of organs with conductivities σ_1 and σ_2 become in such an approach the sources of secondary im-

pressed currents k^i which are determined by potential $V(r)$ at the borders:

$$k^i = -(\sigma_1 - \sigma_2) \cdot V(r) \cdot n(r), \quad (7)$$

where n is unit normal vector, which has the properties of delta function while being integrated.

Potentials and fields could be expressed as functions of j^i and k^i .

One can see that extracting the curl and potential components of j^i will lead to the following expressions for $V(r)$ and $B(r)$:

$$V(r) = -\frac{1}{4\pi\sigma} \int_V \frac{\nabla \cdot j_p(r')}{|r - r'|} d^3r' - \frac{1}{4\pi\sigma} \int_V \frac{\nabla \cdot k^i(r')}{|r - r'|} d^3r', \quad (8)$$

$$B(r) = \frac{\mu_0}{4\pi} \int_V \frac{\nabla \cdot j_p(r')}{|r - r'|} d^3r' + \frac{\mu_0}{4\pi} \int_V \frac{\nabla \cdot k^i(r')}{|r - r'|} d^3r'. \quad (9)$$

It is clear enough that potential $V(r)$ and fields $B(r)$ carry quite different information about the structure of impressed currents' sources that causes their generation. Potentials $V(r)$ describe the potential part of current connected with membrane surface charging and fields $B(r)$ — about its curl part connected with correlated inner currents distribution.

We would like to emphasize that electric potentials and magnetic fields that are being caused by the same source (membrane cell currents) may have similar spatial distributions and temporal dependencies in some cases and significantly different in others, what in turn is determined by the inner construction of organism's current sources.

Author [20] worries about the difficulties connected with the division problem of all the impressed currents to initial and secondary ones. However, at the same time he states that the modeling could be provided by means the assumption of medium homogeneity.

The complicated character of the equations (8) and (9) do not allow to understand clearly the difference in information type provided by the signals of electrical and magnetic nature.

The magnetic signal is registered in certain point of space by one sensor and the electrical signal (potential difference) could be measured by pair of electrodes only.

Thus, we see that magnetic sensor reacts to the strong enough (correlated) currents that flow in the region of activity. At the same time, the distribution of weak surface currents influence significantly the distribution of electrical potentials.

The measurement of electrical and magnetic potentials has a complimentary character. The determination of potentials and fields using the known sources distribution is so called direct problem that could be solved precisely and definitely [21, 22].

However, much more significant and useful will be the resolution of the reverse problem — determination of sources' distribution and structure using experimentally registered potentials and magnetic fields. It was shown [23] that this problem has no definite solution. This signifies that electro- and magne-

to-graphic even registered simultaneously don't comprise the full data set needed for the precise determination of current sources inside living organism.

This difficulty could be dealt with using the assumption of the special model for sources' distribution. One of the assumption of the kind is the heart's electrical vector which is determined as:

$$p = \int_V j^i(r') d^3r'. \quad (10)$$

This vector could be determined using the map of measured potentials.

The heart's magnetic vector is introduced quite analogously:

$$m = \frac{1}{2} \int_V r' \times j^i(r') d^3r'. \quad (11)$$

The restoration of magnetic and electrical vectors of any organ of human organism is not a precise solution of the reverse problem.

However, the value of the registered signals and the dynamics of their evolution could support significantly in diagnostics and monitoring of organ's activity. In many cases, they will assist also to make evaluation of the whole organism's activity efficiency.

7. Neuromagnetism and New Directions in Human Brain Exploration

There are many problems before the science that is engaged in human brain exploration. The essence of sensing, the difference between the understandable and non-understandable things and ideas, the nature of memory, function of dreams, etc., are the experimental fundamental problems of intellect theory.

The last two decades are being characterized by the introduction of the most modern physical methods and apparatus into research laboratories and neuro-surgical clinics. These are the methods of non-invasive and non-destructive type.

Up to the most recent times, the most informative method of non-invasive type was the electroencephalographic method that allows to registrate the electrical signals' distribution over the head's skin [24]. These potentials are only weak reflection of electrical processes in human brain what is caused by the human cranium structure. Conductive layered structure of cranium significantly diminishes the current densities in comparison with the case of homogeneous conductive medium. Besides, it minimizes the spatial variations of current densities (caused by nervous activity) that makes the picture of signal distribution more monotonous.

It was shown [25] that skin effect does not influence in any way the precision of reverse problem solution in biological bodies of real dimensions.

The magnetic field sensors have certain preferences. They react directly to the currents flowing in human brain and thus spatial distribution and temporal dependence of magneto-encephalographic signals reflect the inner electrical activity of the brain non-corrugated by cranium influence.

Concentric non-homogeneties of spinal liquor, cranium and scalp do not influence in any way on intensity and distribution of magnetic field induced by brain activity and spread to outer space.

Magnetic activity of human brain was registered for the first time by Cohen [26] using regular sole-noids. It was very hard to discriminate the useful signal covered by overwhelming noise.

Significant diminuation of the noise level was achieved with the use of superconducting SQUIDS and only after this it become possible to obtain magneto-encephalograms in real time scale.

There is no standard method of taking magneto-encephalogram up to now. Even the first experiments have shown that brain induced magnetic fields have much more fine and thus more informative structure than electrical potentials do.

The recommended density of magnetic sensors distribution has the cell dimensions of 10 mm order [18].

Magneto-encephalography differs principally from electro-encephalography in that magnetic field sensors do not require tight contact with the head of the person under test and they could be removed during experiment quite freely.

The most reliable information could be registered only by multi-sensor systems.

8. Sources of Neuro-Magnetic Fields

The grade of brain bio-currents' sources and corresponding magnetic fields detalization depends on the type of interrelation between neuron form, their structure, interaction with other cells, spatial distribution and electrical activity could be reflected in magneto-encephalogram.

The in-brain electrical activity has such a character that in many cases of interest the inducing processes occur in a comparatively small part of the brain. The key model could be represented by current dipole serving as the primary source of magnetic field.

In reality magnetic field induced by current dipole inside sphere differs from that caused by ideal dipole. Precise account was made in [27] where authors present the result in spherical coordinates:

$$H_r = \frac{aP}{4\pi r^3} \frac{\sin \theta \sin \varphi}{r^{3/2}}, \quad (12)$$

$$H_\theta = \frac{P}{4\pi r^2} \frac{\sin \varphi}{r^{3/2}} \left[\frac{\gamma \cos \theta}{\sin^2 \theta} \left(\cos \theta - \frac{r}{a} + \frac{r\gamma^{1/2}}{a} \right) - \frac{a}{r} \left(\cos \theta - \frac{a}{r} \right) \right], \quad (13)$$

$$H_\varphi = \frac{P}{4\pi r^2} \frac{\cos \varphi}{r^{3/2} \sin \theta} \left(\frac{r}{a} - \cos \theta - \frac{r\gamma^{1/2}}{a} \right). \quad (14)$$

The definition of the kind is used:

$$\gamma = \left[1 - \frac{2a \cos \theta}{r} + \left(\frac{a}{r} \right)^2 \right]. \quad (15)$$

Other types of brain activity that involve large areas of nervous tissue could be represented by system of certain quantity of current dipoles.

There is a lot of experimental evidence [28] indicating that the most intensive source of neuro-magnetic signals is the neocortex of human brain.

The pulse exchange on the short in-cortex distances could not generate sufficient input to neuro-magnetic fields because different phases of nervous pulse (spike) will compensate one another while being averaged over large number of axons needed for generation of signal that could be reliably measured.

It is also very unprobable that the relatively low frequency spectrum of magneto-encephalogram could be explained based on magnetic fields induced by propagating spikes.

At least, one-dimensional ordering of brain compartment is also needed for justification of cooperative type of dipole action.

9. Evoked Magnetic Fields and Fields Caused by Events

The task of neuro-magnetic field mapping that could assist in detection of position and orientation of the source may be significantly simplified in the case when the causing process under investigation is reproducible or periodic.

To our deepest regret, spontaneous processes that go on in human brain have no high enough degree of reproducibility.

The situation is totally changed when brain activity has strict cause-consequence relation with the event out of human nervous system. Such type of magnetic fields are called evoked or event related fields.

This type of investigation is much more complicated because the intensity of the signals is 5... 10 times lower than that of spontaneous brain activity.

Phenomena connected with evoked magnetic fields have demonstrated to be very well explained using the model of current dipole.

When the pulse from outer receptor (human interface) comes the cooperating groups of neurons situated in, various brain compartments begin to generate electrical and magnetic signals. Usually some neuron stations are being activated which generate both spikes and gradually changing signals. Signal, which is registered by outer sensors, has the form of decaying wave with superimposed maximums and minimums.

Authors [29] have registered very high degree of signal source localization in brain cortex. The hard fixation of magnetic gradiometer was proposed and special experimental room with no non-homogeneous fields was required as well.

Localized current dipoles were determined quite reliably in the experiments with eye, ear and other stimulated part of human organism's reception system.

10. Liquid Crystals as the Active Media of Weak Magnetic Field Sensors with Inner Amplification of Signal

The state of substance which is, for some compounds, intermediate between hard crystal anisotropic state and isotropic liquid state is called liquid crystalline (LC) phase or mesophase [30]. The main cause of such strange behavior of LC phase lies in special form of its molecules. In many cases, the molecules of LC are elongated in one preferential direction.

There are two large groups of LC compounds differing by the method of mesophase creating:

- thermotropic;
- lyotropic.

The first type of LC could be transferred into mesophase using heating. The phase transition of the first type (with hidden transition heat and step-like change of molecular density) usually accompany such transformation and each specific LC compound has its own temperature range of mesophase existence. This type of LC is represented generally by artificial organic substances.

Second type of LC organizes mesophase at the certain dilution level when the specific ratio between the concentrations of solvent and solute substance. This kind of LC is represented by organic substances of biological nature.

We have shown previously [19, 31—34] that a lot of liquid components of human organism exhibit LC properties, including blood plasma, lipid system, spinal liquor, tear liquid, bile, urine, etc.

It is quite clear that the difference between two types of mesophase forming lies only in the method of intermolecular distance variation.

The dominant orientation of LC molecules is described by vector-director.

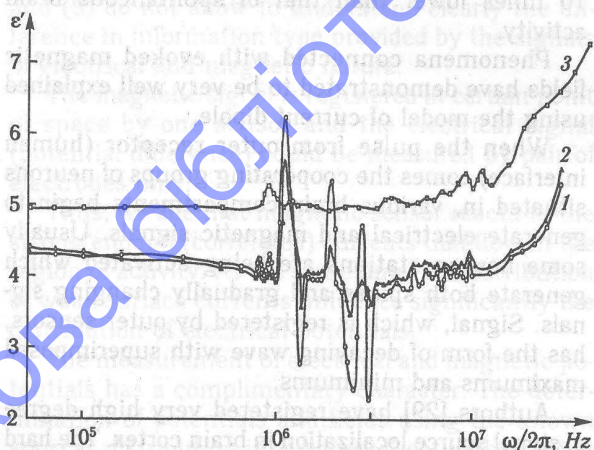


Fig. 3. Dispersion spectrum of real part of complex dielectric permeability:

1 — 27°C; 2 — 32°C; 3 — 52°C ($d = 30 \text{ mm}$)

Degree of orientation homogeneity is presented by order parameter which value lie in the range from

zero to one beginning from isotropic liquid to anisotropic crystal.

We have discovered experimentally for the first time [35] the effect of dielectric response of nematic LC stimulated by order parameter's fluctuations. It was known before [36] that planarly oriented nematic LC demonstrates dielectric spectrum of relaxation type and its exploration does not allow to anything more but director fluctuations.

The inclined director orientation gives more degree of freedom and that why we have explored the dielectric spectra of the model nematic MBBA with the initial inclined at 45° director orientation concerning the bordering surfaces.

In fig. 3, one can see the frequency dependence of the real part of complex dielectric permeability measured in thin layer of MBBA at various temperatures. It is obvious from the figure that the specific resonance response of nematic LC occurs only in mesophase existing temperature region.

The components of the resonance dielectric spectra could be represented by the following formulas:

$$\varepsilon'(\omega/\omega_0) = \frac{1 - (\omega/\omega_0)^2}{(1 - (\omega/\omega_0)^2)^2 + \Gamma^2(\omega/\omega_0)^2}, \quad (16)$$

$$\varepsilon''(\omega/\omega_0) = \frac{\Gamma(\omega/\omega_0)}{(1 - (\omega/\omega_0)^2)^2 + \Gamma^2(\omega/\omega_0)^2}, \quad (17)$$

where braking parameter $\Gamma = 2\gamma/\omega_0$ is connected with resonance frequency of damped oscillator. The dielectric responses at the points of resonance are about million times higher than in the case of regular relaxation response.

The frequencies registered in our experiment were at least three orders greater that the known relaxators' frequencies which are caused by director fluctuations. Therefore, the most probable mechanism of resonance spectra arising could be longitudinal and biaxial fluctuations of order parameter which demonstrate critical behavior near transition isotropic liquid-liquid crystal. In such a way, we have demonstrated the possibility of resonance response of LC thin layer placed between electrodes.

Another our experiment [37] demonstrates 1/f noise induced ferro-electric type phase transition in the vicinity of zero frequencies. The dielectric permeability of nematic LC increases at least by five orders of magnitude in comparison to the value measured at higher frequencies (fig. 4).

Two mentioned mechanisms are connected most probably with the effect of domino which demonstrates common motion of oriented molecular clusters in LC layer. According to the well-known fluctuation theory of phase transitions [38], the probability of phase transition is increased incredibly when orientation nucleus is formed at some point situated at domain wall [39].

The combination of all these requirements could be realized in layered system conductor (semiconductor) — liquid crystal. Before making any conclusions, we propose to describe the surface of perfect crystal material available now — silicon wafer.

We have shown experimentally [40] using the lifetime scanning laser microscopy technique that surface under investigation could be described in terms of fractal physics.

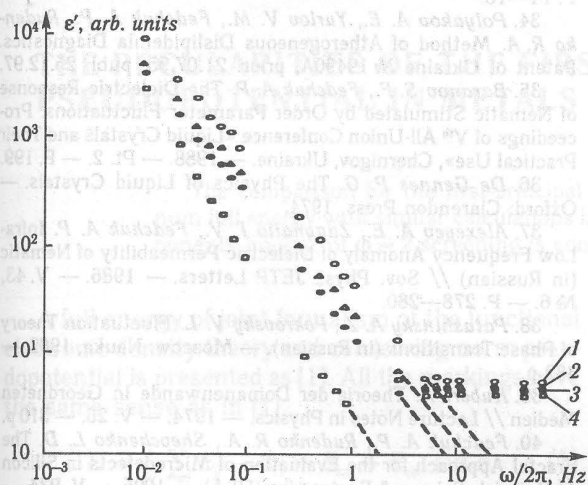


Fig. 4. Frequency dependence of dielectric constant of nematic liquid crystal ZliK-440 for a layer 30/μm thick in lie following fields:

1 — $3.3 \cdot 10^5$ V/m; 2 — $6.5 \cdot 10^5$ V/m; 3 — $1.3 \cdot 10^5$ V/m; 4 — $2.6 \cdot 10^5$ V/m

In progress, this approach [41] has demonstrated to be also useful to minimize the time of silicon substrate inspection. Silicon surface point defects, being self-organized in surface fractal cluster, could serve successfully as the nuclei of the new orientation type for LC layer put in tight contact with it.

We have demonstrated [42] that LC layer being in contact with plane conducting substrate undergo orientational self-organization due to the process of thermoionic emission from substrate which influences the charge distribution near the surface and changes the system's free energy.

Conclusions

Taking into account all presented above, we could make the following conclusions:

1. The bio-magnetic fields could be used successfully as the most informative external part of human brain activity dealing with information exchange in dialogue system artificial intellect vs. natural (human) intellect.
2. It is possible to identify position of current dipoles or their systems acting in strong correlation with the use of biomagnetic fields investigation.
3. Existing methods of weak biomagnetic fields registration including superconducting SQUIDS could be hardly applied in the case of multi-sensor system, which is needed for real investigation of human intellect.
4. The effect of resonance dielectric response of nematic LC stimulated by order parameter fluctuations could be used as the basis of new supersensitive electromagnetic fractal field sensor.

5. $1/f$ noise stimulated self-organization of LC thin layer in the vicinity of zero frequencies could be used as well for experimental investigation of biomagnetic field peculiarities caused by intellectual activity of human brain.

6. Application of LC thin layer over the surface of silicon wafer produces a fractal magnetic field sensor (FMFS) comparable as to its sensitivity to SQUID.

7. Additional effect of FMFS is that it could be realized using well developed planar technology and fiber-optical sensor techniques.

References

1. Novoseltsev V. N. Organism in the World of Technologies // Engineering Aspect (in Russian). — Moscow: Nauka Publishers, 1989. — 240 p.
2. Goldberger E. L., Reagney D. R., West B. J. Chaos and Fractals in Human Physiology // Scientific American. — 1990. — № 4. — P. 25–32.
3. Urgens H., Peitgen H. O., Saupe D. The Language of Fractals // Scientific American. — 1990. — № 10. — P. 36–44.
4. Denny M., Gaines S. Chance in Biology. — Princeton University Press, 2000. — 424 p.
5. Walleczek J. (Ed.) Self-Organized Biological Dynamics and Non-Linear Statistical Physics. — Cambridge University Press, 2000. — 425 p.
6. Bahr C., Kitzerow H. Chirality in Liquid Crystals. — Springer Verlag, 2000. — 430 p.
7. Kadanoff L. P. Statics, Dynamics and Renormalization. — Imperial College Press, 2000. — 450 p.
8. West B. J. Physiology, Promiscuity and Prophecy at the Millennium. — Imperial College Press, 1999. — 452 p.
9. Kostyuk P. G., Grodzinsky D. M., Zima V. L., Magura I. S., Sydorik E. P., Shuba M. F. Biophysics (in Russian). — Kyiv: Vyshcha shkola, 1988. — 504 p.
10. Purcell E. M. Electricity and Magnetism. Berkeley Physics Course. — MacGrow-Hill Book Company, 1965. — V. 2. — 440 p.
11. Crawford F. S. Waves. Berkeley Physics Course. — MacGrow-Hill Book Company, 1967. — 528 p.
12. Azuine B., Azarmi N., Nauck D. Intelligent Systems and Soft Computing. — Springer Verlag, 2000. — 359 p.
13. Selye H. From Dream to Discover in Being a Scientist. — New York: Arno Press, A New York Times Company, 1964. — 368 p.
14. Chemyr I. A., Horney M. A., Anderson-Inman L. Smart Text: Using Agents Supporting Personalized Reading Comprehension // Personal Technologies (USA). — 1998. — V. 2. — P. 152–161.
15. Shabanov-Koushnarenko Y. P. Theory of Intellect. Mathematical Means (in Russian). — Kyiv: Vyshcha Shkola, 1984. — 144 p.
16. Chemyr I. A. Dialogue of Partners as a Method of Non-Formal Problem Solving // Human-Machine Communication for Educational Systems Design. Brouwer-Janse M. D. and Harrington T. Eds., NATO ASI Series. — Springer Verlag, 1994. — V. F129.
17. Gilbert D. The Basement of Geometry (in Russian). — Moscow: Gosteorkekhizdat Publishers, 1948. — P. 382.
18. Leondes C. T. (Ed.) Gordon & Breach International Series in Engineering, Technology and Applied Sciences, 2000. — v. 2, Medical Imaging Systems Techniques and Applications. Brain and Sceletal Systems.
19. Fedchuk A. P., Barnyak E. M., Asmolov A. K., Andreiev V. O., Sydelnikova T. A. The Lyotropic Properties of Human Bile under Cholelitiase (in Russian) // Proceedings of Russian Academy of Sciences. Physical Series. — 1998. — V. 62, № 4. — p. 1710–1714.
20. Modern Techniques in Neuroscience Research / Eds. Uwe Windhorst and Hakan Johansson. — Springer Verlag, 1999. — 1325 p.

21. De Wolf D. A. Essentials of Electromagnetics for Engineering. — Cambridge University Press, 2000. — 550 p.
22. Lopez-Davalos A., Zanette D. Fundamentals of Electromagnetism. — Springer Verlag, 1999. — 294 p.
23. Van Rienen U. Numerical Methods in Computational Electrodynamics. — Springer Verlag, 2000. — 375 p.
24. Lohmann K. J., Johnsen S. The Neurobiology of Magnetoreception in Vertebrate Animals // Trends in Neurosciences, 2000. — V. 23, № 4. — P. 153—159.
25. Bossavit A. Computational Electromagnetism // Academic Press, 1997. — 300 p.
26. Cohen D. Magnetoencephalography: Evidence of Magnetic Fields Produced by Alpha-Rhythm Currents // Science. — 1968. — V. 161. — P. 784.
27. Cuffin B. N., Cohen D. Magnetic Fields of a Dipole in Special Volume Conductor Shapes. IEEE Trans. — 1977. — V. BME-24, № 4. — P. 372.
28. Brown R. G., Pluck G. Negative Symptoms, the «Pathology» of Motivation and Goal-Oriented Behaviour // Trends in Neurosciences, 2000. — V. 23, № 9. — P. 412—417.
29. Reite M., Edrich J., Zimmerman J. T., Zimmerman J. E. Human Magnetic Auditory Evoked Fields // Electroencephalography and Clinical Neurophysiology. — 1978. — V. 45, № 1. — P. 114.
30. Yang O., Can Z., Xing L. J., Zhang X. Y. Geometric Methods in the Elastic Theory of Membranes in Liquid Crystal Phases. Advanced Series in Theoretical Physical Science. — Springer Verlag, 1999. — V. 2. — 244 p.
31. Bouiko A. S., Fedchuk A. P. Numerous Lyotropic Phases and Phase Transition Kinetics in Human Tear Preparations (in Russian) // Journal of Medical Techniques and Technology. — 1994. — № 1—2. — P. 16—21.
32. Fedchuk A. P., Rudenko R. A., Barniyak E. M., Bouiko A. S. The Influence of Electric Field on the Optical Properties of Biological Self-Organizing Media (in Russian) // Proceedings of XXVII International NIS Conference on Dispersed Systems, Odesa, Ukraine. — 1996. — P. 209—210.
33. Polyakov A. E., Fedchuk A. P. Electric Properties of the Atherosclerosis Affected Points of Human Arterial Walls (in Russian) // Ukrainian Cardiological Journal. — 1997. — № 6. — P. 14—18.
34. Polyakov A. E., Yurlov V. M., Fedchuk A. P., Rudenko R. A. Method of Atherogeneous Dislipidemia Diagnostics. Patent of Ukraine № 19490A, prior. 21.07.95, publ. 25.12.97.
35. Baranov S. F., Fedchuk A. P. The Dielectric Response of Nematic Stimulated by Order Parameter Fluctuations. Proceedings of Vth All-Union Conference «Liquid Crystals and Their Practical Use», Chernigov, Ukraine. — 1988. — Pt. 2. — P. 199.
36. De Gennes P. G. The Physics of Liquid Crystals. — Oxford: Clarendon Press, 1974.
37. Alexeyev A. E., Zagynailo I. V., Fedchuk A. P. Infra-Low Frequency Anomaly of Dielectric Permeability of Nematic (in Russian) // Sov. Phys.: JETP Letters. — 1986. — V. 43, № 6. — P. 278—280.
38. Patashinsky A. Z., Pokrovsky V. L. Fluctuation Theory of Phase Transitions (in Russian). — Moscow: Nauka, 1982. — 382 p.
39. Hubert A. Theorie der Domanenwände in Geordneten Medien // Lecture Notes in Physics. — 1974. — V. 26. — 310 p.
40. Fedchuk A. P., Rudenko R. A., Shevchenko L. D. The Fractal Approach for the Evaluation of Microdefects in Silicon // Materials Science & Engineering (USA). — 1995. — V. B34. — P. 164—167.
41. Fedchuk A. P. Fractal Properties of Microdefects' Cluster of Subsurface Layer of Silicon Monocrystals (in Ukrainian) // Photoelectronics, 1998. — № 7. — P. 74—78.
42. Kornienko Y. K., Fedchuk A. P., Barniyak E. M. Orientational Self-Organization in Nematic Thin Film Layer Sandwiched Between Conducting Isotropic Substrates // Smart Materials and Structures (USA). — 1998. — V. 7. — P. 894—898.

Найкова бібліотека ОНУ

THE PECULARITIES OF THE FIRST-PRINCIPAL PSEUDOPOTENTIAL IN METALS

The comparison for the first-principal calculations of lithium, calcium and aluminum full energy with similar calculations in which Fourier model pseudopotential components Fourier of $\varphi = 2$ screening is considered to be a fitting, was carried out.

A full energy of joint formalism of the functional electronic density theory and conserving norm pseudopotential is presented as [1]. All the markings have the same sense as in [1].

$$E = \frac{1}{N} \sum_k E_k - E_H + E_{xc} + E_{es} + \alpha_1 z. \quad (1)$$

The pseudopotential parameters are taken from [2]. To calculate of the amounts in formula (1) in high-symmetrical points of Brillouin zone, a secular equation is solved [3]:

$$\left[\frac{\vec{k} \times \vec{g}}{2} - E(\vec{k}) \right] C_{n,\vec{k}}(\vec{g}) + \sum_{\vec{g}'} W(\vec{k} + \vec{g}, \vec{k} - \vec{g}') C_{n,\vec{k}}(\vec{g}') = 0, \quad (2)$$

where $C_{n,\vec{k}}(\vec{g})$ are factors in decomposition of pseudowave functions along flat waves.

$$\phi(n, \vec{k})(\vec{r}) = \sum_{\vec{g}} C_{n,\vec{k}}(\vec{g}) \cdot I \cdot \vec{k} + \vec{g} > ., \quad (3)$$

where n — zone number, \vec{k} — wave vector in the first Brillouin zone. In Fourier potential model

$$W(\vec{k} + \vec{g}, \vec{k} + \vec{g}') = W_{BHS}(\vec{k} + \vec{g}, \vec{k} + \vec{g}') + W_H(\vec{g} - \vec{g}') + W_{xc}(\vec{g} - \vec{g}') \quad (4)$$

enters alongside with Fourier models of Hartiev and exchange-correlation ones, Fourier model of pseudopotential Bachelet—Hamann—Schluter which is presented as [2].

$$(W_{BHS})_1 = W_{(core)(r)} + \Delta W_1, \quad (5)$$

where $W_{(core)(r)}$ and ΔW_1 — Gauss type functions. On the first type of selfcoordinated-iteration procedure the pseudopotential linear screened local part is usually used as

$$W(\vec{g}) = \frac{W_{loc}(\vec{g})}{\varepsilon(\vec{g})}, \quad (6)$$

where $\varepsilon(\vec{g})$ — dielectric permeability function in Lindhart form.

And further the selfcoordinated calculations are made, on each step of which the crystalline potential is built with the account of received sharing electronic density. Unlike [1] the account of ex-

change-correlating potential adjustments in the given work is made according to the formulae [4]. The integration on the first Brillouin zone is replaced by the summation on two points of Chadi—Cohen [5] or on one point of Balderesky [6].

The equilibrium atomic volumes and full energies were found from the state crystal equation under $p = 0$ and $T = 0$:

$$\left(\frac{dE}{d\Omega} \right)_S = 0, \quad (7)$$

where S is entropy. The results of the first-principal calculations can be defined more exactly by means of fitting as a result of which the contribution of type b/Ω [1] is added to the full energy (which is marked further by letters *ff*).

In table 1 the first-principal calculations results of equilibrium atomic volume and full energy in VCC-lithium under the decomposition of pseudowave functions (3) on 43 and 55 inverse lattice vectors were given (the summation in Brillouin zone was hold at one point of Balderesky).

Table 1

Comparative calculations of equilibrium atomic volumes and full energy in VCC-lithium at decomposition of pseudowave functions on 43 and 55 inverse lattice vectors

(volumes in $(a.u.)^3$, energy — in Ry, *uf* — using a fitting)

Calculations	Ω_{theor}	$\frac{\Omega_{theor} - \Omega_{exper}}{\Omega_{exper}}$	E_{theor}	$\frac{E_{theor} - E_{exper}}{E_{exper}}$
43 v	145,58	0,014	-0,49399	0,046
43 v uf	143,54	—	-0,50655	0,021
55 v	148,94	0,038	-0,49384	0,046
55 v uf	143,56	—	-0,50191	0,030

The values of percentage errors for full energies are slightly distinguished that allows greatly to decrease matrixes order of secular equation under the calculation of lithium energy features and equivalent elements.

The similar calculations made for ECC-structures Ca and Al are present in table 2. The abbreviation point-C and point-B refer to the calculations on two points of Chadi—Cohen and on one point of Balde-

resky, accordingly. In the first-principal calculations the points of Chadi—Cohen the best consent in values of full energy with the experiment is received.

Table 2

The equilibrium atomic volumes and full energies for Ca and Al

(volumes — in $(a.u.)^3$, energy — in Ry , errors — in %)

Element	Calculation	Ω_{theor}	Error	E_{full}	Error
Ca	Point C.	290,75	1,4	-1,486041	1,8
	Point B.	292,43	0,9	-1,534009	5,1
Al	Point C.	121,51	9,2	-4,164484	0,1
	Point B.	122,08	9,7	-4,123838	0,9

Both methods bring about the greater deflection of equilibrium atomic volumes from experimental one for Al.

For the account of nonlocal screening it's necessary to shield the nonlocal part of potential. Because of great complexity of this procedure it is easier to consider this screening to be a fitting procedure.

The results of table 3 are received in the assumption of screening Fourier model of Bachelet—Hamann—Schluter pseudopotential by means of dielectric Lindhart function $\epsilon(q)$

$$\langle \vec{k} + \vec{q} | \Delta W_1 | \vec{k} \rangle. \quad (8)$$

Hence, the results for lithium are worsened, for calcium — practically are not changed, for aluminum — the consents of equilibrium atomic volumes with experimental ones become better without worsening in the consents of full energies with the experiment. For ECC-nickel the calculations bring

about to the percentage error in 2—3% for volumes however significant error appears in the full energy

Table 3

The equilibrium atomic volumes and full energies for Ca and Al at the account of screening components of pseudopotential $1 = 2$

(volumes in $(a.u.)^3$, energy — in Ry , errors — in %)

Element	Calculation	Ω_{theor}	Error	E_{full}	Error
Ca	Point C.	300,04	1,8	-1,480097	1,4
	Point B.	291,50	1,1	-1,533940	5,1
Al	Point C.	117,37	5,4	-4,164379	0,1
	Point B.	119,22	7,1	-4,120838	1,0

calculation which decreases from 12 to 8% while transferring from linear screening to the account of screening nonlocal part of the potential with $1 = 2$.

References

1. Софронков А. Н., Дроздов В. А., Поживащенко В. В. Расчет фазовых переходов под давлением на примере щелочноземельных металлов // ФММ. — 1992. — № 9. — С. 145—147.
2. Bachelet G. B., Hamann D. R., Schluter M. Pseudopotentials that work: from H to Pu // Phys. Rev. B. — 1982. — V. 26, № 8. — P. 4199—4228.
3. Denteneer P. J. H., van Haeringen W. The pseudopotential density-functional method in momentum space: details and test case // J. Phys. C. — 1985. — V. 18. — P. 4127—4142.
4. Krasko G. L. Iteration- perturbation theory of covalent bonding in crystals. 1. General consideration // Z. Naturforsch. — 1981. — V. 36 a, № 11. — P. 1129—1145.
5. Chadi D. J., Cohen M. L., Special points in the Brillouin zone // Phys. Rev. B. — 1973. — V. 8, № 12. — P. 5747—5753.
6. Baldereschi A. Mean-value point in the Brillouin zone // Ibid. — V. 8, № 12. — P. 5212—5215.

where n — zone number, \vec{k} — wave vector in the first Brillouin zone, in Fourier potential model

$$W(\vec{k} + \vec{q}) = W_{\text{loc}}(\vec{k} + \vec{q}) + W_{\text{ex}}(\vec{k} + \vec{q}) + W_{\text{sc}}(\vec{k} + \vec{q}) \quad (4)$$

enters alongside with Fourier models of Hartree and exchange-correlation ones, Fourier model of pseudopotential Bachelet—Hamann—Schluter which is presented as [2]

$$W_{\text{sc}}(\vec{k}) = W_{\text{loc}}(\vec{k}) + \Delta W_{\text{sc}}(\vec{k}) \quad (5)$$

where $W_{\text{loc}}(\vec{k})$ and $\Delta W_{\text{sc}}(\vec{k})$ — Gauss type functions. On the first type of self-consistent iteration procedure the pseudopotential linear screened local part is usually used as

$$W(\vec{k}) = \frac{W_{\text{loc}}(\vec{k})}{\epsilon(\vec{k})} \quad (6)$$

where $\epsilon(\vec{k})$ — dielectric permittability function in Lindhart form.

And further the self-consistent calculations are made, on each step of which the crystalline potential is built with the account of received screening electronic density. Unlike [1] the account of ex-

The values of percentage errors for full energies are slightly distinguished that allows greatly to decrease matrices order of secular equation under the calculation of lithium energy features and equivalent elements.

The similar calculations made for ECC-structures Ca and Al are present in table 3. The approximation point-C and point-B refer to the calculations on two points of Chadi—Cohen and on one point of Balde-

A. Yu. LYASHKOV, A. S. TONKOSHKUR, V. O. MAKAROV

Dnepropetrovsk State University, Dnepropetrovsk, Ukraine

DIELECTRIC PROPERTIES OF ZnO—Ag₂O GAS SENSITIVE CERAMICS

The dielectric properties of ZnO—Ag₂O gas sensitive ceramics were investigated. Obtained results are explained within the framework of models of polycrystalline inhomogeneous structures with intergranular potential barriers.

Introduction

ZnO and SnO₂ based ceramics have gas sensitivity to an adsorption of spirits vapor, in particular ethanol [1—6]. The detail research of conductivity processes in such materials is one of the important problems [1, 7, 8].

In the present paper we report the results of dielectric properties and conductivity investigations of ZnO based ceramics doped by silver.

Experimental results and discussion

The gas sensitive ceramics was made by mixing of ZnO and Ag₂O powders, pressing (at 10 atm) and sintering at 1173 K during 1 hour in an air. For electrical measurements, disk samples were used. The electrodes were produced by burning of silver paste.

The current-voltage characteristics measurements, the frequency dependence of relative dielectric permeability and dielectric losses factor (in frequency band of 50 kHz — 10 MHz), their relations to temperature and other factors were carried out using the standard industrial devices.

The current-voltage characteristics of ZnO—Ag₂O ceramics were linear. The temperature dependence of electrical conductivity of ceramics was described by standard exponential relation and was similar to characteristics for polycrystalline ZnO. The specific conductivity of ceramics at room temperature is $\sigma_0 \approx 2 \cdot 10^6 (\Omega \cdot m)^{-1}$. The activation energy (W_0) of conductivity was about 0.92 eV.

The frequency dependences of dielectric permeability (ϵ') and factor of dielectric losses (ϵ'') of researched ceramics are shown in fig. 1. It can be seen that the dispersion of dielectric permeability is observed in radio frequency range. The increase of temperature results in displacement of dispersion to higher frequencies and maximum of dielectric losses factor clearly appears at temperature of 360 K.

The dielectric permeability of investigated ceramics is high and it has a polycrystalline structure, therefore, it can be assumed, that the migrational polarization on boundaries of ZnO crystallites is responsible for the observable dielectric dispersion.

The activation energy (W_p) of polarization process was estimated from temperature position of disper-

sion area. Taking into account the adopted above polarization mechanism from temperature displacement of the frequency (f) at temperature change (T)

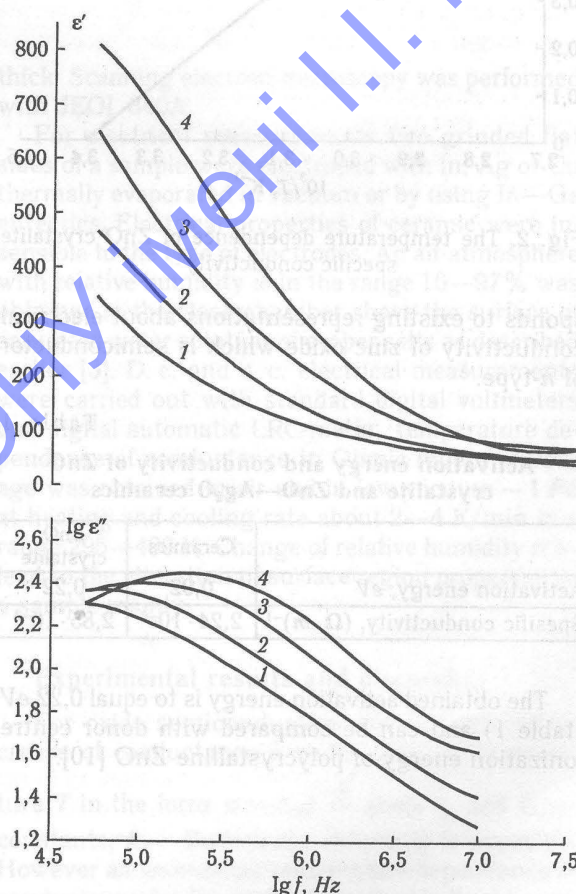


Fig. 1. The frequency of the dielectric permeability and dielectric loss factor at various temperatures:

1 — 292 K; 2 — 315 K; 3 — 345 K; 4 — 359 K

the specific electrical conductivity of ZnO crystallites (σ_v) was estimated using ratio $\sigma_v(T_1)/\sigma_v(T_0) = f_1/f_0$, where indexes «1» and «0» corresponded to different values of temperature. The absolute value of σ_v was estimated from a $\epsilon''(f)$ spectrum using the known bicomponent dielectric Wagner model [9]:

$$\sigma_v = 2\pi \cdot f_{\max} \cdot \epsilon_a \frac{\epsilon_s + \epsilon_d + p_v(\epsilon_s + \epsilon_d)}{1 - p_v},$$

where f_{\max} — frequency of dielectric losses factor maximum, ϵ_a — electrical constant; ϵ_s — dielectric permeability of semiconducting crystallite; ϵ_d — dielectric permeability of intergranular dielectric; p_v — volumetric part of semiconducting phase in inhomogeneous system.

The value of $\sigma_v \approx 3 \cdot 10^{-3} (\Omega \cdot m)^{-1}$ was obtained at the 300 K for investigated ceramics. The temperature dependence of σ_v is shown in fig. 2 and corre-

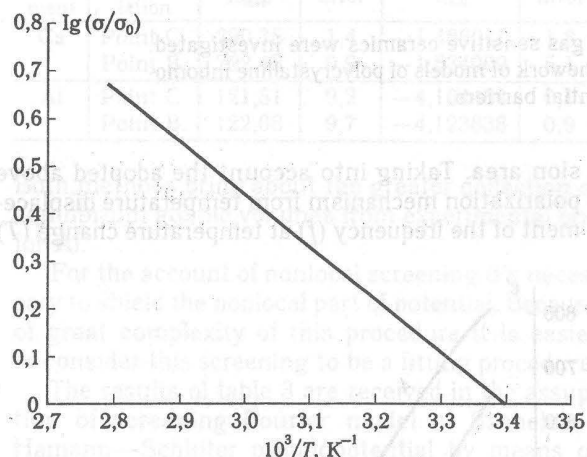


Fig. 2. The temperature dependence of ZnO crystalite specific conductivity

sponds to existing representations about electrical conductivity of zinc oxide which is semiconductor of *n*-type.

Table 1
Activation energy and conductivity of ZnO crystalite and ZnO—Ag₂O ceramics

	Ceramics	ZnO crystalite
Activation energy, eV	0.92	0.22
Specific conductivity, $(\Omega \cdot m)^{-1}$	$2.24 \cdot 10^{-6}$	$2.85 \cdot 10^{-3}$

The obtained activation energy is to equal 0.22 eV (table 1) and can be compared with donor centre ionization energy of polycrystalline ZnO [10].

Conclusions

1. The frequency dependences of complex dielectric permeability have dispersion in the range of radio frequencies, which can be explained by migrational polarization observed in inhomogeneous systems. The structure of investigated ceramics consist of high conducting and semiconducting ZnO crystalite divided by low conducting intergranular phase.

2. The temperature dependence for d. c. specific conductivity of the ceramics $(\sim 2 \cdot 10^{-6} (\Omega \cdot m)^{-1}$ at 300 K) and specific electrical conductivity of grains $(\sim 3 \cdot 10^{-3} (\Omega \cdot m)^{-1}$ at 300 K) have the activation energy of 0.92 and 0.22 eV, accordingly, and electrical properties of investigated ceramics may be explained within the framework of models of polycrystalline inhomogeneous structures with intergranular potential barriers.

References

1. Полупроводниковые сенсоры в физико-химических исследованиях / И. А. Мясников, В. Я. Сухарев, Л. Ю. Куприянов, С. А. Завьялов. — М.: Наука, 1991. — 327 с.
2. Бутурлин А. И., Габузян Т. А., Голованов И. А. Газочувствительные датчики на основе металлооксидных полупроводников. М.: ЦНИИ «Электроника», 1986. — 40 с.
3. Ляшков А. Ю., Тонкошкур А. С. Характеристики активного элемента полупроводникового датчика паров этилового спирта на основе поликристаллической системы ZnO—AgO // Тез. докл. 10-й научно-технич. конф. с участием зарубежных специалистов «Датчик-98». — Гурзуф, 1998.
4. Виглеб Г. Датчики. — М.: Мир, 1989. — 196 с.
5. Frang Y. K., Lee J. J. A tin oxide thin film sensor with high ethanol sensitivity // This Solid Films. — 1989. — 169, № 1. — P. 51—56.
6. Ichinose Noboru. Electronic ceramics for sensor // Amer. Ceram. Soc. Bull. — 1985. — 64, № 12. — P. 1581—1585.
7. Сухарев В. Я., Мясников А. И. Об электропроводности неупорядоченной полупроводниковой системы с межкуристаллитными барьерами при адсорбции активных частиц // ФТТ. — 1985. — Т. 27, № 3. — С. 705—709.
8. Schurmer H. V., Gardner I. W., Chan H. T. The application of discrimination techniques to alcohols and tobaccos using tin-oxide sensors // Sens. and Actuators. — 1989. — 18, № 3—4. — P. 361—371.
9. Афонько Е. Ф., Тонкошкур А. С., Якунин А. Я. Электрические свойства гетерогенных фотоваракторных структур на основе CdS // Оптоэлектроника и полупроводниковая техника. — 1982. — № 1. — С. 66—69.
10. Миллер П. Электрические и оптические свойства окиси цинка // Полупроводниковые материалы / Под. ред. В. М. Туркевича. — М.: Изд. иностр. лит., 1954. — С. 227—237.

conductivity was about 0.92 eV. The frequency dependences of dielectric permeability (ϵ') and factor of dielectric losses (ϵ'') are shown in fig. 1. It can be seen that the dispersion of dielectric permeability is observed in the frequency range. The increase of temperature results in displacement of dispersion to higher frequencies and maximum of dielectric loss factor clearly appears at temperature of 360 K. The dielectric permeability of investigated ceramics is high and it has a polycrystalline structure. Therefore, it can be assumed that the migrational polarization on boundaries of ZnO crystalites is responsible for the observable dielectric dispersion. The activation energy (W) of polarization process was estimated from temperature position of disper-

ELECTRICAL PROPERTIES OF TIN DIOXIDE BASED CERAMICS IN HUMID AIR ATMOSPHERE

Humidity sensitive electrical properties of tin dioxide based ceramics in a system $\text{SnO}_2\text{—ZnO—Ge}_2\text{O}_3$ are observed. Strong dependence of d.c. and a.c. conductivity and capacitance on relative humidity as well as non-Ohmic conduction observed even at high relative humidity and observed anomaly of temperature dependence of conductivity testify that studied ceramics is grain boundary controlled material. Humidity sensitivity of electrical properties is due to the change of grain boundary key potential barriers heights. The correlation between humidity sensitivity of electric parameters and highly developed surface of ceramics is found.

Introduction

Many oxide materials exhibit fairly strong dependence of electrical properties on temperature, electric field, heat treatment and environmental atmosphere [1—4]. Therefore these materials are suitable for the fabrication of different sensors. Creation of new sensors and improvement of their electrical parameters requires to search new composition and clearing up the mechanisms of charge carriers transport. Tin dioxide based ceramics in a system $\text{SnO}_2\text{—ZnO—Bi}_2\text{O}_3$ [3] shows non-Ohmic conduction and it can be grain boundary controlled materials. The enhancement of non-Ohmic behaviour of this ceramics is due mainly to the Bi_2O_3 addition which is responsible for the formation of a thin grain boundary phase. The elimination of Bi_2O_3 from the composition of ceramics may cause the weakening of non-Ohmic properties but on the contrary it could improve the sensitivity of electrical properties to environmental atmosphere [3]. It was found that electrical conduction of ceramics in a system $\text{SnO}_2\text{—ZnO—GeO}_2$ may be influenced by the change of relative air humidity. It is interesting to study the electrical properties of this material because electrically active grain boundaries may be responsible for such behaviour as well. The purpose of this paper is study electrical properties and structure of tin dioxide based ceramics in the system $\text{SnO}_2\text{—ZnO—GeO}_2$ which exhibit humidity sensitive conduction.

Experimental details

Starting oxides were weighted and mixed in distilled water for 1 hour. After drying of obtained mixture at temperature 400 K disks were pressed under pressure of about 100 MPa. Then pressed discs were sintered in air at maximum temperature T_s in the range 1470—1570 K during 1 hour with heating and cooling rate of about 400 K/hour. Sintered samples were 10 mm in diameter and 1 mm

thick. Scanning electron microscopy was performed with JEOL-840A.

For electrical measurements two grinded flat sides of a sample were electroded with In, Ag or Cu thermally evaporated in vacuum or by using In—Ga eutectics. Electrical properties of ceramic were insensitive to the type of electrodes. An air atmosphere with relative humidity w in the range 10—97% was obtained in the close chamber above the surface of saturated water solution of proper salts as described earlier [3]. D. c. and a. c. electrical measurements were carried out with standard digital voltmeters and digital automatic LRC-meter. Temperature dependence of conductance in Ohmic region of voltage was obtained in air and in low vacuum ~ 1 Pa at heating and cooling rate about 2—4 K/min in a range 295—400 K. Change of relative humidity may lead to the alteration of surface region properties of a sample mainly.

Experimental results and discussion

For oxide semiconductors the exponential increase of conductance s under absolute temperature T in the form $\sigma = \sigma_0 e^{-\frac{E_g}{kT}}$ (here σ_0 and E_g — constants, k — Boltzmann constant) is expected. However an anomalous temperature dependence of conductance for the studied tin dioxide based ceramics in the air was found (fig. 1, curve 1). The conductance decreases if temperature increases above room temperature. Then conductance goes other minimum at temperature which is below 373 K. Further rise of temperature leads to increase of conductance. At cooling σ decreases and then increases showing a weak minimum (fig. 1, curve 2).

An anomalous decrease of conductance on temperature for semiconductor ceramics with negative temperature coefficient of resistance $\gamma = \frac{1}{R} \frac{dR}{dT} < 0$ could be explained by a desorption of water mole-

cles from the surface. It should be pointed out that the anomalous $\sigma(T)$ dependence near room temperature takes place even at cooling (fig. 1, curve 2). The reason for that is the adsorption of water molecules penetrated into a great number of pores.

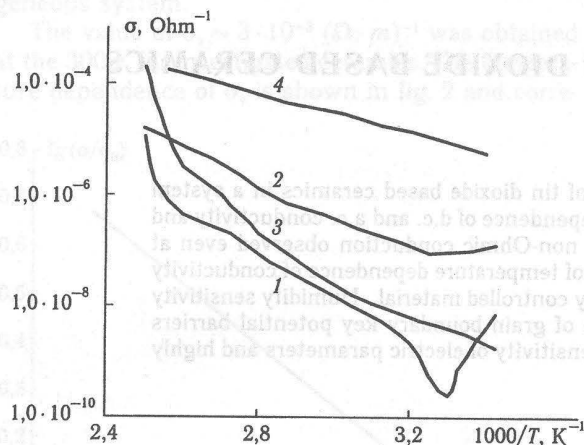


Fig. 1. Temperature dependence of d. c. conductance of ceramics in a system $\text{SnO}_2\text{—ZnO—GeO}_2$ ($T_s = 1470$ K) in the air (1, 2) and in the vacuum (3, 4) at heating (1, 3) and cooling (2, 4)

For the proof of the role of desorption-adsorption of water molecules, temperature dependence of conductance was obtained in a low vacuum as well. In this case the absence of water vapour may exclude the observation of an anomalous $\sigma(T)$ dependence. This suggestion is confirmed by the experiment in vacuum (curves 3 and 4 at fig. 1).

After heating of sample up to about 400 K and cooling, some irreversible conductance increase takes place, so $\sigma(T)$ curve goes higher at cooling (fig. 1, curves 1 and 2). It may be due to the desorption of oxygen. It is known that oxygen plays an important role in the formation of grain boundary potential barriers in tin dioxide based ceramics [3]. At room temperature in vacuum some desorption of oxygen, not only water molecules, can take place and it explains why room temperature conductance in vacuum before heating (curve 3 at fig. 1) is not much lower than conductance in air (curve 1 at fig. 1). The heating of a sample in vacuum up to the same temperature leads to higher irreversible increase of conductance (fig. 1, curves 3 and 4) than heating in air because in vacuum more intensive desorption of oxygen takes place.

The observed temperature dependence of conductance in air atmosphere (fig. 1) shows that tin dioxide based ceramics can be used as humidity sensor material. Therefore let us consider electrical properties of SnO_2 -ceramics in air with fixed humidity.

D. c. voltage-current characteristics for ceramic samples of different composition at low and high relative air humidity are shown at fig. 2. Electrical conductance of certain sample in humid air has bulk and surface contributions. Conduction of oxide ceramics in the bulk is non-Ohmic and is related to electron transport controlled by grain boundary

potential barriers [3, 5]. However humidity influenced surface contribution is rather linear. Therefore voltage-current characteristics of different samples may have different nonlinearity. It is observed that voltage-current characteristic of the sample with

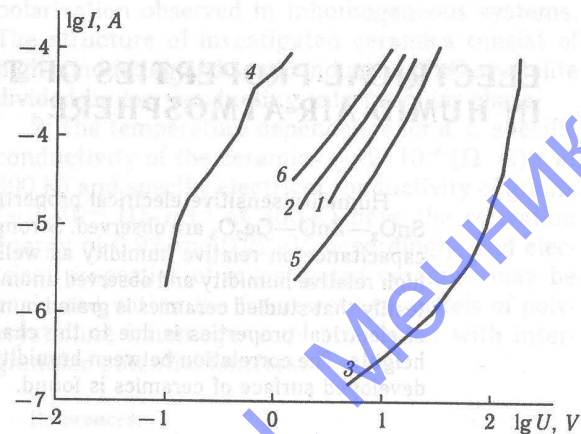


Fig. 2. Voltage-current characteristics of $\text{SnO}_2\text{—ZnO—GeO}_2$ based ceramics without optimum additives (1, 2) and with optimum (3, 4) and with non-optimum additives (5, 6) in the air with relative humidity 10 (1, 3, 5) and 92% (2, 4, 6)

optimal concentration of additives is non-linear not only at low (curve 3 at fig. 2) but at high humidity (curve 4 at fig. 2) and sample was sensitive to high humidity.

The rise of relative humidity causes the shift of adsorption-desorption balance to the adsorption. Then additional adsorbed water molecules H_2O may be dissociated at adsorption centres at the surface for proton H^+ and hydroxyl ion OH^- . Proton H^+ as more mobile can migrate and reach certain grain boundary. The localization of H^+ ion near grain boundary may cause the decrease of absolute value of negative grain boundary localised charge. This process promotes the reduction of potential barriers heights and leads to increase of conductance. Non-linearity coefficient $\beta = \frac{d(\ln I)}{d(\ln U)}$ for ceramics with lower grain boundary potential barriers decreases according to fig. 2.

The decrease of grain boundary potential barriers heights at higher relative humidities causes the increase of a. c. electrical conductance G and capacitance C of ceramic sample as well (fig. 3). The relative change of a. c. conductance on humidity is more strong than the relative change of capacitance as shown at fig. 3. So, the conductance G of individual barrier roughly may be presented as:

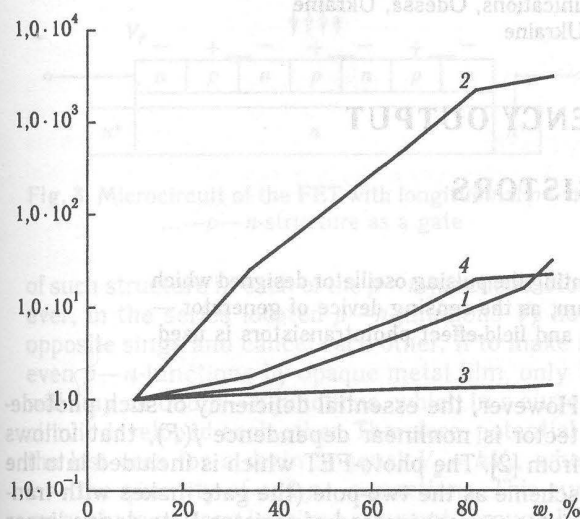
$$G = G_0 e^{-\frac{\varphi_0}{kT}}, \quad (1)$$

where φ_0 — potential barrier height. Capacitance C of individual barrier may be described by the expression:

$$C = S \left(\frac{q^2 \epsilon \epsilon_0 N_D}{8 \varphi_0} \right)^{1/2}, \quad (2)$$

where S — cross-section area of grain boundary,

penetration into ceramic sample is higher. Thus, electrical conductance and capacitance of ceramics become higher in accordance to fig. 3.



Conclusion

D. c. and a. c. electrical conductance and capacitance of tin dioxide based ceramics in a system $\text{SnO}_2\text{—ZnO—GeO}_2$ sintered at 1470—1570 K are strongly dependent on relative humidity of the air. The observation of non-Ohmic conduction even at high relative humidity shows that studied ceramics is grain boundary controlled material. Humidity dependence of electrical properties is due to the change of grain boundary potential barriers heights. Observed anomalous temperature dependence of conductance is due to the influence of desorption-adsorption processes in humid air. The role of adsorption-desorption processes is indirectly confirmed by the found correlation between humidity sensitivity of electrical parameters and highly developed surface of ceramics.

Acknowledgement. One of us (A. B. G.) would like to express the acknowledgement to the British Council Ukraine for the support of his short visit to Brunel University, Uxbridge, U. K.

References

1. *Traversa E.* Sensors and Actuators B. — 1995. — 23, 135—156.
2. *Ratcheva T., Stambolova I., Konstantinov K.* Thin Solid Films. — 1992. — 217. — 187—191.
3. *Glot A. B., Proshkin Y. N., Nadzhafzade A. M.* Ceramics Today — Tomorrow's Ceramics / Ed. P. Vincenzini. Mater. Sci. Monographs, 66C. — Amsterdam—Oxford—New York—Tokyo: Elsevier, 1991. — P. 2171—2180.
4. *Glot A., DiBartolomeo E., Traversa E. J.* Eur. Ceram. Soc. — 1999. — 19. — P. 715—719.
5. *Glot A. B.* Advances in Varistor Technology / Ed. L. M. Levinson. Ceramic Transactions. — Schenectady (U. S. A.): Amer. Ceram. Soc., 1989. — Vol. 3. — P. 194—203.

PHOTODETECTORS WITH FREQUENCY OUTPUT ON THE BASIS OF UNIJUNCTION AND FIELD-EFFECT PHOTOTRANSISTORS

The construction of photodetector representing the pulsing oscillator designed which frequency depends on quantity of light stream, as the sensing device of generator — the silicon chip — consisting of unijunction and field-effect phototransistors is used.

The sensor with frequency output represents the generator of variable voltage, which frequency is the function of measured action (temperature, pressure, light etc.). The signal from such detector may immediately be handled by computer and also by any chip-pulse counting device. Such sensors on the basis of unijunction and field-effect phototransistors are discussed in this paper.

The unijunction transistor (UJT) consists of semiconductor rod with two ohmic base contacts (B_1 , B_2) on testing faces and emitter $p-n$ -junction (e) between them (fig. 1). Its input current-voltage characteristics falls into S-type, that allows to create the generator by prime hook up of capacity to input circuit ($e-B_1$). The condenser C is charged up to potential of basis opposite to the emitter V_1 after insert of the power supply E . The emitter $p-n$ -junction is switched on in a forward direction and the condenser is fast discharged through the bottom of basis. Then the process is iterated. The oscillations of voltage on emitter have a saw tooth view, and their amplitude is equal to the difference between the switch on voltage and residual voltage at current-voltage characteristics:

$$V_a = V_b - V_0. \quad (1)$$

The period of oscillations is defined [1] as

$$T = R_e C \ln \frac{E - V_0}{E - V_b}. \quad (2)$$

The current pulses on the resistance of basis R_1 is possible to use as output signal also.

The UJT can work as the photodetector at irradiating basis. The irradiation increases the concentration of charge carriers in basis, that gives the decrease V_b and T , so also the growth of oscillation frequency $f = 1/T$ with increase of light stream F .

However, the essential deficiency of such photodetector is nonlinear dependence $f(F)$, that follows from [2]. The photo-FET which is included into the scheme as the two-pole (the gate makes with transistor source) instead of resistor R_e to derive linear relation $f(F)$ is offered to use by us [2]. At such insert FET works as current generator, that is charging current for the condenser C and does not depend on voltage, that simplifies the formula (2) to a view [3]

$$T = \frac{I_c}{C} V_b - V_0. \quad (3)$$

The charging current develops of FET-photocurrent and photocurrent of UJT emitter $p-n$ -junction. They are linearly depend on F , that gives the linearity of dependence $f(F)$.

Both of these transistors may be manufactured in one chip of semiconductor as microcircuit. The example of such structure is shown by fig. 2. In the initial base n -semiconductor, there are two n^+ -fields being base contacts UJT (B_1 , B_2), and between them the p -region of the emitter is firmware, on which surface the n -channel of MOS-type FET places. One extremity of the channel (drain) is connected through the basis to contact B_2 , and the second (source) — with the emitter. The dielectric on channel surface is deposited. Behind it semitransparent layer of metal being gate of the FET and jointed with source is superimposed. The light stream falls on FET channel (through transparent metal and dielectric) and on the upper part of the basis UJT. Experimental samples of chips with FET and UJT, manufactured on the basis of epitaxial n -silicon by planar diffusion technology, have shown, that their photosensitivity is higher by not less than order of magnitude than responsibility of the separate UJT.

The further magnification of photosensitivity can be received by usage in microcircuit of the FET with

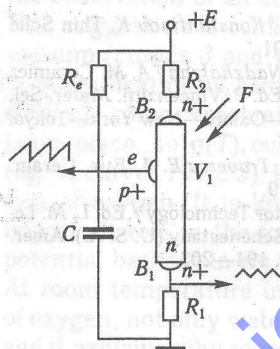


Fig. 1. The unijunction transistor

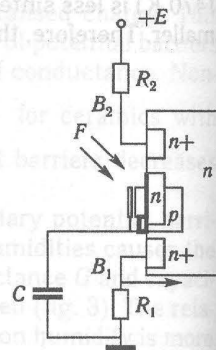


Fig. 2. UJT and FET as a chip

longitudinal $p-n-n-p-n$ -structure as a gate (fig. 3). There is photo-voltage V_F under irradiation

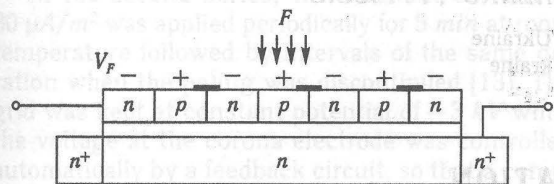


Fig. 3. Microcircuit of the FET with longitudinal $p-n-n-p-n$ -structure as a gate

of such structure in each of the $p-n$ -junctions. However, in the series located $p-n$ -junctions V_F have opposite signs and cancel each other. If to make all even $p-n$ -junctions by opaque metal film, only V_F will stay on odd $p-n$ -junctions, which in a current circuit developed each other. Therefore, potential of the last area for a drain is equal $V_g = kV_F$, where k — the quantity of odd $p-n$ -junctions. This summary photo-voltage is driven a current through FET channel as well as usual voltage on a gate. In this case FET channel works in a mode of the charge carriers enhancement. If, on the contrary, to bring up all the odd $p-n$ -junctions (and even to unlock), the channel will operate in a mode of a depletion. Experimental samples of the MOS-photo-transistors on the basis of silicon epitaxial films covered with silicon dioxide, on which the polycrystalline silicon film of a gate representing six-layer longitudinal $p-n-n-p-n$ -structure was superimposed have shown a photosensitivity being by tens-hundreds fold greater, than responsibility of usual FET with semi-transparent metal gate. Accordingly, using such FET in photosensing chip (fig. 2) in during long time its

responsibility is incremented also. The frequency output of photodetector allows considerably to simplify its jointing with computer and to make micro-miniaturisation of the construction for the measuring device. So, for example, the scheme of the measurer for illumination intensity is implemented as follows. During one measurement the generator UJT feeds one current pulse by duration $t_p = 0,1$ s. Circuit elements of relaxation oscillator are selected so that in absence of light in time t_p UJT generated 100 impulses. The frequency of the generator grows at irradiating. The responsibility of photodetector can be installed so, that magnification of illumination intensity at 1 unity there will corresponds to growth of frequency 1 Hz. Then 200 impulses corresponds 100 units, to 300 impulses — 200 units etc. The impulses from generator move on pulse counting devices, including digital indicators, where the value of illumination intensity is highlighted. The scheme together with the power supply is agglomerated in a housing by the size about usual pen with a photodetector on the face.

Photosensitive chip (UJT and FET) and chip — pulse counting device are made on sample technology silicon microscheme and can be integrated in one chip.

References

1. Vikulin I. M., Stafeev V. I. Physics of semiconductor devices. — M.: Radio and communication. — 1990. — 270 p.
2. Vikulin I. M., Vikulina L. F., Kurmashev Sh. D. Photodetector. — Pat. USSR № 1189301. — 21.03.84.
3. Vikulina L. F., Glauberman M. A. Sensors for control of temperature and magnetic fields. — Odessa: Mayak. — 2000. — 245 p.
4. Vikulin I. M., Vikulina K. I., Kurmashev Sh. D. Photo FET. — Pat. USSR № 1431622. — 14.10.86.

¹ Odessa State Academy of Food Technologies, Odessa, Ukraine² Odessa I. I. Mechnikov National University, Odessa, Ukraine³ Athens National Technical University, Athens, Greece

CORRELATION BETWEEN POLARIZATION AND SPACE CHARGE PHENOMENA IN CORONA POLED FERROELECTRIC POLYMERS

Polarization and space charge phenomena in ferroelectric polymers are interrelated due to existence of the depolarizing field. This field must be compensated anyhow in order to obtain stable residual polarization. It is shown that in corona poled PVDF this compensation is performed by injected and deeply trapped charges. Experimental evidence for the charge trapping has been obtained from the dynamics of apparent conductivity during poling. Irreversible decrease in the conductivity has been observed during the buildup of ferroelectric polarization independently on poling conditions. Appropriate calculations have shown that compensating charges are trapped not at the boundaries of crystallites, as usually believed, but in transition zones separating polarized parts of the volume from non-polarized ones.

1. Introduction

Polyvinylidene fluoride (PVDF) and some of its copolymers belong to the class of ferroelectric polymers, due to possession of spontaneous switchable polarization in one of the crystalline polymorphs called the β phase [1]. It has been proved experimentally that the piezoelectric and pyroelectric coefficients in PVDF were proportional to the magnitude of the remanent polarization [2]. At the same time, there is strong evidence that the injected space charge also affects the specific properties of the ferroelectric polymers [3–5]. The role of the space charge has been discussed for the past twenty years or so, but no agreement has been reached on this point so far. Some researchers believe that presence of space charge in ferroelectric polymers is important, but others think that its influence can be neglected [6]. It is implied in many cases that polarization and space charge do not depend on each other. However, as will be shown below, correlation between them must be certainly considered.

It is known that switching of polarization in ferroelectrics is accompanied by appearance of the depolarizing field that attempts to restore the original electric state with zero average polarization. If this field is not neutralized (or compensated) anyhow, the residual polarization is low and unstable. Compensation of the depolarizing field in conventional ferroelectrics is usually done either by charges adsorbed on the surfaces, or through a short-circuiting of samples between electrodes. In case of the ferroelectric polymers, phenomenon is more complicated, because crystallites are dispersed in disordered amorphous phase. It is not known so far where the compensating charge resides [7–8] and how the charge trapping can be recognized and identified experimentally.

It has been found earlier that the poled PVDF was less conductive than the unpoled one [9]. Measurement in the spatial distribution of polarization has proved that the injection of charges took place and the charges disturbed the uniformity of polarization [3, 5, 7]. We proposed a model for the buildup of polarization in PVDF and other ferroelectric polymers assuming that trapped charges and polarization formed the self-consistent well-balanced system [4, 10–12]. In this work we provide new experimental data on trapping of compensating charges in corona poled PVDF films. It is shown by appropriate calculations that the trapped charges reside at the boundaries of the macroscopic polarized zones.

2. Experimental

The study was performed on 25 μm -thick uniaxially stretched PVDF films containing amorphous and crystalline phases in almost equal proportion. The crystallites consisted of a ferroelectric β phase (56%) and non-polar α phase (44%). Samples were electrodeposited from one side by evaporation of aluminum and placed in corona triode the non-metallized surface exposed to corona ions. A pointed tungsten electrode kept at constant potential of -20 kV initiated the corona discharge. The grid was made vibrating in order to measure effective surface (electret) potential by Kelvin's method directly during the poling and immediately after it was completed [4].

Three different kinds of poling conditions were applied. In the first series of experiments, the quasi-stationary I – V characteristics have been obtained at room temperature by increasing negative d. c. voltage at the control grid in steps of 100 V from 0.6 kV to 3 kV and recording the poling current. The samples were kept at each voltage for 15 min before application of the next voltage step. The ex-

periment was repeated again with already poled samples.

In the second series, the constant current of $80 \mu A/m^2$ was applied periodically for 5 min at room temperature followed by intervals of the same duration when the poling was discontinued [13]. The grid was kept at constant potential of $-3 kV$ while the voltage at the corona electrode was controlled automatically by a feedback circuit, so that a complete poling was performed in 11 charging-discharging cycles. The buildup and the decay of the electret potential were recorded during the corresponding fractions of each cycle.

In the third series of experiments, temperature increased linearly from $20^\circ C$ to $100^\circ C$ at the rate of $3 K/min$, while the grid voltage, and consequently the electret potential, was kept constant. Samples were cooled to room temperature under the applied field and the experiment was repeated again under the same conditions. In presentation of experimental results we use a concept of the apparent conductivity g defining it as

$$g = I_{x_0}/VA,$$

where I is measured current, V is applied voltage, x_0 is thickness of the sample, A is surface area.

3. Results and discussion

There are three elements at I—V characteristics corresponded to three stages of initial poling (fig. 1).

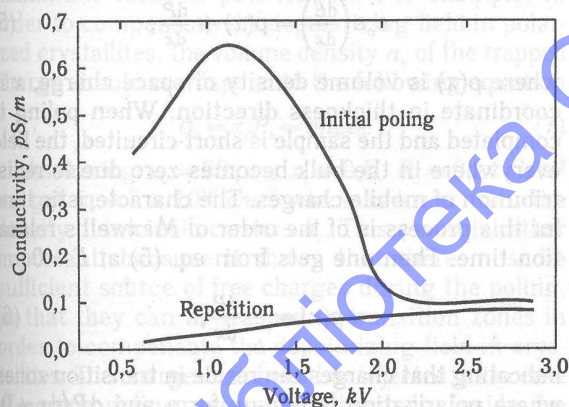


Fig. 1. Dependence of the apparent conductivity on applied voltage. The experiment has been repeated on the poled samples after completion of the initial poling

At first, the current grows faster than the applied voltage until the apparent conductivity reaches its maximum at poling field of $55 MV/m$, being very close to coercive field for PVDF [14]. At the second stage, the conductivity drops abruptly to the minimum at field of $110 MV/m$, followed by slight increase at the higher voltages. Repeated measurements on the same sample show that low values of apparent conductivity are retained in the poled samples, indicating that the changes occurred during the poling are irreversible. The field at the second stage was higher than the coercive value; therefore the

main part of the ferroelectric polarization has been formed at this stage. Since the decrease of conductivity and the buildup of polarization are observed in the same range of the poling field, it is very probable that these two phenomena are interrelated.

Poling conditions have been changed in the second series of experiments, so that the constant current was applied periodically. It is seen in fig. 2 that the electret potential decays almost to zero in 300 s with the time constant of about 200 s after

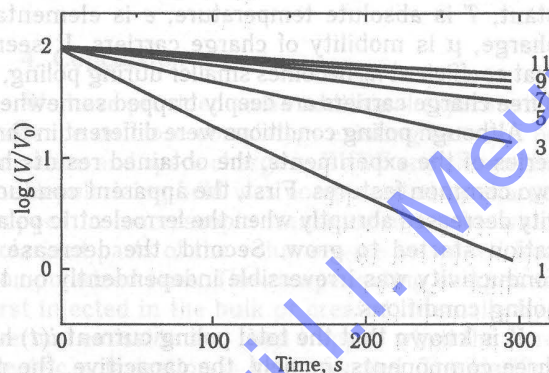


Fig. 2. Decay of the electret potential at intervals between periodic applications of constant poling current. Numbers of the applied poling cycles are indicated beside each curve

completion of the first cycle of poling. This value of time constant corresponds to Maxwell's relaxation time for PVDF at room temperature [15]. The electret potential becomes more stable with increasing number of the poling cycles. For example, the relaxation time of 1300 s was observed after application of 11 poling cycles showing that the apparent conductivity was decreased during the poling in 6.5 times.

At the third series, we observed anomalous behavior of the poling current during the linear increase of temperature at constant applied voltage. as one can see in fig. 3, the apparent conductivity

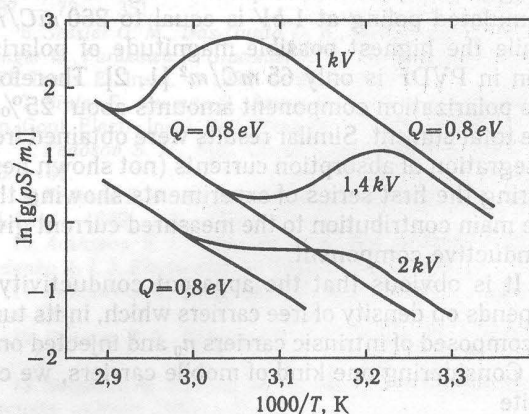


Fig. 3. Dynamics of the apparent conductivity during the initial thermally stimulated poling (solid symbols) and during repeated experiments on the poled samples (hollow symbols). Poling voltage and activation energy are also shown

became lower or remained constant during the poling depending on the value of applied voltage, but the activation energy of the apparent conductivity did not change, being about 0.8 eV in unpoled and poled samples, as it followed from the slope of graphs in fig. 3. It is assumed here that temperature dependence of conductivity obeys the Arrhenius law

$$g = e\mu n_0 \exp\left[-\frac{Q}{kT}\right], \quad (1)$$

where Q is activation energy, k is Boltzmann's constant, T is absolute temperature, e is elementary charge, μ is mobility of charge carriers. It seems that coefficient n_0 becomes smaller during poling, as if free charge carriers are deeply trapped somewhere.

Although poling conditions were different in three series of the experiments, the obtained results had two common features. First, the apparent conductivity decreased abruptly when the ferroelectric polarization started to grow. Second, the decrease in conductivity was irreversible independently on the poling conditions.

It is known that the total poling current $i(t)$ has three components, namely, the capacitive, the polarization and the conductive ones according to the following equation

$$i(t) = \epsilon_0 \epsilon \left(\frac{dE}{dt} \right) + \frac{dP}{dt} + gE, \quad (2)$$

where $i(t)$ is current density, ϵ_0 is permittivity of vacuum, ϵ is dielectric constant, E is field, P is ferroelectric polarization. The capacitive component represented by the first term at the right side of eq. (2) can be neglected, because we applied constant field at the first and the third series of experiments, while the voltage (electret potential) changed very slowly in the second series. It is not possible to calculate precisely the contribution of the polarization component to the total current, but this can be estimated by comparing the integral of total current with the highest theoretically obtainable value of the residual polarization in PVDF. Our calculations show that the integral under the current peak during the thermally stimulated poling at 1 kV is equal to 260 mC/m², while the highest possible magnitude of polarization in PVDF is only 65 mC/m² [1, 2]. Therefore, the polarization component amounts about 25% of the total current. Similar results were obtained from integration of absorption currents (not shown here) during the first series of experiments showing that the main contribution to the measured current gives conductive component.

It is obvious that the apparent conductivity g depends on density of free carriers which, in its turn, is composed of intrinsic carriers n_0 and injected ones n_i . Considering one kind of mobile carriers, we can write

$$g = e\mu(n_0 + n_i). \quad (3)$$

While n_0 depends mostly on temperature, n_i is effected by poling conditions. It seems that charges in our experiments were injected in the bulk dur-

ing the first stage of poling and then trapped when ferroelectric polarization started to grow. We have shown recently that favorable conditions for trapping of charge carriers exist at the boundaries of polarized crystallites [8, 12]. Let us calculate what would be the density of compensating charges, if they were trapped at the boundaries crystallites. Assuming that PVDF has a brick-like structure [16], shown schematically in fig. 4, we get

$$\tilde{n}_c = \frac{abP_s}{eV_c}, \quad (4)$$

where $a = 7.5$ nm and $b = 3.5$ nm are the average length and width of crystallite [16], $V_c = 1.2 \times 10^{-25}$ m³ is volume occupied by one crystallite together with amorphous phase attached to it, $P_s = 0.14$ C/m² [1] is the spontaneous polarization in crystallites. Calculations give the following value for $\tilde{n}_c = 2 \times 10^{20}$ cm⁻³, while the real density of free charge carriers available for trapping is only $n_c = 10^{12} \dots 10^{14}$ cm⁻³, if typical for PVDF values of the apparent conductivity ($10^{-10} \dots 10^{-12}$ S/m) and mobility of charge carriers (2×10^{-8} cm²/Vs) are considered. The difference in value of n_c and \tilde{n}_c is so huge that even a massive injection of charges will not provide sufficient number of carriers for trapping at the boundaries of all crystallites. Therefore, compensating charges are not trapped there, although energetic conditions are favorable for this. How then the depolarizing field is compensated? To answer the question, one should consider Poisson's equation

$$\epsilon_0 \epsilon \left(\frac{dE}{dx} \right) = \rho(x) + \frac{dP}{dx}, \quad (5)$$

where $\rho(x)$ is volume density of space charge, x is coordinate in thickness direction. When poling is completed and the sample is short-circuited, the field everywhere in the bulk becomes zero due to redistribution of mobile charges. The characteristic time for this process is of the order of Maxwell's relaxation time. Then one gets from eq. (5) at $E = 0$

$$\rho(x) = -\frac{dP}{dx}, \quad (6)$$

indicating that charges can reside in transition zones where polarization is non-uniform and $dP/dx \neq 0$. Thus, conditions for charge trapping are favorable not only at the boundaries of crystallites, but also in macroscopic transition zones separating polarized part of the volume from non-polarized ones, as it is shown schematically in fig. 5.

Trapping of charges in transition zones is very important, because these charges indeed compensate the depolarizing field in the crystallites. To prove this, we consider the definite case, for example, the uniform distribution of polarization in the bulk with narrow transition zones near surfaces [5], as it is shown in fig. 4. At equilibrium conditions the density σ_r of real charge at the surfaces is equal to the density of the polarization charge σ_p , and to the magnitude of the average polarization P' , i. e. $\sigma_r = \sigma_p = P'$. In its turn, $P' = x_c P_s$, where x_c is the crystallinity.

Let us find the field applied to a dipole inside a crystallite positioned, for example, at the point A. If the

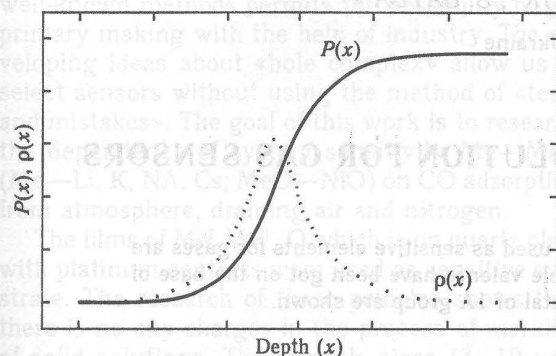


Fig. 4. A typical distribution of polarization and space charge in the thickness direction, according to Poisson's equation. Space charge is localized in a transition zone by which the polarized part of the volume is separated from the non-polarized one

one-dimension approximation is valid, the resulting field is zero, because the number of positively charged layers is equal to that of the negatively charged ones both above this point and below it. Therefore, the depolarizing field inside the crystallites is completely compensated by field of charges trapped either at the surface, or in transition zones. It is easy to show that in both cases the charge density related to the unit area does not depend on thickness of the transition zone and equal to the maximum value of polarization. For example, in order to compensate the depolarizing field in polarized crystallites, the volume density n_v of the trapped charge should correspond to the following equation

$$\sigma_r = x_c P_s = e n_v x_0. \quad (7)$$

Assuming $x_0 = 20 \mu\text{m}$, $x_c = 0.5$, $P_s = 0.14 \text{ C/m}^2$ we get $n_v = 5 \times 10^{16} \text{ cm}^{-3}$ which is lower than the density of intrinsic carriers n_i . This result is rather important, because it shows that there must be sufficient source of free charges during the poling, so that they can be trapped in transition zones in order to compensate the depolarizing field in crystallites. The charges can be either injected, as in case of corona poling, or emitted thermally inside the sample. For example, the required charge can be injected in 15 min, if the poling is performed at room temperature by a constant current of $160 \mu\text{A/m}^2$.

It is known that PVDF poled at elevated temperatures has higher value of residual polarization than that poled at room temperature. The thermal activation, most probably, not only improves alignment of dipoles, as in case of conventional polar electrets, but also provides the high density of free charge carriers necessary for further compensation of the depolarizing field. The electret component of polarization in PVDF is thermodynamically unstable and decays with time, negatively affecting stability of piezoelectric and pyroelectric coefficients. It is clear from fig. 4 that charged layers with density $+\sigma_r$ and $-\sigma_r$ remained uncompensated above and

below the point B positioned in amorphous phase. It means that the field created by those layers supports the electret polarization in amorphous phase. Moreover, this field tries to separate positive and negative charges, pressing them to boundaries of crystallites, but this did not affect the field inside crystallites that remained zero, as it has been already shown. Free movement of the separated charges is somewhat constrained and this can be one of the reason why the apparent conductivity decreases during the poling.

4. Conclusion

We have provided some additional experimental evidence on close correlation existing between polarization and space charge in PVDF and shown that the depolarizing field was compensated by charges trapped in macroscopic transition zones by which polarized parts of the volume were separated from non-polarized ones. The compensating charges are first injected in the bulk or created internally by a thermal emission and then trapped when the ferroelectric polarization is being formed. The clarification was necessary, because it was still commonly believed that charges were trapped at the boundaries of crystallites. Moreover, it is often assumed that the poling field itself is created by the trapped charges [6]. It follows from our results, however, that the charge trapping in PVDF and probably in other ferroelectric polymers is not the cause, but rather the result of the polarization buildup.

Acknowledgment. The support of INTAS is gratefully acknowledged.

References

1. Furukawa T. Phase Transitions. — 1989. — 18. — 143.
2. Kepler R. G., Anderson R. A. Advances in Physics. — 1992. — 41. — 1.
3. Womes M., Bihler E., Eisenmenger W. IEEE Trans. El. Insul. — 1989. — 24. — 461.
4. Fedosov S. N. Phys. stat. sol. (a). — 1989. — 115. — 293.
5. DeReggi A. S., Broadhurst M. G. Ferroelectrics. — 1987. — 73. — 351.
6. Sessler G. M., Das-Gupta D. K., DeReggi A. S., Eisenmenger W., Furukawa T., Giacometti J. A., Gerhard-Multhaupt R. IEEE Trans. El. Insul. — 1992. — 27. — 872.
7. Bihler E., Neuman G., Eberle G., Eisenmenger W. Annu. Rep. Conf. Electr. Insul. Diel. Phenom. — 1990. — P. 140.
8. Fedosov S. N., Mol. Cryst. Liquid Cryst. — 1993. — 230. — 61.
9. Fedosov S. N., Sergeeva A. E., Korolchak O. P. J. Mater. Sci. Let. — 1989. — 8. — 931.
10. Arkhipov V. I., Fedosov S. N., Khranchenkov D. V., Rudenko A. I. J. Electrostat. — 1989. — 22. — 177.
11. Fedosov S. N., Sergeeva A. E. J. Electrostat. — 1993. — 30. — 327.
12. Fedosov S. N., Sergeeva A. E. J. Electrostat. — 1993. — 30. — 39.
13. Sergeeva A., Fedosov S., Pribbe S. Proc. 8th Int. Symp. Electrets. — Paris, 1994. — P. 43.
14. Furukawa S., Nakajama K., Koizumi T., Date M. Jap. J. Appl. Phys. — 1987. — 26. — 1039.
15. Electrets / Ed. Sessler G. M. — Berlin—Heidelberg: Springer-Verlag, 1987. — Chapter 2. — P. 23.
16. Lewis E. L. V., Ward I. M. J. Polym. Sci., Polym. Phys. Ed. — 1989. — 27. — 1375.

PREPARATION OF THE $\text{Li}_x\text{Ni}_{1-x}\text{O}$ -SOLUTION FOR GAS SENSORS

The properties of metal-oxides, which are used as sensitive elements for gases are discussed. The systems of metals with variable valence have been got on the base of the given metals acetates and acetates of metal of 1A group are shown.

Now the complex materials of different metal-oxides are used as the primary sensitive elements to gases (CO , CH_4 , C_2H_2 , NO_x , NH_3). These materials used more often than pure ones because of their high sensitive qualities. The most effective materials are the solid solution of oxides of variable valence metals which have the general formula $\text{Me}_x^I\text{Me}_{1-x}^{II}\text{O}$, where Me_x^I — is the first group metal of the periodic system and the $\text{Me}_{1-x}^{II}\text{O}$ — is variable valence metal. These systems have stable electrophysical characteristics owing the oxygen balance establishment between volume, surface and gas phase at high temperatures. At the same time these systems are very sensitive to adsorption of small gas portions. This quality is their main trait.

We have got the systems on the base of metals with variable valence. The systems have been got on the base of given metals acetates and the acetates of metals of 1A group by decomposition in air during 5 hours by temperature 6000 °C. So we have got the oxides mixtures with the content of 1A group metals — 10, 20, 30, 40 and 50 per cent. These mixtures were the initial material for the obtained systems, by the treatment by different temperatures — 700, 800, 900, 1000 and 1200 °C.

We determined the number of «holes», corresponding to the quantity of inclusion metal of 1A group. The change of crystal lattice constant, electrical conductivity depends on the conditions to form of such systems. Fig. 1 shows the dependence of

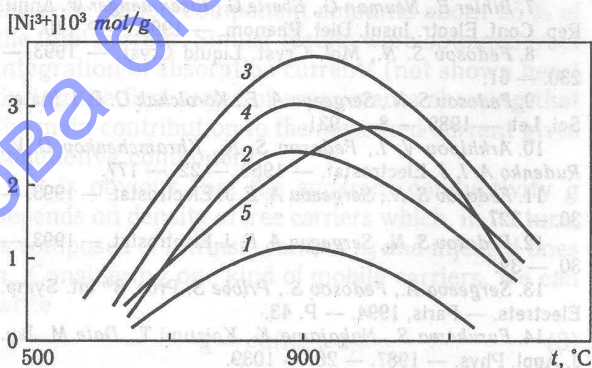


Fig. 1. Solid-solution concentration — temperature dependence. The content of 1A group metals: 1 — 10, 2 — 20, 3 — 30, 4 — 40, 5 — 50%

solid solution concentration on temperature of its formation. Fig. 2 shows the dependence of «hole»

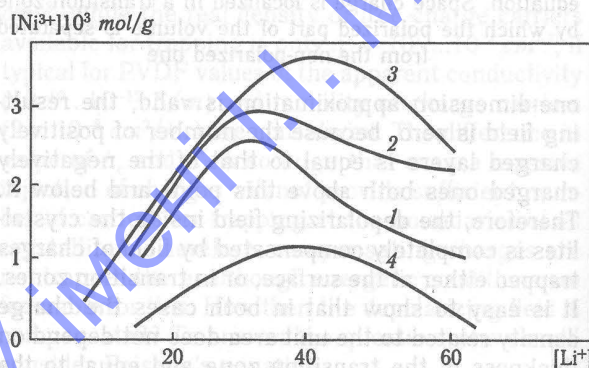


Fig. 2. «Hole» concentration — lithium concentration dependence. The temperature formation:

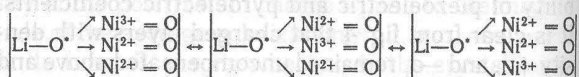
1 — 700, 2 — 800, 3 — 1000, 4 — 1200 °C

concentration on the initial concentration of 1A group metal (lithium).

The quantitative determination of «holes» by chemical method in solid solution consists of determination of trivalent nickel in the system. When solid solution $\text{Li}_x\text{Ni}_{1-x}\text{O}$ is dissolving in the hydrochloric acid owing to oxidizing-reduction process between trivalent nickel and ion of chlorine, the uncombined chlorine is educing. The chlorine is determined by the iodometrical method. The quantity of lithium is increasing when the initial concentration is increasing.

This formula is right for all temperatures to form of solid solution. Fig. 2 shows that the curves go through the maximum (the initial concentration of lithium — at 30%) and then fall down. We have got the region where inclusion more lithium even by the way of another treatment of solid solution was impossible. The inclusion of lithium is desirable because sensor sensitivity depends on the quantity of «holes» in the system.

We can show the inner group of solid solution in mobile conduction as:



So, sensor sensitivity is the cause of the mobility. The possibility of getting the solution by the cheap well-known methods permits the possibility of gas primary making with the help of industry. The developing ideas about «hole complex» allow us to select sensors without using the method of «tests and mistakes». The goal of this work is to research the dependence of system sensitivity $Me-MeO$ ($Me-Li, K, Na, Cs; MeO-NiO$) on CO adsorption from atmosphere, draining air and nitrogen.

The films of $Me_x^{II} Me_{1-x}^{II}O$ which is on quartz plate with platinum contacts were used as sensitive substrate. The research of these pellicles shows that there is no any charges in the process of marking of solid solutions. The crystals sizes ($3...10 \mu m$) are rather the same. We carried out the experiment in gas flow containing CO (2 volume percent, $T = 573 K$). There is no any sharp increasing of electrical conductivity. This preparation brings to nearly full reversibility. We researched the kinetic curve of electrical conductivity $\Delta\sigma/\sigma_0 = f(t)$ and the de-

pending of response upon the structure of solid solution and temperature of its preparation (fig. 3).

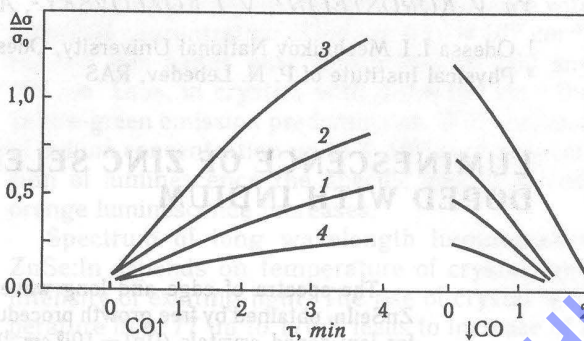


Fig. 3. Kinetic of electroconductivity. The temperature of preparation:

1 — 700, 2 — 800, 3 — 1000, 4 — 1200

The received facts are explained in terms of «hole complex».

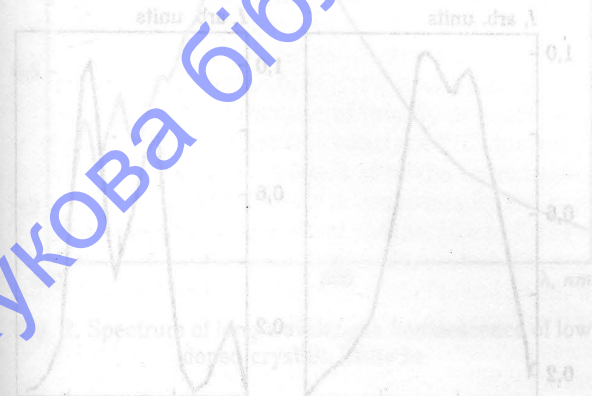


Fig. 1. Spectra of excitation (a) and absorption (b).

Yu. F. VAKSMAN¹, Yu. A. NITSUK¹, Yu. N. PURTOV¹, S. A. IGNATENKO¹,
Yu. V. KOROSTELIN², V. I. KOZLOVSKY², A. S. NASIBOV², P. V. SHAPKIN²

¹ Odessa I. I. Mechnikov National University, Odessa, Ukraine

² Physical Institute of P. N. Lebedev, RAS

LUMINESCENCE OF ZINC SELENIDE SINGLE CRYSTALS DOPED WITH INDIUM

The spectra of edge and long wavelength photoluminescence for single crystals ZnSe:In, obtained by free growth procedure are investigated. Spectrum of edge emission for low doped crystals ($[In] = 10^{16} \text{ cm}^{-3}$) is characterised by lines of emission of free excitons and donor-acceptor pairs (DAP). At concentrations of indium higher 10^{17} cm^{-3} , the emission of excitons, bounded on neutral zinc vacancies, appears. Spectrum of a long wavelength luminescence evidences the presence in the crystals, charged vacancies of zinc ($V_{Zn}^{\cdot-}$, V_{Zn}^{2-}) included in composition of DAP.

Introduction

The zinc selenide of is a wide energy gap ($E_g = 2.68 \text{ eV}$) semiconductor of A^2B^6 group. Due to straight zone structure it has high efficiency of an emission recombination. Now the production of blue light-emitting diodes on the basis of single ZnSe crystals is prospective [1, 2]. However, instability of the emitting characteristics of such diodes is not sufficient for their production. In this connection, the production and investigation of the crystals with perfect structure, low dislocation density and high conductivity is the very important problem. During last years the technique of free growth was designed [3], it consists in growing of crystals of A^2B^6 group from a vapour phase in conditions excluded their contact to growth camera. The obtained crystals had the perfect structure and low (less 10^4 cm^{-2}) dislocation density. In subsequent, the doping of ZnSe crystals with indium during their growth by means of this technique was realised [4]. The high-conductivity crystals ($\sigma = 1 \dots 5 \text{ Ohm}^{-1} \cdot \text{cm}^{-1}$) were obtained as the result of subsequent annealing ZnSe:In in zinc melt [4, 5].

In this paper the luminescence of ZnSe:In single crystals, obtained by method of free growth reserved. The purpose of such investigations is to clear up the mechanisms of emitting recombination and nature of luminescence centres in crystals ZnSe, doped with indium.

Experimental technique

The investigated zinc selenide crystals were obtained by method of free growth in two crystallographic direction (111) and (100). The growth ampoule was installed in the furnace with vertical temperature gradient. The seed, container with initial (ZnSe) and alloying (In_2Se_3) materials was placed in ampoule. Temperature of vapour source was 1430...1470 K. Temperature difference between

source and substrate — 10...70 K. The total pressure of gas mixture was to stationary values in all processes and made about 100 μPa . More detailed description for the technique to obtain the crystals is contained in works [3, 4]. The concentration of indium in crystals was determined through the atomic-emission analysis and varied from 10^{16} up to 10^{18} cm^{-3} .

The spectra of photoluminescence were measured by spectrophotometer ISP-51 within temperature range 77...400 K. As an excitation source, the helium-cadmium laser LGN-403k, emitting on a wavelength 441,6 nm, was used. The spectra of long wavelength luminescence were represented with allowance for spectral sensitivity of the measuring equipment.

Edge luminescence ZnSe:In

The investigations of edge luminescence spectra were carried out at 77 K. In more short-wave (excitonic) range of spectrum, two lines of emission on 2,808 and 2,797 eV (fig. 1, a) are detected. These

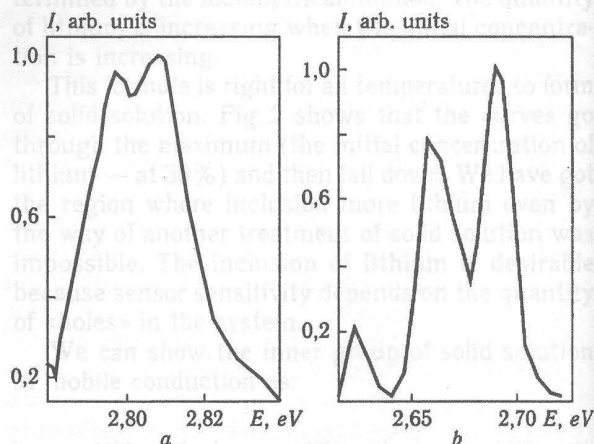


Fig. 1. Spectra of exciton (a) and edge luminescence (b)

lines are characteristic for low doped crystals ($[In] = 2 \cdot 10^{16} \text{ cm}^{-3}$). In accordance with [6], these lines are stipulated by emission transitions of free excitons from states with $n = 2$ and 1, respectively. In spectrum of excitonic luminescence for highly doped crystals ($[In] > 10^{17} \text{ cm}^{-3}$) the line of width 1,6 meV with a maximum on 2,771 eV, stipulated by recombination of bound exciton is detected. In this case energy of emitted photons is described by the equation

$$h\nu = E_g - E_{ex} - E_b, \quad (1)$$

where E_{ex} — bond energy of free exciton, equal to 16 meV [7], E_b — bond energy of localised exciton. In accordance with [7], relationship between activation energy of acceptors (donors) and bond energy of exciton — impurity complex looks like: $E_a \approx 10E_b$; $E_d \approx 5E_b$. The calculation of the equation (1) shows that radiation on 2,771 eV is stipulated by excitons localised on acceptors with an activation energy 190...200 meV. Such acceptors in zinc selenide are the neutral vacancies of zinc V_{Zn}^x [7].

In all investigated crystals, the emission lines on 2,689, 2,657 and 2,623 eV were observed (fig. 1, b). The line with a maximum on 2,689 eV is stipulated by emission transitions within DAP. Apparently, in DAP composition the indium donors In_{Zn}^+ enter. As acceptors the ions of uncontrolled impurities of lithium or sodium can be there. The emission lines on 2,657 and 2,623 eV are LO — phonon repetitions of a line on 2,689 eV.

Features of spectrums of a long wavelength luminescence

The spectra of long wavelength luminescence represent broad bands placed in the range 480...700 nm. In spectrums for luminescence of ZnSe with low concentration of indium ($[In] = 2 \cdot 10^{16} \text{ cm}^{-3}$) there is a broad band with maximum on 490 nm (fig. 2). It is

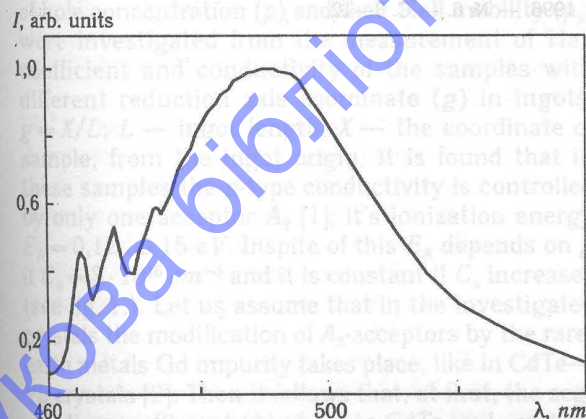


Fig. 2. Spectrum of long wavelength luminescence of low doped crystals ZnSe:In

earlier determined [8], that the isolated centres of oxygen (O_{Se}) stipulate this band of luminescence. Energy of thermal activation for luminescence centres

is equal to 0,13 eV. It also is in agreement with data [8]. In crystals with $[In] > 10^{17} \text{ cm}^{-3}$ the luminescence of oxygen was not observed.

Spectrums of long wavelength luminescence with moderate concentration of indium ($[In] \approx 10^{17} \text{ cm}^{-3}$) contain two bands with maximums on 560 and 625 nm. Thus, in crystals with $[In] = 10^{17} \text{ cm}^{-3}$ the yellow-green emission predominates. With increase of indium concentration up to $3 \cdot 10^{18} \text{ cm}^{-3}$ in spectrum of luminescence the specific weight of red-orange luminescence increases.

Spectrum of long wavelength luminescence ZnSe:In depends on temperature of crystals and intensity of exciting light. The rise of crystal temperature from 77 up to 170 K leads to increase of a specific weight of red-orange radiation (fig. 3). Such

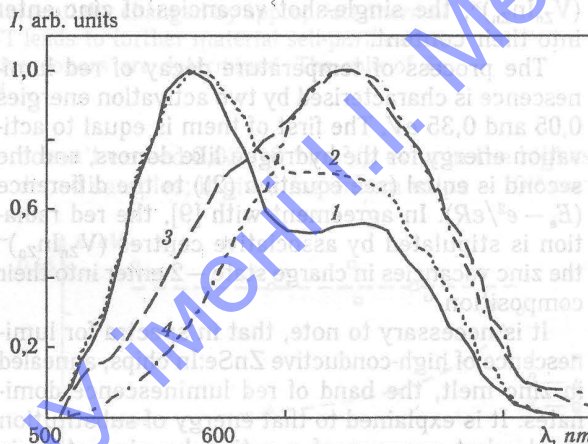


Fig. 3. Spectra of long wave length luminescence ZnSe:In, measured at:

1 — 77, 2 — 108, 3 — 133, 4 — 173 K

characteristic influence of temperature on a spectral distribution of emission evidences about the mechanism of current transfer between luminescence centres, which is characteristic for recombination luminescence.

With decrease of exciting light intensity from 100 up to 20%, a band with a maximum on 625 nm becomes dominating in luminescence spectrum. At the same time the broadening of bands in long wavelength range is observed, that testifies that the indicated photoluminescence spectra, is similar to ZnSe:Al spectrums, described in [9], are not elementary.

To define the nature and the energy position of luminescence centre levels, responsible for yellow-green and red-orange emission, the temperature dependencies of emission intensities were investigated in the range of 560 and 625 nm. Activation energy of the temperature decay process was determined with inclination of linear site of dependence $I(T)$, figured in coordinates $\ln I$ from $1/T$. The temperature luminescence decay in range 560 nm represents a curve with two linear sites. In the range of low temperatures, the weak decay of luminescence with activation energy 0,05 eV was observed. In the range

from 200 up to 250 K the intensity of green emission varies insignificantly. Activation energy, determined in high-temperature range, was 0,11 meV. The temperature dependencies of luminescent emission with two linear decay sites are explained within the framework of model for emission recombination which is carried out on donor-acceptor pairs. In this case energy of emitted quantum is determined by the equation

$$h\nu = E_g - E_d - E_a + \frac{e^2}{\epsilon R}, \quad (2)$$

where E_d , E_a — activation energy of donor and acceptor; R — distance between the donor and acceptor. In accordance with [10], the green emission of ZnSe:In is stipulated by neutral associative centres $(V_{Zn}In_{Zn})^*$, the single-shot vacancies of zinc enter into their content.

The process of temperature decay of red luminescence is characterised by two activation energies 0,05 and 0,35 eV. The first of them is equal to activation energy for the hydrogen-like donors, and the second is equal (see equation (2)) to the difference $(E_a - e^2/\epsilon R)$. In agreement with [9], the red radiation is stipulated by associative centres $(V_{Zn}In_{Zn})^-$ the zinc vacancies in charge state — 2 enter into their composition.

It is necessary to note, that in spectra for luminescence of high-conductive ZnSe:In chips, annealed in zinc melt, the band of red luminescence dominates. It is explained to that energy of substitution single-shot vacancy of a cation by zinc atom is smaller in comparison with the appropriate value for two-charge vacancy.

Outputs

1. Spectrum of edge luminescence of low doped single ZnSe crystals ($[In] \approx 2 \cdot 10^{16} \text{ cm}^{-3}$) are characterised by lines of free exciton emission with $n = 2, 1$ (2,808, 2,797 eV) and line of DAP emission on

2,689 eV with its phonon repetitions (2,657 and 2,623 eV).

2. In low doped ZnSe single crystals ($[In] \approx 2 \cdot 10^{16} \text{ cm}^{-3}$) the long wavelength luminescence is observed in the range of 490 nm. This band of luminescence indicates presence of uncontrolled impurities of oxygen in crystals.

3. Spectrum of edge luminescence for of ZnSe crystals with indium concentration higher than 10^{17} cm^{-3} is characterised by line for emission of excitons, bounded on neutral zinc vacancies and line of DAP emission on 2,689 eV with its phonon repetitions (2,657 and 2,623 eV).

4. Spectrum of long wavelength luminescence ZnSe:In evidences the presence of DAP, containing acceptors V_{Zn}^- , V_{Zn}^{2-} and donors In_{Zn}^+ in crystals.

5. Annealing of ZnSe:In crystal in zinc leads to decreasing of Zn vacancy concentration, responsible for long wavelength luminescence. This is the reason for increase of a specific conductivity of crystals.

References

1. Krasnov A. N., Purtov Yu. N., Vaksman Yu. F., Serdyuk V. V. // J. Cryst. Growth. — 1992. — V. 125, № 1/2. — P. 373—374.
2. Ваксман Ю. Ф., Краснов А. Н., Пуртов Ю. Н. // Физ. и техн. полупроводников. — 1995. — Т. 29, № 7. — С. 1186—1189.
3. Korostelin Yu. V., Kozlovsky V. I., Nasibov A. S., Shapkin P. V. // J. Cryst Growth. — 1996. — V. 159. — P. 181—185.
4. Korostelin Yu. V., Kozlovsky V. I., Nasibov A. S., Shapkin P. V. // J. Cryst Growth. — 1999. — V. 197. — P. 449—454.
5. Ваксман Ю. Ф., Игнатенко С. А., Пуртов Ю. Н., Шанкин П. В. // Фотоэлектроника. — 1999. — № 8. — С. 77—79.
6. Гавриленко В. И., Грегов А. М., Корбутяк Д. В., Литовченко В. Г. Оптические свойства полупроводников. — К.: Наук. думка, 1987. — 608 с.
7. Недеогло Д. Д., Симашкевич А. В. Электрические и люминесцентные свойства селенида цинка. — Кишинев: Штиинца, 1980. — 150 с.
8. Ваксман Ю. Ф. // Физ. и техн. полупроводников. — 1995. — Т. 29, № 2. — С. 346—348.
9. Serdyuk V. V., Korneva N. N., Vaksman Yu. F. // Phys. Stat. Sol. (a). — 1985. — V. 91. — P. 173—183.
10. Ваксман Ю. Ф., Краснов А. Н. // Фотоэлектроника. — 1996. — № 6. — С. 8—12.

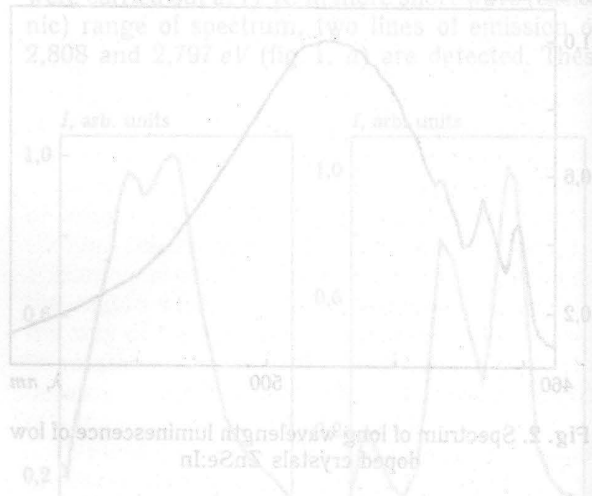


Fig. 2. Spectrum of long wavelength luminescence of low doped ZnSe.

Earlier determined [8] that the isolated centres of oxygen (O_2) stipulate this kind of luminescence. Energy of thermal activation for luminescence centres

E. S. NIKONYUK¹, V. L. SHLYAKHOVYI¹, M. I. KUCHMA¹,
M. O. KOVALETS¹, Y. D. ZAKHARUK²

¹ Rivne State Technical University, Rivne, Ukraine

² Chernivtsi State University, Chernivtsi, Ukraine

THE EFFECT OF SELF-PURIFICATION IN p -CdTe—Gd CRYSTALS

The doping of CdTe by Gd impurity in the synthesis process was made. The effect of matrix purification from shallow acceptors A_1 is found; it is connected with transition of A_1 into electrically nonactive state. The role of Gd impurity to intensify of this process is discussed. The influence of the long thermal treatment (LTT) on electrophysical properties of p -CdTe—Gd crystals is studied. It is shown, that electrophysical properties of p -CdTe—Gd crystals may be essentially changed by appropriate thermal treatment. The conditions, at which the LTT leads to further material self-purification from shallow acceptors A_1 and compensative donors are determined. The role of Te precipitates in these processes is discussed.

The doping of semiconductor crystals, in particular, A^3B^5 and A^4B^6 by rare-earth metals is accompanied by their purification from non-controlled impurities (effect of self-purification). In the doping of CdTe crystals, this effect practically is not studied. The content of this paper is the result of CdTe-crystals electrophysical investigation; these crystals were doped by Gd impurity according to Cd—Te—Gd scheme without the excess of Te. The doping was made during the synthesis process, for the reason that at high temperature Gd reacts with the quartz even if it is protected by pyrolytical graphite layer. The concentration of dopand in the melt (C_0) varied from $3 \cdot 10^{17}$ to $3 \cdot 10^{19} \text{ cm}^{-3}$. The doped crystals grown by Bridgman method, has the n -type of conductivity, if $C_0 < 3 \cdot 10^{18} \text{ cm}^{-3}$ and the p -type of conductivity, if $C_0 \geq 3 \cdot 10^{18} \text{ cm}^{-3}$. The crystals of p -CdTe—Gd will be examined

The temperature dependences ($t = 80 \dots 400 \text{ K}$) of hole concentration (p) and their Hall mobility (μ_p) were investigated from the measurement of Hall coefficient and conductivity of the samples with different reduction axis coordinate (g) in ingots: $g = X/L$; L — ingot length, X — the coordinate of sample, from the ingot origin. It is found that in these samples the p -type conductivity is controlled by only one acceptor A_2 [1]; its ionization energy $E_A = 0,12 \dots 0,15 \text{ eV}$. In spite of this E_A depends on g if $C_0 = 3 \cdot 10^{18} \text{ cm}^{-3}$ and it is constant if C_0 increases (see fig. 1.). Let us assume that in the investigated crystals the modification of A_2 -acceptors by the rare-earth metals Gd impurity takes place, like in CdTe—Yb crystals [2]. Then it follows that, at first, the segregation coefficient (k) of Gd in CdTe $\ll 1$, and, at secondly, the Gd solubility is so small that the product $K \cdot C_0$ is limited by maximum solubility even if $C_0 = 10^{19} \text{ cm}^{-3}$. The result of magnetic investigation points to small content of Gd impurity in the most part of the crystal ($g = 0 \dots 0,95$). The paramagnetic component of magnetic susceptibility at 100 K

doesn't exceed $0,03 \cdot 10^{-6} \text{ cm}^3/\text{g}$ even in the highest doped samples; it gives maximum value $\sim 10^{18} \text{ cm}^{-3}$

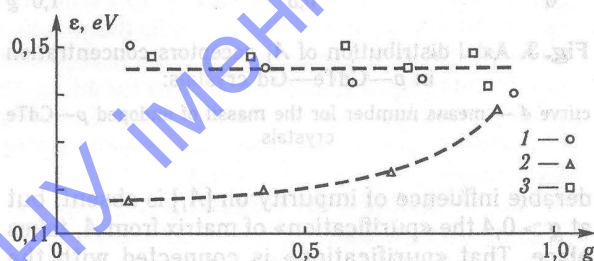


Fig. 1. Axial distribution of A_2 acceptors ionization energy in p -CdTe—Gd crystals with different C_0 value:

1 — $3 \cdot 10^{18}$, 2 — 10^{19} , 3 — $3 \cdot 10^{19} \text{ cm}^{-3}$

for concentration of Gd impurity. Consequently, nearly all dopand drives back to the end of ingots ($g > 0,95$); there, really strong paramagnetism takes place.

Distribution of A_2 acceptors concentration as well as more shallow completely compensated acceptors A_1 , obtained from analysis of p and mp temperature dependences, is presented in fig. 2, 3. It is seen, that

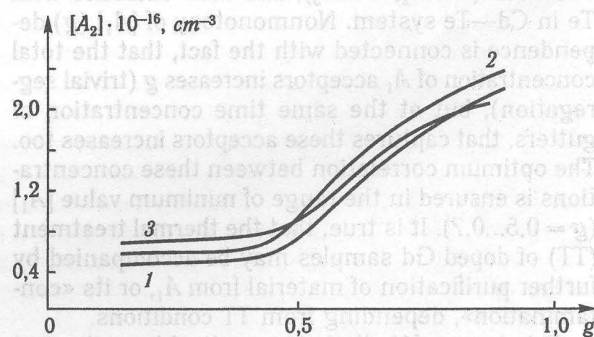


Fig. 2. Axial distribution of A_2 acceptors concentration in p -CdTe—Gd crystals with different C_0 value:

1 — $3 \cdot 10^{18}$, 2 — 10^{19} , 3 — $3 \cdot 10^{19} \text{ cm}^{-3}$

if $g < 0,4$ content of A_2 acceptors ($[A_2] = 5 \dots 7 \cdot 10^{15} \text{ cm}^{-3}$) is similar to the same value in undoped crystals, that was grown from zone purified initial components, but at $g > 0,4$ its increase is anomalously rapid and it shows tendency to saturation at $g > 0,8$. The dependence of $[A_2]$ on C_0 at $g < 0,4$ and its nonmonotony for $g > 0,5$ (if the doping with the different purity is made) indicates that the donor component of A_2 complex is conditioned by uncontrolled impurities at initial components as well as at Gd.

Let us come to the analysis of $[A_1]$ (g) curves (see fig. 3.). It is seen, that at small g , the consi-

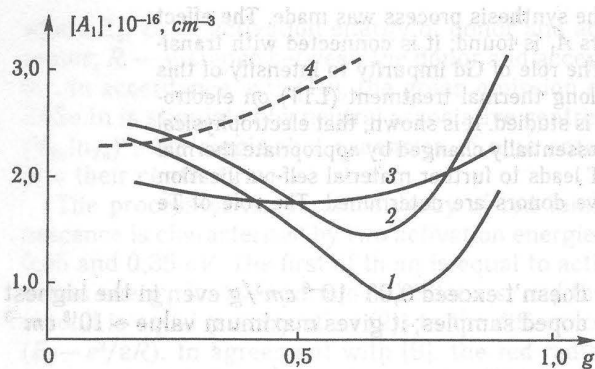


Fig. 3. Axial distribution of A_1 acceptors concentration in p -CdTe—Gd crystals:

curve 4 — means number for the massif of undoped p -CdTe crystals

derable influence of impurity on $[A_1]$ is absent, but at $g > 0,4$ the «purification» of matrix from A_1 takes place. That «purification» is connected with the introduction of Gd impurity. This effect is not connected directly with the driving back A_1 impurity to the end of ingot, owing to the segregation of crystallization front, but it is connected with transition of A_1 into electrically inactive state: precipitation or capture by other precipitates, particularly, by Te ones [3]. In that case, the role of Gd impurity consists in intensification of process, that leads to the creation of the gutters for A_1 acceptors on a mass scale of Te-contained precipitates and inclusions. The possibility of such intensification is bound up with existence of the number of chemical combinations (GdTe_2 , GdTe_3), and their eutectics with Te in Cd—Te system. Nonmonotony of $[A_1]$ (g) dependence is connected with the fact, that the total concentration of A_1 acceptors increases g (trivial segregation), but at the same time concentration of gutters, that captures these acceptors increases too. The optimum correlation between these concentrations is ensured in the range of minimum value $[A_1]$ ($g = 0,5 \dots 0,7$). It is true, that the thermal treatment (TT) of doped Gd samples may be accompanied by further purification of material from A_1 , or its «contamination», depending from TT conditions.

It is known [1], that the result of long thermal treatment (LTT) for p -CdTe crystals in temperature range 420...480°C during the tens of hours considerably decreases the concentration of shallow ac-

ceptors A_1 , i. e. the material self-purification takes place. Influence of LTT on CdTe—Gd crystal parameters is presented in table.

Table 1

C_0 , cm^{-3}	g	LTT conditions		Parameters after LTT			
		t , °C	τ , h	E , eV	$\frac{\mu_{80}}{\mu_{300}}$	$[A_2] \times 10^{-15} \text{ cm}^{-3}$	$[A_1] \times 10^{-16} \text{ cm}^{-3}$
$3 \cdot 10^{18}$	0,33	450	48	0,114	8,4	7,3	3,6
$3 \cdot 10^{18}$	0,47	420	100	0,135	14,5	7,7	0,3
$3 \cdot 10^{18}$	0,47	440	72	0,120	11,0	7,3	1,6
$3 \cdot 10^{18}$	0,47	480	24	0,040	7,3	—	19,0
$3 \cdot 10^{18}$	0,68	400	100	0,139	13,4	12,0	0,7
$3 \cdot 10^{18}$	0,68	420	90	0,137	13,0	11,0	1,0
$3 \cdot 10^{18}$	0,68	480	24	0,043	5,7	—	33,0
$1 \cdot 10^{19}$	0,38	400	90	0,150	10,5	7,0	1,3
$1 \cdot 10^{19}$	0,86	400	90	0,144	10,0	21,0	1,6
$3 \cdot 10^{19}$	0,72	400	120	0,152	11,1	15,0	1,6

The first obvious conclusion from presented data is the following: the upper boundary of «self-purification» temperature range is reduced considerably in comparison with that for undoped crystals. In particular, LTT at 480°C is accompanied by total decompensation of A_2 acceptors because of sharp increasing in A_1 acceptors concentration; this acceptors begin to control p -conductivity at low temperatures. It is found, that «contamination» of samples by A_1 acceptors increases with increasing g and Gd impurity concentration in melt. After LTT at 450°C sample «contamination» by acceptors A_1 is less appreciable, and A_2 acceptors continue to control p -conductivity. And so we may affirm that upper temperature boundary of effective «self-purification» area for doped Gd samples doesn't exceed 440°C.

The lowest value of A_1 acceptors concentration was obtained after LTT at 400...420°C on the samples with minimal content of Gd impurity. It is possible, that temperature range of effective «self-purification» is removed a bit lower in the crystals with larger content of Gd impurity, but it demands longer duration of LTT.

It is noted, that «self-purification» effect at LTT is always accompanied by increasing of acceptor A_1 ionization energy; with regard to obvious ratio $E_{A_2} = E_{A_0} - \alpha[D^+]^{1/3}$ [1], the latter testifies simultaneous «purification» from compensative donors. We cannot do simple conclusions about «self-purification» from A_2 acceptors, because of relatively small changes of $[A_2]$ at LTT.

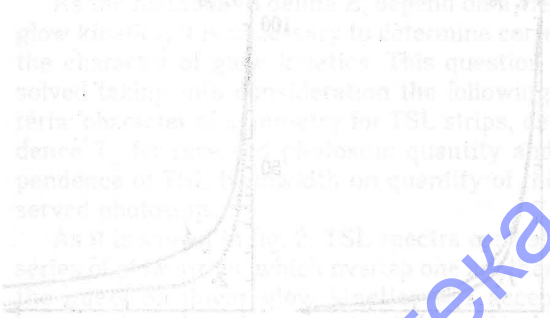
Thus, LTT ($\tau \approx 10^2 \text{ h}$) of Gd-doped p -CdTe crystals ($C_0 = 3 \cdot 10^{18} \dots 3 \cdot 10^{19} \text{ cm}^{-3}$) in temperature range $t = 330 \dots 440^\circ\text{C}$ is accompanied by material «self-purification» from shallow acceptors A_1 and compensative donors. Precipitates which main component is Te, take the part of gutters for this defects. Temperature lowering in the area of effective «self-purification» is caused by concentration of Gd gutters, that creates the combination with tellurium. In par-

ticular, temperature of $\text{GdTe}_3 + \text{Te}$ eutectic, that is equal to 400°C , hits just in «self-purification» area. It is known [4] that segregation coefficient of practically all impurities in $\text{CdTe(s)}-\text{Te(l)}$ system is less than one; this fact ensures possibility of impurities' concentration by liquid phase. This possibility has practically been realized already in cooling process for the grown crystal. But in practice cooling velocities, used ($50\ldots 100\text{ K/h}$), leave the significant part of impurities in CdTe matrix. Estimation in the radii of «purificative action» of precipitates was made from low-angle boundary density, ($\sim 10\ldots 100\text{ cm}^{-1}$ in CdTe); with regard to time of LTT ($\tau \approx 100\text{ h}$) we have obtained value $\sim 10^{-9}\text{ cm}^2/\text{c}$ for diffusion coefficient of impurities. For many impurities, espe-

cially if they have a rapid component of diffusion flow (Cu , Li , for example) diffusion coefficients at $t = 400\ldots 450^\circ\text{C}$ exceed the estimative value. Hence, the segregation of matrix from impurities at LTT can be realized in practice.

References

1. Nikonyuk E. S., Shlyakhooyi V. L., Zakharuk Z. I. et al. // *Neorgan. Mater.* — 1995. — 31, № 2. — P. 185—187.
2. Nikonyuk E. S., Shlyakhooyi V. L., Kovalets M. O. et al. // *Journal Of Crystal Growth.* — 1996. — 161, № 1—4. — P. 186—189.
3. Pautrat J. L. et al. // *J. Appl. Phys.* — 1982. — 82, № 12. — P. 8668—8677.
4. Zanio K. // *Semiconductors and semimetals.* — New York: Academic Press, 1978. — Vol. 13, Cadmium Telluride. — P. 138.



Among semiconductors of A²B⁶ group zinc sulphide is of special interest. Zinc sulphide is wide band and direct band compound with width of energy gap 3.6 eV (when T = 300 K) — 3.5 eV (at room temperature). In energy gap of ZnS there is a set of energy levels with various distances between them. These levels are formed by the presence of defects. Usually, the undoped ZnS contains defects practically independent on production process, have conductance of n-type. One of methods to produce desired properties of ZnS is to synthesize it by self-spreading high-temperature synthesis (SHS) [1]. With its help it is possible to gain both stoichiometric and doped polycrystals. The investigation of spectra for thermally stimulated luminescence (TSL) is one of methods to define the energy position trapping levels. We have investigated ZnS(Cr) polycrystals. The measurements of TSL spectra were carried out as follows: at the temperature of fluid nitrogen the sample was lighted during 20—30 minutes by laser and at the same time the defined photoluminescence was conducted. Photoluminescence was conducted in the lack of external magnetic field (in dark). After the sample was essentially filled with electrons, the light source was switched off. Then the heating of sample was produced with constant velocity and the dependence of TSL curves on various heat rates ($\beta = 5, 10, 20, 30, 50, 100$ degrees/minutes) were obtained. The given curves are stipulated by superposition of two processes: by the kinetics of photoluminescence signal damping and thermally stimulated luminescence. Judging by the form of curves, it is possible to tell that change of intensity and displacement of glow band maximum depend on the chosen heat rate in samples. The intensity of luminescence for ZnS(Cr) polycrystals with heat velocity of 20 degrees

THERMALLY STIMULATED LUMINESCENCE OF POLYCRYSTALS ZnS

Thermally stimulated luminescence and kinetics of signal attenuation of glow of zinc sulphide polycrystals received by method of high-temperature synthesis are investigated. The persistence of samples in green region of spectrum ($\lambda_{\max} = 520 \text{ nm}$) with anomalously major duration of glow is revealed. In TSL spectrum a series of strips are revealed. It is observed, that the spectrum TSL can be surveyed in approach of repeated capturing absence. The activation energies relevant to chlorine levels are calculated. It is shown, that for the indicated features for glow kinetics and TSL spectrum the impurity of chlorine is responsible.

Among semiconductors of A^2B^6 group zinc sulphide is of special interest. Zinc sulphide is wide band and direct band compound with width of energy gap 3.6 eV (when $T = 77 \text{ K}$) — 3.7 eV (at room temperature). In energy gap of ZnS, there is a set of energy levels with various occurrence depths stipulated both by availability of impurities and native defects. Usually, the undoped crystals of zinc sulphide practically independent on production procedure, have conductance of n -type.

One of methods to produce deriving polycrystalline materials distinguished by simple technology and low energy costs, is self-spreading high-temperature synthesis (SHS) [1]. With its help it is possible to gain both stoichiometric, and doped polycrystals. The investigation of spectra for thermally stimulated luminescence (TSL) is one of methods to define the energy position trapping levels.

We have investigated ZnS(Cl) polycrystals. The measurements of TSL spectra were carried out as follows: at the temperature of fluid nitrogen the sample was lighted during 20–30 min by laser and at the same time the defined photosum was stocked on traps. Photoexcitation was conducted in the lack of exterior padding illumination (in darkness). After the traps were essentially filled with electrons, the light source was switched off. Then the heating of sample was produced with constant velocity.

TSL curves of ZnS(Cl) polycrystals under three various heat rates ($\beta_0 = 20 \text{ degree/min}$, $\beta_0 = 10 \text{ degree/min}$, $\beta_0 = 5 \text{ degree/min}$) were obtained. The given curves are stipulated by superposition of two processes: by the kinetics of photoluminescence signal damping and thermally stimulated luminescence. Judging by the form of curves, it is possible to tell, that change of intensity and displacement of glow band maximums depend on the chosen heat rate in samples. The intensity of luminescence for ZnS(Cl) polycrystals with heat velocity of 20 degrees

per one minute (0.3 degree/sec) is more, than with other velocities of heat.

To separate the kinetics process from that of TSL, we measured photoluminescence kinetics under temperature and temperature of fluid nitrogen within 1 hour after the moment when stimulating light was lockout (fig. 1). It was noticed, that the shape of

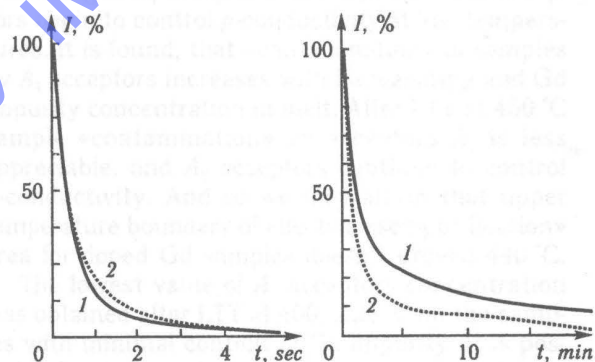


Fig. 1. Kinetics for signal attenuation of ZnS(Cl) photoluminescence for various time intervals (a, b):

1 — under ambient temperature; 2 — at the temperature of fluid nitrogen

curves of a relaxation did not vary during of excitation of sample with various waves lengths.

Under measurement of relaxation curves in the course of different temperatures ($T_1 = 80 \text{ K}$, $T_2 = 173 \text{ K}$ and $T_3 = 290 \text{ K}$) it was observed, that the dependence on temperature has not practically come to light. Therefore, the curves of photoluminescence signal attenuation were measured only at temperature $T = 290 \text{ K}$, but for various time intervals relevant to duration of measurement of TSL curves with various heat rates: $t_1 = 15 \text{ min}$ for $\beta_0 = 20 \text{ degree/min}$, $t_2 = 30 \text{ min}$ for $\beta_0 = 10 \text{ degree/min}$ and $t_3 = 60 \text{ min}$ for $\beta_0 = 5 \text{ degree/min}$.

By deduction of curves of photoluminescence relaxation from the above-stated curves, the TSL

spectra without contribution imported by kinetics of photoluminescence signal attenuation have been obtained. The results for various heat rates are shown in fig. 2.

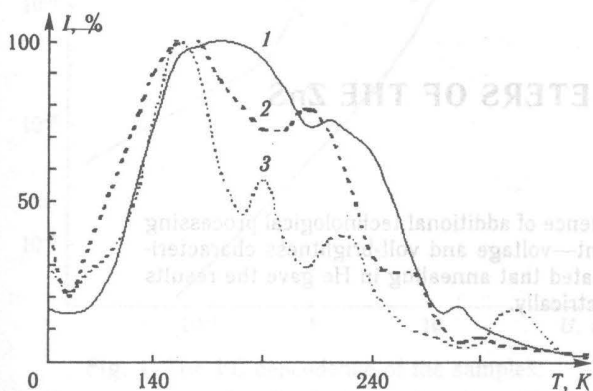


Fig. 2. TSL spectra measured under of heat velocities:

1 — 20 degree/min, 2 — 10 degree/min, 3 — 5 degree/min

The received dependencies represent integral curves composed for a series of partial strips of glow, stipulated by the contribution of various trap centres. On maximums for sectional individual strips of glow it is possible to define their quantity and to calculate the depth of occurrence centres of traps E_t .

As the methods to define E_t depend on a view of glow kinetics, it is necessary to determine correctly the character of glow kinetics. This question was solved taking into consideration the following criteria: character of symmetry for TSL strips, dependence T_m for reserved photosum quantity and dependence of TSL bandwidth on quantity of the reserved photosum.

As it is shown in fig. 2, TSL spectra consist of a series of glow strips, which overlap one another. So the guess on linear glow kinetics was accepted, because the spectra broadened to the leg of low temperatures, and, hence, parameters of glow T_m strip and δ did not depend on quantity n_0 .

To define the quantity E_t the approximate computational methods were used.

1. The quantity E_t was calculated on the basis of relations, determining dependence, δ or E_t of half-width. When TSL is linear the formula can be obtained as followed:

$$E_t = \frac{2kT_m^2}{\delta}$$

At the same time, calculation of quantity E_t it was required to define only two parameters TSL — T_m and δ .

2. For the case of the linear kinetics, the quantity E_t can be rather simply calculated under the availability of two radiation spectra measured under various heat rates of crystalline phosphor. Let temperature position of TSL strip maximum corresponds to T'_m under heat rate β'_0 and to T''_m — under β''_0 . Taking into consideration the approaches of linear

kinetics, the temperature standing of maximum is defined by the formula

$$T_m = \frac{E_t}{k} \cdot \left[\ln \left(\frac{W_0}{\beta_0} \cdot \frac{kT_m^2}{E_t} \right) \right]^{-1}$$

The relation of quantities T'_m/T''_m allows to determine quantity E_t as follows:

$$E_t = k \cdot \left(\frac{1}{T'_m} - \frac{1}{T''_m} \right)^{-1} \cdot \ln \left[\frac{\beta'_0}{\beta''_0} \cdot \left(\frac{T'_m}{T''_m} \right)^2 \right],$$

3. On initial stages of thermally stimulated luminescence, when the difference $T - T_0$ is such, that the reserved photosum quantity has not enough time to change considerably, the relations for two types of the kinetics determining TSL spectrum, irrespective by character of kinetics, acquires the following form:

$$I(T) = A \cdot e^{-\frac{E_t}{kT}}$$

where A — stationary value, not temperature-dependent. Hence, at the initial TSL stages, the dependence $I(T)$, constructed in $\ln I \sim T^{-1}$ coordinates, is represented as direct line with E_t/k declination. To calculate E_t quantity from figure 2, the quantities T_m and δ were measured. The values T_m are also shown in table 1.

Table 1
Temperatures of maximums of TSL strip intensities s for three heat rates and half-width of apparent glow strips

β_0	T_{m1}, K	δ_1, K	T_{m2}, K	δ_2, K	T_{m3}, K	δ_3, K
20	168	212	219	94	276	20
10	160	260	210	52	254	24
5	150	162	190	46	224	31

The average results on E_t , particular three approximate methods are shown in table 2.

The nature of centres, responsible for traps has not already been defined.

According to the printed sources [2] depth for occurrence of chlorine levels $\sim 0,25$ eV, that is well

agreed with energy standing of one sticking levels the define by us. It is supposed, that the intrinsic defects of polycrystal and impurity of chlorine (Cl_i) are responsible for the relevant centres.

References

1. Козицкий С. В., Ваксман Ю. Ф. Люминесценция селенида цинка, полученного методом самораспространяющегося высокотемпературного синтеза // Прикл. спектроскопия. — 1997. — Т. 64, № 3. — С. 333—337.
2. Ваксман Ю. Ф., Зубрицкий С. В., Пуртов Ю. Н., Станкова Е. В. Люминесценция поликристаллов ZnS, полученных методом CBC // Фотоэлектроника. — 1998. — Вып. 7. — С. 15—18.

THE OPTIMIZATION METHODS FOR THE ELECTROOPTIC PARAMETERS OF THE ZnS TRANSDUCERS

The results of investigations in the influence of additional technological processing of electrooptical converters on their current—voltage and volt-brightness characteristics are presented in this paper. It was stated that annealing in He gave the results close to the data for structures formed electrically.

Introduction

The forming processes in the electrical-to-optic transducers were investigated. Such transducers' basis is the barrier structure of metal-dielectric-semiconductor type, produced by means of silicium oxide thin film deposition on the ZnS film surface. The aluminium, deposited in vacuum served as the upper electrode.

The active layer of the electric-to-optic transducers is the semiconductor zinc sulphide film, produced by the electro-hydro-dynamic sputtering (EHDS) and pyrolysis of metal-organic compounds (MOC) method. All the obtained structures required the additional treatment — the forming of radiative parameters. The transducers' parameters became stable only after the preliminary keeping of them under the electric field action.

The processes of the electric field energy to optic radiation transformation take place in the active zinc sulphide layer. Before silicon oxide deposition, the additional technological treatments of the layers were fulfilled: annealing in the air, in He vapours and in vacuum. The annealing in vacuum and in the open air did not change the parameters of the transducers produced, and the forming procedure was needed as previously.

The most interesting behaviour had the structures obtained on the ZnS layers, annealed in He vapours. The transducers' radiative characteristics compared with those, where the active layer was not annealed, makes it possible to conclude about the possibility for the substitution of the electric forming procedure by the active layer annealing in vapours. Besides that the volt-brightness slope was noticed for the layers annealed in He which are the main electroluminescent cells' parameters.

Among the devices for optical representation of information, the thin film electrooptical transducers are widely used. Having enough level of brightness, low operating voltage, they provide high resolving power. The active layer of such transducers is fulfilled using the wide zone A^2B^6 semiconductors, particularly ZnS doped by Mn [1, 2].

The advantages of the thin films sources of light: the low operating voltage with enough level of brightness, high resolving power, the plane type construction, the wide possibility in choosing dimensions, packaging density and the shapes of the illuminating signs.

The goal of the work: investigation of the additional technological processing influence on the electrophysical and luminescent properties of the electrooptical transducers.

The ZnS layers deposition was fulfilled on the glass substrates, coated by the transparent conductive SnO_2 layer. Using this production technology, the two different methods were applied: method of electrohydrodynamic sputtering (EHDS), which was previously used for the production of other A^2B^6 compounds [3], and now applied for the zinc sulphide; the modified method of chemical deposition of the vapour phase of metallorganic compound. The overheated water vapour was used as a transforming gas. The thickness of the films obtained for the period of 60...180 min was 1,5...2 μm .

For the improvement of the illuminating characteristics of layers investigated, the additional heat treatment was carried out. The types of annealing: in vacuum, in the air, in the atmosphere of helium.

Experimental results and interpretation

The structures based on the initial layers were investigated as follows: the volt—current dependence measurements; the volt—brightness dependence measurements.

The structures investigated did not show the radiation at the initial application of the electric field in the range of 0...8 V (fig. 1). The luminescent glow was registered after the samples were treated at the voltage of 8...10 V for 20 min and only after the electric current achieved the critical value of 20...25 μA . Just after the glow was registered the current decreased sharply ten times of the order. The electroluminescent brightness was notably increased. The further voltage increase lead to the super-

linear $U-I$ dependence and to the electroluminescent brightness growth.

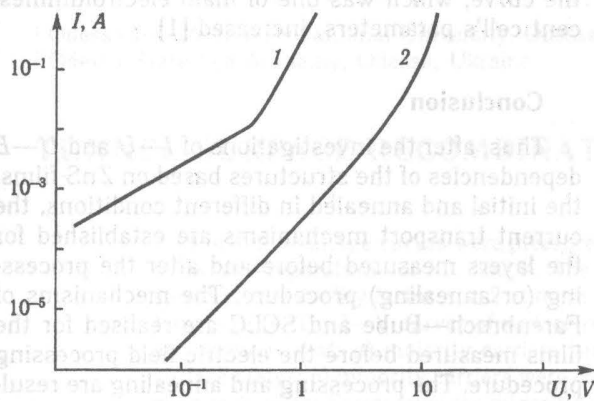


Fig. 1. The VC dependence of the samples:

1 — initial films; 2 — after the electric treatment

So the conclusion was made that the electric treatment was necessary for the electroluminescence appearance.

At the recurrent $U-I$ dependencies measurements (curve 2), the volt—current dependence had two superlinear sections: in the region of low voltages ($U < 10$ V), where the current—voltage dependence was described by the law $I \sim U^{1.4}$. The EL glow appeared at this section when $U = 8$ V. When the voltage achieves 10 V the mentioned dependence changes for the sharp current growth.

As the structural analysis showed, the investigated ZnS layers were the closely packed crystallites, the average size of each was $0,1 \mu\text{m}$. At the same time, in the separate regions where three or more crystallites join, one may notice the little crystals presence, the linear dimensions of each is $0,01 \mu\text{m}$ or less. The mentioned regions may be connected with the ZnO phase inclusion. Their presence is supported by the X-ray analysis, or with the possible segregation of different impurities. Besides that they may be little crystallites of ZnS suppressed at the process of growth by the bigger crystallites.

Taking into consideration the X-ray analysis results, the treatment process may be explained as the following: in the structures initially prepared, the current flows along the channels which are formed by the intercrystallites inclusions, which have a great amount of defects and, hence, are lower ohmic than the matrix film. When some critical heat power is emitted within these channels they may be irreversibly switched off the current transport when the voltage is increased. When the following measurements were made on the structures the current flows along the chains made of big crystallites of zinc sulphide. As the films thickness was $1,5...2 \mu\text{m}$, then $15...20$ intercrystallite barriers appeared to be switched to the current channel. The linear section of the $I-U$ dependence in the region of low voltages may be explained in the frames of the polycrystalline layer Farenbruch—Bube model for the event when a great amount of intercrystal-

lite barriers form the current channel [4]. The superlinear volt—current dependence may be connected with the space charge limited currents (SCLC) regime for the intercrystallite interlayers, or with the high electric field tensions in the regions of the reversed biased barriers of the intercrystallite interlayers [5]. The volt—current characteristic of the structure formed, which had the superlinear character as in the region of low voltages and in the region of higher voltages, may also be explained by the SCLC regime in the zinc sulphide layer.

Influence of the thermoprocessing on the structures' parameters. The annealing of the films in the open air and in vacuum did not change their volt—current dependencies. The radiation in such structures appeared only after they were preliminary treated in the electric field. It may be supposed that the current transport mechanisms did not change after said annealing. The structures based on the films annealed in helium atmosphere had specific characteristics. When the structure was switched on reversed polarity at low ($U < 1$) voltages then $U-I$ had the linear dependence, i. e. $I \sim U$ (fig. 2). While

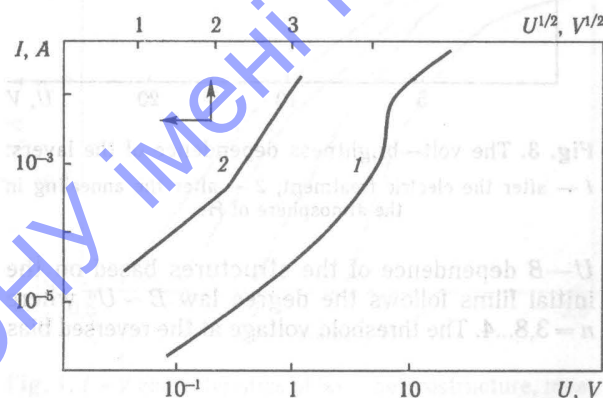


Fig. 2. The VC dependence of the films after annealing in the atmosphere of He

the voltage increases, the linear dependence changes for the exponential law $I \sim \exp(\text{const } U^{1/2})$. This part of the $U-I$ curve is plotted in $\ln I \sim U^{1/2}$ coordinates (curve 2). In this figure one may notice two linear parts with different slope coefficients: from 1 V to 5 V $I \sim \exp(2,7 U^{1/2})$, and from 5 V to 10 V $I \sim \exp(3,8 U^{1/2})$. The rectification of $U-I$ curve at the reversed voltage polarity in $\ln I - U^{1/2}$ coordinates, witnesses that the current transport mechanism in the structure is the above-barrier Shottky emission [6]. The part of saturation which is registered on the $I-U$ dependencies is connected with the charge polarisation effects.

Comparing $I-U$ dependencies of the initial films after the processing (fig. 1, curve 2) and of the films annealed in helium atmosphere (fig. 2) one may notice the following specific features: the $U-I$ dependencies for the annealed structures has exponential law $I \sim \exp(\gamma U^x)$. Such dependencies are specific for the Shottky emission through the reverse biased metal-semiconductor barrier and also for the

intercrystallite potential barriers. The γ coefficient in the given dependence is defined by the ionised donors' density. The electric field processing followed by the helium annealing resulted in the increase of the samples' resistance. This differs from the initial lower ohmic samples (fig. 1, curve 1). It seriously contributes to the current transfer. The resistance increase of the layers after they were annealed in helium might be connected with the ionised donors density change.

The fig. 3 presents the volt-brightness luminescence characteristic of the structures discussed. The

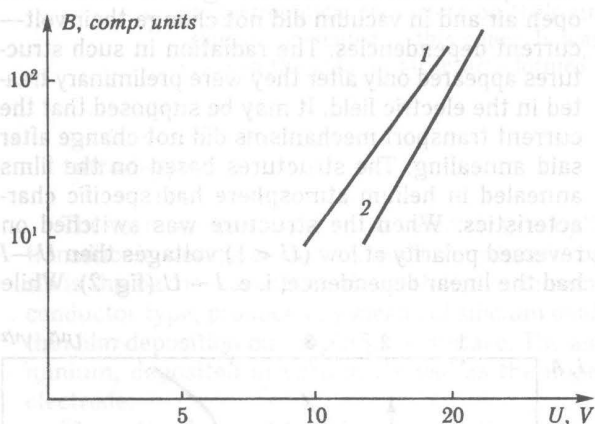


Fig. 3. The volt—brightness dependence of the layers: 1 — after the electric treatment; 2 — after the annealing in the atmosphere of He

U — B dependence of the structures based on the initial films follows the degree law $B \sim U^n$ where $n = 3,8 \dots 4$. The threshold voltage at the reversed bias

was ~ 10 V. But for the structures based on the annealed in helium films, n was 5,5, i. e. the slope of the curve, which was one of main electroluminescent cell's parameters, increased [1].

Conclusion

Thus, after the investigations of I — U and U — B dependencies of the structures based on ZnS films, the initial and annealed in different conditions, the current transport mechanisms are established for the layers measured before and after the processing (or annealing) procedure. The mechanisms of Farenbruch—Bube and SCLC are realised for the films measured before the electric field processing procedure. The processing and annealing are resulted in the exclusion of the little crystallites out of the current channel and the current flows as the above-barrier Shottky emission. The results obtained, allow to conclude about the possibility to change the electric field processing for the annealing in the He vapours for the ZnS electrooptical structures.

References

1. Вережагин И. Л. Электролюминесценция кристаллов. — М.: Наука, 1990. — 279 с.
2. Полукристаллические полупроводники. Физические свойства и применение / Под ред. Г. Харбеке. — М.: Мир, 1989. — 342 с.
3. Борщак В. А., Затовская Н. П., Куталова М. И., Смытнына В. А. // Фотоэлектроника. — 1998. — С. 47—48.
4. Фаренбрух А., Бьюб Р. Солнечные элементы. Теория и эксперимент. — М.: Энергоиздат, 1987. — 560 с.
5. Беляев А. П., Рубец В. П., Полежаев К. А. // Поверхность. Физика и химия. — 1993. — № 6. — С. 85—88.
6. Herbert G. Elektrische eigen shaften inhomogener Metell-Halbleiter-Grenzflächen. — Stuttgart, 1991. — 185 p.

TUNNEL SURFACE RECOMBINATION IN $p-n$ JUNCTIONS

Current—voltage curves were measured on AlGaAs-GaAs laser double heterostructures at temperatures of 77...300 K. The exponential sections of $I-V$ curves correspond to the ideality factor $n_t \leq 2$ at room temperature, which increases with lowering temperature. The $I-V$ curves of surface recombination current were calculated under assumptions that: *a*) majority carriers tunneled to the surface and were captured to surface states; *b*) minority carriers were captured by surface states «classically»; *c*) the change in quasi Fermi level for minority carriers in surface depletion channel linearly depended on the surface barrier height. The obtained expression for $I-V$ curves explains the features of measured current-voltage characteristics of laser heterostructures.

1. Introduction

Surface recombination reduces the performance parameters of diode lasers (DL) [1-3], bipolar transistors [4], photodiodes, solar cells and other devices on III—V semiconductors [5-6]. Surface recombination in a $p-n$ junction results in forward current component [6]

$$I_s(V) = I_0 e^{\frac{qV}{n_t kT}}, \quad (1)$$

where I_0 is constant; q is electron charge; V is bias voltage; k is Boltzmann's constant; T is temperature; n_t is ideality factor. Under some conditions $n_t \approx 2$ [6]. The most important of these conditions are the following:

- a*) surface states form deep levels in energy gap, which produce depletion channel at surface;
- b*) density of surface states is large, that usually occurs in III—V semiconductors such as GaAs, Al—GaAs, GaP, GaAsP, InP, InGaAsP;
- c*) quasi Fermi levels for electrons and holes are constant in surface depletion channels.

The purpose of this paper is to investigate the dependence $n_t(T)$ experimentally and theoretically.

2. Experimental results and model assumptions

The measurements were made on AlGaAs—GaAs laser double heterostructures (DHS) with stripe geometry, described in our previous papers [7-9]. The temperature of sample was varied in the range of 77...400 K. Fig. 1 represents the current—voltage characteristics of DHS, measured at various temperatures. It is seen that $I-V$ curves plotted in semilogarithmic scale have linear sections corresponding to expression (1). The ideality factor was $n_t = 1.75...2.0$ (for various samples) at room temperature and $2.0...4.2$ at 80 K. For each sample the value of n_t increased with lowering temperature.

The calculations of forward current component in a $p-n$ junction, due to surface recombination,

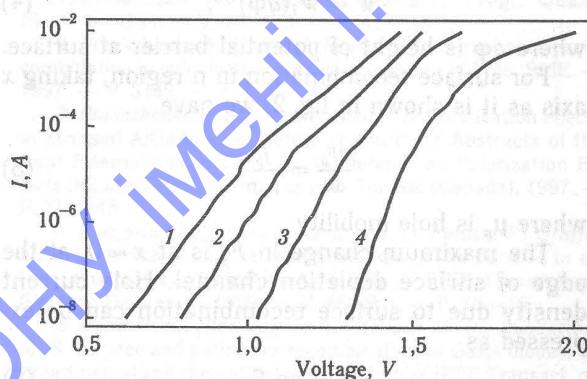


Fig. 1. $I-V$ characteristics of laser heterostructure, measured at various temperatures:

1 — 293; 2 — 247; 3 — 183; 4 — 97 K

were performed under assumptions of [6], but quasi Fermi levels F_n , F_p were taken not constant in surface depletion channel. Surface recombination in n region occurs as shown in fig. 2: an electron tun-

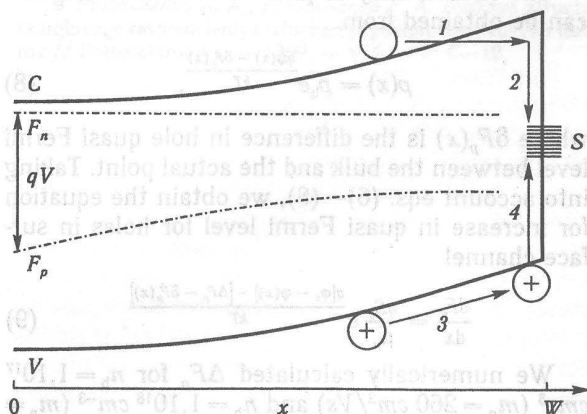


Fig. 2. Energy band diagram and electron and hole transitions in surface depletion channel

nels to surface (arrow 1) and is then captured to surface states (arrow 2). Minority carrier (a hole) moves to surface (arrow 3) and is then «classically» captured by the surface states (arrow 4). At the crossing of bulk- and surface depletion regions both electrons and holes tunnel to surface and are captured by surface states. In case of tunneling electrons, the electron current density at the edge of surface depletion channel is determined by [2]

$$j_1 = j_{t0} e^{\frac{e\phi}{n_0 kT}}, \quad (2)$$

where j_{t0} is constant; the coefficient n_{t0} is determined by

$$n_{t0} = \frac{1}{1 - \frac{\hbar^2}{6m_1 W_1^2 (kT)^2}}, \quad (3)$$

where m_1 is «tunnel» effective mass of charge carriers; W_1 is the coefficient in the expression for barrier width in surface depletion channel

$$W = W_1 (q\phi)^{1/2}, \quad (4)$$

where $q\phi$ is height of potential barrier at surface.

For surface recombination in n region, taking x axis as it is shown in fig. 2, we have

$$\frac{dF_p}{dx} = \frac{j_p}{\mu_p p}, \quad (5)$$

where μ_p is hole mobility.

The maximum change in F_p is at $x \approx 0$, at the edge of surface depletion channel. Hole current density due to surface recombination can be expressed as

$$j_p = qp_s S_0, \quad (6)$$

where S_0 is velocity of surface recombination. Hole density at surface can be written as

$$p_s = p_b e^{\frac{q\phi_s - \Delta F_p}{kT}}, \quad (7)$$

where p_b is density of holes at $x = 0$; $q\phi_s$ is surface band bending; ΔF_p is the change in F_p in surface channel.

The hole density at point x in surface channel can be obtained from

$$p(x) = p_b e^{\frac{q\phi(x) - \delta F_p(x)}{kT}}, \quad (8)$$

where $\delta F_p(x)$ is the difference in hole quasi Fermi level between the bulk and the actual point. Taking into account eqs. (6)–(8), we obtain the equation for increase in quasi Fermi level for holes in surface channel

$$\frac{dF_p}{dx} = \frac{qS_0}{\mu_p} e^{\frac{q[\phi_s - \phi(x)] - [\Delta F_p - \delta F_p(x)]}{kT}}. \quad (9)$$

We numerically calculated ΔF_p for $n_b = 1,10^{17} \text{ cm}^{-3}$ ($m_p = 260 \text{ cm}^2/\text{Vs}$) and $n_b = 1,10^{18} \text{ cm}^{-3}$ ($m_p = 170 \text{ cm}^2/\text{Vs}$), as well as ΔF_n in p region for $p_b = 1,10^{17} \text{ cm}^{-3}$ ($\mu_n = 4800 \text{ cm}^2/\text{Vs}$) and $p_b = 1,10^{18} \text{ cm}^{-3}$ ($\mu_n = 2800 \text{ cm}^2/\text{Vs}$), taken $S_0 = 4,10^5 \text{ cm/s}$.

The results are shown in fig. 3. It is seen that over wide range of surface barrier heights, the change

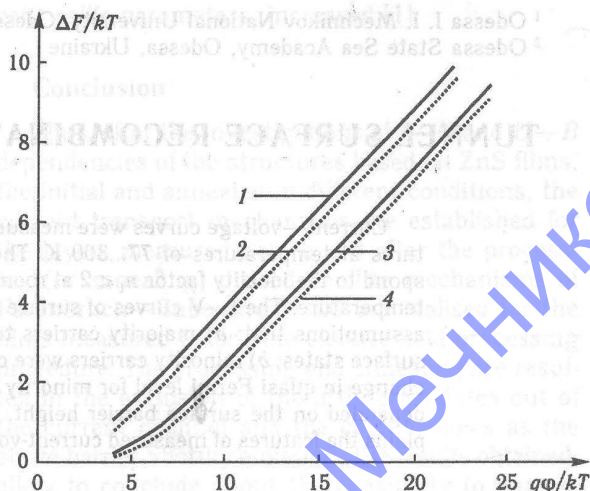


Fig. 3. The change in quasi Fermi level for minority carriers in surface depletion channel:

1 — for holes in n region at $n_b = 1,10^{17} \text{ cm}^{-3}$, 2 — for holes in n region at $n_b = 1,10^{18} \text{ cm}^{-3}$; 3 — for electrons in p region at $p_b = 1,10^{17} \text{ cm}^{-3}$, 4 — for electrons in p region at $p_b = 1,10^{18} \text{ cm}^{-3}$

in quasi Fermi level for minority carriers in surface depletion channel can be approximated as

$$\frac{\Delta F_n}{kT} = a \frac{q\phi_s}{kT} - b, \quad (10)$$

where coefficients a and b depend on the sign and concentration of majority carriers.

3. Current component due to tunnel surface recombination

Let us consider the surface recombination in p region of $p-n$ junction and in the adjacent section of depletion region, where $p_b \gg n_b$. For electrons, as minority carriers, the rate of «classical» capture by surface states can be written as

$$R_{sn} = C_n P_s n_s, \quad (11)$$

where P_s is density of empty surface states,

$$C_n = \sigma_n V_n, \quad (12)$$

where σ_n is the appropriate cross-section; V_n is thermal velocity of electrons. Electron density at surface is defined by

$$n_s = n_b e^{\frac{q\phi_s - \Delta F_n}{kT}}, \quad (13)$$

where ΔF_n is the change in electronic quasi Fermi level in surface channel. We assume that relation (10) between ΔF_n and ϕ_s holds (with appropriate coefficients a and b), so

$$n_s = n_b e^{b(1-a)\frac{q\phi_s}{kT}}. \quad (14)$$

For holes, as majority carriers, the change in quasi Fermi level is negligible [6], and their rate

of tunnel capture to surface states can be described by

$$R_{sp} = C_p p_b N_s e^{-\frac{q\Phi_s}{n_i kT}}, \quad (15)$$

where, similarly to eq. (12),

$$C_p = \sigma_p V_p, \quad (16)$$

N_s is density of filled surface states; n_i is given by eq. (3).

Equating R_{sp} and R_{sn} in steady state we obtain for surface capture rate of electrons and holes

$$R_s = [(C_p N_s)^{(1-a)n_i} C_n P_s e^b]^{1/n_i} \times \frac{n_i^{2/n_i}}{p_b^{(2-n_i)/n_i}} e^{\frac{F_{nb}-F_{pb}}{n_i}}, \quad (17)$$

where F_{nb} and F_{pb} are bulk values of F_n and F_p ,

$$n_i = 1 + (1-a)n_{t_0}, \quad (18)$$

The expression for surface recombination current I_s can be obtained from

$$I_s = q L_s I_p R_s, \quad (19)$$

where L_s is effective surface diffusion length [6]; I_p is the perimeter of p - n junction, under an assumption that

$$F_{nb} - F_{pb} = qV, \quad (20)$$

where V is bias voltage.

Thus, for surface current component we obtain eq. (1),

$$I_0 = q L_s I_p [(C_p N_s)^{(1-a)n_i} C_n P_s e^b]^{1/n_i} \frac{n_i^{2/n_i}}{p_b^{(2-n_i)/n_i}}, \quad (21)$$

n_i is defined from eq. (18).

4. Conclusions

The obtained expression for surface tunnel recombination current explains the features of I - V curves of AlGaAs-GaAs laser double heterostructures, measured at various temperatures. The ideality factor of 1.75...2.0 at room temperature, estimated for various samples, corresponds to the change in the quasi Fermi level of electrons in surface depletion channel, given by eq. (10), where $0 < a < 0.25$.

The temperature behavior of the ideality factor n_i , obtained from analysis of measured I - V curves, is described by eq. (3), where $W_1 = 60...220 \text{ nm eV}^{-1/2}$. The temperature dependence of pre-exponential factor in eq. (1) for the measured I - V curves can be approximated by

$$I_0(T) \sim (kT)^{1/2} e^{-\frac{\Delta E}{kT}}, \quad (22)$$

where $\Delta E = 0.03...0.07 \text{ eV}$. This value is consistent with the estimation of coefficient a in eq. (10) for the change in quasi Fermi level for minority carriers in the surface depletion channel.

The results of our measurements on laser heterostructures, giving the ideality factor $n_i < 2$ at room temperature, provide evidence that the change in quasi Fermi level for minority carriers in surface depletion channel can be approximated by eq. (10).

References

1. Gribkovskii V. P. Injection Lasers // Progr. Quant. Electr. — 1994. — V. 19, № 1. — P. 41—88.
2. Ptashchenko A. A., Ptashchenko F. A. Tunnel surface recombination in optoelectronic device modelling // Proc. SPIE. — 1997. — V. 3182. — P. 145—149.
3. Ptashchenko A. A., Ptashchenko F. A. Polarization effects in stressed AlGaAs laser heterostructures // Abstracts of the First International School and Conference on Polarization Effects in Lasers and Spectroscopy. — Toronto (Canada), 1997. — P. TU.2:45.
4. Borgarino M., Plana R., Delage S. L., Fantini F., Graffini J. Influence of surface recombination on the burn — in effect in microwave GaInP/GaAs HBT's // IEEE Transact. on Electron Devices. — 1999. — V. 46, № 1. — P. 10—15.
5. Dodd P. E., Stellwag T. B., Melloch M. R., Lundstrom M. S. Surface and perimeter recombination in GaAs diodes: an experimental and theoretical investigation // IEEE Transact. on Electron Devices. — 1991. — V. 38, № 6. — P. 1253—1260.
6. Mazhari B., Morkoc H. Surface recombination in GaAs p - n junction diode // Journ. of Appl. Phys. — 1993. — V. 73, № 11. — P. 7509—7514.
7. Ptashchenko A. A., Deych M. V., Mironchenko N. V., Ptashchenko F. A. Polarization of the spontaneous radiation of stressed laser heterostructures // Solid-State Electronics. — 1994. — V. 37, № 4—6. — P. 1255—1258.
8. Ptashchenko A. A., Ptashchenko F. A. «Excess» polarization of the spontaneous emission in laser heterostructures // Solid-State Electron. — 1996. — V. 39, № 10. — P. 1495—1500.
9. Ptashchenko A. A., Ptashchenko F. A. Tonkaya struktura ugovogo raspredeleniya izlucheniya poluprovodnikovyykh lazorov // Fotoelektronika. — 1999. — V. 8. — P. 6—12.

THE MAGNETIC SUSCEPTIBILITY OF Si-Ni ALLOYS RICH ON SILICON: INFLUENCE OF PHASES DISTRIBUTION AND THEIR DISPERSITY

The results of the investigation for the influence of the phases distribution and their dispersity upon the static magnetic susceptibility (MS, χ) of Si-Ni alloys rich in silicon are presented in this paper. The MS measurements of these alloys carried out immediately after their fusion have demonstrated the following: *a*) for all samples, on the one hand, MS value was not equal to the sum for MS and their phase component (i. e. the law of additivity is violated); *b*) on the other hand, the non-linearity of MS dependence upon magnetic field tension ($\chi(H)$) was observed here. We suppose that the first circumstance is connected with the large quantity of structural defects and the second one is connected with the presence of electron spins' magnetic ordering on dislocation structures. To verify our assumptions we carried out the heat treatment of samples in two regimes: at 400 °C and at 800 °C during 21 days in both cases. The heat treatment of samples at 400 °C led only to increase of diamagnetism, but did not influence upon $\chi(H)$ character. The heat treatment of samples at 800 °C led to disappearance of non-linearity in $\chi(H)$ dependencies. Law of additivity satisfactorily describes magnetic susceptibility of alloys after the heat treatment at 800 °C.

1. Introduction

The complex investigation of Si-Ni alloys rich in semiconductor component (66,7...95,0 mass p. c. of Si) (static susceptibility (MS, χ), X-ray- and microstructural analyses) has shown that they consist of two phases: silicon (Si) and nickel disilicide (NiSi_2). Depending on the character of NiSi_2 fragment distribution in lattice of alloys, great number of defects arise, non-grown dislocation and donor-acceptor complexes take the considerable place among them [1].

The aim of this paper is to examine the influence of phase distribution and phase dispersity in Si-Ni alloys rich in silicon on their magnetic properties.

These alloys were obtained by fusion of Si-Ni components in electro-arch furnace on copper bottom cooling by water in argon atmosphere. The melt was cooled with the furnace.

The composition of alloys, their quantitative phase composition, the magnitudes of static magnetic susceptibility in the region of its independence on tension of external magnetic field H (i. e. χ magnitudes in field $H = 5,0 \text{ kOe}$ ($\chi_{5,0}$)) of alloys measured immediately after their fusion and after heat treatment at 400 °C and at 800 °C (the duration of each heat treatment cycle is similar — 21 hours), the magnitudes for magnetic susceptibility of alloys calculated according to the law of additivity, and also for MS-magnitude of primary silicon, which was used during the synthesis of the given alloys, are listed in the table.

Fig. 1 presents the microstructures of poly crystalline alloy $\text{Si}_{95}\text{Ni}_5$ after fusion (*a*), after heat treat-

ments at 400 °C (*b*) and at 800 °C (*c*). As one can see (fig. 1), immediately after fusion, the low-dispersed

Table

Phase and magnetic characteristics of investigated Ni-Si alloys

Sample	Alloys composition	Quantitative phase composition	Magnitudes of $\chi(5,0) 10^8, \text{cm}^3 \text{g}^{-1}$			
			After fusion of alloys	Annealing		Calculated by (I)
				At 400° C	At 800° C	
1	$\text{Si}_{67}\text{Ni}_{33}$	NiSi_2	-1,6	-7,1	19,4	19,4
2	$\text{Si}_{70}\text{Ni}_{30}$	$\text{NiSi}_2 + 0,25\text{Si}$	2,0	-8,3	12,4	11,7
3	$\text{Si}_{70}\text{Ni}_{30}$	$\text{NiSi}_2 + 0,67\text{Si}$	0,7	-9,3	-1,9	-1,3
4	$\text{Si}_{90}\text{Ni}_{10}$	$\text{NiSi}_2 + 0,88\text{Si}$	-2,3	-4,7	-6,9	-7,8
5	$\text{Si}_{95}\text{Ni}_5$	$\text{NiSi}_2 + 0,94\text{Si}$	-2,8	-6,8	-10,2	-9,6
6	Si	Si	-11,5	-11,5	-11,5	-11,5

structure is observed, it is inherent for the casting material. Heat treatment of samples at 400 °C (fig. 1, *b*) causes the partial amalgamation of the separate phases, and heat treatment of samples at 800 °C (fig. 1, *c*) leads to accumulation of NiSi_2 polycrystals (dark phase) in pure silicon lattice (light phase). Thus, heat treatment at 800 °C leads to the sharp separation of the different phases (silicon and nickel disilicide) in Si-Ni polycrystals.

The experimentally obtained $\chi(H)$ dependencies of Si-Ni alloys as function of their composition have some peculiarities, which can be demonstrated as

the example of two extreme alloys: $\text{Si}_{67}\text{Ni}_{33}$ (forms pure NiSi_2 -phase) and $\text{Si}_{95}\text{Ni}_5$ (forms two-phase poly-

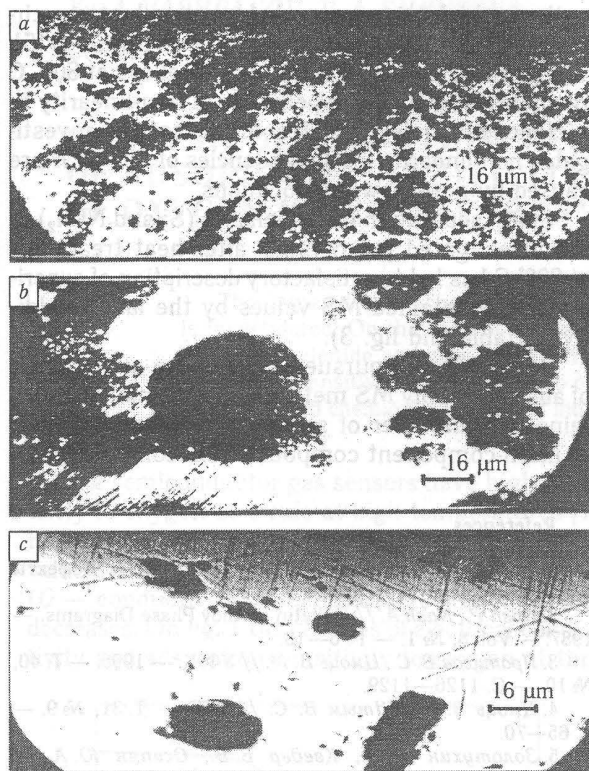


Fig. 1. The microstructures of poly crystalline $\text{Si}_{95}\text{Ni}_5$ sample after:

a — fusion; *b* — heat treatment at 400°C ; *c* — heat treatment at 800°C

crystal which consist of NiSi_2 -phase and pure silicon). Fig. 2, *a*, *b* illustrates $\chi(H)$ dependencies for samples of these compositions after their fusion (curve 1) and after annealing at 400°C (curve 2) and at 800°C (curve 3). The curves illustrated by fig. 2, *a* are typical for samples 1—3, for which the second annealing (at 800°C) leads to the sharp decrease of diamagnetism and to the appearance of considerable paramagnetism (samples 1 and 2). The curves illustrated by fig. 2, *b* are typical for samples 4 and 5, for which the second annealing leads to the further increase of diamagnetism. Thus, as one can see in fig. 2, after heat treatment at 800°C $\text{Si}_{95}\text{Ni}_5$ alloy remains diamagnetic, but $\text{Si}_{67}\text{Ni}_{33}$ alloy becomes paramagnetic. Heat treatment of samples at 400°C leads only to increase of diamagnetism for all the samples without exception but does not influence on the character of $\chi(H)$ dependencies. One should note, that heat treatment of Si-Ni samples at 800°C leads to the disappearance of non-linearity for $\chi(H)$ dependencies (fig. 2, *a*, *b*, curves 3).

The equation which describes the dependence for the specific MS of alloys on the mass part of NiSi_2 in it, can be written as follows:

$$\chi_L = (1 - N)\chi_{\text{Si}} + N\chi_{\text{NiSi}_2}, \quad (1)$$

where N is mass part of NiSi_2 -phase in each alloy;

χ_{NiSi_2} and χ_{Si} are the specific MS of NiSi_2 and Si, respectively.

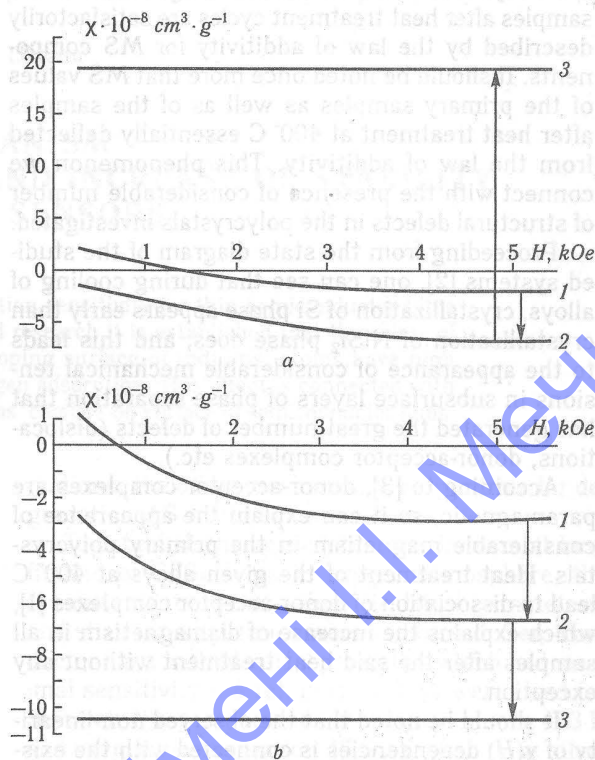


Fig. 2. Experimental dependencies $\chi(H)$ of NiSi_2 -phase (*a*) (sample 1) and two-phased alloy $\text{Si}_{95}\text{Ni}_5$ (*b*) (sample 5):

1 — MS values of these samples immediately after their fusion; 2 — after heat treatment at 400°C ; 3 — after heat treatment at 800°C

Fig. 3 shows theoretical (calculated by formula (1)) values for the specific MS of alloys depending

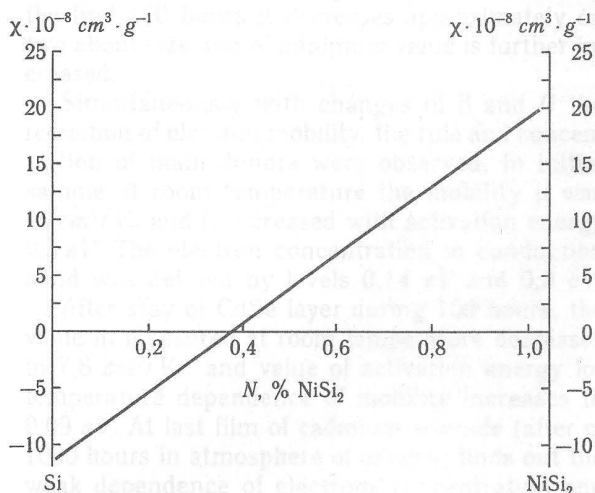


Fig. 3. Specific MS values of Si-Ni alloys (straight line) calculated theoretically by expression (1) and experimentally obtained for MS after heat treatment for Alloys at 800°C

on the mass part of NiSi_2 -phase (N) in each alloy (straight line) and χ magnitudes for the samples after

heat treatment at 800° C (curve °) obtained experimentally. One can see that MS magnitudes of the samples after heat treatment cycles are satisfactorily described by the law of additivity for MS components. It should be noted once more that MS values of the primary samples as well as of the samples after heat treatment at 400° C essentially deflected from the law of additivity. This phenomenon we connect with the presence of considerable number of structural defects in the polycrystals investigated.

Proceeding from the state diagram of the studied systems [2], one can see that during cooling of alloys, crystallization of Si phase appears early than crystallization of NiSi₂ phase does, and this leads to the appearance of considerable mechanical tensions in subsurface layers of phase separation that has generated the great number of defects (dislocations, donor-acceptor complexes etc.).

According to [3], donor-acceptor complexes are paramagnetic, so it can explain the appearance of considerable magnetism in the primary polycrystals. Heat treatment of the given alloys at 400° C lead to dissociation of donor-acceptor complexes [1], which explains the increase of diamagnetism in all samples after the said heat treatment without any exception.

It should be noted that the observed non-linearity of $\chi(H)$ dependencies is connected with the existence of magnetic ordering in electron spins at dis-

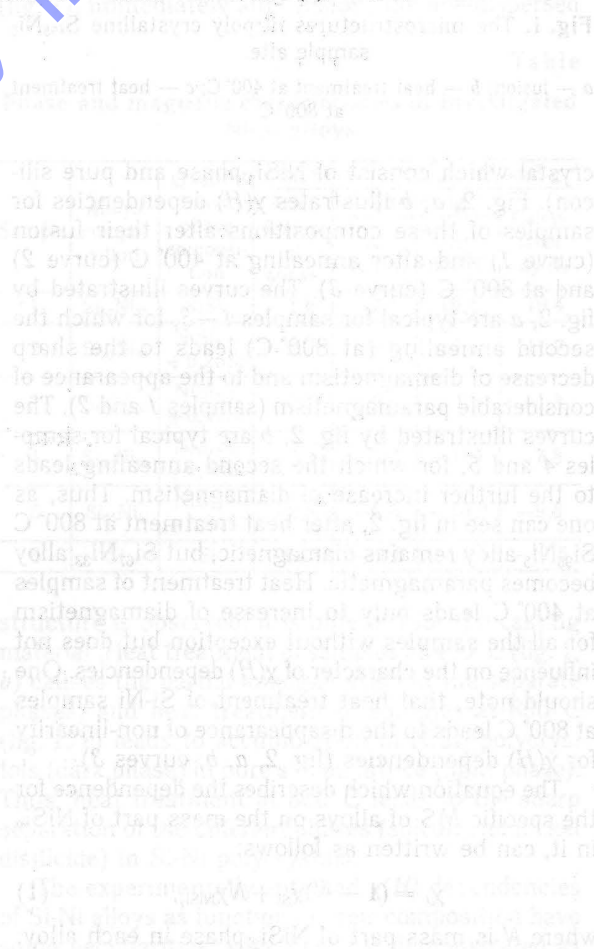
location structures [4]. Heat treatment of samples at 790° C leads to nuclei reconstruction of dislocations which is accompanied by «two-by-two» circuit of the broken bonds at the state with $S = 0$ [5]. The pursued heat treatment of Si-Ni alloys at 800° C really leads to the disappearance of non-linearity in $\chi(H)$ dependencies, which confirm that this investigated non-linearity for dependencies of MS on H are caused by non-grown dislocations.

Sharp separation of two phases (Si and NiSi₂) in the investigated polycrystals after heat treatment at 800° C has led to satisfactory description of experimentally contained MS values by the law of additivity (table and fig. 3).

Basing on the pursued studies the supposition of ability to apply MS method has been made to examine the character of separate phase distribution in multi-component compound semiconductors.

References

1. Вавилов В. С., Киселев В. Ф., Мукашев Б. Н. Дефекты в кремнии и на его поверхности. — М., 1990.
2. Nash P., Nash A. // Bulletin of Alloy Phase Diagrams. — 1987. — Vol. 8, № 1. — P. 6—13.
3. Протасов В. С., Цмоць В. М. // УФЖ. — 1995. — Т. 40, № 10. — С. 1126—1129.
4. Цмоць В. М., Штым В. С. // ФТТ. — Т. 31, № 9. — С. 65—70.
5. Золотухин М. Н., Кведер В. В., Осипян Ю. А. // ЖЭТФ. — 1981. — Т. 81, № 1 (7). — С. 299—307.



STUDY IN DEGRADATION MECHANISM OF ADSORPTION SENSITIVITY AND INCREASE OF STABILITY OF OXYGEN MICROELECTRONIC SENSORS

The degradation mechanism of adsorption sensitivity for thin semiconductor films is investigated. On the base of the carried research it is established that thin films of cadmium selenide and zinc oxide with doping surface of indiums' atoms have high adsorption sensitivity and stability to oxygen adsorption. This effect is connected with electronic and chemical properties of indiums' clusters on surface of semiconductor films.

The semiconductor gas sensors have high sensitivity to oxygen as a rule at high temperatures [1]. However, at the repeated recurrence of gas cycle, the value of adsorption sensitivity (AS) $\beta = G^{-1}dG/dp$ [2] (G — conductivity of semiconductor) continuously decreases. On fig. 1 the changes of electrical conductivity and adsorption sensitivity to oxygen at time

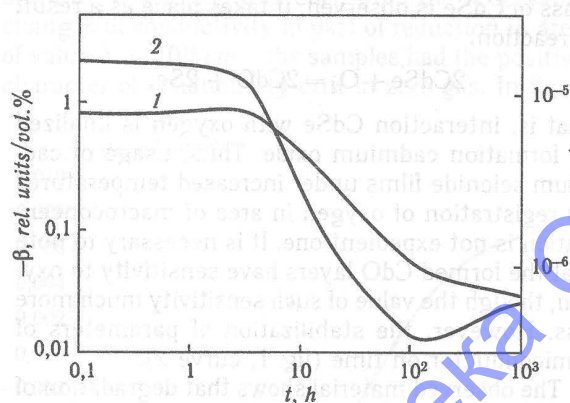


Fig. 1. The dependence of conductivity G and adsorption sensitivity β on time

magnification for thin films of cadmium selenide (curves 1 and 2 accordingly) are shown.

It was possible to assume that as far as the temperature of measurements was high the changes of ADS are connected with structural transformations. It took place because at this temperature structure changes from cubic to hexagonal form. To eliminate the influence of structural changes, the layers of cadmium selenide were subjected to additional annealing on air then the change of electric conduction G of layers down to establishment of stable value was measured. The establishment of stationary value G happens the faster, the higher the temperature of preliminary annealing.

At measurements on gas stand it was found out that after annealing the layers have considerably smaller by a factor of sensitivity β and by adsorption's ability. However, stabilisation of AS not happens. It testifies that except for structural transfor-

mations, the other mechanisms, responsible for degradation AS in time, exist.

To establish the degradation mechanism at long finding of CdSe films in oxygen atmosphere, the measurements of AS value, electrical parameters, and structures on times were conducted. Semiconductor films with identical properties which had maximal sensitivity 0.8 rel. units/vol. % were used for research the temperature of measurements 453 K and oxygen concentration 45.6 vol. % in pure nitrogen was chosen. The values β and G were measured, without removing the samples from the chambers. The temperature dependencies of Hall effect were measured preliminary and after 100 and 1000 hours of testing.

The long stay of CdSe films in oxygen atmosphere results in reduction of β by an order of value. Thus the AS value remained practically constant during first 10 hours of stay in oxygen atmosphere. During the first 100 hours it decreases approximately on two about size and of minimum value is further increased.

Simultaneously with changes of β and G the reduction of electron mobility, the rule and concentration of main donors were observed. In initial sample at room temperature the mobility μ was $60 \text{ cm}^2/\text{Vs}$ and it increased with activation energy 0.3 eV . The electron concentration in conduction band was defined by levels 0.14 eV and 0.3 eV .

After stay of CdSe layer during 100 hours, the value m measured at room temperature decreases to $7.8 \text{ cm}^2/\text{Vs}$, and value of activation energy for temperature dependence of mobility increases to 0.09 eV . At last film of cadmium selenide (after of 1000 hours in atmosphere of oxygen) finds out the weak dependence of electrons concentration and mobility from temperature. The layers have the orange colour and contain CdO about than the data X-ray of analysis testifies this.

As far as after 100 hours of layer stay in atmosphere of oxygen, the increase of barrier between crystallite takes place, reduction β and G is possibly is connected with diffusion of oxygen into intercrystalline grains. The oxygen atoms diffuse at the grain

boundaries deeply into layer being moved on selenium vacancies. Thus, free electron concentration in surface area of crystallites decreases and the barrier height between crystal grains grows.

The oxygen atoms on semiconductor surfaces are formed as a result of molecule dissociation which is stimulated by presence of [Se] at the surface. One of oxygen atoms is built in the structure of selenium vacancy surface, the second atom forms on surface deep centre of electrons in band gap or recombining with the other atom forming again the oxygen molecule. The participation in exchange with gas phase of ions O^- causes the initial high sensitivity to oxygen.

During the degradation process the reduction in centre number 0,14 eV selenium vacancies stipulated by the availability in CdSe lattice is observed. The reduction of concentration [Se] can take place as a result of oxygen atom diffusion deeply into the layer and as a result of the exitance of donors [Se] on surface under action of field of space charge area where oxygen atom is built in on location of oxygen vacancy. To reduce AS in time it is necessary that the atom O was built irreversibly into the structure of semiconductor and, thus, did not participate the interaction of surface with gas environment, hereinafter.

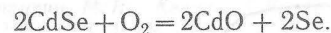
The reduction of free electrons number in volume of semiconductor, which should take place as a result of reduction of number of selenium vacancies, is accompanied by approach of Fermi level to the middle of band gap. The increase occurring in accordance to accounts β is possible, if in diffusions process of oxygen ions in volume the number of [Se] on surface (the adsorption's centres of oxygen ions) remains constant one. The output of positive donors on surfaces of layer under electrical field created negative charge of oxygen ions should resulted in, on one hand in reduction of donor number in volume of semiconductor, and, on the other hand, in decrease of surface potential barrier at the expense of compensation in negative charge of oxygen ions by positively charged donors. Both these processes are resulted in AS growth.

However, the reduction of sensitivity in time is experimentally observed. To think that the filling of vacancies happens irreversibly, speed dissociation and formation of oxygen ions will be defined by speed of formation [Se] on surface for account of diffusion them. The value of diffusion factor of Se atoms on selenium vacancies was $10^{-12} \text{ cm}^2/\text{s}$ [3] that more then diffusion factor of oxygen atoms on the grain space and in volume of layer. Therefore, the speed of exit [Se] on surface was more then speed of ions O^- deeply into material. Hence, on initial degradation stages, AS limited the process is the exit [Se] on surface which stimulates dissociation of oxygen molecules and supports the number of adsorption centres, providing the high sensitivity to oxygen. It is the reason that on initial stages of degradation AS changes slightly. To measure the depletion of semiconductor volume by selenium vacancies and

reduction their concentration on surface for account recombination with oxygen ions is observed the reduction of centres connected with them. Thus, the adsorption form of oxygen changes, and main by donors condition is the level 0,3 eV. The increase of concentration of interstitial cadmium on surface happens for account of diffusion of Cd value of diffusion factor at which below than at selenium vacancies. The reduction of binding energy with surface of material as a result of change in nature of adsorption centres is main reason for reduction AS in due course.

The long stay of CdSe layers at temperatures 453 K in oxygen atmosphere results in irreversible changes of semiconductor structures. Initial films mixed the phase structure with prevalence of cubic improvement. Degradation process observes the increase of share of hexagonal phase for account temperature recrystallisation. The structural changes are accompanied by reduction of number in main of donors conditions that causes the changes of AS.

After stay of 1000 hours in oxygen atmosphere the layers CdSe are covered by CdO films which has higher conductivity than the initial layers. It results in shunting high-resistance crystallites and in growth of conductivity. The reduction of crystalline mass of CdSe is observed. It takes place as a result of reaction:



That is, interaction CdSe with oxygen is finalized by formation cadmium oxide. Thus, usage of cadmium selenide films under increased temperatures for registration of oxygen in area of macroconcentration is not expedient one. It is necessary to note that the formed CdO layers have sensitivity to oxygen, though the value of such sensitivity much more less. However, the stabilization of parameters of semiconductor on time (fig. 1, curve 2).

The observed material shows that degradation of AS is connected with physical and chemical processes in which as the surface of semiconductor as its volume are involved. The received data force to think that diffusion of positive donors from volumes on surface is main process responsible for change AS on initial stages. The intensity of diffusion processes is sharp and increases with growth of measurement temperature. Therefore, to reduce degradation, AS follows to use the low temperatures for measurements at which the processes of diffusion proceed slowly. It is necessary also to accept the measures for reductions of number of metalloid vacancies. However, the fall AS to oxygen is thus observed also. As at the end the use of metal oxides for oxygen registration, transformation in oxide takes place expediently which do not observe the change of chemical formula during finding in oxygen atmosphere, and the change of structure and layer structures only happens. The decision of this task is possible at surface doping by metal atoms which enable to create the new adsorption centres of oxygen and binding energy E is thus minimum. There-

fore it was possible to receive the high-sensitive layers at low measurement temperatures.

We was undertake the approach to define the best type of additive for reception of best stability AS. The samples thin films of zinc oxide received by method of plasma sputtering of metal in argon and oxygen atmosphere and surface doping by atoms Ag, Cd, In, Sn, Pb, Bi were investigated. Table submits the results of measurements of sensitivity β and drift conduction in zero gas Δ for concentration 6,7 vol. % of oxygen.

Table

Quantities of adsorption sensitivity and drift of electrical conductivity of the samples with heavy metal atoms on the surface

Doping atoms	$-\beta$, rel. units/vol. %	Δ , rel. units/hour
Ag	0,12	-0,6
Cd	0,15	-0,2
In	0,23	+0,03
Sn	0,19	-0,21
Sb	0,07	-0,13

The value Δ for samples by doping atoms of indium is positive. In difference from the observable changes of conductivity in part of reduction in area of value $N_s = 10^{14} \text{ cm}^{-2}$ the samples had the positive character of conductivity drift in zero gas. In fig. 2

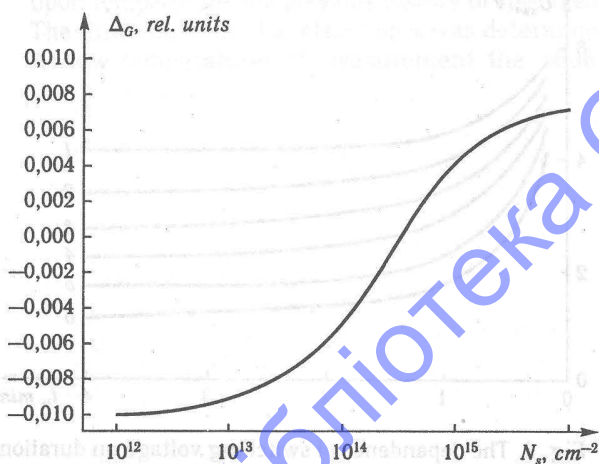


Fig. 2. Dependence of drift of electrical conductivity from the doping degree of surface by indium's atoms the dependence Δ_G from doping degree by atoms of indium is submitted. As it is seen for the given

conditions of measurements in areas of $N_s = 10^{14} \dots 10^{16} \text{ cm}^{-2}$ the drift had practically the zero value.

As it has been shown by electron microscopic research of films, there were clusters of metal atoms at surface. The availability of clusters is the necessary condition for high sensitivity to gas. During the long operation the disappearance of cluster structure on surface of semiconductor takes place initially.

As it is known, contact of metal surface with oxygen is accompanied by its oxidation. The clusters formation on semiconductor surface, at their surface doped by metal atoms results in growth of adsorption ability and AS to oxygen. But there are observed the changes of forms and sizes of clusters at finding in oxygen to environment. As the given structural analysis shows, the growth in layer of indium oxide is observed. And than more time 1000 hours the contact of semiconductor located at temperature 353 K with oxygen in area of concentration large 20,3 vol. %, the speed of growth of oxide film. It is interesting to note that the conductivity of phase indium oxide appears more higher than conductivity of matrix. The oxidation of indium's clusters in this area of temperature proceed extraordinarily slow [5]. Therefore swelling of clusters at oxidation should result in partial, and on late stages to total merge of clusters structures. Results in formation of conductivity channels on surfaces of material and growth of conductivity in time.

At optimum degrees, the action of oxygen will be compensated by increase of conductivity at growth of clusters. It is thus possible equalisation of speeds of increase and reduction of conductivity under adsorption of oxygen. The resource of work for such sensors is defined by operating modes and constitutes the some thousands of hours at temperatures to 353 K.

References

1. Göpel W. Metal oxide sensors // New Devices. — Weinheim, Germany, 1996. — 285 p.
2. Waschpanow Yu. A Die Empfindlichkeit des elektrischen Leitwert der Halbleiterdünnschichten zum Sauerstoff // Festkörperlchemie komplexer oxidischer Systeme. — Greifswald, Germany, 1990. — S. 170—180.
3. Physical quantities. The manual / Ed. I. S. Grigorjev. — Moscow, 1991. — 1232 p.
4. Waschpanow Yu. A. Eigenschaften realer Oberflächen dünner CdSe Schichten dotiert mit Indium // Physik der Halbleiteroberfläche. — Berlin, Germany, 1989. — Vol. 20. — S. 69—74.
5. Fendler J. H. Nanoparticles and Nanostructures // Characterisation and Applications. — Chichester, USA, 1998. — 400 p.

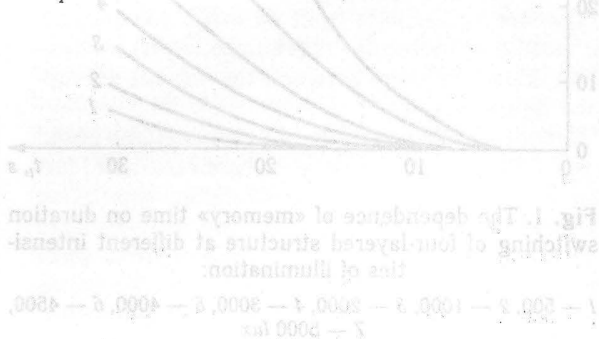


Fig. 1. The dependence of 'memory' time on duration switching of low-layer structure at different intensities of illumination.

PHOTOSENSORS WITH Si—GaAs HETEROJUNCTION AS MEMORY ELEMENTS

The photosensors with non-ideal heterojunction, prepared by special technique, have property of anode voltage independent accumulation and memory. The regularity of structure switching was found in dependence on intensity and duration of light signal. The mechanism of memory effects is proposed. The possibility of creating of energy independent memory devices is shown.

In this paper the realization of possibility creation $p^+(Si)-n(Si)-p(Si)-n^+(GaAs)$ photohetero-thyristors with memory effect is presented. The principle of operation of these devices allows to exclude negative influence of defects on interface of heterojunction and even to use them [1].

The structures of the devices were made on the base of n -Si substrates. On one side of n -Si wafer with the help of diffusion method a homojunction was produced. On the other side the GaAs layer was grown with the help of LPE method by special technology. Additional $n(Si)-p(Si)$ homojunction was formed during the epitaxy process.

Current voltage characteristic of grown structures with region of negative differential resistance was able to vary under action of light impulse [2]. During the illumination of the structure, the switching voltage reduced. Independently on the anode voltage such feature of current voltage characteristics was kept some time at darkness after the light signal was switched off.

Every next switching of this structure occurred at voltage smaller then the first switching voltage at darkness. Such ability of the device was preserved certain time dependent on duration of preliminary illumination. On fig. 1 the curves verifying this de-

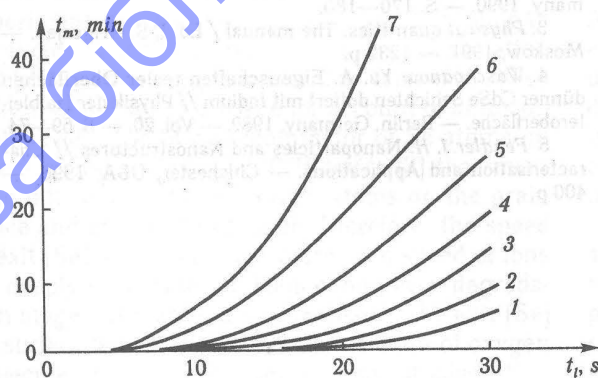


Fig. 1. The dependence of «memory» time on duration switching of four-layered structure at different intensities of illumination:

1 — 500, 2 — 1000, 3 — 2000, 4 — 3000, 5 — 4000, 6 — 4500, 7 — 5000 lux

pendence are shown. The regularity of a course of curves is that with increase in time of structure illumination the time of U_1 switching voltage relaxation increased. The change of light intensity from 500 up to 5000 lux results in increase of storage time.

It was established, that the voltage of dark switching decreases with increase of time and intensity for preliminary illumination of photohetero-thyristors (fig. 2). Therefore, the laws of dark switching voltage recovery versus time and intensity of illumination coincide qualitatively.

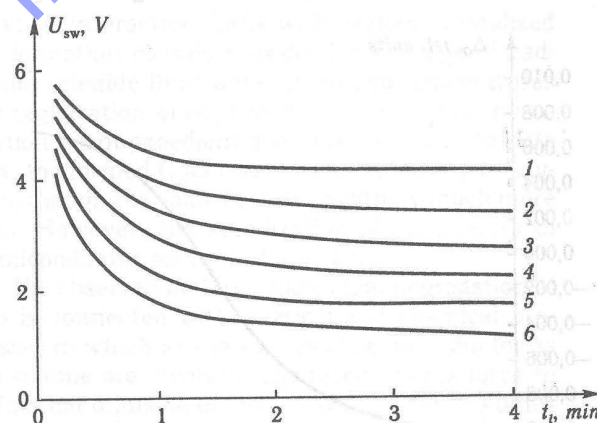


Fig. 2. The dependence of switching voltage on duration of illumination at different intensities of lighting:

1 — 500, 2 — 1000, 3 — 2000, 4 — 3000, 5 — 4000, 6 — 5000 lux

The memory ability was estimated by drift of the switching voltage U_{sw} after lighting the sample at different temperatures and without voltage during operation of a light signal. The drift of voltage U_{sw} at zero shifts in the course of lighting was investigated in the interval of temperatures 253...303 K. At lower temperatures the switching voltage shifts to the area of large voltage where measurements are difficult.

Dark switching voltage was determined at each stated temperature from a current—voltage characteristics. After that the sample was lighting during 3 minutes (maximum illumination). During this time current—voltage characteristics of structure wa:

measured several times and the drift of switching voltage (fig. 3) was observed. After the light was

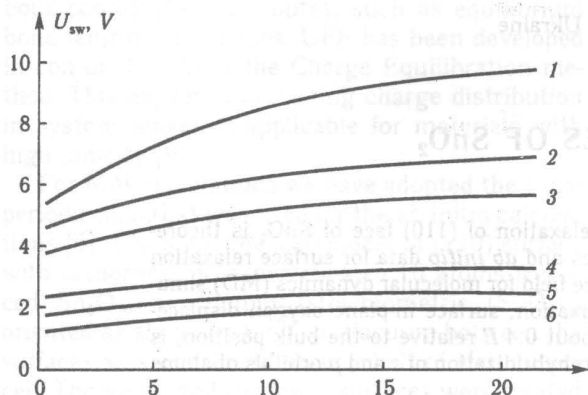


Fig. 3. Drift of switching voltage after the illumination of structure for different temperatures:

1 — 253, 2 — 263, 3 — 273, 4 — 283, 5 — 293, 6 — 303 K

switched off, the voltage U_{sw} was less, than before illumination. However, in the course of time it increased up to large values. It was established that at low temperatures (fig. 3) relaxation U_{sw} was longer, than at high temperature. Full relaxation of switching voltage for different specimens occurred 24 hours to several month. The researches carried out allows to establish the dependence of temporary drift U_{sw} upon temperature and previous history of specimens. The time constant of a relaxation τ was determined. At low temperatures of measurement the value τ

changes from 2 up to 4 min correspondingly and at higher heats (283...303 K) a time constant $\tau = 5$ min.

All observable effects can be stipulated by fact that after switching off $p-n-p-n$ of structure the charge of exuberant carriers in bases does not disappeared completely. There is a non-equilibrium charge, which is less than threshold charge, necessary for switching, but which makes easy the switching of the device by a next impulse.

The effect of storage, which photoheterothyrists have, can be connected with trap centres with a large relaxation time. In our case such centers are the broken off bounds, which are formed by mismatch dislocations in a boundary layer of heterojunction. The concentration of trap centres amounted $N = 2,5 \cdot 10^{14} \text{ cm}^{-2}$. The memory effect is grounded on the change of a charge condition of trap centres under action of incident light. The similar effects were observed in heterostructures on the basis of other «nonideal» heterojunctions, for example, ZnTe—ZnSe.

The ability of photoheterothyrists to accumulate and to store the information allows to create on their base highly sensitive memory devices, independent of voltage.

References

1. Vasilenko N. D., Terletskaya L. L. // Optoelectronics and semiconductors technique. — 1991. — V. 21. — P. 28—40.
2. Terletskaya L. L., Skobeleva V. M. // Proceeding of the Workshop «Sensors Springtime in Odessa». — 29—30 May, 1998. — Odessa, 1998. — P. 84.



Fig. 1. Crystal structure of the material of ZnO.

...the present study we examine the relaxation of surface atoms. This is coupled with calculation of force field, as many details of potential functions are hybridization dependent. We employ the Universal force field (UFF) which is suitable for our purposes. It is a general purpose force field that has been parametrized from a set of rules based on element hybridization and connectivity.

...the present study by comparing with the experimental data, we search for the best fitting Universal force field (UFF) of range of all [2], where hybridization is explicitly assigned to the atoms. Such comparison of the data from our calculations and results of molecular mechanics (MM) minimization allows to judge between the various proposed hybridizations. A more detailed analysis of hybridizations based on our ab initio electronic structure results [3] has been included here, too. The Mulliken population analysis of LCAO electronic structure has been used to project molecular or crystal one-electron wave functions onto atomic orbitals, which were used as the basis set. Together with the energy eigenvalues,

¹ Odessa I. I. Mechnikov National University, Odessa, Ukraine² University of Oulu, Oulu, FinlandREHYBRIDIZATION AT (110) FACES OF SnO₂

Rehybridization of surface atoms and relaxation of (110) face of SnO₂ is theoretically examined. Using molecular mechanics and *ab initio* data for surface relaxation we choose the best hybridization related force field for molecular dynamics (MD) simulations. The most prominent feature of relaxation, surface in-plane oxygen displacement of the reduced surface outwards of about 0.4 Å relative to the bulk position, is analyzed in details. This is done in terms of rehybridization of *s* and *p* orbitals of atoms at reduced surface of SnO₂.

1. Introduction

Tin dioxide (SnO₂) is a wide-gap semiconductor with applications as gas sensor material and catalyst. The structure and electronic properties of its surface have been experimentally studied in detail [1, 2]. Also theoretical investigations of oxide surfaces based on an accurate first-principles calculations have been carried out [3–6]. Such approaches allow to create the atomistic picture of sensing mechanisms and methods to prognosticate gas response properties of the semiconducting materials.

However, *ab initio* calculations of SnO₂ (110) face based on utilizing the different computational methods reveal diversity of bare surface relaxation data [3–6]. Therefore, calculations based on different methods are welcome to establish reliable structure of relaxed SnO₂ (110) atomic plane and to understand the related differences in rehybridization occurring at stoichiometric and reduced surfaces.

Recently, we have investigated the structure of (110) face of rutile structure SnO₂ (cassiterite) with *ab initio* — DFT calculations, the local-density approximation (LDA) and the generalized-gradient approximation (GGA) [5]. There are also semi-empirical approaches available for surface relaxation and electronic structure of (110) face of SnO₂ to compare with [10].

In the present study, by comparing with the *ab initio* data, we search for the best fitting Universal force field (UFF) of Rappe et al. [8], where hybridization is explicitly assigned to the atoms. Such comparison of the data from *ab initio* calculations and results of molecular mechanics (MM) minimization allows to judge between the various presupposed hybridizations.

A more detailed analysis of hybridizations based on our *ab initio* electronic structure results [5] has been included here, too. The Mulliken population analysis of LCAO electronic structure has been used to project molecular or crystal one-electron wave functions onto atomic orbitals, which were used as the basis set. Together with the energy eigenvalues,

this defines the hybridization of original atomic orbitals and also reveals the remaining lone pair electrons.

2. Slab Model and Computational Method

The rutile structure of SnO₂ is 6 : 3 coordinated and Sn⁴⁺ ions in the structure are centered in slightly distorted oxygen octahedron. (110) layers of the structure consist of neutral groups of three parallel planes O—Sn₂O₂—O and the cleavage cut between these groups of planes breaks the least number of cation–anion bonds. This results in (110) stoichiometric face, which is the most dominant surface of the SnO₂ material. Removal of the surfacemost bridging oxygen layer of stoichiometric surface results in the reduced (110) surface, see fig. 1, *a*.

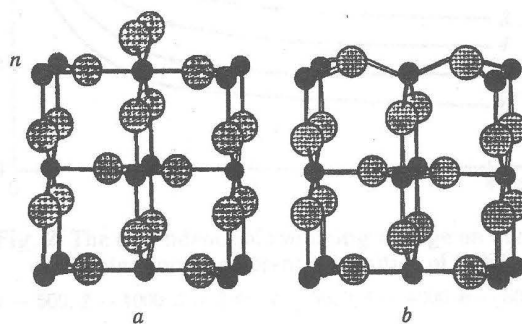


Fig. 1. Orthorhombic supercell of the slab model of SnO₂ (110) surface:

a — for stoichiometric surface (upper) with bridging oxygens and reduced surface (lower), *b* — a schematic drawing of relaxations at the reduced surface

In the present study we examine the rehybridization of surface atoms. This is coupled with consideration of force field, as many details of potential functions are hybridization dependent. We employ the Universal force field (UFF) which is suitable for our purposes. It is a general purpose force field that has been parametrized from a set of rules based on element, hybridization and connectivity.

UFF has been carefully validated for many structure types. In UFF the hybridization is explicitly assigned to the atoms, defining the nearest neighbour coordination attributes, such as equilibrium bond lengths and angles. UFF has been developed in conjunction with the Charge Equilibration method. This approach predicting charge distribution in system makes it applicable for materials with high ionicity [9].

For MM calculations we have adopted the same periodic slab that was used for the *ab initio* calculations [5]. We adopt the slab model of (110) surface with orthorhombic supercell with 16 atoms (reduced, Sn_6O_{10}) or 18 atoms (stoichiometric, $(\text{SnO}_2)_6$) oriented as shown in fig. 1, *a*. Vacuum between the surfaces was chosen to occupy half of slab supercell. The upper and the lower surfaces were treated identically.

3. Results and Discussion

Total energy minimization of the bulk SnO_2 using *ab initio* calculations and starting from the experimental lattice constants with LCAO method leads to about 2% expansion, whereas the expansion with PWPP is somewhat less [5]. We were able to find a force field for molecular mechanics calculations that exhibited negligible shrinking of lattice constants (0.001%), table 1. These bulk relaxed structures were used as reference to surface relaxation.

Table 1
Bulk relaxation of cassiterite, SnO_2

	Experimental	LCAO	PWPP	PWPP [3]	MM
<i>a</i>	4,737	4,832	4,730	4,637	4,721
<i>c</i>	3,186	3,266	3,212	3,060	3,185
<i>u</i>	0,307	0,307	0,306	0,307	0,307

The bonding between atoms in SnO_2 has a relatively strong ionic character. At stoichiometric surface, tin atoms appear also to be fivefold coordinated with less ionic character. Removal of the bridging oxygen changes the coordination of tin atoms from sixfold to fourfold, which in turn, change ionic character of bonding. Reduction of the surface leads to rehybridization of surface tin atoms and oxygen atoms that couples to surface reconstruction or relaxation. Establishing the correct electronic structure of reduced and stoichiometric SnO_2 surfaces is important for the further investigations of adsorption/desorption and catalytic properties connected with construction of adsorbate-surface site conformations and understanding of the different reaction paths at tin oxide surfaces.

The most prominent feature of surface relaxation confirmed by two different *ab initio* methods is outward displacement of in-plane oxygen of 0,4 *E* relative to perfect-lattice (or truncated bulk) positions. On one hand, such surface deformation at reduced surface may be connected with rehybridization of

in-plane oxygen environment. On the other hand, strong outward displacement of in-plane oxygen not connected directly with rehybridization of Sn and/or O surface ions may be attributed to the changes in electrostatic interactions between atoms, coupled with changes in the ionicity of surface bonding.

Possible rehybridizations at the (110) surface of SnO_2 , leading to the outward displacement of in-plane oxygen ions, may be assigned to subbridging tin atoms, in-plane oxygen itself, or both of those at the same time.

Most of surface Sn^{4+} ions usually have the octahedral valence state of hybrid sp^3d^2 orbitals. At fully oxidized surface Sn^{4+} ions carry two oxygen monodentately coordinated on it. If these oxygens are eliminated then the cations becomes four-coordinated. This arrangement is energetically less favorable owing to the relatively high degree of coordinate unsaturation of the cation and could lead to the surface reconstruction. The possible mechanism of the reconstruction is the change in rehybridization of cation into some inactive form, for example, into distorted sp^3 . Usually [10, 11], the surface reconstruction resulted in such rehybridization displaces the superficial cations down and causes oxygen raise above the surface plane (fig. 1, *b*).

Another possible reason for the relaxation leading to the outward displacement of in-plane oxygen atoms at reduced surface is rehybridization of in-plane oxygen from bulk configuration, which is sp^2 plus non-bonding, lone-electron pair. At reduced surface, oxygen atoms are in effort to lower their electronic energies, attempt to move out from surface into more tetrahedral sp^3 configuration.

It would be noted, that change in coordination of subbridging tin from sixfold to fourfold at reduced surface, generates unsaturated dangling bonds, making rehybridization highly probable. In-plane oxygen at reduced surface remains three-fold coordinated and its rehybridization can take place only if it is energetically more favorable.

The surface geometry of SnO_2 (110) face from *ab initio* calculations and molecular mechanics (MM) minimization with various hybridizations is shown in table 2. For reduced surface both octahedrally and tetrahedrally hybridized tin and oxygen are considered. For stoichiometric surface octahedrally hybridized tin leads to a better description of relaxation. According to previous predictions [10, 11] tetrahedral hybridization of subbridging tin atoms at reduced surface is accompanied by outward displacement of in-plane oxygens. At the same time, subbridging tin atoms move down significantly, that displays main difference between the MM calculations and *ab initio* results, where an outward displacement is found, instead. Such strong difference between MM and *ab initio* results makes this choice of FF rather unreliable.

As it follows from MM calculations (table 2), assignment of tetrahedral hybridization to in-plane oxygen ions is not enough to provide an outward displacement of 0,4 *E*.

Table 2
Vertical displacements of the surface atoms from their original «bulk cut» lattice sites (in E) from the *ab initio* calculations (LCAO and PWPP) and molecular mechanics (zero temperature molecular dynamics). Tin is considered in octahedral and tetrahedral, and oxygen in trigonal and tetrahedral hybridizations

	LCAO (GGA) [5]	PWPP (GGA) [5]	Sn-oct O-tri	Sn-oct O-tet	Sn-tet O-tri	Sn-tet O-tet
Stoichiometric						
Bridging tin (6 fold)	+0,13	+0,21	+0,043	+0,033		
Bridging oxygen	+0,05	+0,13	-0,038	-0,050		
In-plane oxygen	+0,18	+0,22	+0,100	+0,124		
Reduced						
Bridging tin (4 fold)	+0,14	+0,20	-0,125	-0,147	-0,26	-0,33
In-plane oxygen	+0,39	+0,49	+0,034	+0,073	+0,38	+0,50

Moreover, minimization of flexible outermost surface layer of (110) SnO_2 face, consisted of local environment of superficial Sn and O ions, reveals antisymmetrical (110) surface for oxygen in tetrahedral state (fig. 2, *b*), and makes this setting less

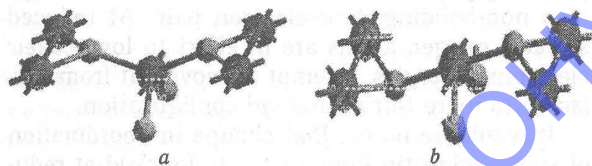


Fig. 2. Model of the outermost surface layer of (110) SnO_2 face for the hybridization states:

a — Sn-tet + O-tri, *b* — Sn-oct + O-tet

probable. The surface symmetry was restored, however, for more rigid slab model (fig. 1, *b*). Nevertheless, applying the tetrahedral hybridization for tin and oxygen surface atoms leads to increase of slab total energy (table 3), which demonstrates that such

Table 3
Comparison of the total energies of stoichiometric and reduced slabs with different hybridizations

	Sn-oct O-tri	Sn-oct O-tet	Sn-tet O-tri	Sn-tet O-tet
Reduced	-151,12	-153,11	-165,15	-166,38

choice is energetically less favorable. Such results are also in good agreement with [10], where it was concluded that oxygen atoms cannot fully rehybridize, because of the large local strain field (i. e., the large energy cost associated with significant accompanying changes in bond lengths).

Mulliken population analysis of LCAO electronic structure gives information on rehybridization at

tin oxide surface directly. Computed energy levels from the stoichiometric and reduced surfaces of reduced, Sn_6O_{10} or stoichiometric, $(\text{SnO}_2)_6$ slabs are presented in fig. 3.

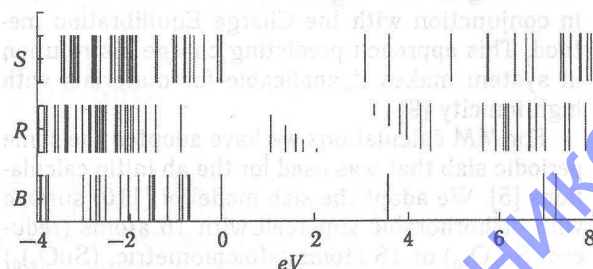


Fig. 3. Computed LCAO one-electron levels for:

S — stoichiometric $(\text{SnO}_2)_6$ surfaces, *R* — reduced, Sn_6O_{10} surfaces, *B* — for the bulk. A scissor operator of 2,2 eV has been applied to make band gap close to its bulk value. The fractional occupation numbers in the case of reduced surface are illustrated by the barlength. For bulk and stoichiometric cases, VBM is adjusted to 0 eV and for reduced case it is adjusted to fit the bands in ref. 5b

Mulliken population analysis performed for stoichiometric and reduced surfaces of SnO_2 displays presence of lone-electron pair at in-plane oxygen atoms in both surface states (fig. 3) indicating that these ions remain in trigonal hybridization state — sp^2 plus a non-bonding, lone-electron pair. Such conclusion is in agreement with results of our MM calculations.

At stoichiometric surface *d*-orbitals are involved in the bonding of subbridging tin ions, supporting conclusion made from MM calculations about the octahedral valence state of the hybrid sp^3d^2 orbitals. It is extremely significant that *d*-orbitals are still involved in the bonding of subbridging tin atoms at the reduced surface. Such results exclude capability for tetrahedral sp^3 state of the superficial tin orbitals and also go along with data of MM calculations. Participation of *d*-orbitals in the bonding of subbridging tin atoms allows to assume, for instance, the distorted trigonal bipyramidal sp^3d hybridization state for such cations, where $5s-5p$ hybrid lone pair occupying stereochemical position on the vacuum side of ions.

P. A. Cox et al [12] has suggested that, after removal of bridging oxygen atoms at (110) face, two electrons remains at subbridging tin making it Sn^{2+} . The defect states near valence-band maximum (VBM) are due to rehybridization of Sn $5s-5p$ states at reduced Sn^{2+} sites adjacent to oxygen vacancies or in local SnO -like environments at surface. An alternative suggestion explaining appearance of Sn^{2+} -like ions is that the inert pair of $5s$ electrons occupies the apex of tetragonal pyramid, as it takes place in tetragonal SnO structure.

Mulliken population analysis performed on SnO_2 structure allowed to attribute an occupied electron energy levels related to subbridging tin ions with $5s-5p$ hybrid lone pair located near the VBM ($-4,33$ eV), fig. 3. Removal of bridging oxygen atoms

results in strong dispersion at VBM, which has four-fold tin 5s and 5p character. These levels do not relate to the bonds to the neighbouring in-plane oxygen atoms, however. Thus, these are loosely bound electrons from bridging oxygen vacancies, the levels which are experimentally seen in band gap [12].

Mulliken population analysis allows one to understand the ionic character of the bonding in crystal. Localized orbitals may be constructed from hybrids on both Sn and O and these overlap, forming occupied bonding and unoccupied antibonding orbitals. Because of the very different electronegativities of Sn and O, the bonding orbitals are concentrated on O atoms and antibonding — on Sn. The ionic crystal can be, therefore, regarded as the case where bonding and antibonding orbitals become completely localized on oxygen and metal, respectively. It was found, that at the reduced surface the bonding orbitals related to subbridging tin atoms were localized on the metal ions rather than on oxygens, displaying covalent character of the bonding for such tin atoms. This is in agreement with well-known covalent character of the bonding in SnO crystal.

The results of the *ab initio* and MM calculations indicate that two electrons left behind after removal of bridging oxygen ions occupy orbitals (a mixture of 5s and 5p) on surface Sn ions, converting them to Sn^{2+} [12, 13] and abnormal stereochemistry with inert electron pair at reduced surface of SnO_2 is due to this s-p hybridizations. Therefore observed strong outward displacement of in-plane oxygen ions cannot be connected directly with tetrahedral rehybridization neither superficial tin or oxygen atoms and may be attributed to the changes in electrostatic interactions between atoms, coupled with changes in the ionicity of surface bonding.

As it has been mentioned SnO_2 must be regarded as essentially ionic crystal. On the other hand, appearance of Sn^{2+} atoms at reduced surface of SnO_2 changes the character of the bonding to the essentially covalent. Therefore, bond between subbridging tin and in-plane oxygen became weaker at reduced SnO_2 surface. Atomic configuration of the surface is determined by superposition of stretching surface bondings and repulsion electrostatic interaction with neighbouring oxygen atoms. Weakening of the superficial Sn—O bonding, due to the reduction of tin ions from Sn^{4+} to Sn^{2+} leads to the domination of electrostatic repulsion interaction and results in the observed outward displacement of in-plane oxygen atoms.

4. Conclusion

Relaxation of (110) surface of SnO_2 occurs essentially in the perpendicular direction, only. In-plane relaxation is negligible. Symmetry breaking reconstruction was found only in case where the in-plane oxygen has been allowed to rehybridize. The most prominent feature is the surface layer anion relaxation outwards with respect to their bulk positions at the reduced surface. This appears to be strong at the reduced surface, about 0.4 E. The mechanism responsible for such relaxation is supposed to be rehybridization of the subbridging tin cation from octahedral to tetrahedral state. Some arguments were found to assume that in-plane oxygen remains in trigonal hybridization state.

References

1. Henrich V. A., Cox P. A. The Surface Science of Metal Oxides. — Cambridge: University Press, 1994. — P. 432.
2. Egdell R. G. The Science of Ceramics Interfaces II // Ed. J. Nowotny. — N. Y.: Elsevier, 1994. — P. 527.
3. Manassidis I., Gillan M. J. First-principles study of SnO_2 (110) // Surf. Rev. and Lett. — 1994. — V. 1, № 4. — P. 491—494.
4. Manassidis I., Goniakowski J., Kantorovich L. N., Gillan M. J. The structure of the stoichiometric and reduced SnO_2 surface // Surf. Sci. — 1995. — 339, 258. — P. 381—394.
5. Rantala T. T., Rantala T. S., Lantto V. Surface relaxation of the (110) face of rutile SnO_2 // Surf. Sci. — 1999. — 420. — P. 103—109; Rantala T. T., Rantala T. S., Lantto V. Electronic structure of SnO_2 (110) surface // Materials Science in Semiconductor Processing, in print.
6. Goniakowski J., Gillan M. J. The adsorption of H_2O on TiO_2 and SnO_2 (110) studied by first-principles calculations // Surf. Sci. — 1996. — 350. — P. 145—158.
7. Prutton M. Surface physics. — London: Oxford Univ. press, 1975. — P. 245.
8. Rappe A. K., Casewit C. J., Colwell K. S., Goddard W. A. III, Skiff W. M. UFF, a full periodic table force field for molecular mechanics and molecular dynamics simulation // J. Am., Chem. Soc. — 1992. — 114. — P. 10024—10035.
9. Rappe A. K., Goddard W. A. III. Charge equilibration for molecular dynamics simulations // J. Phys. Chem. — 1991. — 95. — P. 3358—3363.
10. Godin T. J., LaFemina J. P. Surface atomic and electronic structure of cassiterite SnO_2 (110) // Phys. Rev. B. — 1993. — V. 47, № 11. — P. 6518—6523.
11. Egashira M., Nakashima M., Kawasumi S. Temperature programmed desorption study of water adsorbed on metal oxides. 2. Tin oxide surfaces // J. Phys. Chem. — 1981. — 85. — P. 4125—4130.
12. Cox D. F., Fryberger T. B., Semancik S. Oxygen vacancies and defect electronic states on the $\text{SnO}_2(110)-1 \times 1$ surface // Phys. Rev. B. — 1988. — V. 38, № 3. — P. 2072—2083.
13. Rantala T. T. *Ab initio* studies of compound semiconductor surfaces in Computational Studies of New Materials / Ed. D. A. Jelski and T. F. George. — Singapore: World Scientific, 1999. — P. 6—26.

INTERACTION OF PARAMETERS IN DEGRADATION OF OPTOELECTRONIC DEVICES AS INTERACTION OF PARAMETERS IN COMPOSITE SYSTEM

The interaction of parameters in degradation of optoelectronic devices is considered from the viewpoint of parameter's interaction in composite system.

1. Introduction

It is known, that the formalized mathematical exposition of any management system includes such concepts, as controllable quantities, assigning and control actions, errors (deflections in real values of parameters of controllable quantities from their assigning actions) and others.

In this paper we picked optoelectronic devices (OED) — light emitting diodes, photodetectors, optocouplers, lasers as an object of control (OC), and indexes of their degradation (see tab. 1 and [1]) as controllable quantities. The assigning action — are norms (reference values) for the controllable quantities of a degradation of OED, given by regulating documents. The spectator (experimenter) inspects current values of controllable quantities and compares them with reference values; as a result of this the errors are fixed. The signs and values of these errors are parsed and the relevant guidelines on their elimination are made. If it is necessary to do the corrective actions of controllable quantities, the controlling system — the subject of control (SC) ensures the relevant requirements for its embodying.

The phenomenon of a degradation of OED we characterise as a composite system (fig. 1), therefore, we investigate the interaction of parameters in degradation of OED from a position orderliness and integrity of composite systems.

The composite systems are represented as systems satisfying to the logic requirement, which combines the different aspects in complexity of their operation (multifunctionality of application, hierarchy of structure, diversity of component, embodying of subsystems on different physical principles, complexity of control and decision making). The special attention is given to examination of the plan for the compendancy of a composite system and to definition of force of interaction between subsystems.

The expedient for integrating of subsystems in a single unit determines streams of the information, and, therefore, forces of action for one subsystem on another. The forces of interaction between system components and between levels of hierarchy determine complexity of a system. This concept in the literature [2, 3] is named, as the plan of interaction

of subsystems or a plan for compendancy and it is one of the important characteristics of the composite system.

Table 1

Degradation of OED as the object of control (OC) and system indexes of a degradation

Groups of system indexes	Component of indexes of groups
Controllable quantities (indexes of a degradation)	<ol style="list-style-type: none"> 1. Radiation intensity of the light-emitting device. 2. Electrical indexes: <ol style="list-style-type: none"> 2.1. Reverse current of a photodetector; 2.2. Threshold current of the laser. 3. Quantum yield: <ol style="list-style-type: none"> 3.1. Photometer parameters of a light-emitter: <ol style="list-style-type: none"> 3.1.1. Light intensity; 3.1.2. Radiation power. 3.2. Responsibility of a photodetector. 4. Detectability of photodetector.
Exterior perturbations	<ol style="list-style-type: none"> 1. Temperature condition: <ol style="list-style-type: none"> 1.1. Storage without feeding an electrical displacement; 1.2. Storage without an exposure; 1.3. Temperature mode of trials and operation. 2. Direct voltage on p-n-junction of a light-emitter. 3. Mechanical indexes (vibrating strength, shock strength, action of pressure). 4. Action of light radiations. 5. Stability to moisture. 6. Action of gas mediums. 7. Action of magnetic fields.
Interior perturbations (attributes of OED)	<ol style="list-style-type: none"> 1. Constructive: <ol style="list-style-type: none"> 1.1. Geometrical sizes; 1.2. Shape. 2. Physical and chemical indexes. 3. Physical and technological: <ol style="list-style-type: none"> 3.1. Impurity concentration and duration of their diffusion; 3.2. Parameters of host materials (semiconductor) 4. Electrical and electromechanical: <ol style="list-style-type: none"> 4.1. Resistance and electric capacity of p-n-junction; 4.2. Shorting voltage; 4.3. Amplification factor.
Control actions	<ol style="list-style-type: none"> 1. Provision of regulating requirements in technical operation of OED. 2. Monitoring of controllable quantities 3. Generation of control actions by SC

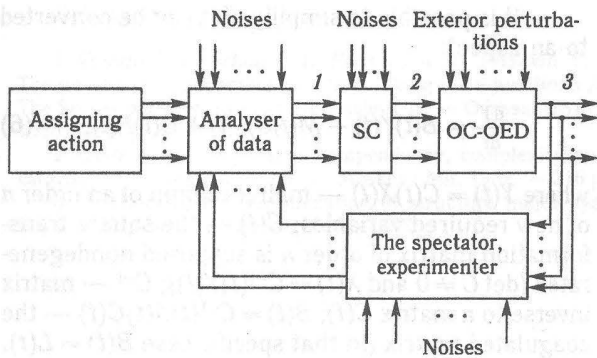


Fig. 1. Functional diagram for experiment to examine a degradation of OED:

OED — optoelectronic device; OC and SC — object of control and subject of control; 1 — error (diversion of controllable quantities); 2 — control actions; 3 — controllable quantities (indexes of a degradation of OED)

Let's reduce some mathematical research techniques for interaction of subsystems of composite systems.

2. The set-theoretical means

It is initially obvious, that it is necessary to apply mathematical methods to examine the information aspects in interaction of subsystems of composite systems, operating sets of interacting connections. The conspicuity of this fact consists that the essence of the set-theoretic means makes concept a mathematical set, and in turn concept «set» rather frequently by many authors is identified with determination «a composite system». However, it is the narrow explanation of the concept for composite system: it does not take into account a general purposes for performance of the system, correlations of subsystems, velocity of process flow (different time scales), qualitative modification for properties of the system as a whole, hierarchy of structure, information complexity etc. the filling the mathematical concept «set» by the axioms of composite systems is possible only partially, for example, by introduction to it of particular structure of a geometrical or algebraic aspect. The similar set with particular interactions (number and character of operations above them) is termed as space.

We have applied expert methods to join the elements of a set in a subset.

If $M(\Psi_A S, \Psi_B S)$ is a symmetric measure for connection of an order a between subsystems $\Psi_A S$ and $\Psi_B S$ from a system S , then it is equal to number a , which is considered retrieved, in other words: the subsystems $\Psi_A S$ and $\Psi_B S$ are linked by a function for coupling f^a of an order a — $\Psi_A S f^a \Psi_B S$, if $M(\Psi_A S, \Psi_B S) = a$. For an arbitrary relation $\Psi_A S f_2^a \Psi_B S$ and $\forall \Psi_C S \in S$ should be satisfied condition: if $\Psi_A S f^a \Psi_C S$, then $\Psi_C S f^a \Psi_B S$. The assertion: system S , which consists of subsystems, is termed as linked system by $n > 0$ subsystems of an order a , if for all couples $\Psi_A S$ and $\Psi_B S \in S$ the requirement $\Psi_A S f_i^a \Psi_B S$ is satisfied even at one value

of number i from an interval $1 \leq i \leq n$; otherwise we have the unlinked system of an order a .

The class of compendency of subsystems of an order a from a system S is a set K_s^a , for which the following properties are fulfilled:

- 1) if $\Psi_A S \in K_s^a$ and $\Psi_B S \in K_s^a$, then $\Psi_A S f^a \Psi_B S$;
- 2) if $\Psi_C S \in K_s^a$, then $\Psi_A S \in K_s^a$ such, that the relation $\Psi_A S f^a \Psi_C S$ is not fulfilled.

The class of compendency of a rank j and an order a — $K_{j,s}^a$ is a class of compendency in relation to function f_j^a taking into account a membership $K_{j,s}^a$ to one class or several classes $K_{j+1,s}^a$. Internal links between subsystems $\Psi_A S$ and $\Psi_B S$ and the external links of each of subsystems S_i are termed as contacts. Number of interior contacts in the class $K_j^a \in \Psi_A S \in K_s^a$ we designate as $P(K_s^a)$. If $x(\Psi_A S)$ — number of subsystems, linked by a function of coupling such as f^a with $\Psi_A S$, then the number of exterior contacts of the class of connectivity K_s^a is equal $X(K_s^a) = \sum_A x(\Psi_A S)$.

2. The statistical correlation of indexes for degradation of OED with indexes of exterior and interior actions

The indexes for the degradation of OED (see tab. 1 and fig. 1) are both functions of quality of OED, and of function of exterior and interior actions. In turn quality of OED is determined both by the process engineering of their manufacture, and by host materials for manufacture, i. e. indexes of quality.

Therefore, the degradation of OED we represent by expression:

$$D(d_{ew}) = \Phi[Q(q_{ij}), F(f_{ms})], \quad (1)$$

where Φ — functional, $Q(q_{ij})$ — quality of OED as function for indexes of quality of OED q_{ij} for $\forall i = 1 \dots N, j = 1 \dots J$ (i — number of the group of quality indexes of OED, j — number of quality index of OED in the group, N — number of groups, J — number of quality indexes in the group); $F(f_{ms})$ — function from indexes of exterior and interior actions f_{ms} for $\forall m = 1 \dots M, s = 1 \dots \Gamma$ (m — number of index group for perturbations and attributes, s — number of an index in group, M — number of groups, Γ — number of indexes for exterior and interior perturbations in the group).

On controlled quantities (indexes and characteristics for degradation of OED) are superimposed conditions of an aspect:

$$d_{ew1} \leq d_{ew}^{ms}(q_{ij}, f_{ms}) \leq d_{ew2}, \quad (2)$$

for $\forall e = 1 \dots E, w = 1 \dots W, i = 1 \dots N, j = 1 \dots J, m = 1 \dots M, s = 1 \dots \Gamma$, where d_{ew1} and d_{ew2} — accordingly lower and upper tolerance limits for modification of degradation indexes of OED (e — number for the group of controlling magnitudes, w — number of the index in the group, E — number of groups, W — number of controlling magnitudes in group).

The OED are considered efficient for an index of the degradation, if all indexes d_{ew} are in the regulated boundaries (2); otherwise there is a degradation of OED.

The quantitative assessment of degradation lack of OED we designate by P_{EW}^{MT} — observance probability for all indexes of the inequality (2) at their mutual noncorrelatedness:

$$P_{EW}^{MT} = \prod_{e=1}^E \prod_{w=1}^W \prod_{m=1}^M \prod_{s=1}^S P_{ew}^{ms}, \quad (3)$$

where P_{ew}^{ms} — correspondence probability for the actual value of the index d_{ew}^{ms} to conditions (2) (correspondence for the real values of controlled magnitudes of OED degradation to the required values).

It is obvious, that:

$$P_{ew}^{ms} = \frac{(\Theta - n_{ew}^{ms})}{\Theta}, \quad (4)$$

where Θ — number of operated OED of one type and of one batch; n_{ew}^{ms} — number of degraded OED on the index d_{ew}^{ms} at f_{ms} external actions.

Having defined

$$P_{ew}^{ms} \{d_{ew1} \leq d_{ew}^{ms}(q_{ij}, f_{ms}) \leq d_{ew}\},$$

it is easy to develop a procedure of an estimation for the correlation coupling between indexes of OED degradation.

3. Optimisation of structure of composite systems

The structure of connectivity for a composite system of an aspect $\left(\frac{dX}{dt} = AX\right)$ is determined by a degree in filling of a square matrix A of an order n (presence of elements $a_{ij} \neq 0$ for $i \neq j$ [3]). This plan of the compendancy characterises complexity of processes, happening in a system, however, high order of the matrix A cannot completely determine a system as composite. Even the very major dimension n of the system uniquely does not determine it as composite. For example, in the case of diagonal (canonical) structure $\left(\frac{dY}{dt} = \Lambda Y\right)$ or quasi diagonal $\left(\frac{dZ}{dt} = BZ\right)$ of rarefied structure (there are not a lot of off-diagonal elements $a_{ij} \neq 0$ for $i \neq j$), the system behaviour appears predicted, as the equations, which describe the system, are easily integrated, and the structure is considered as simple.

The forces of interaction between system components and between levels of hierarchy determine complexity of a system. Sometimes interactions can be converted in such a manner that the system becomes simpler.

Determination: the matrix equation of an aspect

$$\frac{dX}{dt} = A(t)X(t) + K(t)U_{IN}(t) + P(t)F(t) \quad (5)$$

— it is possible to simplify, if it can be converted to an aspect:

$$\frac{dY}{dt} = B(t)Y(t) + M(t)U_{IN}(t) + G(t)F(t), \quad (6)$$

where $Y(t) = C(t)X(t)$ — matrix-column of an order n of new required variables; $C(t)$ — the square transformation matrix of order n is supposed nondegenerated ($\det C \neq 0$ and $X(t) = C^{-1}(t)Y(t)$); C^{-1} — matrix inverse to a matrix $C(t)$; $B(t) = C^{-1}(t)A(t)C(t)$ — the coagulated matrix (in that specific case $B(t) = L(t)$, $L(t)$ — diagonal (canonical) matrix); $M(t) = C(t)K(t)$; $G(t) = C(t)P(t)$.

The solution of the task for simplification of structure of composite systems is considered retrieved, if the following problems are defined: a) conditions superimposed on matrixes $A(t)$, $K(t)$ and $P(t)$, which display, whether the simplification of the equation (5) is possible; b) procedure of deriving of a matrix $C(t)$, which allows to reduce the equation (5) in the equivalent form (6); c) an aspect of matrixes $B(t)$, $M(t)$, $G(t)$.

The general view of original transformation matrixes $C(t)$ and $C^{-1}(t)$, and also the simplified (triangular) forms are retrieved in the monograph [3]. Thus, at an algorithmic level it is possible to produce conversions of structures and to calculate correlations between indexes for the degradation of OED. The procedure for determination of such correlations in quantitative calculus is reduced in paper [4].

4. The qualitative correlation regression analysis

The considerable number of correlations in hierarchy of subsystems of composite systems has correlation connection carrying qualitative character. The determination of correlation between qualitative indexes in comparison with quantitatively defined indexes requires additional gains, or generally it is impossible. For the partial solution of this problem we design the methodology of application qualitative correlation and regression of the analysis, which purpose is to determinate the correlation between subsystems of composite systems. The examples for a similar solution of the task in the analysis of the OED degradation are published in papers [5, 6].

5. Conclusions

The uniform approach to the investigation of the phenomena of OED degradation is offered on the basis of the theory for composite systems. Within the framework of this approach it is possible to construct algorithmic model for investigation of interaction between parameters describing the degradation of OED.

References

1. *Vikulin I. M., Irkha V. I., Panfilov M. I., Prisekin V. I.* The nonradiating recombination in emitting $p-n$ -junctions // The Survey paper on an electronic technique. — Odessa: USAC, 1996. — 47 p.
2. *Casti J.* Major systems. compendancy, complexity and catastrophe / Transl. from engl. — Moscow: Mir, 1982. — 216 p.
3. *V. I. Borsch, etc.* Optimization of structure major systems. — K.: Naukova dumka, 2000. — 320 p.

4. *Borsch V. I., Borsch N. I.* Calculation of a cross-coupling between input signals in multicoupling electric circuits, optimum on speed // In proceedings USAC named by A. S. Popov. — Odessa: USAC. — 1971. — Vol. 19. — P. 34—37.
5. *Borsch V. I., Irkha V. I., Makarenko G. V.* The qualitative correlation regression analysis of parameters of optoelectronic devices // Photoelectronics. — 1999. — № 8. — P. 93—95.
6. *Irkha V. I., Makarenko G. V.* Qualitative-correlation model of a degradation of optoelectronic devices // Photoelectronics. — 2000. — № 9. — P. 73—77.

TO THE INVESTIGATION OF THE PROPERTIES OF CUBIC MONOCRYSTALS

The definition of Green's tensor is of the main problems of Solid State physics. The attempts to definite it were made by various authors. Unfortunately the Green's tensor reserved expression for materials with cubic symmetry was not obtained before. It's first carried out a reserved expression of equilibrium equation Green's function of cubic single monocrystal. It has main important significance for the problems of electronic material science.

Most of semiconductor materials used in photoelectrons are the cubic crystals. That is why exact prediction of their properties is very actually. The Green function of the equilibrium equation plays very important role while the properties of these materials are investigated. Therefore the finding of a reserved expression of equilibrium equation Green's function of materials with arbitrary symmetry is an important task. Lifshits and Rozencveig [1] have obtained the Green function reserved expression for hexagonal monocrystal and showed that in case of cubic monocrystal, when the elastic moduli are considered in relation to frame connected to the crystal lattice axes, reserved expression for Green function is not obtained. It is possible to obtain the reserved expression only in case of low anisotropy in this case. In the present paper the way of reserved Green tensor calculation for the basic equation of the elastic theory for a cubic monocrystal is offered. In [2] the method of texture polycrystal properties calculation with known tensor dimension for a case of cubic symmetry crystallites was described on the basis of one pole figure (111). It is based on the elastic properties isotropy of crystallographic plane (111) of cubic crystal and it uses the substitution of effective hexagonal crystallites for polycrystal cubic ones with appropriate properties. We have applied this method to the different cubic monocrystals. The further calculation does not differ from the hexagonal medium Green function calculation.

Let's consider an unlimited cubic monocrystal. Let's connect frame $X'Y'Z'$ with crystallographic axes $[001]$, $[010]$, $[100]$. This crystal has three independent components of elastic moduli tensor, i. e. three not zero diagonal components in frame, in which the axes coincide with the main axes of symmetry of a monocrystal. It is known that crystallographic plane (111) in a cubic monocrystal is isotropic one concerning elastic properties. Let's go from system of coordinates $X'Y'Z'$ to system of coordinates XYZ , connected with the given plane in such a manner that the axis OZ coincides with perpendicular to her, and the axes OX and OY are arbitrary focused in a plane (111) and perpendicular to each other. Having

transformed the components of elastic moduli tensor according to the law of transformation of the fourth rank tensor

$$C_{iklm}^r = \alpha_{ip} \alpha_{kq} \alpha_{lr} \alpha_{ms} C_{pqrs}^k \quad (1)$$

it is possible to obtain five not zero components of elastic moduli tensor in system of coordinates XYZ [1] analogously to the case of hexagonal crystal symmetry

$$\begin{aligned} C_{11} &= C_{11}^k - \frac{1}{2}k, & C_{12} &= C_{12}^k + \frac{1}{6}k, \\ C_{13} &= C_{13}^k + \frac{1}{3}k, & C_{33} &= C_{11}^k - \frac{2}{3}k, \\ C_{44} &= C_{44}^k + \frac{1}{3}k. \end{aligned} \quad (2)$$

α_{ik} — elements of a rotational matrix [3],

$$k = C_{11}^k - C_{12}^k - 2C_{44}^k \quad (3)$$

is an anisotropy index of monocrystal.

Further we will not examine cubic monocrystal with elastic properties C_{iklm}^k but we will examine hexagonal monocrystal with elastic properties C_{iklm}^r . These properties are calculated out of C_{iklm}^k on the basis of (2).

The displacement \vec{u} arisen in the examined medium under influence of force \vec{f} is satisfied with equation system

$$C_{iklm}^r \frac{\partial^2 u_l}{\partial x_k \partial x_m} = -\delta(\vec{r}) \vec{f}_i \quad (4)$$

with boundary data $u_l \rightarrow 0$ if $l \rightarrow \infty$. C_{iklm}^r are the components of cubic medium elastic moduli tensor in the frame XYZ . It is known Green's tensor of equation (4) is a solution of system

$$C_{iklm}^r \frac{\partial^2 G_{lp}}{\partial x_k \partial x_m} = -\delta(\vec{r}) \delta_{ip}.$$

It is possible to decompose δ -function in Furie-integral

$$\delta(\vec{r}) = \frac{1}{(2\pi)^3} \int e^{i\vec{r}\vec{\xi}} d\vec{\xi}. \quad (5)$$

The solution of equation (4) is looked for in the form of Furie-integral too

$$u_l(\vec{r}) = \int v_l(\vec{\xi}) e^{i\vec{r}\vec{\xi}} d\vec{\xi}. \quad (6)$$

Substituting (5) and (6) in (4), we will get the equation system for Fourier-amplitude

$$u_{il}(\vec{\xi})v_l(\vec{\xi}) = f_i, \quad (i = 1, 2, 3). \quad (7)$$

The coefficients $u_{il}(\vec{\xi})$ are determined by correlations

$$u_{il}(\vec{\xi}) = (2\pi)^3 C_{iklm} \xi_k \xi_m. \quad (8)$$

It is known the crystallographic elastic moduli of hexagonal monocrystal (axis x_3 is hexagonal, axes x_1 and x_2 are perpendicular to axis x_3 and each other) are determined by formula

$$C_{iklm} = a\delta_{ik}\delta_{lm} + b(\delta_{il}\delta_{km} + \delta_{im}\delta_{kl}) + \gamma\delta_{i3}\delta_{k3}\delta_{l3}\delta_{m3} + \chi(\delta_{i3}\delta_{k3}\delta_{lm} + \delta_{il}\delta_{k3}\delta_{m3}) + \rho(\delta_{im}\delta_{k3}\delta_{l3} + \delta_{i3}\delta_{m3}\delta_{kl} + \delta_{il}\delta_{k3}\delta_{m3} + \delta_{km}\delta_{i3}\delta_{l3}). \quad (9)$$

Determining a , b , γ , χ and ρ from here and substituting elastic moduli C_{iklm}^k in the obtained expressions instead of C_{iklm} we will get after elementary transformations

$$a = C_{12}^k + 1/6k, \quad b = C_{44}^k + 1/6k, \\ \chi = 1/6k, \quad \rho = -1/3k, \quad \gamma = -3/6k. \quad (10)$$

Here k is determined by formula (3). The calculation of hexagonal medium Green's function is adduced following [1]. Substitution of equation (9) in (7) gives the equation system for definition of Fourier-amplitude $v_l(\vec{\xi})$. Its solution

$$(2\pi)^3 v_a(\vec{\xi}) = \frac{f_a}{b\xi^2 + \rho\xi_3^2} + \frac{1}{\text{Det}(\vec{\xi})} \times \\ \times \left\{ \frac{\xi_a(\xi_1 f_1 + \xi_2 f_2)}{b\xi^2 + \rho\xi_3^2} [(a+b)(b+\rho)\xi^2 + (a+b)(\gamma+\rho)\xi_3^2 - \right. \\ \left. - (\chi+\rho)^2\xi_3^2] + (a+b+\chi+\rho)\xi_a\xi_3 f_3 \right\}, \\ (2\pi)^3 v_3(\vec{\xi}) = \frac{1}{\text{Det}(\vec{\xi})} \{ (a+b+\chi+\rho)(\xi_1 f_1 + \xi_2 f_2)\xi_3 + \\ + [-(a+2b)\xi^2 + (a+b-\rho)\xi_3^2] f_3 \},$$

where

$$\text{Det}(\vec{\xi}) = (a+b+\chi+\rho)\xi_3^2(\xi_1 f_1 + \xi_2 f_2)\xi_3 + \\ + [-(a+2b)\xi^2 + (a+b-\rho)\xi_3^2] f_3.$$

In [1] it was shown that the task of Green's function calculation is reduced in general to the solution of six power equation

$$F(z) = a_0 z^6 + a_1 z^5 + a_2 z^4 + a_3 z^3 + a_4 z^2 + \\ + a_5 z + a_6 = 0,$$

where $F(z)$ is a determinant of third order

$$F(z) = |C_{iklm} a_k(z) a_m(z)|,$$

a Green's function is defined by correlations

$$G_{ln}(\vec{r}) = \frac{2\pi}{r} \sum_{m=1}^3 \left(\frac{f_m(z)}{F(z)} \right)_{z=z_m},$$

where $f_m(z)$ are algebraic additions of corresponding elements of determinant $F(z)$. The functions $a_k(z)$ are defined by equalities:

$$a_1(z) = \sin \varphi - z \cos \theta \cos \varphi, \\ a_2(z) = -\cos \varphi - z \cos \theta \sin \varphi, \quad a_3(z) = z \sin \theta,$$

and z_m are root of equation $F(z) = 0$, θ and φ — polar angles of radius-vector \vec{r} .

In our case this equation is fallen to two ones (quadratic and bequadratic):

$$(b + \rho \sin^2 \theta) z^2 + b = 0, \quad (11)$$

$$(m \sin^4 \theta - l \sin^2 \theta - k) z^4 - \\ - (l \sin^2 \theta + 2k) z^2 - k = 0, \quad (12)$$

where the coefficients k , l , m are

$$k = (a + 2b)(b + \rho),$$

$$l = (a + 2b)\gamma + (2b - \chi)(\chi + 2\rho),$$

$$m = (a + b - \rho)\gamma - (\chi + 2\rho^2).$$

The roots of equations (11) and (12) are

$$z_{1,2} = \pm \sqrt{-\frac{b}{b + \rho \sin^2 \theta}},$$

$$z_{3,4,5,6} = \pm \sqrt{-\frac{2k + (l \pm \sqrt{l^2 + 4km}) \sin^2 \theta}{2(k + l \sin^2 \theta - m \sin^4 \theta)}}.$$

Further calculations are depended on correlations, which the elastic moduli are satisfied with. Let's examine the case when

$$z_{1,2} = \pm \sqrt{-\frac{b}{b + \rho \sin^2 \theta}},$$

$$z_{3,4,5,6} = \pm \sqrt{-\frac{2k + (l \pm \sqrt{l^2 + 4km}) \sin^2 \theta}{2(k + l \sin^2 \theta - m \sin^4 \theta)}}.$$

Let's mean $p_1(n_3)$, $p_2(n_3)$, $q(n_3)$ the expressions

$$p_1(n_3) = 2k + (l + \sqrt{l^2 + 4km})(1 - n_3^2),$$

$$p_2(n_3) = 2k + (l - \sqrt{l^2 + 4km})(1 - n_3^2),$$

$$q(n_3) = 2[k + l \sin^2 \theta - m \sin^4 \theta].$$

Let is $\vec{n} = \vec{r}/r$, $B(n_3) = b + \rho - \rho n_3^2$,

$$A_p(n_3) = (a + b)(b + \rho) \frac{1}{p_p(n_3)} + \\ + \frac{(a + b)(b\gamma - \rho^2) - b(\chi + \rho)^2}{B(n_3)p_p(n_3) - q(n_3)} (1 - n_3^2) \sqrt{p_p(n_3)},$$

then the function $u_l(\vec{r})$ of unlimited hexagonal monocrystal is defined by formulas

$$4\pi r(1 - n_3^2) u_a(\vec{r}) = \\ = - \left[\frac{\sqrt{q(n_3)}}{b\sqrt{l^2 + 4km}} \sum_{\beta=1}^2 (-1)^\beta A_\beta + \frac{B(n_3) + b n_3^2}{(b + \rho)\sqrt{Bb}} \right] + \\ + \left[\frac{1}{b\sqrt{(l^2 + 4km)q(n_3)}} \sum_{\beta=1}^2 (-1)^\beta A_\beta (q(n_3) + p_p(n_3)n_3^2) + \right. \\ \left. + \frac{B(n_3) + b n_3^2}{(b + \rho)\sqrt{Bb}} \right] \frac{n_a(n_1 f_1 + n_2 f_2)}{1 - n_3^2} - \\ - \frac{a + b + \chi + \rho}{\sqrt{(l^2 + 4km)q(n_3)}} \sum_{\beta=1}^2 (-1)^\beta n_a n_3 f_3 \sqrt{p_p(n_3)}, \\ \alpha = 1, 2, \quad (13)$$

$$4\pi r(1 - n_3^2)u_3(\vec{r}) = -\frac{1}{\sqrt{(l^2 + 4km)q(n_3)}} \times$$

$$\times \left\{ (a + b + \chi + \rho) \sum_{\beta=1}^2 (-1)^\beta \sqrt{\rho_\beta(n_3)} n_3 (n_{1f1} + n_{2f2}) + \right.$$

$$+ [(b + \rho) + (a + b - \rho)n_3^2] \sum_{\beta=1}^2 (-1)^\beta \sqrt{\rho_\beta(n_3)} -$$

$$\left. - (a + 2b)q(n_3) \sum_{\beta=1}^2 \frac{(-1)^\beta}{\sqrt{\rho_\beta(n_3)}} \right\} f_3. \quad (14)$$

Substituting a , b , γ , χ and ρ in these equations out of equation (10) and making a substitution $f_i \rightarrow \delta_{in}$ we will obtain in equations (13) and (14) the component $G_{in}(\vec{r})$ of Green's tensor of cubic monocrystal instead of $u_i(\vec{r})$. Thus it is putted an end to the

task of Green's tensor finding in the connected to crystallographic plane (111) of cubic monocrystal frame and Green's tensor can be obtained in reserved form.

References

1. Lifshits I. M., Rozencweig L. M. About construction of Green's tensor for the basic equation of the elastic theory in case of unlimited elastic anisotropic medium // JETP. — 1947. — Issue 9. — Vol. 17. — P. 783—791.
2. Gokhman A. R. To the texture polycrystal with cubic crystallites properties calculation on the basis of pole figure (111) // Zavodskaya laboratoriya (the materials diagnosis). — 1996. — № 2. — C. 27—30.
3. Bogachev I. N., Vainshtein A. A., Volkov S. D. The introduction to statistical metal science. — M.: Metallurgiya, 1972. — 216 p.

Наукова бібліотека ОНУ імені І. І. Мечникова

INFLUENCE OF γ -IRRADIATION ON PHOTOLUMINESCENCE OF POROUS GERMANIUM OBTAINED BY TREATMENT IN ELECTRIC SPARK DISCHARGE

The porous Ge layers are produced by spark discharge method. The photoluminescence spectra of these layers are compared with ones for porous Ge obtained by stain, chemical and electrochemical etching. There are the data in references that for porous Ge layers obtained by different methods the maximum for photoluminescence spectrum may be localized by two different wavelengths depending on the production procedure. In contrast to it, our spectra consist of both peaks. Using the results of photoluminescence spectra studies, the comparison of aging effects for porous Ge layers produced by different methods was made. The influence of γ -quanta action on photoluminescence spectra of porous Ge layers was studied.

1. Introduction

The discovery of intensive photoluminescence in visible range of spectrum from porous silicon [1] is interesting to search the similar effects in the other semiconductor nanostructures used in electronics. The detection of photoluminescent properties in porous germanium obtained by chemical etching [2] and by anodization [3] gives the basis to search the similar quantum phenomena in the other porous materials and allows to hope for creation of the new optoelectronic devices on the base of these materials. The above-mentioned expectations are also confirmed by the studies in porous silicon carbide [4] and in porous gallium arsenide [5]. However, the low intensity of photoluminescence for these structure hampers their practical application. This fact forces the search for methods to magnify luminescence. One of them is the development of radiating surface that can be easily realized by creation of nanoclusters in different porous structures, which are already known [6—7].

In contrast to porous silicon, only some papers [2, 3, 8—12] are devoted to porous germanium. In our opinion, it may be explained mainly by complexity of its production, by bad reproducibility of material and by lower intensity of photoluminescence in visible range of spectrum comparing to porous silicon. In the above-mentioned papers the samples obtained by different technologies, were treated by various procedures (for example, laser irradiation, thermal annealing, oxidizing on air or in water vapour etc) during investigation. At the same time, the studies of radiative effect on the given nanostructures are practically missed. In present paper we try to make up for this deficiency.

2. Experimental technique

As the initial material, *p*-type germanium wafer with specific resistance $\rho = 30 \Omega \cdot \text{cm}$ was used. We applied the same germanium as material for electrode during the treatment of sample by spark discharge, though it was of little importance [10—11]. The production of porous layers was carried out by the setup consisting of high-voltage source, contact maker and two-coordinate manipulator (fig. 1). The treatment by electric spark discharge up to 20 hours allows to obtain layers of noticeably luminescent porous germanium with diameter of a spot of about 5 mm. Just this size is the minimal to dispense with photon counter. During the process rather thick white scurf of germanium oxide arises on wafer surface, which is necessary to remove periodically to facilitate the formation of porous layer. The growth strength of porous germanium layer allows to remove the referred «coat» mechanically, without any solvent, as it usually takes place, while using chemical etching [2], when porous layer is obtained thin and friable.

The distinctive feature for the treatment by electric spark is that the spark at each subsequent discharge hits in a place with the lower resistance because of porous layer and oxide on sample surface. Thus, the rather uniform layer results in continuous treatment (even at — 100 μm of layer thickness). This fact distinguishes favourably the spark

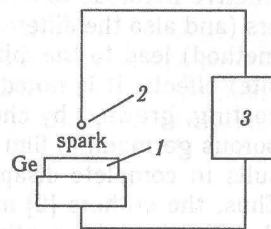


Fig. 1. The scheme of setup to produce porous material by electric spark discharge:

1 — sample; 2 — electrode;
3 — high-voltage source of current

treatment techniques of porous germanium from that obtained by anodization. The investigation of these layers by optical and electronic microscopes (fig. 2, *a* and *b*) specifies the fundamental similarity of porous silicon layers obtained by anodization (fig. 2, *c*).

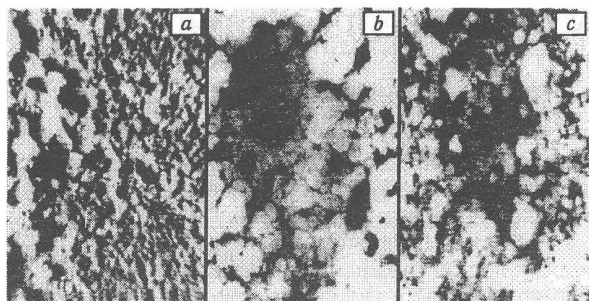


Fig. 2. Photos of porous Ge and porous Si surfaces: *a* — Ge (optical microscope); *b* — Ge (electron microscope); *c* — Si (electron microscope)

The obtained Ge sample with porous layer was exposed to γ -irradiation from ^{60}Co isotope with dose $5 \cdot 10^4 \text{ rad}$. The photoluminescence spectra before and after this irradiation were registered at excitation with ultraviolet laser ILGI-501 (wavelength $\lambda = 337 \text{ nm}$, pulse duration 10 ns , repetition frequency from 10 Hz up to 100 Hz , mean power 25 mW), by the setup consisting of quartz monochromator SF-4, photoelectric multiplier FEU-59, selective amplifier U2-8 and xy-plotter H-307.

3. Results and discussion

As well as in case of porous silicon [13], the distinctive methods to obtain porous germanium layers (and also the different regimes within the same method) lead to the different (and often the opposite) effects. It is noted in [2], that the white thin coating, growing by chemical procedure to obtain porous germanium film and removing in water, results in complete disappearance of luminescence. Thus, the authors [2] make quite valid conclusion that the given thin coating consisted mainly of GeO_2 is responsible for photoluminescence.

Aforesaid, white thin coating of oxide has also appeared when the spark discharge method was used. However, at its subsequent more and more careful mechanical removal, the photoluminescence not only does not disappear, but its intensity, on the contrary, increases without change in shape of spectrum and shift in the peaks (fig. 3).

Both results are not inconsistent if one takes into account that the presence of oxide is only one of the necessary requirements to appear luminescence. The second necessary requirement consists in the presence of nanoclusters provided the quantum confinement effect inside pores. It becomes obvious, that in case of electric spark discharge treatment, the nanoclusters of Ge and oxide will form more strong structure, than in case of anodization [2].

The similar explanation is also confirmed by the results of paper [3], where the anodized layers of porous germanium were oxidized at 600°C in oxy-

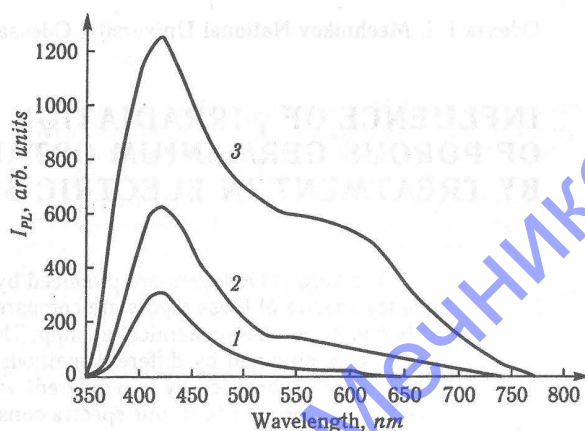


Fig. 3. Photoluminescence spectra of porous germanium:

1 — with oxide layer formed as the result of electric spark treatment; 2 — after mechanical removal of thin oxide layer; 3 — after more complete removal of oxide layer

gen and nitrogen atmosphere in the ratio 1:9, respectively. The results of this work show the strong shift of photoluminescence maximum to the short-wave direction. This phenomenon is accompanied by approximately 150-fold increase in photoluminescence efficiency comparing to the initial value. This effect is explained [3] as displacement of bound hydrogen and as its substitution by oxygen. Thus, the part of oxide increase that allows to make conclusion about the decisive role of localized states on Ge— GeO_2 interface in shaping of photoluminescence.

From results of [2] one can see, that in samples obtained by stain-etching, there is photoluminescence peak with maximum near 420 nm (with wavelength of exiting light 325 nm), whereas, for the anodized samples, the peak lies within the range $560\text{--}580 \text{ nm}$ (but at excitation by wavelength 488 nm). The necessity to use excitation at the greater wavelength in the second case is explained, obviously, by abrupt degradation of photoluminescence. It prevents the possibility to compare the results even within the paper. At the same time, in our case, when electric spark discharge is used to obtain porous germanium, both maxima (420 nm and 540 nm) are present in photoluminescence spectrum under excitation with wavelength 337 nm (fig. 4). Taking into account that in [2] excitation energy for photoluminescence of anodized porous germanium is lower than in present work, it is possible to assert, that the corresponding maxima are identical with the high probability.

The fact [2] that photoluminescence of chemically etched layers of porous germanium degrades promptly and strongly enough under the influence of laser excitation while the noticeable decrease of photoluminescence is not observed for our samples under the same conditions, should be taken into

account. This proof out of the photostimulated changes we explain by the assumption that nano-

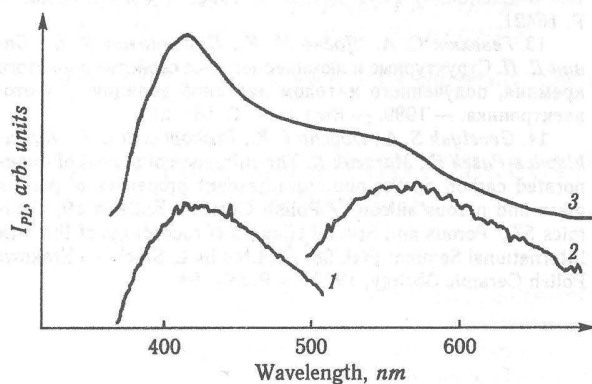


Fig. 4. Photoluminescence spectra of porous germanium: 1 — obtained by stain etching ($\lambda_{exc} = 325 \text{ nm}$); 2 — obtained by anodization ($\lambda_{exc} = 488 \text{ nm}$); 3 — obtained by spark discharge ($\lambda_{exc} = 337 \text{ nm}$)

clusters of germanium (1) in our structure are implanted in solid bed of oxide (2) (fig. 5).

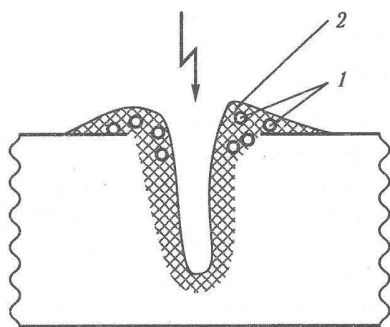


Fig. 5. Schematic image for dislocation of Ge clusters in oxide layer after electric spark discharge treatment: 1 — Ge clusters; 2 — oxide layers

In the paper [7] devoted to studies of Ge clusters in porous silicon, the diminution in photoluminescence intensity and shift in its maximum to the short-wave direction after one year of storage was demonstrated. This result is stipulated by oxidation through Ge clusters, i. e. increase in width of oxide layer and diminution in germanium core of cluster. The similar phenomenon also takes place with Si clusters in porous silicon during long-time storage on air and at annealing with saturated carbon (carbonic treatment) [14]. The absence of the noticeable result for the given effect in our samples and also the absence of luminescence degradation under excitation by UV laser testifies to the initial prevention in them from the further oxidation of nanoclusters through oxide film. This «defence» may be explained by the steeping of nanoclusters in rather thick oxide layer that is stipulated by procedure of sample preparation.

The research of the influence for the small doses of γ -irradiation has shown that it led to decrease in photoluminescence efficiency with simultaneous

smoothing and broadening of spectrum (fig. 6). The obtained effect can be explained by formation of

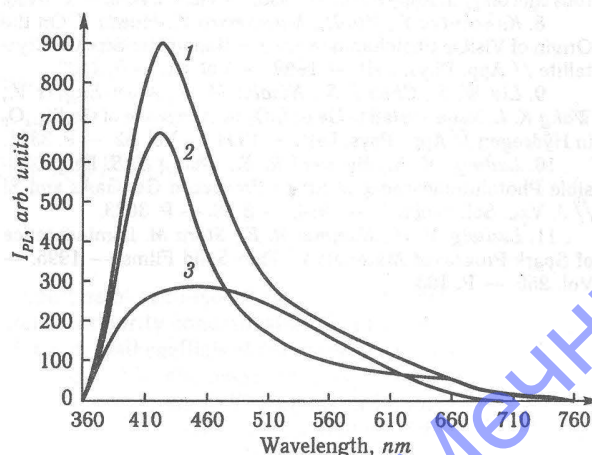


Fig. 6. Photoluminescence spectra of porous germanium: 1 — initial spectrum; 2 — after storage on air during one month; 3 — after γ -irradiation with dose $5 \cdot 10^4 \text{ rad}$.

additional centers for light absorption. These centers allow to recombine radiatively for donor—acceptor pairs with low energy.

3. Conclusion

1. The decisive role of Ge—GeO₂ interface during photoluminescence of porous germanium is shown.

2. The absence of noticeable degradation in intensity of photoluminescence of porous germanium during long-time storage is explained by preliminary good prevention of Ge clusters during material production by using the electrical spark discharge method.

3. The decrease in photoluminescence intensity of porous Ge with simultaneous smoothing and broadening of spectrum under influence of small γ -irradiation doses is explained by formation of additional centers for light absorption in oxide layer.

References

1. Canham L. T. // *Appl. Phys. Lett.* — 1990. — Vol. 57. — P. 1046.
2. Sendova-Vassileva M., Tzenov N., Dimova-Malinovska D., Rosenbauer M., Stutzman M., Jozepovits K. V. Structural and Luminescence Studies of Stain-Etched and Electrochemically Etched Germanium // *Thin Solid Films.* — 1995. — Vol. 255. — P. 282.
3. Miyazaki S., Sakamoto K., Shiba K., Hirose M. Photoluminescence from Anodized and Thermally Oxidized Porous Germanium // *Thin Solid Films.* — 1995. — Vol. 255. — P. 99–102.
4. Matsumoto T., Takahashi J., Futagi T., Mimura H. Blue-green Luminescence from Porous Silicon Carbide // *Appl. Phys. Lett.* — 1994. — Vol. 64. — P. 226.
5. Горячев Д. Н., Сресели О. М. Фотолюминесценция пористого арсенида галлия // *ФТП.* — 1997. — Т. 31, № 11. — С. 1383.
6. Savin D. P., Geveliyuk S. A., Roizin Y. O., Mugenski E., Sokolska I. Comparison of Some Properties of Nanosized Clusters in Porous Glasses // *App. Phys. Lett.* — 1998. — Vol. 72, № 23. — P. 3005–3007.

7. Feng-Qi Liu, Zhan-Guo Wang, Guo-Huo Li, Guang-Hou Wang. Photoluminescence from Ge Clusters Embedded in Porous Silicon // *J. Appl. Phys.* — 1998. — Vol. 83, № 6. — P. 3435.
8. Kanemitsu Y., Uto H., Matsumoto Y., Maeda Y. On the Origin of Visible Photoluminescence in Nanometer-Size Ge Crystallite // *App. Phys. Lett.* — 1992. — Vol. 61. — P. 2187.
9. Liu W. S., Chen J. S., Nicolet M. A., Arbet-Engels V., Wahg K. L. Nanocrystallite Ge in SiO_2 by Annealing of GeSi_3O_2 in Hydrogen // *Appl. Phys. Lett.* — 1993. — Vol. 62. — P. 3321.
10. Ludwig M. H., Hummel R. E., Chang S.-S. Bright Visible Photoluminescence of Spark Processed Ge, GaAs and Si // *J. Vac. Sci. Technol.* — 1994. — B 12. — P. 3023.
11. Ludwig M. H., Hummel R. E., Stora M. Luminescence of Spark-Processed Materials // *Thin Solid Films.* — 1995. — Vol. 255. — P. 103.

12. Okamoto S. and Kanemitsu Y. Photoluminescence Properties of Surface Oxidized Ge Nanocrystals: Surface Localization of Excitons // *Phys. Rev. B.* — 1996. — Vol. 54, № 23. — P. 16421.
13. Гевелюк С. А., Дойчо И. К., Прокопович Л. П., Савин Д. П. Структурные и люминесцентные свойства пористого кремния, полученного методом лазерной абляции // *Фотоэлектроника.* — 1999. — Вып. 8. — С. 18—21.
14. Geveliyuk S. A., Doycho I. K., Prokopovich L. P., Rysiekiewicz-Pasek E., Marczuk K. The influence of anneal of incorporated carbon on the photoluminescent properties of porous glass and porous silicon // *Polish Ceramic Bulletin 19, Ceramics 57 / Porous and Special Glasses (Proceedings of the 4th International Seminar PGL'98) / Edited by L. Stoch.* — Krakow: Polish Ceramic Society, 1998. — P. 59—64.

ELECTRIC AND PHOTOELECTRIC PROPERTIES
OF CdTe:V CRYSTALS

Equilibrium electric and photoelectric properties of semi-isolating CdTe:V crystals, obtained by Bridgman method were investigated. Impurity concentration C_0 in the melt was in the limits from $2 \cdot 10^{18}$ to $1 \cdot 10^{20} \text{ cm}^{-3}$. From Hall coefficient temperature dependences in the energies range of 0,67...0,85 eV a set of levels, ascribed to V_{Cd}^{2+} defect in the isolated state or in associate composition was determined. The bands of impurity photoconductivity (at 1,1 eV and 1,35 eV) explained by the photoionization of V_{Cd}^{2+} defect were revealed. The peculiarities of recombination processes in cadmium telluride doped with V, Ge and Sn are compared.

Cadmium telluride is widely used in opto- and microelectronics due to great number of its specific properties. It is mostly applied in production of infrared (IR) elements, devices of ionizing radiation as well as substrates for CdTe and CdHgTe epitaxial layers.

Last years great interest in CdTe has grown as the photorefractive material being suitable for application in telecommunication systems. It becomes possible because of a high value of CdTe electro-optical coefficient which is three times greater than the analogous one in A^3B^5 compounds, and also owing to the possibility to widen the photosensitivity range in IR region by doping with certain impurities. The data in [1] show that CdTe:V crystals are the most perspective material in this trend.

Since the vanadium impurity has the unfilled 3d-shell and intrinsic magnetic moment, the considerable amount of investigations in CdTe:V crystals were carried out by optical, magneto-optical and resonance methods.

Theoretical calculations have indicated [2] that impurity of V taking Cd site created deep donor levels near the middle of CdTe forbidden gap. It is supposed that rigid pinning of Fermi level to the position of these levels is the reason for semi-isolated state of CdTe:V crystals.

However, there isn't any divergence in the interpretation of the results for many experimental studies of CdTe:V properties. Particularly, for energy position of V^{2+}/V^{3+} vanadium level, which stipulated equilibrium characteristics of material, various data were presented: E_c — 0,67 eV [1, 3], E_c — 0,8 eV [2], E_c — 0,9 eV [4]. Authors of [4, 5] have revealed two traps with energies of 0,95 and 0,78 eV being present in all samples with vanadium and undoubtedly they were the results of this impurity. The nature of vanadium compensation effect in CdTe is not clear so far as the general amount of impurities dissolved in the crystal is much more greater than their contents in cadmium sites (V^{2+} , V^{3+}).

This paper concerns the partial solutions of these problems. The results of electric and photoelectric properties research in CdTe:V crystals, doped with different quantities of impurity in liquid phases C_0 : from $2 \cdot 10^{18} \text{ cm}^{-3}$ up to $1 \cdot 10^{20} \text{ cm}^{-3}$ are presented. The crystals were grown by Bridgman method under the low pressure of Cd vapour ($p_{\text{Cd}} \approx 0,02 \text{ atm}$). Initial components (Cd, Te) were of 99,9999 purity. Synthesized material was additionally cleaned by vacuum sublimation method and impurity was put into the container directly before the growing process.

The treatment of the samples and putting of the contacts are standard [3]. Temperature measurements of Hall coefficient (R_H), specific resistivity (ρ) were carried out by direct current method using electrometric amplifier with input resistance of $\sim 10^{12} \Omega$. Voltage on the sample was $\leq 5 \text{ V}$. To exclude from the secondary signals, the measurements were performed at two directions of current and magnetic field at every temperature.

Photoelectric measurements were made in direct field regime in the sample. Spectral (in 0,5...1,8 eV energy interval) and temperature (at $80 \leq T \leq 295 \text{ K}$) dependences of photoconductivity and IR-quenching were investigated.

Equilibrium characteristics of samples at 295 K are presented in the table. All the crystals were semiisolated with electron-type conductivity. Intrinsic conductivity was observed in several samples (example 2 in the table). Experimental temperature

Table

№	Impurity concentration $C_0, \text{ cm}^{-3}$	Carrier concentration $n, \text{ cm}^{-3}$	Carrier mobility $\mu_H, \text{ cm}^2/\text{V} \cdot \text{s}$	Energy of level $\Delta E, \text{ eV}$
1	$2 \cdot 10^{18}$	$2,5 \cdot 10^7$	780	0,67
2	$5 \cdot 10^{18}$	$2,0 \cdot 10^6$	711	1,60
3	$1 \cdot 10^{19}$	$2,8 \cdot 10^8$	830	0,76
4	$1 \cdot 10^{19}$	$6,2 \cdot 10^6$	126	0,67
5	$1 \cdot 10^{20}$	$4,7 \cdot 10^6$	903	0,854

dependences of $\rho(T)$ and $R_H(T)$ for this sample are shown in fig. 1. Dashed line is a temperature depen-

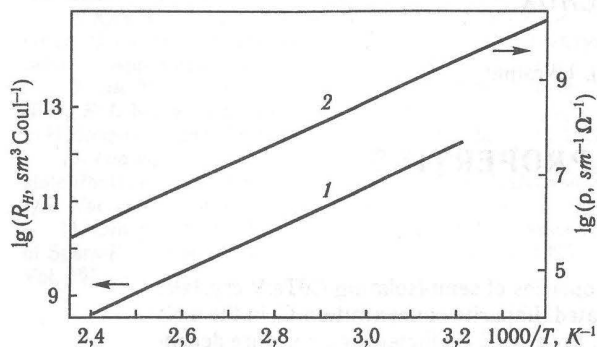


Fig. 1. The temperature dependences of Hall coefficient (1) and specific resistance (2) in CdTe:V crystals. Dashed line is the calculated values of R_H at the intrinsic conductivity.

dence of R_H in intrinsic conductivity range calculated using the expression

$$R_i = \frac{r}{en_i} \left(\frac{1-b}{1+b} \right),$$

here n_i — intrinsic carrier concentration [6]; $r = 1$; $b = \mu_n/\mu_p = 14$. Repeated measurements of electro-physical parameters during the cooling from 430 K to room temperature have shown that in contrast to the undoped CdTe [6], our crystals revealed great thermal stability. The dependence between C_0 and equilibrium carrier concentration was not observed. The depth of operating levels, caused the equilibrium conductivity was in the interval of $E_c = 0.67 \dots 0.85$ eV. These values were equal or close to the values obtained by the other authors [1–4]. The reason to appear such set of levels appears, in our opinion, is that there is no majority of vanadium impurity (V_{Cd}) in the isovalent state, but it enters into the associates content with cadmium vacancy. Cadmium telluride like other A^2B^6 compounds is characterized with the high degree of complex creation. Thus, the investigated crystals were grown at low cadmium vapour pressure and had a lot of its vacancies. It is known [7] that ionization energy of defect which is a part of the associate, decreased comparing with the corresponding value for non-interacting state. Taking the energy position of V_{Cd}^{2+} isolated defect as $E_c = 0.9$ eV [4], such explanation for the big number of activation energies appeared is rather possible.

Photoelectric investigations show that doping of CdTe with vanadium has caused the long-wave limit photoconductivity (PC) shift to the region of smaller energies comparing with the undoped CdTe, where only its proper maximum was observed (fig. 2). When temperature decreases, the low-temperature photosensitivity edge shifts from ~ 0.7 eV (295 K) to ~ 0.9 eV (80 K) and photosensitivity slightly improves. In PC spectrum at 80 K it is possible to distinguish two bands with spreaded maximums at 1.1 eV and 1.35 eV. Similar bands with close ener-

gies were observed in [4] where maximum at 1.3 eV was connected with the direct V_{Cd}^{2+} defect photoioni-

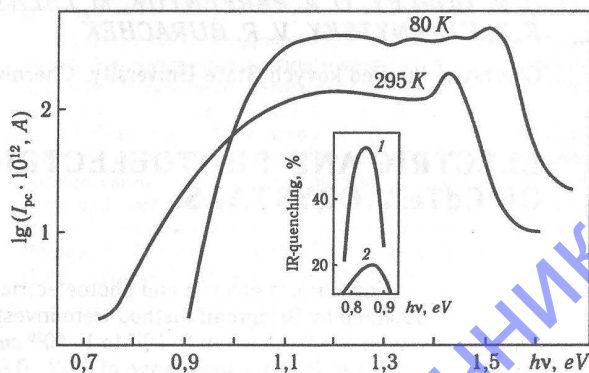


Fig. 2. The spectral dependences of photoconductivity in CdTe:V at different temperatures. The insertion shows the spectral dependences of the infrared quenching of photoconductivity for two intensities of intrinsic excitation: $L_1: L_2 = 1: 10$.

zation and it was supposed that the band about 1.1 eV was caused by photoionizing ion V_{Cd}^{2+} transition over its excited state of $4T_1$ (4P). An essential difference between optical and thermal ionization energy of V_{Cd}^{2+} was explained [4] by strong lattice relaxation.

PC temperature dependence without any peculiarities monotonously decreases when temperature rises from 80 to 295 K. In the whole temperature interval, photocurrent I_p dependence on the intrinsic excitation level is expressed by power function with index of $1.0 \leq \gamma \leq 1.1$.

At nitrogen temperatures, IR-quenching of PC was observed in energy range of $0.75 \leq hv \leq 0.95$ eV (insertion in fig. 2). Maximum magnitude of quenching factor was more than 50%. When the light was switched in and switched off, the transition processes were observed displaying in short-time decrease of I_p at IR-light cut-off and following increase in its initial quantity of I_0 and vice versa — when the light was switched in. These processes could be explained by the double optical transition of V_{Cd}^{2+} and V_{Cd}^{3+} . Data presented in fig. 2 also show that IR-quenching is a reason that at 80 K long-wave PC limit shifts at the higher energies.

Practically important peculiarity of CdTe:V crystals is almost complete absence of long-wave «tails» damping of PC when excitation at switch-in (fig. 3) that is characteristics for high-ohmic semiconductors.

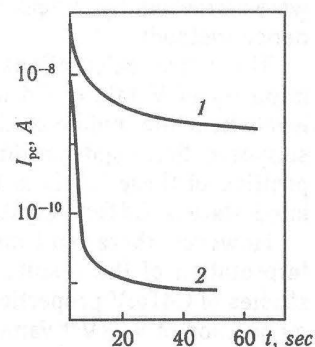


Fig. 3. Time dependences of photocurrent decrease after excitation switch-off in CdTe:Sn (1) and CdTe:V (2) crystals.

Analysis of the results show that in CdTe:V, the centres with sharp asymmetric capture cross-sections for electrons and holes [8] found in photosensitive CdTe:Ge, Sn crystals are not created [9]. That is why we may consider that deep centres created by Ge and Sn impurities in CdTe have influenced on recombination processes quite differently from the analogous ones for CdTe:V.

As a conclusion it should be noted that the doping of cadmium telluride with vanadium caused the production of semi-isolated n-type material. The correlation between the quantity of impurity and estimated parameters of CdTe:V was not founded. To explain electric and photoelectric properties of the material it should be taken into account a great probability that vanadium may introduce into the associates with cadmium vacancies. The wide spectral range of photosensitivity and high speed of stationary values, determined after switch-in and switch-off the light, are of great importance for practical use of this material.

References

1. Christmann P., Kreiss L. J., Hoffmann D. M., Meyer B. K., Schwarz R., Benz K. W. // Journal Crystal Growth. — 1996. — V. 161. — P. 259—263.
2. Kikoin K. A. Electronical properties of the transition metals impurities in semiconductors. — M.: Energoatomizdat, 1991 (in Russian).
3. Savitsky A. V., Ilashchuk M. I., Parfenyuk O. A., Ulyanysky K. S., Burachek V. R., Kadelnyk D. V. Scientific News of Chernivtsi State University. Physics. — Chernivtsi, 1998. — № 29. — P. 79—84 (in Ukrainian).
4. Mishchenko L. A. The vanadium impurity influence on the defects form in cadmium telluride: Autoref. diss.... cand. phys.-math. sci. — K., 1998 (in Ukrainian).
5. Zerrai A., Marrakchi G., Bremond G. et al. // Journal Crystal Growth. — 1996. — V. 161. — P. 264—270.
6. Savitsky A. V., Ilashchuk M. I., Parfenyuk O. A., Ulyanysky K. S., Fochouk P. M. // Ukr. Fiz. Zhurnal. — 1996. — V. 41, № 1. — P. 89—91 (in Ukrainian).
7. Kroger F. A. The chemistry of imperfect crystals. — Amsterdam: North-Holland Publ. Co, 1964.
8. Rouz A. The photoconductivity theory principles. — M.: Mir, 1966.
9. Nykonyuk E. S., Parfenyuk O. A., Matlak V. V., Tovstyuk K. D., Savitsky A. V. // Fiz. Techn. Poluprov. — 1975. — V. 9, № 7. — P. 1271—1278 (in Russian).

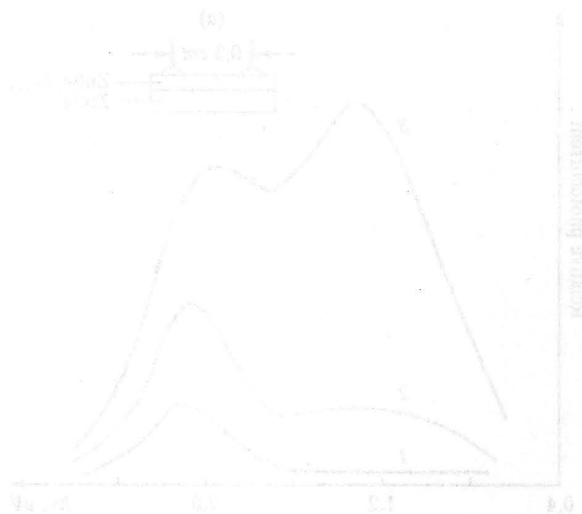


Fig. 1. Photocurrent spectra of CdTe:V for voltages 10 V (1), 20 V (2) and 30 V (3).

RESIDUAL PHOTOCONDUCTIVITY EFFECT IN SEMI-INSULATOR FILMS $\text{ZnSe}_x\text{Te}_{1-x}$

The features of photoconductivity in semi-insulating layers $\text{ZnSe}_x\text{Te}_{1-x}$ have been studied. The dependence of the photocurrent on applied voltage has been investigated. It is observed that the voltage under which the space-charge-limited (SCL) current flows the impurity maximum with $h\nu = 1,4 \text{ eV}$ appears in the spectra of photocurrent. The residual photoconductivity is observed under illumination of impurity absorption region. And the ratio of photocurrent to the dark one reaches of value 10^5 . The observed phenomena are explained by space inhomogeneity of the layers.

1. Introduction

The epitaxial films $\text{ZnSe}_x\text{Te}_{1-x}$ combine the high resistivity with the high photosensitivity. However there is no complete information on photoelectric properties of solid solution in literature. Generally, the available information concerns the researches in the dependence of bandgap (E_g) on film composition [1]. In the present work the unknown effects, being discovered in the semi-insulating $\text{ZnSe}_x\text{Te}_{1-x}$ films grown on ZnSe substrate are described.

2. Experimental procedure

The epitaxial films of solid $\text{ZnSe}_x\text{Te}_{1-x}$ solution were produced by liquid phase epitaxy on high-resistant ZnSe (111) substrate. The growth took place under the epitaxial temperature 980–1050 K out of Bi melt. The geometry of Ohmic contacts is presented in fig. 1, insertion (a). The films have p -type conductivity and their resistivity was $10^8 \text{ Ohm} \cdot \text{cm}$. The value of resistivity for (ZnSe) sub-

strate are not more ($\text{ZnSe}_x\text{Te}_{1-x}$) than two or three order. The composition of solid solution $\text{ZnSe}_x\text{Te}_{1-x}$ was defined by Raman spectroscopy [1]. The value x , of growing films changes in the range 0,2–0,3, that corresponds to $E_g = 2,14 \text{ eV}$. Photoconductivity spectra were measured within the wavelength range 0,4–3,0 μm using DMR monochromator. The PZh-100 incandescent lamp was used as excitation source. Photoconductivity spectra were taken with constant number of light quanta being incident on the sample.

3. Results and Discussion

The spectral response of photocurrent measured under the different applied voltages and at $T = 500 \text{ K}$ are showed on Fig. 1. Figure 1 presents one intrinsic peak with maximum $h\nu_{\text{max}} = 2,14 \text{ eV}$, under low voltages (curve 1), which corresponds to the band-to-band transitions $\text{ZnSe}_x\text{Te}_{1-x}$. The additional band with $h\nu_{\text{max}} = 1,4 \text{ eV}$, corresponded to photoionization of impurity centres, appears in spectrum (curves 2, 3) under voltage increase, beginning from the certain critical value (U_{cr}). The induced impurity photocurrent increases with the voltage more quickly than the intrinsic peak. One more experimental fact, being observed on $\text{ZnSe}_x\text{Te}_{1-x}$ films, consists in the following, if the samples, mounted in darkness under the voltage $U < U_{\text{cr}}$, are illuminated by light with energy $h\nu = 1,4 \text{ eV}$, current increases to some value, which relaxes quickly to the primary one after switching off the light. When $U > U_{\text{cr}}$ current increases slowly to its maximum value. The relaxation time depends on voltage, intensity and sample temperature. The maximum value of ratio for the impurity photocurrent to the dark one I_d was equal 10^5 . When the turning off the light the impurity photocurrent slightly decreases, but the state with the large conduction is reminded for long time ($10^5 \dots 10^6 \text{ s}$). So, the phenomenon of residual photoresistivity can be observed.

The current voltage characteristics (CVC) of dark current and impurity photocurrent were measured.

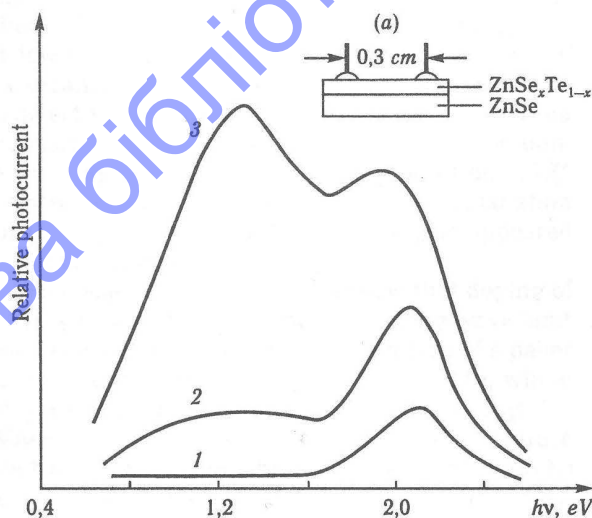


Fig. 1. Photocurrent spectra of $\text{ZnSe}_x\text{Te}_{1-x}$ for voltages 10 V (1), 20 V (2) and 30 V (3)

Figure 2 shows, that the dark current changes, firstly, in accordance with Ohm law, and then is dis-

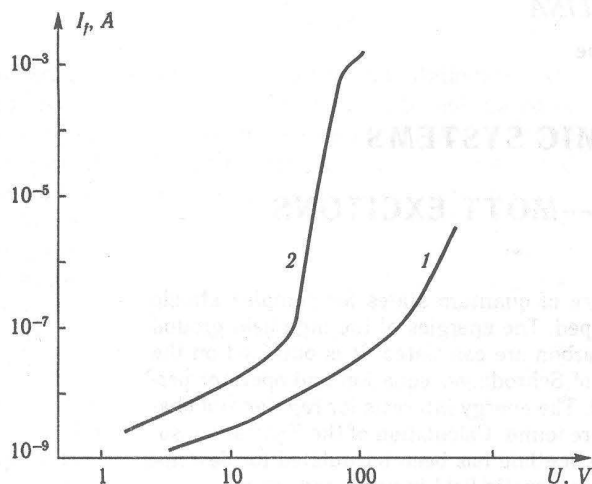


Fig. 2. CVC dark current (1) and impurity photocurrent (2)

cribed by the response, which is characteristic law for the current-limited space (CLS). CVC of the impurity photocurrent are also described by the law of the monopolar injection (curve 2). The voltage, threshold population traps V_{tp} , equal

$$V_{tp} = 4eN_t L^2 / 3\epsilon,$$

here e — is electron charge, L — is distance between cathode and anode, ϵ — static dielectric constant, N_t — traps concentration. The evaluation of N_t under the given geometry of contacts shows the value $10^{15} m^{-3}$. However, such very low concentration is not determined by general purity of films, but it shows that in our case (SCL) flows in small regions of high resistivity and it regulates current flow in films. At voltage increase, the resistance of both regions are equalized at the expense of its injection currents. The investigations in nature of inhomogeneity

showed, that it is connected with the inhomogeneity distribution of electrical defects in films volume, but not with the inhomogeneities distribution of $ZnSe_xTe_{1-x}$ composition. We suppose, that the centres of extrinsic photosensitivity are in the low resistance regions. So the impurity peak appears in photocurrent spectra under the high voltage. The recombination barriers with height E_{rec} , existed on the boundary of electrical inhomogeneities and provided the space separation on nonequilibrium carriers. Life time of nonequilibrium carrier and relaxation time of residual conductivity (τ) are determined by the expression

$$\tau = \tau_0 \exp(E_{rec}/kT),$$

here τ_0 — time of thermal equilibrium carrier. By 300 K $\tau_0 = 10^{-4} C$, $kT = 0,025 eV$, $\tau = 10^5 \dots 10^6 C$, obtained value $E_{rec} = 0,5 eV$.

4. Conclusion

The $ZnSe_xTe_{1-x}$ films of solid-solution growing on ZnSe substrates show the photosensitivity inducing by electrical field and residual photoconductivity exciting by light from absorption impurity region. The investigation of mechanism of current flow in $ZnSe_xTe_{1-x}$ showed that it contained the electric inhomogeneity. The residual conductivity in films is explained the existence of recombination barriers providing the space separation of carriers on the boundary of inhomogeneity. The received results in work could be practically applied in optic switching devices. To these also promote that, the effects are observed under the high temperature (300...350 K), have the high value and the films have of the mechanical durability and the high adhesion to substrate.

References

1. Skobeleva V. M., Serdyuk V. V. Application of Raman spectroscopy for investigation of solid of II—VI semiconductors // SPIE. — 1993. — V. 1983. — P. 769.

STOCHASTIC DYNAMICS OF ATOMIC SYSTEMS IN MAGNETIC FIELD. ZEEMANE EFFECT FOR WANNIER—MOTT EXCITONS

A new method to calculate the structure of quantum states for complex atomic systems in a static magnetic field is developed. The energies of the high-field ground states for neutral atoms of hydrogen and carbon are calculated. It is obtained on the basis of numeral finite differences solution of Schrodinger equation and operator perturbation theory for atoms in magnetic field. The energy intervals for regular and chaotic dynamics of systems in magnetic field are found. Calculation of the Zeemane resonances widths is carried out. The analogous method has been formulated for description of Wannier—Mott excitons behavior in magnetic field in semiconductors.

1.

The electron structure of atomic systems in strong magnetic field can be drastically changed (i. e., white stars, pulsars etc.). The interest to problem of hydrogen, hydrogen-like and multielectron atoms in static magnetic field has been also stimulated during last years by experimental observation of complicated spectra with narrow resonances coexisting with broad one (c. f. [1—18]). The hydrogen atom in static magnetic field has been considered as a prototype of quantum chaotic system. Theoretical estimates of its spectrum have been carried out on the basis of different approaches, in particular, Random Matrix theory, WKB approximation, two-dimensional mesh Hartree—Fock method, $1/Z$ expansion theory (c. f. [1—18]). It has been shown that the predictions of the theory in the immediate vicinity of ionization threshold are to be improved. The same is regarding Wannier-Mott excitons. It is well known that the availability of excitons in semiconductors resulted in the special form of the main absorption band and appearance of discrete levels structure (i. e. hydrogen-like spectra in Cu_2O). Beginning from the known papers of Gross—Zaharchenya, Elliott and Loudon, Thomas and Hopfield et al (c. f. [18]), the calculation of Zeemane effect for exciton attracts a great interest. In this paper we present a new method for exact calculation of the structure of quantum states for complex atomic systems and Wannier—Mott exciton in semiconductors in static magnetic field is developed. The energies of high-field ground states for neutral atoms of hydrogen and carbon are calculated. An effective representation for wave function of problem hamiltonian is used in calculation. It is obtained on the basis of numeral finite differences solution of Schrodinger equation for system in magnetic field. We consider and calculate the structure for quantum states of H-like atomic systems in static magnetic field ($Y = B/B_0 = 0.01—10000$; in units: $B_0 = m^2 e^3 c / \hbar^3 Z^3$). We have constructed the effective

representation for the wave function of problem hamiltonian. It is obtained on the basis of the numeral solution for Schrodinger equation within the operator perturbation theory method and the well-known «distorted-wave» approximation in scattering theory (c. f. [8, 11—13]). It is shown that the wave functions and spectrum structure are intermediate between regular structure and chaotic one. The estimates of the resonances widths are presented. We calculate also the energies of high-field ground states of neutral atoms of hydrogen and carbon. The comparison of obtained data with recent calculations results is presented.

2.

The Hamiltonian in the cylindrical coordinates (ρ, z) is (the atomic units are used):

$$\begin{aligned} H\psi(\rho, z) &= E\psi(\rho, z), \\ H &= -\frac{1}{2}\left(\frac{\partial^2}{\partial \rho^2} + \frac{1}{\rho}\frac{\partial}{\partial \rho} + \frac{\partial^2}{\partial z^2} - \frac{m^2}{\rho^2}\right) + V(\rho, z), \\ V(\rho, z) &= -(\rho^2 + z^2)^{-1/2} + 1/8\omega^2\rho^2 + \\ &\quad + \omega m/2 + V_c(\rho, z), \end{aligned} \quad (1)$$

here ω denotes magnetic field (along the z -axis); m is magnetic quantum number ($m = 0, 1, 2, \dots$); V_c is effective potential for an account of field for electron shells of multielectron atom. The paramagnetic term in (1) is dropped when one considers $L_z = 0$. The diamagnetic potential $1/8\omega^2\rho^2$ confines the motion in the direction which is transverse to magnetic field. For solution of equation (1) we use the finite differences method (c. f. [6, 15, 17]). Under the differences solution (1), an infinite region is exchanged by rectangular region: $0 < \rho < L_\rho$, $0 < z < L_z$. It has sufficiently large size; inside it the rectangular uniform grid with steps h_ρ, h_z was constructed. The external boundary condition, as usually, is: $(\partial\psi/\partial n)_r = 0$. The knowledge of the asymptotic behavior for wave function in the infinity allows

to get numeral estimates for L_p , L_z . When $\omega \neq 0$, along axe z , wave function has an asymptotic of the kind as:

$$\exp[-(-2E)^{1/2}r],$$

where $(-E)$ is ionization energy from stationary state to lowest Landau level. Then L can be estimated as $L = 9(-2E)^{-1/2}$. The more exact estimate is found empirically. The differences scheme is constructed as follows. The three-point symmetric differences scheme is used for second derivative on z . The derivatives on r are approximated by $(2m+1)$ -point symmetric differences scheme with the use of Lagrange interpolation formula differentiation. The eigen values of hamiltonian are calculated by means of the inverse iterations method. The corresponding system of inhomogeneous equations is solved by Thomas method. To increase an accuracy of the calculated eigen values, Richardson extrapolation method on the grid step is used (c. f. [6, 15, 17]).

To calculate the values of width G for Zeemane resonance, we have used the operator perturbation theory method (see details in ref. [1, 13—14]). Note that the resonance width is defined by the imaginary part of the state energy in the lowest PT order:

$$\text{Im}E = G/2 = \pi < \Psi_{Eb} | H | \Psi_{Es} > 2$$

with the total Hamiltonian (1).

3.

We have used our approach to calculate the energies for atoms of hydrogen and carbon in magnetic field. Also we have carried out the estimates of the resonances widths G for different energy intervals for hydrogen atom. In tables 1, 2, 3 we present the results of our calculation of the energies for high-field ground states of neutral atoms of hydrogen and carbon. For comparison we also indicate data, which are obtained on the basis of the calculation within the expansion of the problem hamiltonian wave functions as the linear superposition with the use of hydrogen-like (in table it is designated as [*]) and Slater functions (in table — [**]) basis's (c. f. [10]). In table 1 we present the results of calculations for the energies of H and C atoms from ref. [6, 10] on the basis of two-dimensional mesh Hartree—Fock method and operator perturbation theory. The static magnetic field is changed in the interval: $Y = B/B_0 = 0,01—10000$, where units: $B_0 = m^2 e^3 c / h^3 Z^3$. One can note a great difference between presented data. This fact confirms the complexity of the problem considered. Presented data provide an information about the behavior of the neutral atoms of H and C in the complete high-field regime. For the energy interval of $[(n-1/2)\omega < E < (n+1/2)\omega]$ we have found that the resonances widths are $\sim 0,003...0,005$ in the hydrogen atom. This is in good agreement with experimental data [4, 5] and theoretical predictions [7, 8]. For the energy interval of $(-1/2 \omega < E < 1/2 \omega)$, there is the regular dynamics behavior. However, when $E \sim \omega$, there is the chaotic one. Landau levels

Table 1

Energies (in atomic units) of ground states for neutral atom of H

Atom Ref.	Y=0,5	Y=1	Y=2	Y=5
H [*]	-0,88996	-0,66223	—	—
[**]	-0,88910	-0,66049	—	—
[6]	-0,69721	-0,83117	-1,02221	-1,38040
[10]	-0,78656	-0,85980	-1,16605	-1,42620
this work	-0,70965	-0,83979	-1,04486	-1,40005
	Y=10	Y=20	Y=50	Y=100
H [6]	-1,74780	-2,21540	-3,01786	-3,78980
[10]	-1,75821	-2,22890	-3,04369	-3,80322
this work	-1,74998	-2,22042	-3,02682	-3,79854
	Y=200	Y=500	Y=1000	Y=10 000
H [6]	-4,72715	-6,25709	-7,66242	-14,14097
[10]	-4,73942	-6,26854	-7,67380	-15,01276
this work	-4,73002	-6,25999	-7,66852	-14,52542

Table 2

Energies (in atomic units) of ground state ($1s2p_{-1}3d_{-2}4f_{-3}5g_{-4}6h_{-5}$ configuration) for neutral atom of C

Atom Ref.	Y=0,5	Y=1	Y=2	Y=5
C [*]	—	-2,4000	—	—
[6]	-25,1007	-26,7843	-29,4282	-35,1815
this work	-25,4565	-26,9856	-29,6782	-35,9884
	Y=10	Y=20	Y=50	Y=100
C [6]	-42,0799	-52,0890	-71,6285	-92,4552
this work	-42,7895	-52,8619	-72,5113	-92,4571
	Y=200	Y=500	Y=1000	Y=10000
C this work	-120,9211	-169,3792	-218,0992	-481,7904

are strongly mixed [14]. In case of carbon atom, the chaotic dynamics is more complicated.

4.

The analogous method can be formulated for description of Wannier—Mott excitons behavior in semiconductors (CdS , Cu_2O). Schrodinger equation for Wannier—Mott exciton has a standard form:

$$\left[-\frac{\hbar^2 \nabla_e^2}{2m_e^*} - \frac{\hbar^2 \nabla_h^2}{2m_h^*} - \frac{e^2}{\epsilon r_{eh}} + \frac{ie\hbar}{m_e^* c} A(r_e) \nabla_e - \frac{ie\hbar}{m_h^* c} A(r_h) \nabla_h + \frac{e^2}{2m_e^* c^2} A^2(r_e) + \frac{e^2}{2m_h^* c^2} A^2(r_h) \right] \Psi = E \Psi. \quad (2)$$

Here all notations are standard. The vector potential is as follows: $A(r) = 1/2 [\text{Hr}]$. A transition to system of exciton masses center by means of introducing the relative coordinates:

$$r = r_e - r_h \quad \rho = \frac{m_e^* r_e + m_h^* r_h}{(m_e^* + m_h^*)}$$

and canonic transformation for wave function in the form:

$$\Psi(\rho, r) = \exp \left[i \left(K - \frac{e}{\hbar c} A(r) \right) \rho \right] F(r)$$

allow to rewrite the equation (2) as follows:

$$\left[-\frac{\hbar^2 \nabla^2}{2\mu} - \frac{e^2}{\epsilon r} + \frac{ie\hbar}{c} \left(\frac{1}{m_e^*} - \frac{1}{m_h^*} \right) A(r) \nabla + \frac{e^2}{2\mu c^2} A^2(r) - \frac{2e\hbar}{(m_e^* + m_h^*)} A(r) K \right] F = \left(E - \frac{\hbar^2 K^2}{2(m_e^* + m_h^*)} \right) F. \quad (3)$$

Equation (3) then can be solved in cylindrical system of coordinates by the method, described above. Preliminary estimates show this approach in case of strong magnetic field gives the results for Zeeman shift in a reasonable agreement with known results of Elliott and Laudon.

References:

1. Kleppner D., Chun-Ho I., Welch G. R. Irregular Atomic Systems and Quantum Chaos / Ed. J. C. Gay. Kluwer. — N-Y., 1990.
2. Benvenuto F., Casati G., Shepelyansky D. L. Rydberg Stabilization of atoms in strong fields: «magic» mountain in chaotic sea // Z. Phys. B. — 1994. — Vol. 94. — P. 481—486.
3. Dando P. A., Monteiro T. S. Atoms in Static Fields: Chaos or Diffraction? // Photonic, Electronic, Atomic Collisions. — Singapore: World Sci. Pub., 1997. — P. 621—630.
4. Dupret K., Zakrzewski J., Delande D. Resonances in the Diamagnetic Rydberg Spectrum: Order and Chaos // Europhys. Lett. — 1995. — Vol. 31, № 5—6. — P. 251—256.
5. Glushkov A. V., Ivanov L. N. Radiation Decay of Atomic States: atomic residue and gauge noninvariant contributions // Phys. Lett. A. — 1992. — Vol. 170, № 1. — P. 33—37.
6. Ivanov M. V., Schnelcher P. Ground States of H, He, ..., Ne and their singly positive ions in strong magnetic fields: the high-field regime // Phys. Rev. A. — 2000. — Vol. 61. — P. 022505-1—022505-13.
7. Галушков А. В. Negative Ions of Inert Gases // JETP Lett. — 1992. — Vol. 55, № 2. — P. 97—100.
8. Glushkov A. V., Ivanov L. N. DC Strong-Field Stark Effect: consistent quantum-mechanical approach // J. Phys. B:

At. Mol. Opt. Phys. — 1993. — Vol. 26, № 16. — P. L379—L386.

9. Glushkov A. V., Ambrosio S. V. et al. Resonances in Quantum Systems in strong external fields: Consistent Quantum Approach // Journal of Technical Physics. — 1997. — Vol. 38, № 2. — P. 215—218.

10. Kuklina I. V., Shevchuk V. G. H-like and He-like Systems in Superstrong magnetic field: Numerical Calculation // Uzhgorod University Scientific Herald. Series Physics. — 2000. — T. 8, № 2. — P. 361—364.

11. Kuklina I. V. H-like and He-like Systems in Superstrong magnetic field: Numerical Calculation // Proc. International Conf. «Elementary Processes in Atomic Systems». — Uzhgorod (Ukraine). — 2000. — P. 114.

12. Kuklina I. V. Multielectron systems in superstrong magnetic field. Density functional calculations // Proc. International Conf. on Applied Density Functional Theory. — Vienna (Austria). — 2001. — P. 94.

13. Glushkov A. V., Kuklina I. V., Boulham B. Chaos and regular dynamics of complex atomic systems in magnetic field // Proc. XVII International Conf. On Atomic Physics. — Firenze (Italy). — 2000. — P. 517—518.

14. Glushkov A. V., Kuklina I. V., Boulham B. Chaos and regular dynamics of complex atomic and molecular systems in magnetic and laser field // Proc. International Satellite Seminar of ICAP'5 «Atoms, Molecules and Quantum Dots in Laser fields: Fundamental Processes». — Pisa (Italy). — 2000. — P. 70—71.

15. Glushkov A. V., Kuklina I. V. Chaos and regular dynamics of complex atomic in magnetic field // Proc. 32nd International Conf. Of European Group on Atomic Spectroscopy EGAS'32. — Vilnius (Lithuania). — 2000. — P. 165—166.

16. Kuklina I. V. Influence of magnetic field on the Radiation Intensity of Alkali atoms in the hydrogen-oxygen flame // Proc. European Science Foundation REHE School and Workshop on «Spin-Orbit Coupling in Chemical Reactions». — Torun (Poland). — 1998. — P. 18.

17. Kuklina I. V. Numerical Calculation of multielectron Atomic systems in strong magnetic field. Chaos and regular dynamics // Proc. V International Conf. On Atomic and Molecular Physics. — Berlin (Germany). — 2001. — P. A313.

18. Brodin M. C., Blonsky I. V., Nitsovich B. M., Nitsovich B. B. Dynamical Effects in Multicomponent Gas of Quasiparticles. — K.: Nauk. dumka, 1990. — 176 p.

A. V. GLUSHKOV¹, S. V. AMBROSOV², V. M. IGNATENKO²¹ Odessa Hydrometeorological Institute, Odessa, Ukraine² Atomic-Nuclear-Laser Spectroscopy Centre

NONHYDROGENIC ATOMS AND WANNIER—MOTT EXCITONS IN DC ELECTRIC FIELD: PHOTOIONIZATION, STARK EFFECT, RESONANCES IN IONIZATION CONTINUUM AND STOCHASTICITY

DC Stark effect for non-hydrogenic atoms and Wannier—Mott excitons in external uniform electric field is calculated within the modified operator perturbation theory. New adequate model for description of the unique specialities in photoionization spectra of alkali atoms is proposed. The positions of high-excited resonances in ionization continuum are calculated in good agreement with known experiment of Freeman et al. It is noted that the analogous unique specialities may possibly take place in Wannier—Mott excitons spectra in semiconductors (of Cu_2O or CdS type) near threshold boundary.

1.

Observation of dc Stark effect near threshold in alkali atoms led to the discovery by Freeman et al (c. f. [1—3]) of resonances extending into ionization continuum. The unique distinctions in photoionization spectra are connected with the presence of non-hydrogenic core which produces the interference dips below threshold and attenuates the modulations above threshold. Though the known semi-empirical approach of Harmin (c. f. [1—3]) is quite effective, however, the full adequate consistent theory of this phenomena is absent hitherto. Calculation of characteristics for atom in strong electric field remains very important problem of modern atomic physics [1—15]. As it is well known, external electric field shifts and broadens the bound state atomic levels. The standard quantum-mechanical approach relates complex eigen-energies (EE) $E = E_r + 0.5iG$ and complex eigen-functions (EF) to the shape resonances. The calculation difficulties in the standard quantum mechanical approach are well known. The WKB approximation overcomes these difficulties for the states, lying far from «new continuum» boundary and, as rule, is applied in the case of relatively weak electric field. The same is regarding the widespread asymptotic phase method [2, 3], based on Breit—Wigner parameterisation for phase shift dependence on scattering energy. Some modifications of WKB method were introduced by Popov et al and Ostrovsky et al (c. f. [1—3, 5]). Quite another calculation procedures are used in Borel summation of divergent perturbation theory (PT) series and in the numerical solution of difference equations following from expansion of wave-function over finite basis. In ref. [1] it has been developed the consistent uniform quantum — mechanical approach to the non-stationary state problems solution including Stark effect and also scattering problems. The essence of the method is the inclusion of the well known me-

thod of «distorted waves approximation» in the frame of formally exact PT. The zeroth order Hamiltonian H_0 of this PT possesses only stationary bound and scattering states. To overcome formal difficulties, the zeroth order Hamiltonian was defined by the set of orthogonal EF and EE without specifying the explicit form of the corresponding zeroth order potential. In case of the optimal zeroth order spectrum, PT smallness parameter is of the order of G/E , where G and E are field width and bound energy of state level. One can see that $G/E \leq 1/n$ even in the vicinity of the «new continuum» boundary (n is principal quantum number). This method is called as operator PT (OPT) [1]. In ref. [5, 6] the modified versions of OPT approach have been developed for solution of isotopes separation problem and an account of non-hydrogenic effects and also an improvement of convergence procedure. Then it is very important to note that hamiltonian H_0 is defined so that it coincides with the total Hamiltonian H at $\varepsilon \rightarrow 0$ (ε is electric field strength). Note that perturbation in OPT does not coincide with electric field potential though they disappear simultaneously. An influence of the corresponding electric potential model function choice on the values of Stark resonances energies and widths does not significantly change the final results for resonances shifts and widths [1, 6]. The abovesaid is regarding Wannier—Mott exciton in semiconductors (c. f. [16]). It is well known that the availability of excitons in semiconductors resulted in the special form of main absorption band and appearance of discrete levels structure (i. e. hydrogen-like spectra in Cu_2O). Beginning from the known papers of Gross—Zaharchenya, Thomas and Hopfield et al (c. f. [18]), a calculation of Stark effect for exciton attracts a great interest.

In this paper we present a new approach, based on OPT method, for exact calculation of DC Stark effect for non-hydrogenic atoms and Wannier—Mott excitons in external uniform and the corresponding

photoionization spectra in non-hydrogenic atoms. New adequate model for description of the unique distinctions in photoionization spectra of alkali atoms is proposed. The positions of high-excited resonances in ionization continuum are calculated in good agreement with the known experiment of Freeman et al. It is noted that the analogous unique peculiarities may possibly take place in Wannier—Mott excitons spectra near threshold boundary.

2.

As usual, Schrodinger equation for electron function with taking into account the uniform electric field and the field of the nucleus (Coulomb units are used: a unit is \hbar^2/Ze^2m and a unit of mZ^2e^4/\hbar^2 for energy) looks as

$$[-(1 - N/Z)/r + ez - 0,5\Delta - E]\psi = 0, \quad (1)$$

where E is electron energy, Z — nucleus charge, N — number of electrons in atomic core. Our approach allow to use more adequate forms for core potential (c. f. [10—15]), including the most consistent quantum electrodynamics procedure for construction of optimized one-quasi-electron representation and ab initio core potential, providing the spectroscopic accuracy. After separation of variables equation (1) in parabolic co-ordinates transformed to the system of two equations for the functions f, g :

$$f'' + \frac{|m|+1}{t} f' + \left[0,5E + \frac{\beta_1 - N/Z}{t} - 0,25\varepsilon(t)t\right] f = 0, \quad (2)$$

$$g'' + \frac{|m|+1}{t} g' + [0,5E + \frac{\beta_2}{t} + 0,25\varepsilon(t)t] g = 0 \quad (3)$$

coupled through the constraint on separation constants: $\beta_1 + \beta_2 = 1$. For the uniform electric field $\varepsilon(t) = \varepsilon$. Potential energy in equation (4) has the barrier. Two turning points for the classical motion along the η axis, t_1 and t_2 , at the given energy E are the solutions of the quadratic equation ($\beta = \beta_1, E = E_0$). In ref. [7], the uniform electric field ε in (3) and (4) was substituted by model function $\varepsilon(t)$ with parameter τ ($\tau = 1,5t_2$). Here we use another function, which satisfies to necessary asymptotic conditions (c. f. [7]):

$$\varepsilon(t) = \frac{1}{t} \varepsilon \left[(t - \tau) \frac{\tau^2}{\tau^2 + t^2} + \tau \right]. \quad (4)$$

The final results do not depend on parameter τ . To calculate the width G of the concrete quasi-stationary state in the lowest PT order it is necessary to know two zeroth order EF of H_0 : bound state function $\Psi_{Eb}(\varepsilon, \nu, \varphi)$ and scattering state function $\Psi_{Es}(\varepsilon, \eta, \varphi)$ with the same EE. First, one has to define the EE of the expected bound state. It is the well known problem of states quantification in case of penetrable barrier. We solve the (2, 3) system with the total Hamiltonian H under the conditions [1, 5, 6]:

$$f(t) \rightarrow 0 \text{ at } t \rightarrow \infty$$

and

$$\frac{\partial x(\beta, E)}{\partial E} = 0 \quad (5)$$

with

$$x(\beta, E) = \lim_{t \rightarrow \infty} \left[g^2(t) + \left(\frac{g(t)}{k} \right)^2 \right] t^{|m|+1}.$$

These two conditions quantify bound energy E , separation constant β_1 . The further procedure for this two-dimensional eigenvalue problem is resulted in the solution for the system of ordinary differential equations(2, 3) with probe pairs of E, β_1 . The bound state EE, eigenvalue β_1 and EF for the zero order Hamiltonian H_0 coincide with those for the total Hamiltonian H at $\varepsilon \rightarrow 0$, where all the states can be classified due to quantum numbers: n, n_1, n_2, m (principal, parabolic, azimuthal) that are connected with E, β_1, m by the well known expressions. We preserve the n, n_1, m states-classification in $\varepsilon \neq 0$ case. The scattering state functions must be orthogonal to the above defined bound state function and to each other. According to OPT ideology [7], the following form of g_{Es} is possible:

$$g_{Es}(t) = g_1(t) - z'_2 g_2(t) \quad (6)$$

with f_{Es} and $g_1(t)$ satisfying the differential equations (2) and (3). The function $g_2(t)$ satisfies the non-homogeneous differential equation, which differs from (3) only by the right hand term, disappearing at $t \rightarrow \infty$. The coefficient z'_2 ensures the orthogonality condition and can be defined as:

$$z'_2 = \frac{\iint d\zeta d\eta (\zeta + \eta) f_{Es}^*(\zeta) g_{Eb}(\eta) g_1(\eta)}{\iint d\zeta d\eta (\zeta + \eta) f_{Es}^*(\zeta) g_{Eb}(\eta) g_2(\eta)}.$$

The imaginary part of state energy in the lowest PT order is:

$$\text{Im } E = G/2 = \pi < \Psi_{Eb} | H | \Psi_{Es} > 2 \quad (7)$$

with the total Hamiltonian H (G -resonance width). The state functions Ψ_{Eb} and Ψ_{Es} are assumed to be normalized to unity and by the $\delta(k-k')$ -condition, accordingly. Photoionization cross section can be define as follows:

$$\sigma^F = \frac{4\pi^2 \hbar \omega}{137} \times \sum_{i, l'} < 0 | r_m | \Psi_r > [< \Psi' | \Psi >^{-1}]_{l, l'} < \Psi_l | r_m | 0 >, \quad (8)$$

where $|0\rangle$ is initial state of the atom, $r_m = z$ for π -polarized light and $r_m = (1/\sqrt{2})(x \pm iy)$ for σ -polarization; $< \Psi_r | \Psi_l >$ — overlap matrix of the set $\{\Psi\}$ (see details of its definition in [1] and cited ref. there). Note then that the whole calculation procedure at the known resonance energy E and separation parameter β has been reduced to the solution of one system of the ordinary differential equations. For its solution it is used our numeral atomic code [1—3, 10—15].

3.

The calculation results for Stark resonances energies and widths for some states of H atom are presented in table 1. For comparison we have indicat-

ed the data, obtained within other approaches: WKB-approximation, the summation of divergent PT series, numerical solution of differential equations, standard OPT [1—3, 6]. In table 2 the calculated and experimental energy positions of Stark resonances in the photoionization spectrum of Na $3^2P_{3/2}$ in a field 3,59 kV/cm are presented.

Table 1
The energies and widths of Stark resonances of hydrogen atom¹

(n n ₁ n ₂ m)	e	Method	E _r (at. units)	G (at. units)
2 0 0 1	0,010	G	0,1342	0,636 · 10 ⁻²
		A	0,1345	0,637 · 10 ⁻²
		C	0,1345	0,628 · 10 ⁻²
2 0 1 0	1,8 · 10 ⁻⁴	G	0,2061	0,277 · 10 ⁻⁵
		A	0,2062	0,278 · 10 ⁻⁵
		B	0,2062	0,228 · 10 ⁻⁵
		D	0,2062	0,228 · 10 ⁻⁵
		F	0,2062	0,222 · 10 ⁻⁵

Table 2
Photoionization spectrum of Na $3^2P_{3/2}$ in a field 3,59 kV/cm: energies positions of resonances (in 10 cm⁻¹)

State	Theory	Experiment
(22,2) m=0	2438,9	2439,3
(23,0) m=0	2439,5	—
(23,1) m=0	2440,2	2440,8
(23,2) m=0	2441,3	—
(24,0) m=0	2442,1	2442,4
(24,1) m=0	2442,7	2443,1
(25,0) m=0	2444,0	—
(26,0) m=0	2445,8	2446,3
(22,0) m=1	2438,7	2439,2
(22,1) m=1	2439,8	—
(23,0) m=1	2441,1	2441,5
(24,0) m=1	2443,3	—

4.

The analogous method can be formulated for description of Stark effect in Wannier—Mott excitons in semiconductors (CdS, Cu₂O). Schrodinger equation for Wannier—Mott exciton has standard form:

$$\left[\frac{\hbar^2 \nabla_e^2}{2m_e^*} + \frac{\hbar^2 \nabla_h^2}{2m_h^*} - \frac{e^2}{\epsilon r_{eh}} - eEr_e - eEr_h \right] \Psi = E\Psi. \quad (9)$$

Here all notations are standard. A vector potential is as follows: $A(r) = 1/2 [Hr]$. Transition to system of exciton masses centre by means of introducing the relative coordinates:

$$r = r_e - r_h \quad \rho = \frac{m_e^* r_e + m_h^* r_h}{(m_e^* + m_h^*)},$$

¹ A — Glushkov and Ivanov (1992); B — Damburg, Kolosov (1976); C — Kolosov (1989); D — Benassi, Grecchi (1988); F — Popov et al (1992); G — present paper.

one can rewrite (9) as:

$$\left[-\frac{\hbar^2 \nabla^2}{2\mu} - \frac{e^2}{\epsilon r} - \frac{\hbar}{2} \left(\frac{1}{m_h^*} - \frac{1}{m_e^*} \right) K \cdot p - eEr \right] F = \left[E - \frac{\hbar^2 K^2}{8\mu} \right] F.$$

This equation then can be solved by the method, described above. Preliminary estimates show the this approach in a case of electric field gives the results for Stark states in reasonable agreement with the known results of Thomas and Hopfield (TH). Stark shift for the 2S and 2P_z states of excitons in CdS semiconductor at electric field strength 600 V/cm is 5,6 · 10⁻⁴ eV (TH), our result — 5,2 · 10⁻⁴ eV. The states 2S and 2P_z in CdS in electric field are mixing. Under weak electric fields the quadratic Stark effect takes place. Ionization of exciton in electric field occurs if a change of potential on a distance (the orbits diameter) is comparable with bond energy of particle on this orbit. According to data of Thomas and Hopfield, the corresponding electric field is 500 V/cm. For CdS the absorption lines, which correspond to exciton of large radius (n > 3), are broadening and fusing. Near ionization boundary, hydrogen atom has the behaviour of quantum chaotic system, including the diffusion mechanism of ionization. Besides, for non-H atoms there are unique especialities in photoionization spectra (alkali atoms). Probably, the analogous unique especialities may take place in Wannier—Mott excitons spectra in semiconductors (of Cu₂O or CdS type) near threshold boundary. One can suppose very interesting mechanism of exciton ionization under different values of electric field strength.

References:

1. Glushkov A. V., Ivanov L. N. DC Strong-Field Stark-Effect: consistent quantum-mechanical approach // J. Phys. B: At. Mol. Opt. Phys. — 1993. — Vol. 26, № 16. — P. L379—L386.
2. Glushkov A. V., Ambrosov S. V., Ignatenko V. M., Prepelitsa G. P. Stochastic instability of multioscillator systems and highly excited atoms in electromagnetic field and chaotic dynamics of diatomic molecules in resonance high-intensity IR field // Proc. V International Conf. On Atomic and Molecular Physics. — Berlin (Germany). — 2001. — P. A313.
3. Glushkov A. V., Ignatenko V. M. Photoionization spectra of alkali atoms in a dc electric field: New model and new results // Proc. European Science Foundation REHE School and Workshop on «Spin-Orbit Coupling in Chemical Reactions». — Torun (Poland). — 1998. — P. 19.
4. Ivanov L. N., Ivanova E. P., Knight L. Energy Approach to consistent QED theory for calculation of electron-collision strengths // Phys. Rev. A. — 1993. — Vol. 48, № 6. — P. 4365—4374.
5. Glushkov A. V., Ambrosov S. V., Shpinareva I. M. et al. Resonances in Quantum Systems in strong external fields: Consistent Quantum Approach // Journal of Technical Physics. — 1997. — Vol. 38, № 2. — P. 215—218.
6. Shumlyansky I. I., Shevchuk V. G., Ignatenko V. M., Prepelitsa G. P. Atom of hydrogen in a strong uniform electric field: Modified operator perturbation theory method // Uzhgorod University Scientific Herald. Series Physics. — 2000. — T. 8, Ч. 2. — C. 372—375.
7. Kleppner D., Chun-Ho I., Welch G. R. In: Irregular Atomic Systems and Quantum Chaos / Ed. J. C. Gay. Kluwer. — N-Y., 1990.

- 3rd Symposium on Atomic Spectroscopy. — Chernogolovka (Russia). — 1992. — C. 113—125.
13. *Glushkov A. V., Dan'kov S. V., Prepeliitsa G. P et al.* QED Theory of nonlinear Interaction of the complex Atomic Systems with Laser field. Multiphoton Resonances // J. Techn. Phys. — 1997. — Vol. 38, № 2. — P. 219—224.
14. *Glushkov A. V.* Deuterium lines spectra analysis in Tokamak // Proc. 24th Europ. Conf. on Thermonucl. Fusion & Plasma Phys. — Garching (Germany). — 1996. — P. 95.
15. *Ivanova E. P., Ivanov L. N., Glushkov A. V., Kramida A. E.* High order corrections in the Relativistic Perturbation Theory with the model Zeroth Approximation, Mg-like and Ne-like ions // Phys. Scripta. — 1985. — Vol. 32, № 4. — P. 512—524.
16. *Brodin M. C., Blonsky I. V., Nitsoyich B. M., Nitsoyich B. B.* Dynamical Effects in Multicomponent Gas of Quasiparticles. — K.: Nauk. dumka, 1990. — 176 p.

SELECTIVE PHOTOIONIZATION OF ATOMS AND MOLECULES IN ELECTRIC FIELD: NEW MODELS

Within the consistent quantum mechanical approach we have studied the selective resonance excitation of atoms by laser radiation and further ionization decay of excited states under action of external electric field. New numeral models are proposed and realized for ionization of alkali atoms (Na, Rb) in electric field. We also propose a new method to calculate the energies and ionization characteristics for molecules in electric field.

1.

One of the most effective approaches to the solution of laser separation for isotopes and nuclear isomers is a method of selective ionization of atoms, based on the selective resonance excitation of atoms by laser radiation into states near ionization boundary and further photo-ionization of excited states by additional laser radiation field or ionization of autoionization resonances by an electric field. It has firstly proposed and realized in laboratory conditions by Letokhov (c. f. [1—8]). Electric field changes the electron spectra so that the part of discrete spectra levels (near the ionization boundary) partly moves into continuum and the other levels become the autoionization ones. The probability of their autoionization decay quickly increases with growth of the main quantum number. The most optimal situation is when atom is excited up to the state, which it has autoionization probability more than radiation decay one. To receive accurate information about optimal scheme for selective ionization of atom by light and electric field, it is necessary to carry out the accurate calculation for the process of sequent excitation of atoms by laser field (it is trivial task) and probability of ionization of the highly excited atoms by electric field. Such a problem is exactly solved for hydrogen atom, but in case of multielectron atom it is quite complicated one. In this paper we propose new numerical models and their realizations for ionization of alkali atoms (Na, Rb) in electric field and also a new method to calculate energies and ionization characteristics of molecules in electric field. From the mathematical point of view these problems are quite similar.

An effective potential energy of electron in electric field is:

$$V(r) = -1/r - Ez. \quad (1)$$

It has maximum value on a distance $r_{\max} \sim E^{-1/2}$ along axis z and equal to $V(r_{\max}) \sim -2E^{1/2}$. Autoionization of H-like atom from down states of highly lying terms is quite well described in hydrogen-like approximation, but behaviour of the upper compo-

nents is drastically differed from down ones. The error in description of these states in H-like approximation is $> \sim 15-20\%$. This is essentially more than the experimental inaccuracy.

We consider non-H-like (alkali atoms) atom with electron in excited state n in electric field with strength E . In ref. [4—7] we have proposed a new effective method of solution for Stark problem for multielectron atom in electric field. Transition to parabolic co-ordinates and separation of variables due to the use of model potentials of special form gives the corresponding basis of atomic wave functions Ψ . Probability of autoionization decay in electric field is defined as follows:

$$W = \int_0^\infty |\Psi|^2 V_z 2\pi r dr, \quad (2)$$

where V is velocity of electron in z direction. Note that the analogous expression for probability in H-like approximation is defined by the known expression [1]:

$$W = \frac{1}{n^3} \left(\frac{4}{en^2} \right)^{2n_2 + |m| + 1} \left[\frac{1}{n_2!} (n_2 + |m|)! \right] \times \exp \left[-\frac{2}{3} en^3 + 3(n_1 - n_2) \right]. \quad (3)$$

In case of atomic ionization by pulsed field, the probability of process is defined by the following expression:

$$W(nlm) = \sum_{n_2} (a_{n_1 n_2}^{nlm})^2 W(n_1 n_2 m),$$

where $W(n_1 n_2 m)$ is $\Psi_{n_1 n_2 m}$ states decay probability; a are the coefficients for expansion of $y(nlm)$ functions on parabolic functions $\psi(n_1 n_2 m)$. To reach the effective optimal situation, it is necessary to switch on the field for time which is small in comparison with excited state radiation decay time. To find the expansion coefficients, we have elaborated the numerical procedure for calculation of the corresponding matrix elements and the matrix diagonalization. In real multi-electron atom it is necessary to account for the influence of electron shells, which results in changing potential barrier and wave func-

tions. To define the wave functions and electron states energies in external electric field, one needs to carry out the diagonalization of energy matrix, calculated between states with the same n . In table 1 we present the calculated values for characteristics of the most quickly decayed states for the Rb atom (field strength $3 \cdot 10^4$ V/cm; $n = 7-12$).

Table 1
The characteristics
of the most quickly decayed states for Rb atom
(field strength $3 \cdot 10^4$ V/cm; $n = 7-12$)

n	7	8	9	10	11	12
$E, \text{ cm}^{-1}$	31405	31904	32229	32456	32614	32761
n_2^*	4,7	5,8	7,0	8,0	8,9	9,0
a_f^2	0,27	0,26	0,14	0,14	0,015	0,13
a_s^2	$< 10^{-6}$	$< 10^{-6}$	$< 10^{-5}$	$< 10^{-5}$	$6 \cdot 10^{-5}$	0,024
a_p^2	$< 10^{-6}$	$9 \cdot 10^{-6}$	$2,6 \cdot 10^{-5}$	0,0002	0,0028	0,17
a_d^2	0,00029	0,0008	0,0038	0,016	0,047	0,009

Note that our results are differed from the analogous data of ref. [8] (probably more exact data because of the use of relativistic model). The influence of electron shells leads to more sharp dependence of decay probability upon number n . Thus, one can realize a scheme of the selective photo-ionization of atoms by means of resonance excitation into states near ionization boundary (the optimal scheme requires the accurate estimates of atomic characteristics); then these states undergo to autoionization decay in a weak electric field (< 30 kV/cm). In fig. 1 we present the results of calculation for dependence of ionization velocity of excited atom upon the electric field strength for states with quantum numbers $n = 8, \dots, 16$ and $m = 0, n_2 = n - 1$. In fig. 2 we present our calculation results regarding critical electric field strength in dependence upon effective quantum number n^* for atoms of Na, Rb (dots — experimental data; line 1 is theoretical estimate from classical relation $E \sim 1/16n^*$ without account of

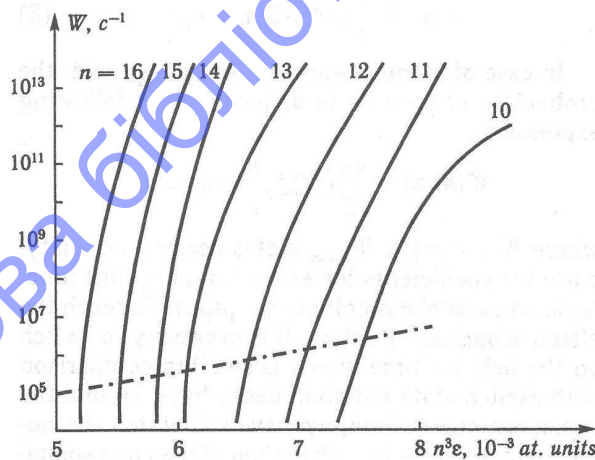


Fig. 1. Dependence of ionization velocity of excited atom upon electric field strength for states with quantum numbers $n = 8, \dots, 16$ and $m = 0, n_2 = n - 1$; The dashed line shows radiation decay velocity

Stark shift and electron tunnelling effect [1]; line 2 is calculation on the basis of expression (3); dashed

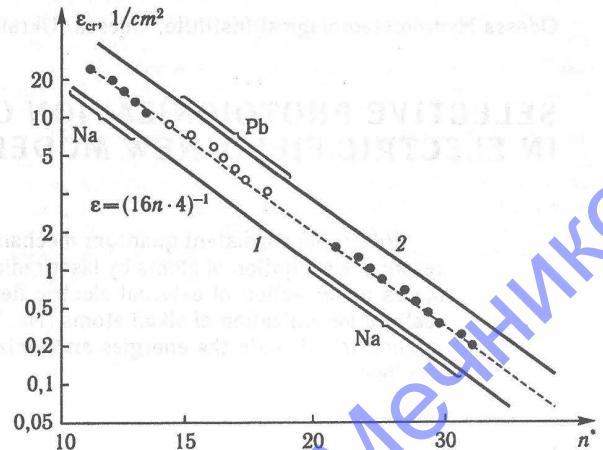


Fig. 2. Dependence of critical electric field strength upon effective quantum number n^* for Na, Rb

dots — experiment; 1 — classical theoretical estimate; 2 — calculation on the basis of (3); dashed line is corresponding to (2)

line is corresponding to our results on the basis of (2)). One can see that H-like approximation gives the inaccuracy 15—20%. Consider in details the selective ionization scheme for the Na (Na vapours at temperature 450 K). The first ionization step: excitation of Na atoms to state $3p^2P_{1/2}$ and then photoionization by laser pulse: excitation cross-section $\sigma_1 = 10^{-11} \text{ cm}^2$, ionization cross-section from excited state: $\sigma_2 = 10^{-17} \text{ cm}^2$, from ground state $\sigma_2 \sim 10^{-19} \text{ cm}^2$ [1]. For selective photoionization scheme with excitation to Rydberg S and D states with $n = 12 \dots 18$ and further ionization by electric field ($E = 10 \text{ kV/cm}$) our calculation (cross-section is defined in standard way) gave the values: for $3^2P_{1/2} - 15^2D_{3/2}$ transition $\sigma_2 = 0,76 \cdot 10^{-14} \text{ cm}^2$, experimental value: $\sigma_2 = 0,7 \cdot 10^{-14} \text{ cm}^2$. So, selective photoionization scheme with use of Rydberg states is to be quite effective especially from energetic point of view (but the ionization output here $< 100\%$).

2.

Now we consider a new method to calculate energies, widths and ionization characteristics of diatomic molecules in electric field. Hamiltonian in the cylindrical coordinates (ρ, z) is (the atomic units are used):

$$H \psi(\rho, z) = E \psi(\rho, z), \quad (4)$$

$$H = -\frac{1}{2} \left(\frac{\partial^2}{\partial \rho^2} + \frac{1}{\rho} \frac{\partial}{\partial \rho} + \frac{\partial^2}{\partial z^2} - \frac{1}{[(z + R/2)^2 + \rho^2]^{1/2}} - \frac{1}{[(z - R/2)^2 + \rho^2]^{1/2}} - Ez + V(\rho, z) \right).$$

Here E denotes an electric field; V_c is effective potential for an account of field of molecular electron shells. For solution of equation (1) we use the finite differences method (c. f. [9]). Under the differ-

ences solution (1), an infinite region is exchanged by a grid (ρ , $L_z < z < L_z$). For $z < 0$ it is used the condition of the smallness of wave function on the boundary. For $z > 0$ the boundary condition has the form of plane divergent wave: It has sufficiently large size; inside it a rectangular uniform grid with steps h_ρ , h_z was constructed. The differences scheme is constructed in the same way as the known Ivanov model [9]. The eigen values of hamiltonian are calculated by means of inverse iterations method. The corresponding system of inhomogeneous equations is solved by Thomas method. To calculate the width of energy state we use the standard operator perturbation theory formalism of Glushkov—Ivanov [2]. As the example, we present in table 2 the results of

Table 2
Energies and widths for molecular ion of H_2^+
under electric field

Electric field (atomic units)	Energy		Width	
	[9]	present	[9]	present
0,02	-0,6037	-0,6041	—	—
0,04	-0,6069	-0,6072	—	—
0,06	-0,6130	-0,6135	$2,23 \cdot 10^{-11}$	$2,23 \cdot 10^{-11}$

our calculation for energy and width for molecular ion of H_2^+ and also data of Ivanov [6]. Preliminary results are also received for non- H_2^+ molecules (hydrogen molecule) and will be published in the separate paper. Here we only note that such an approach for non- H_2^+ systems is proposed at first.

References

1. Letokhov V. S. Nonlinear Selective Photoprocesses in atoms and molecules. — M, 1997. — 480 p.
2. Glushkov A. V., Ivanov L. N. DC Strong-Field Stark-Effect: consistent quantum mechanical approach // J. Phys. B: At. Mol. Opt. Phys. — 1993. — Vol. 26, № 16. — P. L379—86.
3. Ambrosov S. V., Shpinareva I. M. Selective Ionization of Atoms by Electric and Light Field. Autoionization Rydberg Resonances in Heavy Atoms. Optimal Isotope-Separation Selective Molecular Vibration Levels Excitation Schemes // Proc. 32nd Europhys. Conference EGAS. — Vilnius (Lithuania). — 2000. — P. 197.
4. Shpinareva I. New Quantum Mechanical Method to Calculation of Autoionization Resonances in Heavy Atoms in Electric Field: Gd, Tm. Optimal Schemes of Selective Ionization of Atoms by Electric, Laser field // Proc. 5th Europ. Workshop «Quantum Systems in Phys. & Chem.». — Uppsala (Sweden). — 2000. — P. 131.
5. Glushkov A. V., Ambrosov S. V., Shpinareva I. M. et al. Resonances in Quantum Systems in Strong External Fields: Consistent Quantum Approach // J. Techn. Phys. — 1997. — Vol. 38, № 2. — P. 215—219.
6. Glushkov A. V., Ambrosov S. V., Shpinareva I. M. et al. Resonances in Quantum Systems in Strong External Fields: Nonlinear Effects. Autoionization Resonances in Tm // J. Techn. Phys. — 1997. — Vol. 38, № 2. — P. 211—
7. Shpinareva I. M. Selective photoionization of atoms by light and electric field: optimal constants for elementary processes and schemes; Preprint / Nauchno-Issledov. Institute for physics of I. I. Mechnikov's Odessa National University; Ph-L-3-00. — Odessa, 2000. — 8 p.
8. Ambrosov S. V. Relativistic Stark Effect and selective ionization in electric field. — Preprint / Nauchno-Issledov. Institute for physics of I. I. Mechnikov's Odessa National University; Ph-L-5-01. — Odessa, 2001. — 9 p.
9. Ivanov M. Grid calculation of energies and widths for ground state of H molecular in string electric field // Opt. Spectr. — 1994. — Vol. 78, № 5. — 711—713.

STRUCTURE OF GROUND STATE OF SUPERATOM. IONIZED SUPERATOM AS SINGLE ELECTRONS COUNTER

Calculation of the structure for the ground state of superatom (spherical nucleus of some semiconductive material, alloyed selectively by donors and surrounded by non-admixed matrix of the material with lesser forbidden gap) is carried out within a new ab initio method [1—3]. It is based on QED and quantum mechanical perturbation theory method and polarization functional formalism. It is shown for superatom (nucleus: $\text{Al}_{0.35}\text{Ga}_{0.65}\text{As}$; nuclei charge $Z = 20$; nucleus radius: 180 Å; matrix: GaAs) that the configuration $1s^2 2p^6 3d^{10} f^2$ is corresponding to the ground state of system and the superatoms radius is ~ 420 Å. Possible application of the ionized superatom as the single electrons requires to develop a model for superatoms ionization in external electric that may be done by analogy with the theory for ionization of atoms. The value for ionization energy of superatom considered is 1,3 meV.

In last years a great interest attracts the study of bound states energies for the following systems: superatom and 1D super-lattice (c. f. [1—3] and refs. there). Superatom represents the spherical nucleus of some semiconductive material, alloyed selectively by donors and surrounded by non-admixed matrix of the material with less forbidden gap. All these systems can be calculated on the basis of the same unified quantum mechanical method. Especial interest attracts the calculation of configuration that is corresponding to the ground state of superatom under different values of nucleus radius and model potential parameters. In ref. [1—3] a new quantum approach to calculations of energy characteristics for systems above cited has been proposed. It based on perturbation theory with effective potential of the zeroth order (energy approach), ab initio quasi-particle density functional formalism (Dirac—Kohn—Sham—Ivanov schemes). In [3] the calculation of superatom structure under nucleus radius 120 Å (other parameters see in [3]) has been carried out and the configuration of the ground state as $1s^2 2p^6 3d^{10} 2s^2$ and value of superatom radius 390 Å has been obtained. In this work the calculation of ground state configuration for superatom is carried out within [1—3] under the other values of parameters and, in particular, it is shown for superatom (nucleus: $\text{Al}_{0.35}\text{Ga}_{0.65}\text{As}$; nuclei charge $Z = 20$; nucleus radius: 160 Å; Matrix: GaAs) that configuration $1s^2 2p^6 3d^{10} f^2$ is corresponding to ground state of system and superatoms radius is ~ 420 Å.

Let us give the comments regarding calculation method. The zeroth approximation is usually generated by effective ab initio model functional, constructed on the basis of gauge invariance principle. (c. f. [6—9]). The wave functions zeroth basis can be defined from Schrodinger equation with spherically symmetric potential which includes the potential of ionized donors, Hartree—Fock—Kohn—Sham functional and the positive difference of minimums

for nucleus and matrix conductivity zones. The non-relativistic Schrodinger equation:

$$\Psi'' + \frac{2}{r}\Psi' + \frac{2m}{\hbar^2} \left[E - V(r) - \frac{l(l+1)}{r^2} \right] \Psi = 0, \quad (1)$$

where Ψ is radial part of wave function, E — energy of system, l — orbital quantum number, r — distance from center of nucleus, the other designations are standard. Effective potential V for super atom is supposed to be by spherically symmetric and has the following form:

$$V(r) = V_0 \theta(r_0 - r) + V_N(r) + V_H + V_{xc}(r), \quad (2)$$

where r_0 is nuclear radius, V_0 — the positive difference of minimums for nucleus and matrix conductivity zones; $\theta(x) = 0$, $x < 0$ and $= 1$ if $x > 0$; V_N is ionized donors potential. For Hartree potential V_H and exchange-correlation potential V_{xc} there are usually used approximations known in atomic structure calculations. The shape of potential (2) is presented in Fig. 1 The correlation corrections of the high orders can be taken into account within Green

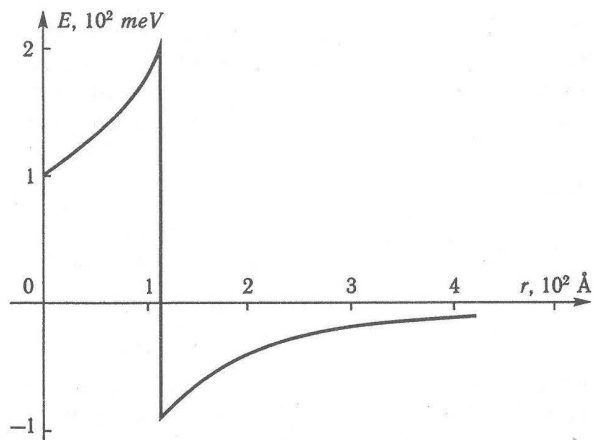


Fig.1. Potential of superatom, according the formula (2).

functions method and relativistic polarization functional formalism [8—10]. We take into account for all correlation corrections of the second order and dominated classes of the higher orders diagrams (electrons screening, particle-hole interaction, mass operator iterations).

It is very important to note that nuclear diameter in the superatom is compared with general size of system and there is absent the singularity in coordinates center in despite from the heavy atoms case. That is why, the levels with large angular momentum (maximum of wave function is lying far from nucleus than for s-states) become more energetically profitable. We have carried out the calculation of superatom system (nucleus: $\text{Al}_{0.35}\text{Ga}_{0.65}\text{As}$; nuclei charge $Z = 20$; matrice: GaAs) and obtained the corresponding sequence of energy levels $1s^2 2p^6 3d^{10} 2f^2$ under nucleus radius 180 Å. The superatoms radius is estimated as 420 Å. It is differed from known results of Watanabe—Inoshita and result of [3] for superatom: nucleus: $\text{Al}_{0.35}\text{Ga}_{0.65}\text{As}$, nuclei charge $Z = 20$, configuration of ground state $1s^2 2p^6 3d^{10} 2s^2$, superatom radius 390 Å.

In conclusion we note that quite possible perspective application of superatom system is to create the single electrons counter on the basis of ionized superatom and memory cells for computer systems on the basis of superatoms massive (c. f. [1—3] and refs. there). A model for ionization of superatom system in external electric field may be naturally developed on the basis of the corresponding theory of ionization of atoms (c. f. [8]). Preliminary estimate for ionization energy of superatom considered

here is 1,3 meV. Thus it is possible to change its state by means of sufficiently little external field.

References:

1. Loboda A. V. Quantum Calculation of Superatoms structure and its application in massive memory cells // Proc. V International Conf. On Atomic and Molecular Physics. — Berlin (Germany). — 2001. — P. A314.
2. Loboda A. V. Density Functional Approach to multistable systems on Semiconductors and two-level mediums. Density Functional and Response Functions approach in the neural networks theory // Proc. International Conf. on Applied Density Functional Theory. — Vienna (Austria). — 2001. — P. 97.
3. Glushkov A. V., Loboda A. V., Zuda M. Bound states in quarkonium and superatoms systems: energy levels splitting // Uzhgorod University Scientific Herald. Series Physics. — 2000. — № 8, P. 2. — C. 394—397.
4. Loboda A. V., Loboda N. S., Glushkov A. V. Dynamics of interaction of atom with laser field. Photon Echo and its use in the theory of neural networks // Uzhgorod University Scientific Herald. Series Physics. — 2000. — № 8, P. 2. — C. 328—332.
5. Loboda A. V., Loboda N. S., Glushkov A. V. Dynamics of polarization of the two-level medium in a laser field. Photon Echo and its applications in the neural networks theory // Proc. International Conf. «Elementary Processes in Atomic Systems». — Uzhgorod (Ukraine). — 2000. — P. 118.
6. Glushkov A. V., Ivanov L. N. Radiation Decay of Atomic States: atomic residue and gauge noninvariant contributions // Phys. Lett. A. — 1992. — Vol. 170, № 1. — P. 33—37.
7. Glushkov A. V. Negative Ions of inert Gases // Pis'ma to JETP. — 1992. — T. 55, № 2. — C. 104—107; JETP Lett. — 1992. — Vol. 55, № 2. — P. 97—100.
8. Glushkov A. V., Ivanov L. N. DC Strong-Field Stark-Effect: consistent quantum-mechanical approach // J. Phys. B: At. Mol. Opt. Phys. — 1993. — Vol. 26, № 16. — P. L379—L386.
9. Ivanova E. P., Ivanov L. N., Glushkov A. V., Kramida A. E. High order corrections in the Relativistic Perturbation Theory with the model Zeroth Approximation, Mg-like and Ne-like ions // Phys. Scripta. — 1985. — Vol. 32, № 4. — P. 512—524.

SELECTIVE PHOTOIONIZATION OF ATOMS BY LASER FIELD: OPTIMAL SCHEME. AUTOIONIZATION RYDBERG RESONANCES IN HEAVY ATOMS

Within the consistent relativistic quantum mechanical approach we have studied the selective resonance excitation of atoms by laser radiation into states near ionization boundary and further autoionization decay of excited states under action of external electric field. We have carried out the theoretical study of autoionization resonances (AR) in multielectron heavy atoms (rare earth atoms: Yb, Tm etc.) in the external electric and laser field. An effect of the giant AR widths broadening in relatively weak external field is calculated within relativistic quantum approach to Stark effect for autoionization resonances. Two AR decay channels (traditional Beutler-Fano channel and new reorientation decay one) are examined. An appreciable dependence of the reorientation decay velocity at the moderately weak (~ 100 V/cm) electric field is analyzed. The optimal selective photoionization scheme presumes the compromise between the high excitation probability and high decay rate that determines the lower and upper boundaries for the AR decay rate.

The method of selective ionization of atoms, based on selective resonance excitation of atoms by laser radiation into states near ionization boundary and further photo-ionization of excited states by additional laser radiation, has been firstly proposed and realized by Letokhov (c. f. [1]). This method represents a great interest for laser separation of isotopes and nuclear isomers. Due to the known significant disadvantage for two-step selective ionization of atoms by laser radiation method, quite perspective photoionization scheme bases on the usage of autoionization levels. Hitherto, detailed data about AR for many atoms are often absent. Letokhov—Ivanov (c. f. [1]) have considered the possibility of selective ionization of atoms, based on selective resonance excitation of atoms by laser radiation into states near ionization boundary and further ionization decay of excited atoms by external electric field. Electric field changes electron spectra so that the part of discrete spectra levels (near the ionization boundary) partly moves into continuum and the other levels become the autoionization ones. The probability of their autoionization decay quickly increases with growth of the main quantum number. The most optimal situation is when atom is excited to state, which has the autoionization probability more than the radiation decay one. To receive accurate information about optimal scheme for selective ionization of atom by light and electric field, it is necessary to carry out the accurate calculation for the process of sequent excitation of atoms by laser field (it is trivial task) and probability of ionization of the highly excited atoms by electric field. Significant step in this direction has been undertaken by Shpinareva (c. f. ref. [2]). The accurate calculations of elementary atomic processes in different photoionization schemes were carried out, including photoionization schemes with the use of

AR. As a rule, non-relativistic approximation has been used. More consistent approach to solution of such a problem must be based on relativistic models, as the most interesting elements for laser isotopes separation are heavy and the role of relativistic corrections is often very dramatic. In this paper we have carried out the theoretical study of autoionization resonances (AR) in multielectron heavy atoms (rare earth atoms: Yb, Tm etc.) in external electric and laser field. An effect of giant AR widths broadening in relatively weak external field is calculated within relativistic quantum approach to Stark effect for autoionization resonances.

The effect of electric field on autoionization states (AS) is interesting from several points of view (c. f. [1—10]). One can note a great role of AS in many processes in plasma and gases. Their account is important for correct determination of excitation and de-excitation rates of ions in dense plasma and in examination of dielectron recombination in plasma. Especially interesting effects occur in the complex heavy atom when its broad autoionization resonances mix with much narrower resonances of opposite parity by means the external electric field. We consider Tm atom, which represents the undoubted interest for experimental spectroscopy, in controlling the population and decay kinetics of excited states or the selective ionization under laser radiation action [1—3, 10]. In ref. [2—4] calculation for the behaviour of Tm AS in weak electric field and effect of drastic broadening of reorientation type AR (at first this effect has been discovered by Glushkov and Ivanov; c. f. [4]) already in the field were calculated. Here we will receive the more accurate numeral data. We use here a new relativistic quantum mechanical approach to Stark problem for heavy atomic systems (c. f. [2]). The main autoionization decay channels for Tm states are illustrated in fig. 1.

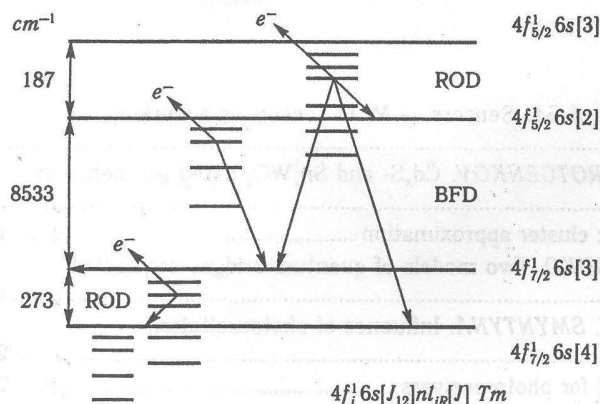


Fig 1. Position of near lying first ionization limits $4f^{-1}6snl$ Tm and scheme of autoionization decay of $4f^{13}6snl$ Tm autoionizing Rydberg states

The availability of two pairs of near-lying ionization limits (with vacancy states $4f^{7/2}$ and $4f^{5/2}$) provides two main types of AD:

- (BFD) $4f^{-1}_{5/2} 6s_{1/2} (J_{12}) nl - 4f^{-1}_{7/2} 6s_{1/2} [J'_{12}]$
 $Tm^+ + leje,$
 $n > 7 \quad J_{12} = 2; 3, J'_{12} = 3; 4$
- (ROD) $4f^{-1}_j 6s_{1/2} (J_{12}) nl - 4f^{-1}_j 6s_{1/2} [J'_{12}]$
 $Tm^+ + leje,$
 $n > 25 \quad J_{12} = 3, J'_{12} = 2; 4 \quad j = 5/2, 7/2.$

These AR decay channels are discussed in details in [6, 10]. ROD means the reorientation AR decay, and BFD means Beutler-Fano AR one. The states $4f^{-1}_{5/2} 6s_{1/2} (J_{12} = 3) nl$ undergo simultaneously both BFD and ROD. Remember that contrary to BFD, ROD is the low energy process preserving all the single electron quantum numbers of atomic residue: $4f^{-1}_j$ and $6s_{1/2}$. ROD can be of monopole or quadrupole character. We mean here the multipolarity of inter-quasi-particle interaction causing AD. The states with $J_{12} = 2; 4$ do not undergo ROD. Nevertheless, their admixture with states undergoing ROD can significantly amplify the monopole ROD. In table 2 we present the calculated values of energy E , autoionization width of the $4f^{7-1}/26s(3)ns, np$ Tm states ($n = 25$). For Rydberg series, the only possible AS decay is the reorientation one. Any two states of different parity can be mixed by external electric field. The mixing leads to redistribution of autoionization widths. In the case of degenerated or near-degenerated resonances this effect becomes

observable even at moderately weak field. In case of Tm we deal with reorientationally decaying ns and np series, converging to the same ionization limit, i.e. They are nearly degenerated states of different parity. Among them one can find some pairs of ns and np states with widths Γ , differing by several orders. We consider the $f^{-1}_{7/2} 6s(3)25s[5/2]$ state, decaying due to quadrupole interaction and $f^{-1}_{7/2} 6s(3)25p_{1/2}[5/2]$ undergoing to monopole ROD. The diagonalization of complex energy matrix leads to complex energy correction: $Re E - i\Gamma/2$, where $Re E$ is level shift, Γ is level width, including radiation and autoionization widths simultaneously. If the effects of AR decay are only included in the matrix M , then Γ presents only autoionization width of state. The results of relativistic [2] calculation of states widths are given in table 1 for different values of field strength. For comparison, the results of calculation [3] are also presented. The difference between the results of both calculations is connected with the more accurate account of relativistic effects. In our work. Naturally in weak electric field, strong change of the width of autoionization resonance occurs. Optimal scheme presumes a compromise between high excitation probability and high decay rate that determines the lower and the upper boundaries for AD rate.

References

1. Letokhov V. S. Nonlinear Selective Photoprocesses in atoms and molecules. — M., 1983. — 408 c.
2. Ambrosov S. V., Shpinareva I. M. Selective Ionization of Atoms by Electric and Light Field. Autoionization Rydberg Resonances in Heavy Atoms. Optimal Isotope-Separation Selective Molecular Vibration Levels Excitation Schemes // Proc. 32nd Europhys. Conference EGAS. — Vilnius (Lithuania). — 2000. — P. 197.
3. Shpinareva I. M. New Quantum Mechanical Method to Calculation of Autoionization Resonances in Heavy Atoms in Electric Field: Gd, Tm, U. Optimal Schemes of Selective Ionization of Atoms by Laser field // Proc. 5th Europ. Workshop «Quantum Systems in Phys. & Chem.». — Uppsala (Sweden). — 2000. — P. 131.
4. Glushkov A. V., Ivanov L. N. DC Strong-Field Stark-Effect: consistent quantum-mechanical approach // J. Phys. B: At. Mol. Opt. Phys. — 1993. — Vol. 26, № 16. — P. L379—386.
5. Glushkov A. V., Ivanov L. N. Radiation Decay of Atomic States: atomic residue and gauge noninvariant contributions // Phys. Lett. A. — 1992. — Vol. 170, № 1. — P. 33—37.
6. Glushkov A. V., Ambrosov S. V., Malinovskaya S. V. Calculations of spectroscopic characteristics of complex atoms in electric field // Proc. 5th Simp. on Atom. Spectra, Oscillator Strengths for Astrophys. & Laboratory Plasmas. — 1995. — P. 131; Bound Volume of Paris-Meudon Observatory. — Paris (France). — 1996. — P. 140—145.
7. Glushkov A. V., Malinovskaya S. V., Ambrosov S. V., Shpinareva I. M. and Troitskaya O. V. Resonances in Quantum Systems in Strong External Fields: Consistent Quantum Approach // J. Techn. Phys. — 1997. — Vol. 38, № 2. — P. 215—219.
8. Glushkov A. V., Ambrosov S. V., Borik S. A., Shpinareva I. M., Antonenko T. N. Resonances in Quantum Systems in Strong External Fields: Nonlinear Effects. Autoionization Resonances in Tm // J. Techn. Phys. — 1997. — Vol. 38, № 2. — P. 211—214.
9. Wojcik A., Parzynski R. Dark-state effect in Rydberg-atom stabilization // J. Opt. Soc. Amer. B. — 1995. — Vol. 12, № 3. — P. 369—376.
10. Vidolova-Angelova E., Ivanov L. N. Autoionizing Rydberg states of thulium. Re-orientation decay // J. Phys. B: At. Mol. Opt. Phys. — 1991. — Vol. 24. — P. 4147—4158.

Table 1

Autoionization width Γ for some values of field strength ε ($V \cdot cm^{-1}$)

State	$4f^{13}_{7/2} 6s_{1/2} 2(3)25s[5/2]$		$4f^{13}_{7/2} 6s_{1/2} 2(3)25p_{1/2}[5/2]$
	Present work	[3]	Present work
$E, \varepsilon = 0$	49854,7 cm^{-1}		49865,3 cm^{-1}
$\Gamma, \varepsilon = 0$	1,18D—05	1,18D—05	1,22D—01
$\Gamma, \varepsilon = 50$	1,28D—04	1,16D—04	1,21D—01
$\Gamma, \varepsilon = 100$	4,39D—04	4,27D—04	1,21D—01
$\Gamma, \varepsilon = 150$	10,25D—04	9,34D—04	1,20D—01

30/26 CONTENT

J. KAPPLER, N. BARSAN, U. WEIMAR. State of the Art of Gas Sensors — MOX sensors as a working example	3
V. GOLOVANOV, V. SMYNTYNA, V. BRINZARI, G. KOROTCENKOV. Cd _x S- and Sn _x WO ₃ -based gas sensors: the role of chemical composition in CO sensing	6
V. KOVALCHUK. Real nanodimensional silicon particles: cluster approximation	12
V. EVTEEV, M. MOISEENKO, E. ZHURAVEL, E. GLUSHKO. Two models of quantum bridges connected with semiconductors or metals	18
V. BORSHCHAK, N. ZATOVSKAYA, M. KUTALOVA, V. SMYNTYNA. Influence of photoexcitation on the parameters of surface potential barrier	25
V. ZAVADSKY, V. MOKRITSKY. CdHgTe grown by LPE for photoreceivers	29
A. NOSENKO, R. LESHCHUK. Luminescence of Ca ₃ Ga ₂ Ge ₄ O ₁₄ single crystals and thin films doped with Tb ³⁺ and Eu ³⁺ ions	31
P. FEDCHUK, I. CHEMYR, O. FEDCHUK, M. HORNEY. Semiconductor and liquid crystalline sensors in the problem of artificial intellect	34
V. DROZDOV, V. POZHIVATENKO, M. DROZDOV, A. TOTSKAYA. The Peculiarities of the First-Principal Pseudopotential in Metals	43
A. LYASHKOV, A. TONKOSHKUR, V. MAKAROV. Dielectric properties of ZnO—Ag ₂ O gas sensitive ceramics	45
A. GLOT, R. BULPETT, A. NADZHAFZADE, I. SKURATOVSKY. Electrical properties of tin dioxide based ceramics in humid air atmosphere	47
I. VIKULIN, L. VIKULINA, Sh. KURMASHEV. Photodetectors with frequency output on the basis of unijunction and field-effect phototransistors	50
S. FEDOSOV, A. SERGEEVA, V. SOLOSHENKO, P. PISSIS. Correlation between polarization and space charge phenomena in corona poled ferroelectric polymers	52
Sh. KURMACHEV, A. SOFRONKOV, A. GAVDZIK, S. GAYDA. Preparation of the Li _x Ni _{1-x} O-solution for gas sensors	56
Yu. VAKSMAN, Yu. NITSUK, Yu. PURTOV, S. IGNATENKO, Yu. KOROSTELIN, V. KOZLOVSKY, A. NASIBOV, P. SHAPKIN. Luminescence of zinc selenide single crystals doped with indium	58
E. NIKONYUK, V. SHLYAKHOVYI, M. KUCHMA, M. KOVALETS, Y. ZAKHARUK. The effect of self-purification in p—CdTe—Gd crystals	61
S. ZUBRITCKY, V. BEIZYM. Thermally stimulated luminescence of polycrystals ZnS	64
A. CHEBANENKO, V. GRINEVICH, L. PHYLEVSKAYA. The optimization methods for the electrooptic parameters of the ZnS transducers	66
A. PTASHCHENKO, F. PTASHCHENKO. Tunnel surface recombination in p—n junctions	69
V. TSMOTS, V. SHTYM. The Magnetic susceptibility of Si-Ni alloys rich on silicon: influence of phases distribution and their dispersity	72
Yu. VASHPANOV, V. SMYNTYNA. Study in degradation mechanism of adsorption sensitivity and increase of stability of oxygen microelectronic sensors	75
L. TERLETSKAYA, V. SKOBEEVA, V. GOLUBTSOV. Photosensors with Si—GaAs heterojunction as memory elements	78
V. GOLOVANOV, T. RANTALA, T. RANTALA, V. LANTTO. Rehybridization at (110) faces Of SnO ₂	80
V. BORSCH, V. IRKHA, G. MAKARENKO, V. GORBACHEV. Interaction of parameters in degradation of optoelectronic devices as interaction of parameters in composite system	84
V. DROZDOV, Yu. IVANOV, M. DROZDOV. To the investigation of the properties of cubic monocrystals	88
S. GEVELYUK, I. DOYCHO, M. KOVALENKO, D. LISHCHUK, V. MAK, L. PROKOPOVICH, V. CHISTYAKOV. Influence of g-irradiation on photoluminescence of porous germanium obtained by treatment in electric spark discharge	91
P. GORLEY, O. PARFENYUK, M. ILASHCHUK, K. ULYANYTSKY, V. BURACHEK. Electric and photoelectric properties of CdTe:V crystals	95
N. MALUSHIN, V. SKOBEEVA, V. SMYNTYNA, A. DALI. Residual photoconductivity effect in semi-insulator films ZnSe _x Te _{1-x}	98
A. GLUSHKOV, A. FEDCHOUK, I. KUKLINA. Stochastic dynamics of atomic systems in magnetic field. Zeemane effect for Wannier—Mott excitons	100
A. GLUSHKOV, S. AMBROSOV, V. IGNATENKO. Nonhydrogenic atoms and Wannier—Mott excitons in DC electric field: photoionization, stark effect, resonances in ionization continuum and stochasticity	103
I. SHPINAREVA. Selective photoionization of atoms and molecules in electric field: new models	107
A. LOBODA. Structure of ground state of superatom. Ionized superatom as single electrons counter	110
S. AMBROSOV. Selective photoionization of atoms by laser field: optimal scheme. Autoionization rydberg resonances in heavy atoms	112